

Liquid Layer Combustion Instabilities in Paraffin-Based Hybrid Rocket Fuels

A thesis accepted by the Faculty of Aerospace Engineering and Geodesy of the University of Stuttgart in partial fulfilment of the requirements for the degree of Doctor of Engineering Sciences (Dr.- Ing.)

by
Anna Petrarolo, M.Sc.
born in Terlizzi (Italy)

Committee chair: Prof. Dr.-Ing. Jörg Wagner
Committee members: Prof. Dr.-Ing. Stefan Schleichriem
Prof. Luciano Galfetti

Date of Defence: 23.10.2020

Institute of Space Systems
University of Stuttgart

2020

*Imagination is more
important than knowledge.
Knowledge is limited.
Imagination encircles the world.*
—Albert Einstein

Contents

List of Figures	vii
List of Tables	xii
Nomenclature	xiii
Abstract	xviii
Kurzfassung	xx
1 Introduction	1
1.1 Hybrid Rocket Engines	1
1.2 Research Motivation	5
1.3 State of the Art of Optical Investigations on Hybrids Combustion Process	6
1.4 Objectives of the Work	11
1.5 Outline	11
2 Hybrid Combustion Theory	13
2.1 Diffusion Limited Model	13
2.1.1 Hybrid Combustion Model	14
2.1.2 Thermal Radiation Effects	19
2.1.3 Chemical Kinetics Effects	19
2.1.4 Pressure Effects	21
2.1.5 Regression Rate Behaviour	21
2.2 Liquefying Hybrid Theory	22
2.2.1 Entrainment Model	23
2.2.2 Liquid Layer Stability	28
2.3 Extended Hybrid Theory	32
3 Kelvin-Helmholtz Instability and Droplets Entrainment	35
3.1 Mechanism of Liquid Film Destabilization	35
3.2 State of the Art of Flow Instabilities and Droplets Entrainment	36
3.2.1 Atomization Mechanism of a Liquid Film	36
3.2.2 Shear Flow Instabilities	41
3.3 Parameters Affecting Kelvin-Helmholtz Instability	45
3.4 Theoretical Models	46

4	Decomposition Methods	49
4.1	Proper Orthogonal Decomposition	49
4.1.1	Motivation	49
4.1.2	NIPALS Algorithm	52
4.2	Independent Component Analysis	54
4.2.1	Motivation	54
4.2.2	FastICA Algorithm	57
4.3	A Practical Example	59
4.3.1	POD vs. ICA	59
4.3.2	Choice of the contrast functions for ICA	63
5	Experimental Activity Set-Up	67
5.1	Paraffin-Based Fuels Properties	67
5.1.1	Investigated Paraffin-Based Fuels	67
5.2	Paraffin-Based Fuels Characterization	68
5.2.1	Viscosity Measurements	69
5.2.2	Surface Tension and Liquid Density Measurements	71
5.2.3	Thermogravimetric Analysis and Differential Scanning Calorimetry	74
5.3	Experimental Set-Up and Data Acquisition	77
5.3.1	Atmospheric Combustion Facility	77
5.3.2	Pressurized Combustion Facility	78
5.3.3	Test Bench Control System and Test Sequence	79
5.3.4	Combustion Tests Set-Up	80
6	Combustion Tests Analysis	83
6.1	Combustion Video Analysis	83
6.1.1	High-Speed Videos	83
6.1.2	CH* Chemiluminescence Videos	89
6.2	Test Data Analysis	90
6.3	Challenges and Limitations of the Analysis	91
7	Results and Discussion	95
7.1	Theoretical Results	95
7.1.1	Kelvin-Helmholtz Instability Onset	95
7.1.2	Boundary Layer Thickness and Flame Position	100
7.2	Algorithms Configuration	101
7.2.1	Choice of the Components Number	102
7.2.2	Choice of the Contrast Function for ICA	107
7.2.3	Interpretation of the Components	108
7.3	Experimental Results of Atmospheric Combustion Tests	116
7.3.1	Study on the Liquid Film Destabilization	117
7.3.2	Flame Characteristics	132
7.3.3	Analysis of the Burning Phases	141
7.4	Experimental Results of Pressurized Combustion Tests	143

8	Conclusions and Future Developments	153
8.1	Overview	153
8.2	Main Findings of the Study	154
8.3	Outlook	157
	Bibliography	159
A	Appendix	167
A	Sensors and Measurement Devices List	167
	Acknowledgements	175
	Curriculum Vitae	180

List of Figures

1.1	Classical hybrid rocket system configuration	2
1.2	Necessary features to make hybrids competitive	4
1.3	Burning fuel image	7
1.4	Thickness of the visible flame at atmospheric (top) and elevated (bottom) pressures	8
1.5	Video images taken during combustion at 70 psi: nominal combustion (left) and blowing event (right)	8
1.6	Schlieren images taken during combustion at 40 psi (left) and 70 psi (right)	8
1.7	Boundary layer edge (blue), flame location (magenta) and original fuel position (orange) overlaid on grayscale Schlieren and OH* images	8
1.8	Paraffin combustion at 1.9 MPa and 50 kg/m ² s	9
1.9	Combustion image of paraffin-based fuel during ignition at atmospheric pressure	9
2.1	Diffusive flame structure in a hybrid rocket engine	14
2.2	Thermo-physical processes near the surface of a conventional hybrid fuel	15
2.3	Blocking effect dependence on the blowing parameter B	17
2.4	Variation of the regression rate with the total mass flux	22
2.5	Entrainment of droplets from the melt liquid layer in a liquefying fuel	23
2.6	Liquefying fuel combustion image created within this research	23
2.7	Normal alkanes expecting to exhibit high regression rate	24
2.8	Schematic of the thermal model used by Karabeyoglu in the melt layer thickness estimation	24
2.9	Effect of regression rate and slab temperature on the melt layer thickness for pentane	28
2.10	Schematic of the stability model	29
2.11	Amplification curves for various liquids	31
2.12	Blocking factor correction as a function of the blowing parameter	33
2.13	Liquid layer theory predictions for vaporization, entrainment and total regression rates for four pentane tests	34
2.14	Space-time averaged regression rate vs. average oxidizer mass flux for various liquefying materials and HTPB	34
3.1	Mechanism of liquid film destabilization and breakup	36

3.2	Comparison of various entrainment correlations for water-airflow at 15 °C	37
3.3	Wavelets atomization mechanism	38
3.4	Wavelets displacement	38
3.5	Various entrainment mechanism	39
3.6	Schematic inception boundary for a particular combination of liquid and gas	40
3.7	Horizontal velocity profiles	42
3.8	Induced vertical motion at the interface	42
3.9	Amplification curves for various film Reynolds numbers for pentane	44
3.10	Non-dimensional amplification rate as a function of wave number	44
3.11	Representation of the 2D unbounded model	46
3.12	Representation of the 2D bounded model	47
4.1	Decomposition process: collection of scores and loadings	53
4.2	Principal components in the case of two variables	53
4.3	Vector matrix representation of the mixing process for tICA and sICA	56
4.4	Source signals	60
4.5	Linearly mixed signals (top) and computed source signals with PCA (middle) and ICA (bottom)	60
4.6	PSD of the principal components (PCA) of the linearly mixed signals	61
4.7	PSD of the independent components (ICA) of the linearly mixed signals, computed with G_3	61
4.8	Non-linearly mixed signals (top) and computed source signals with PCA (middle) and ICA (bottom)	62
4.9	PSD of the principal components (PCA) of the non-linearly mixed signals	62
4.10	PSD of the independent components (ICA) of the non-linearly mixed signals, computed with G_3	63
4.11	PSD of the independent components of the linearly mixed signals, computed with different contrast functions	65
4.12	PSD of the independent components of the non-linearly mixed signals, computed with different contrast functions	66
5.1	Different fuel configurations used in this research	68
5.2	20° FFR fuel slab before (top) and after (bottom) combustion test	69
5.3	Rotational rheometer and cone-plate geometry used in the framework of this research	70
5.4	Viscosity of paraffin 6805 with different additives at a constant shear rate	70
5.5	Tensiometer used in the framework of this research	72

5.6	Surface tension of paraffin 6805 with different additives	72
5.7	Liquid density of paraffin 6805 with different additives	73
5.8	Thermal analyzer used in the framework of this research	75
5.9	TGA and DSC measurements of pure paraffin 6805	76
5.10	TGA and DSC measurements of 6805+5% polymer	76
5.11	Sideview of the atmospheric combustion chamber set-up	77
5.12	Combustion chamber set-up with optical diagnostic	78
5.13	Sideview of the pressurized combustion chamber set-up	79
5.14	Pressurized combustion chamber set-up	80
5.15	Feed-line scheme of the test bench M11.3	81
6.1	Video pre-processing steps	84
6.2	PSD of time and space coefficients coming from the POD	86
6.3	PSD of time and space coefficients coming from the sICA	87
6.4	Contour plots of the space coefficients coming from the POD applied to high-speed videos	88
6.5	Contour plots of the space coefficients coming from the POD applied to CH* videos	90
6.6	Typical pressure (top) and oxidizer mass flow (bottom) time traces from combustion test	91
7.1	Neutral curve of pure paraffin 6805 for the inviscid unbounded model	96
7.2	Neutral curve of 6805+5%polymer for the inviscid unbounded model	96
7.3	Neutral curve of pure paraffin 6805 for the viscous bounded model	97
7.4	Neutral curve of 6805+5%polymer for the viscous bounded model	98
7.5	Influence of OF and fuel viscosity on the critical gas speed . .	98
7.6	Neutral curve of pure paraffin 6805 at $OF = 2$	99
7.7	Influence of OF on the critical gas speed for pure paraffin 6805 for each model	99
7.8	Boundary layer thickness δ versus distance x for various values of B	101
7.9	Boundary layer thickness δ versus distance x for various values of \dot{m}_{Ox}	101
7.10	Energy fraction associated to each POD mode	103
7.11	Cumulative energy fraction associated to each POD mode . .	103
7.12	First POD mode, representing the average flame structure . .	103
7.13	Frame 20001 of test 203, original and reconstructed	104
7.14	Frame 20001 of test 203, original and reconstructed	106
7.15	Frame 20001 of test 203, original and reconstructed	107
7.16	Contour plots and PSD of the first 3 spatial independent com- ponents (sICA) of test 233, computed with G_1	109

7.17	Contour plots and PSD of the first 3 spatial independent components (sICA) of test 233, computed with G_2	110
7.18	Contour plots and PSD of the first 3 spatial independent components (sICA) of test 233, computed with G_3	111
7.19	Contour plots and PSD of the first 3 spatial independent components (sICA) of test 233, computed with G_4	112
7.20	Contour plots and PSD of the first 3 principal components (POD) of test 279	113
7.21	Contour plots and PSD of the first 3 spatial independent components (sICA) of test 279	114
7.22	Contour plots and PSD of the first 3 temporal independent components (tICA) of test 279	115
7.23	Fuel slab and combustion flame with 5° FFR	119
7.24	Fuel slab and combustion flame with 20° FFR	119
7.25	Fuel slab and combustion flame with 90° FFS	120
7.26	Flow field over a FFS	120
7.27	Contour plot and PSD of the POD modes of test 241	122
7.28	Contour plot and PSD of the POD modes of test 203	123
7.29	Contour plot and PSD of the POD modes of test 233	124
7.30	Contour plot and PSD of the POD modes of test 254	125
7.31	Dependency of the KHI frequencies on the fuel viscosity and oxidizer mass flow	126
7.32	Dependency of the KHI frequencies on the fuel viscosity and oxidizer mass flux	126
7.33	Dependency of the KHI longitudinal wavelengths on the fuel viscosity and oxidizer mass flow	127
7.34	Dependency of the KHI longitudinal wavelengths on the fuel viscosity and oxidizer mass flux	127
7.35	Critical gas speed curves with experimental values for 6805 (top) and 6805+5%polymer (bottom)	128
7.36	Critical mass flow curves with experimental values for 6805 (top) and 6805+5%polymer (bottom)	129
7.37	Experimental regression rate curves	130
7.38	Dependency of the KHI frequencies on the regression rate	131
7.39	Dependency of the KHI longitudinal wavelengths on the regression rate	131
7.40	Dependency of the regression rate on the fuel liquid viscosity	132
7.41	Combustion flame of 6805 (top) and 6805+5% polymer (bottom) taken from high-speed videos	133
7.42	Flame speed dependence on fuel composition and oxidizer mass flow	135
7.43	Flame surface length dependence on fuel composition and oxidizer mass flow	135

7.44	Flame height dependence on fuel composition and oxidizer mass flow	137
7.45	Average flame and fuel grain position for 6805 and 6805+5%polymer at three oxidizer mass flows	137
7.46	Regression rate dependence on liquid layer thickness for 6805 .	138
7.47	Boundary layer thickness δ and flame position versus distance x for 6805 and 6805+5%polymer at three oxidizer mass flows .	139
7.48	Contour plots of the first POD mode taken from CH* images .	140
7.49	PSD of the time coefficients of the first 12 POD mode of test 203	142
7.50	Combustion flame of the three burning phases taken from test 203	143
7.51	Contour plots of the first POD mode of test 203	144
7.52	Pressure and oxidizer mass flow time traces of Test 04	146
7.53	Pressure and oxidizer mass flow time traces of Test 01	147
7.54	Exhaust plume during a high-pressure firing test	147
7.55	Comparison of ignition combustion flames	148
7.56	Blowing event with droplets ejection from Test 01	149
7.57	Flame bursting event from Test 01	150
7.58	Comparison of steady-state combustion flames	151
A.1	Cone-plate geometry parameters given by the manufacturer . .	170
A.2	Measuring range of sensor given by the manufacturer	171
A.3	Schematic diagram of the Wilhelmy plate method	171
A.4	Sketch of the thermal analyzer used in the framework of this work	172

List of Tables

1.1	Comparison of chemical propulsion systems	3
1.2	Overview of the optical studies on hybrid combustion	10
5.1	Measured viscosity values at different temperatures	71
5.2	Measured surface tension values at different temperatures	73
5.3	Measured liquid density values at different temperatures	74
5.4	Automatic test sequence	81
7.1	Critical values for different fuels at different OF (inviscid un- bounded model)	96
7.2	Critical values for different fuels at different OF (viscous bounded model)	98
7.3	Combustion test parameters	116
7.4	Camera settings	117
7.5	Amplified frequencies and wavelengths from POD and ICA for 6805+5%polymer at $\dot{m}_{Ox} = 50$ g/s	121
7.6	Experimental flame height compared to the theoretical bound- ary layer thickness	139
7.7	Combustion test parameters	144
7.8	Camera settings	145
A.1	Photron Fastcams specifications	167
A.2	Pressure sensors used in the atmospheric optical combustion chamber set-up	168
A.3	Pressure sensors used in the pressurized optical combustion chamber set-up	168
A.4	Coriolis mass flow meter specifications	169
A.5	Tensiometer specifications	172
A.6	Thermal analyzer specifications	173

Nomenclature

Abbreviations

AP	Ammonium Perchlorate
CEA	Chemical Equilibrium with Applications
DLR	Deutsches Zentrum für Luft-und Raumfahrt
DSC	Differential Scanning Calorimetry
FFR	Forward-Facing Ramp
FFS	Forward-Facing Step
FFT	Fast Fourier Transform
GOX	Gaseous Oxygen
HDPE	High-Density PolyEthylene
HTPB	Hydroxyl-Terminated PolyButadiene
HRE	Hybrid Rocket Engine
ICA	Independent Component Analysis
KER	Kerosene
KHI	Kelvin-Helmholtz Instability
LOX	Liquid Oxygen
LT	Low melting point Thermoplastics fuel
MO	Mineral Oil
NASA	National Aeronautics and Space Administration
PE	Polyethylene
PMMA	Poly-Methyl Methacrylate
POD	Proper Orthogonal Decomposition
PSD	Power Spectral Density
PUF	PolyUrethane Foam
SEBS	Styrene Ethylene Butadiene Styrene
SPLab	Space Propulsion Laboratory
TGA	ThermoGravimetric Analysis
VS1	vortex shedding produced at the beginning of the fuel ramp
VS2	vortex shedding produced at the end of the fuel ramp

Symbols

A	POD modes time series matrix, ICA mixing matrix [-]
<i>A</i>	constant for the perturbation expression, [-]
<i>A_b</i>	burning area [m ²]
<i>B</i>	blowing parameter [-]
<i>B_t</i>	transfer mass number [-]
<i>C_f</i>	friction coefficient [-]
<i>C_{f0}</i>	friction coefficient without blowing [-]
<i>C_h</i>	heat exchange coefficient
<i>Da</i>	Damköhler number [-]
E	errors/noise matrix [-]
<i>G</i>	mass flux [kg/(m ² s)]
<i>K_{0,1,2}</i>	Dispersion relation constants, [-]
<i>L_f</i>	solid grain length [m]
<i>M</i>	mean molecular mass of the combustion products [g/mol]
<i>Nu</i>	Nusselt number [-]
<i>OF</i>	mixture ratio [-]
P	loadings matrix [-]
<i>P_d</i>	dynamic pressure [bar]
<i>Pr</i>	Prandtl number [-]
<i>Q_{rad}</i>	total collimated radiative flux [W/m ²]
<i>R</i>	universal gas constant [J/(K mol)]
<i>Re</i>	Reynolds number [-]
<i>Re_f</i>	film Reynolds number [-]
<i>Re_x</i>	free-stream Reynolds number [-]
S	source components matrix [-]
<i>Sr</i>	Strouhal number [-]
T	scores matrix [-]
<i>T</i>	temperature [K]
<i>T_f</i>	flame temperature [K]
<i>U</i>	mean axial velocity [m/s]
<i>U_c</i>	critical gas flow speed [m/s]
W	ICA un-mixing matrix [-]
X	video data matrix [-]
<i>ΔM_f</i>	total mass of the fuel burned [kg]
<i>Δh</i>	enthalpy absorbed in the combustion [J/kg]
<i>ṁ</i>	mass flow rate [kg/s]
<i>q_r</i>	radiation flux [W/m ²]
<i>q_s</i>	heat flux on the fuel surface [W/m ²]
<i>a</i>	first power law interpolation coefficient
<i>b</i>	liquid blowing parameter [-]
<i>c</i>	average speed of sound in the chamber [m/s]
<i>c_f</i>	skin-friction coefficient [-]

c_p	specific heat at constant pressure [J/kg K]
d	diameter [m]
d_i	initial port diameter [m]
f	frequency [Hz]
g_0	gravitational acceleration [m/s ²]
h	enthalpy [J]
h_L	thickness of the liquid layer [mm]
h_m	latent heat of melting of the fuel [J/kg]
h_v	latent heat of vaporization of the fuel [J/kg]
k	mean specific heat ratio of the exhaust gases [-]
k_g	gas thermal conductivity [W/(m K)]
m	mass [kg]
n	second power law interpolation coefficient
p_c	combustion chamber pressure [bar]
r_f	regression rate [mm/s]
t	time, [s]
u_e	free stream velocity [m/s]
u_T	friction velocity [m/s]
x	longitudinal coordinate, [m]
y	vertical coordinate, [m]

Greek Symbols

α	wave number [1/m]
$\alpha_{l,s}$	absorption coefficient of liquid/solid phase [1/m]
β	amplification parameter [1/s]
γ	specific heat ratio [-]
δ	characteristic thermal thickness, boundary layer thickness [mm]
ε	emissivity coefficient [-]
η	efficiency [%]
κ	wave number [1/m]
$\kappa_{l/s}$	thermal diffusivity of liquid and solid phase [m ² /s]
λ	longitudinal wavelength [mm], thermal conductivity [W/(m K)]
λ_c	critical wavelength [cm]
μ	dynamic viscosity [Pa s]
ν	kinematic viscosity [m ² /s]
ρ	density [kg/m ³]
σ	surface tension [J/m ²]
σ_{SB}	Stefan-Boltzmann constant [W/(mm ² K ⁴)]
τ_{bl}	boundary layer delay time [s]
Φ	POD modes matrix [-]
φ	stream function [m ² /s]
ω	wave frequency, [1/s]

Subscripts

<i>I</i>	imaginary part
<i>Ox</i>	oxidizer
<i>R</i>	real part
<i>VS</i>	vortex shedding
<i>a</i>	ambient
<i>b</i>	burning
<i>c</i>	chamber
<i>conv</i>	convective
<i>e</i>	free stream
<i>ent</i>	entrainment
<i>ex</i>	exhaust
<i>f</i>	fuel
<i>fl</i>	flame
<i>g</i>	gas phase
<i>i</i>	initial
<i>inj</i>	injector
<i>l</i>	liquid phase
<i>m</i>	melting
<i>rad</i>	radiative
<i>s</i>	solid phase
<i>t</i>	throat
<i>v</i>	vaporization
<i>w</i>	wall

Abstract

In recent years, there has been a renewed interest in hybrid rocket propulsion due to its peculiar safety, costs and environmental advantages. Due to the fact that the propellants are stored in two different states of matter, hybrids are safer than solid motors. This also contributes to reduce the total costs of the engine. Moreover, they are characterized by controllable thrust, including shut-off and restart capability. With respect to liquid engines, they are mechanically simpler and, consequently, cheaper. Finally, they have increased performance compared to solids and generally a specific impulse nearly comparable to liquid systems. Unfortunately, this technology presents some disadvantages, due to the characteristic diffusive flame mechanism, like poor regression rate performance for conventional polymeric fuels, time varying parameters and scaling difficulties. However, most of these drawbacks can be solved through a correct design process and by choosing convenient approaches.

This work is focused on the study of the combustion mechanism of a class of fast-burning fuels, the so-called liquefying fuels. They are characterized by low viscosity and surface tension and they experience a different combustion mechanism with respect to conventional polymeric fuels. They form a thin liquid layer on the fuel surface during the combustion. It is expected that the low viscosity and surface tension of the liquid fuel enable an additional mass transfer by entrainment of liquid droplets. The gas flow over the surface induces liquid layer instabilities (Kelvin-Helmholtz instability) which produce the droplets entrainment. The entrainment mechanism works like a spray injection along the length of the motor, which increases the effective fuel burning area and reduces the blocking effect given from the pyrolysis of the fuel. Unfortunately, this phenomenon has not been well understood yet and still needs to be fully characterized. Current theoretical models are not able to accurately predict the burning rate of a hybrid rocket fuel without a rigorous test campaign for the desired propellant combination. On the other hand, in order to build-up some accurate models, it is necessary to experimentally quantify the inputs of the theoretical equations, such as the location of the flame in the boundary layer or the liquid and boundary layer thicknesses.

The main goal of this research is to better characterize the hybrid combustion process and, therefore, facilitate the development of more accurate burning models. Particular attention is paid to understanding the relation between the unstable waves that enable the droplets entrainment process and the regression rate. In order to do so, optical investigations on the com-

bustion behaviour of different paraffin-based hybrid fuels burning with GOX (Gaseous Oxygen) are performed at the test complex M11 of the German Aerospace Center (DLR), Institute of Space Propulsion in Lampoldshausen. First, the main parameters influencing the fuel droplets entrainment and, consequently, the burning process are identified. A theoretical study on the Kelvin-Helmholtz instability mechanism, which controls the formation of unstable roll-waves and the liquid-layer break-up process, is performed. In this way, the theoretical stability limit and entrainment onset for the investigated fuels are found. Second, a detailed characterization of the paraffin samples is necessary, since the entrainment process is found to strongly depend on the fuel properties. Liquid viscosity, surface tension and density of the paraffin-based fuels used in this research are evaluated in the M3 chemical laboratory at the DLR Lampoldshausen. Finally, four main test campaigns are run with two different combustion chamber set-ups, two 2D slab burners working at atmospheric and at elevated operating pressures. The main focus of the experimental combustion tests is to separately study the dependence of the burning process on four main parameters: fuel slab configuration (forward-facing step angle), fuel slab composition (mainly viscosity), oxidizer mass flow and combustion pressure. High-speed videos are recorded and analyzed with two different decomposition algorithms, which allows to get insights into the main combustion processes. In particular, Proper Orthogonal Decomposition (POD) and Independent Component Analysis (ICA) are applied to the scalar field of the flame luminosity. The results show that the combustion is dominated by periodic, wave-like structures for all the investigated operating conditions. Frequencies and wavelengths characterizing the liquid melt layer depend on the identified experimental parameters, especially on fuel viscosity and oxidizer mass flow. Moreover, for very low mass flows, no wavelength peaks are detected for the higher viscosity fuels. A dependency of the entrainment rate, which partially influences the regression rate, on the most excited frequencies and longitudinal wavelengths is also found. This is important to better understand the relation between the increased regression rate and the onset and development of the entrainment process, which is connected to the amplification of longitudinal unstable waves caused by the high velocity gas flow over the fuel surface.

Kurzfassung

In den letzten Jahren stieg das Interesse an Hybridrakentriebwerken wieder an, vor allem wegen ihrer sicheren Handhabung sowie der Kosten- und Umweltvorteile. Da die Treibstoffe in zwei unterschiedlichen Aggregatzuständen gelagert werden, sind Hybridtriebwerke sicherer als Feststoffmotoren. Dies reduziert die Gesamtkosten des Triebwerks stark. Charakteristisch ist zudem die Möglichkeit der Schubregelung, mit der Möglichkeit der Abschaltung und Wiederzündbarkeit. Verglichen mit Flüssigtriebwerken sind Hybridtriebwerke mechanisch einfacher und dadurch billiger. Letztlich haben sie eine verbesserte Leistung verglichen mit Feststoffraketen, und im Allgemeinen einen spezifischen Impuls der fast die Werte von Flüssigantrieben erreicht. Bedauerlicherweise hat diese Technologie auch einige Nachteile, Grund hierfür sind die typischen Diffusionsflamme, eine schlechte Abbrandrate bei konventionellen polymeren Treibstoffen, zeitlich variierende Parameter und Skalierungsschwierigkeiten. Allerdings lassen sich die meisten Nachteile durch einen guten Entwicklungsprozess und geeignete Annäherungen nivellieren.

Diese Arbeit setzt den Fokus auf die Verbrennungsmechanismen einer Klasse von schnell abbrennenden Treibstoffen, den sogenannten “liquefying fuels”. Es handelt sich hierbei um Treibstoffen, die durch eine niedrigere Viskosität und Oberflächenspannung charakterisiert sind. Hierbei treten verglichen mit konventionellen polymeren Treibstoffen, andere Verbrennungsmechanismen auf. Sie formen während der Verbrennung eine dünne geschmolzene Schicht auf der Treibstoffoberfläche. Man geht davon aus, dass die niedrige Viskosität im Verbund mit der niedrigen Oberflächenspannung des verflüssigten Treibstoffes, einen zusätzlichen Masseintrag durch das Eintragen von Flüssigkeitstropfen verursacht. Der Gasstrom über die Oberfläche induziert Instabilitäten in der Flüssigschicht (Kelvin-Helmholtz Instabilitäten) welche die Tropfenbildung verursachen. Dieser Mechanismus funktioniert wie eine Sprühinjektion über die Länge des Motors, welches die effektive Verbrennungsoberfläche des Treibstoffes erhöht und den Blockierungseffekt der Pyrolyse reduziert. Leider wird dieses Phänomen noch nicht sehr gut verstanden und muss noch besser untersucht werden. Aktuelle theoretische Modelle sind, ohne eine gründliche Testkampagne für die gewünschte Treibstoffkombination, nicht in der Lage, die Abbrandrate von Hybridmotoren korrekt vorherzusagen. Ebenso ist es nötig um akkurate Modelle aufbauen zu können, die Eingangswerte der theoretischen Gleichungen experimentell zu quantifizieren.

Das Hauptziel dieser Studie ist es, die hybriden Verbrennungsprozesse besser zu beschreiben und dadurch die Entwicklung exakterer Verbrennungsmo-

delle zu erleichtern. Besondere Aufmerksamkeit wird dabei auf das Verständnis der Beziehung zwischen den instabilen Wellen in der Flüssigkeitsoberfläche, welche den Tropfeneintragsprozess ermöglichen, und der Abbrandrate gelegt. Dafür werden am Prüfstand M11 des Deutschen Zentrums für Luft- und Raumfahrt e.V. (DLR), Institut für Raumfahrtantriebe in Lampoldshausen, optische Untersuchungen des Verbrennungsprozesses verschiedener paraffinbasierter Hybridtreibstoffe, die mit gasförmigem Sauerstoff (GOX) verbrennen, durchgeführt. Zunächst werden die Hauptparameter, welche den Treibstofftropfeneintrag und dadurch auch den Verbrennungsprozess beeinflussen, identifiziert. Eine theoretische Studie des Mechanismus der Kelvin-Helmholtz Instabilitäten wird durchgeführt. Diese beeinflussen die Bildung von instabilen Rollwellen sowie die Prozesse die zum Aufbrechen der Flüssigkeitsschicht führen. Auf diese Art werden die theoretischen Stabilitätslimits und der Beginn des Tropfeneintrags für die untersuchten Treibstoffe gefunden. Des Weiteren ist eine detaillierte Charakterisierung der Paraffinproben nötig, da sich herausstellt, dass der Eintragprozess sehr stark von den Treibstoffeigenschaften abhängt. Viskosität, Oberflächenspannung und Dichte der verflüssigten paraffinbasierten Treibstoffe die in dieser Untersuchung verwendet werden, wurden im M3 Chemielabor des DLR Lampoldshausen evaluiert. Schließlich, werden vier Haupttestkampagnen mit zwei unterschiedlichen Brennkammern, die bei atmosphärischem und erhöhtem Druck arbeiten, durchgeführt. Das Hauptaugenmerk der experimentellen Verbrennungstests liegt darin, die Abhängigkeiten des Verbrennungsprozesses von seinen vier Hauptparametern unabhängig voneinander zu untersuchen: die Konfiguration der verschiedenen Brennstoffplatten (Rampe am Brennstoff), die Zusammensetzung der Brennstoffe (hauptsächlich Viskosität), der Oxidatormassenstrom sowie der Verbrennungsdruck. Hochgeschwindigkeitsvideos wurden aufgenommen und mit zwei unterschiedlichen Zerlegungsalgorithmen analysiert, um einen Einblick in die Verbrennungsprozesse zu ermöglichen. Im Besonderen wurden die Verfahren der Proper Orthogonal Decomposition (POD) und Independent Component Analysis (ICA) auf das Skalarfeld der Flammenlumineszenz angewendet. Die Ergebnisse zeigen, dass die Verbrennung bei allen untersuchten operativen Bedingungen von periodischen, wellenmäßigen Strukturen dominiert wird. Die Charakterisierung von Frequenz und Wellenlänge der geschmolzenen Schicht hängt von den identifizierten, experimentellen Parametern ab, vor allem von der Viskosität und dem Oxidatormassenstrom. Ferner wurden für höherviskose Treibstoffe und niedrige Massenströme keine Extrema der Wellenlänge gefunden. Ebenfalls wurde eine Abhängigkeit der Tropfeneintragsrate, welche vor allem die Abbrandrate beeinflusst, von den am stärksten erregten Frequenzen und longitudinalen Wellenlängen gefunden. Dies ist wichtig um die Beziehung zwischen der erhöhten Abbrandrate und dem Beginn der Entwicklung des Eintragprozesses zu verstehen, letzterer hängt mit der Amplifizierung der longitudinalen, instabilen Wellen zusammen, welche vom Gasfluss, der mit hoher Geschwindigkeit über die Oberfläche strömt, verursacht werden.

1 Introduction

In this chapter, a short introduction about hybrid rocket engines design and technology is presented, in particular their general configuration working principles. Advantages and disadvantages with respect to solid and liquid propulsion are discussed. Objectives of the thesis are also presented. Finally an overview on the different chapters is given.

1.1 Hybrid Rocket Engines

Despite being born at the same time of solid and liquid propulsion systems, hybrid rocket engines (HRE) are still considered a “young” technology. In fact, they were the least used during the years because of historical reasons and consolidated habits. Only recently more studies have been conducted on hybrid propulsion.

A hybrid rocket engine is somehow placed between solid motors and liquid engines since propellants are stored in two different state of matter, solid and liquid (or gaseous). In the common configurations, referred as a “direct hybrid”, the fuel is solid and the oxidizer is liquid (or gaseous). The “reverse hybrid”, which is less common, presents the opposite propellant configuration, with a solid oxidizer and a liquid or gaseous fuel. The following dissertation will refer to direct hybrid engines. In a hybrid engine general configuration, shown in Fig. 1.1, the liquid oxidizer is stored in a pressurized tank, like in a liquid system, while solid fuel grain is stored into the combustion chamber, like in a solid motor. The oxidizer is injected by an injector into the head end of the combustion chamber where it reacts with the fuel vapours in the fluid-dynamic boundary layer developed along the surfaces of the solid fuel. Burning reactions are completed in a post combustion chamber. Reaction products are then accelerated through a gas-dynamic nozzle in order to generate the thrust.

Even if it is often claimed that hybrids combine the low performance of a solid motor and the complexity of a liquid engine, a well design hybrid could deliver a specific impulse higher than a solid and could be simpler than a liquid. It is, therefore, possible to say that hybrid engines combine some advantages and disadvantages of solid motors to those of the liquid engines. Some of the advantages of hybrid engines are:

- intrinsic safety in manufacturing, transportation, storage, testing and launch operation phases: fuel and oxidizer are stored remotely from

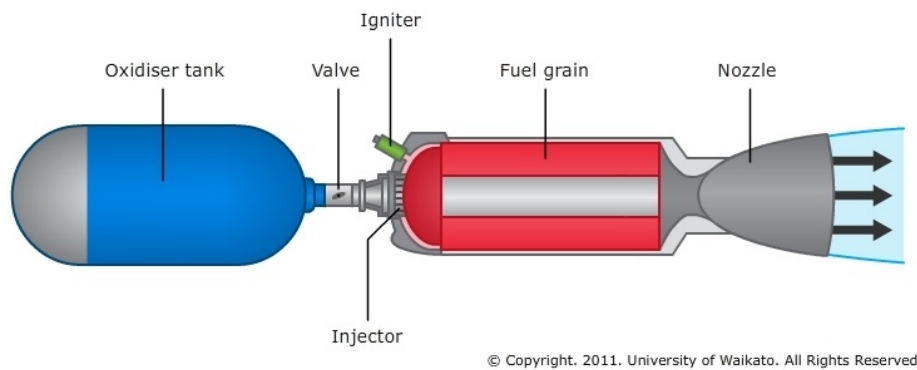


Figure 1.1: Classical hybrid rocket system configuration

each other in different phases thus eliminating the risk of accidental ignitions due to shocks, vibrations or static electricity;

- operational flexibility: possibility of throttling and controlling the motor thrust through a variation of the oxidizer mass flow rate and on/off capability. This feature implies a mission flexibility of hybrid engines with respect to the solid ones;
- low system cost: hybrid propellants are usually cheaper than solids and liquids. Moreover, transport, storage and safety costs are contained;
- higher specific impulse than solid rocket motor and higher volumetric specific impulse than some liquid engines;
- operational reliability: easier manufacturing with respect to liquid systems, higher fault tolerance of the solid grain and reduced thermal sensitivity with respect to solid motors (the combustion is not sensitive to cracks and debondings of the solid grain due to the diffusive flame situated inside the boundary layer and not on the fuel surface, thus eliminating the requirement for expensive quality control operations);
- reduced environmental impact: since green and non-hazardous materials can be easily used as propellants;
- more simplicity with respect to liquid engines: less sub-systems are required, for example no active cooling of the hybrid chamber is necessary since it is protected by the fuel grain;
- flexibility of propellants choice with respect to solid and liquid systems;
- good theoretical propulsive performance.

However, some drawbacks must be highlighted:

- time varying performances: mixture ratio changes during steady state operation and throttling leading to a variation of all propulsive performances. This is due to the diffusive nature of the flame that leads the regression rate to be primarily dependent on the oxidizer and fuel mass fluxes, which, in turn, depend on the time-varying burning area ($r_f \propto (1/A_b(t))^n$);
- poor regression rate performance for conventional fuels: this is due to the diffusive nature of the combustion process which is limited by the physical phenomena of heat and mass transfer from the flame zone to the fuel surface, thus making the fuel regression rate primarily mass flux dependent;
- scaling difficulties;
- possible instabilities (for solid and liquid as well).

A comparison of the advantages and disadvantages of the different chemical propulsion systems is shown in Tab. 1.1.

Table 1.1: Comparison of chemical propulsion systems

Solid Motor	Hybrid Engine	Liquid Engine
+ Simple design	+ Inherent safety	+ Highest <i>ISP</i>
+ Easy ignition	+ Flexibility	+ Flexibility
+ High volumetric <i>ISP</i>	+ Low system cost	+ Highest maturity
– No shut-off	+ Reliability	– Complex set-up
– Low safety	+ Medium <i>ISP</i>	
– Lowest <i>ISP</i>	+ Green propellants	
	+ Medium complexity	
	– <i>OF</i> -shift	
	– Scaling difficulties	

In order to be competitive with liquid and solid systems, hybrids need to have equal or better performance while retaining their simplicity, low cost and safety advantages (Fig. 1.2). In particular, these features make hybrid engines appreciable to all those missions requiring intrinsic safety and reliability as, for example, suborbital launchers with human crew for private access to space.

As stated before, good performance in hybrids are theoretically achievable but they can be practically limited due to their nature. In fact, since fuel and oxidizer are stored separately, the combustion in a hybrid engine is controlled by fluid dynamics and not by chemical reactions, as in solid and liquid systems. This leads to a diffusive flame which stands at a certain distance from the solid fuel surface, so that the combustion does not happen on the solid grain surface but in the reacting boundary layer, where the oxidizer and the

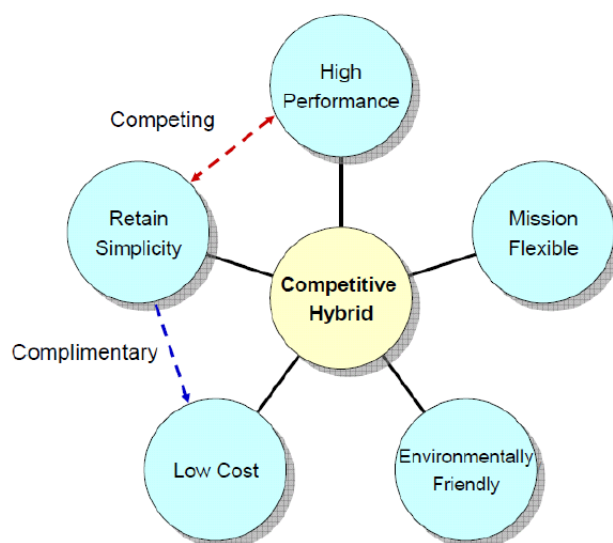


Figure 1.2: Necessary features to make hybrids competitive [46]

fuel vapours reach the stoichiometric mixture ratio. The energy released from the flame by convection and radiation, together with the continuous introduction of liquid oxidizer, causes the vaporization of the solid grain that, in turn, feeds the flame. This self-sustained combustion is, thus, limited by the processes of heat and mass transfer from the flame zone to the fuel surface and by the oxidizer mass flux, leading to the low regression rate that is typical of hybrids. The combustion products are then transported downstream by the convective flux and mixed with the fuel under the flame sheet and with the oxidizer over the flame sheet.

In order to overcome the problem of the low regression rate caused by the diffusive nature of the flame, which is the main disadvantage of hybrid engines, some solutions can be evaluated:

- use of fuel with low effective heat of gasification. However, this causes modest improvements since the exponent of the heat of gasification is a small number;
- increasing the burning area by using multi-perforated grains. However, this leads to a decrease in the mass of fuel that can be loaded into a given volume, an increase in complexity of the system and a decrease in the combustion efficiency due to the non uniform regression rate in each port. This anisotropy of the combustion leads to larger burning residuals and compromised grain integrity;
- increasing the turbulence and thus the heat transfer rates in the chamber. However, this complicates the design, increases the likelihood of failure and may lead to non uniform burning along the port;

- addition of swirl to increase the effective mass flux and thus improve the heat transfer rate. However, it causes uneven burning of the fuel and bring difficulties in scaling the engine;
- addition of oxidizing agent (such as ammonium perchlorate *AP*) or self decomposing materials in the hybrid fuel. However, this leads to a quasi-solid design eliminating the inherent safety characteristic of hybrid engines, in addition the regression rate becomes sensitive to chamber pressure;
- addition of metal additives to increase the fuel density and the radiative heat transfer to the fuel grain. However, it also increases two-phases losses, the vulnerability to instabilities (the regression rate might become pressure dependent) and the environmental impact;
- increasing the roughness of the burning surface by adding dispersed solid particles in the fuel, but large solid particles injected in the gas stream might reduce the efficiency of the system and fuel grain manufacturing costs would increase;
- formulation of a hybrid fuel that will generate mass transfer by mechanical means in addition to the mass transfer by direct gasification from the fuel surface, that is entrainment of liquid droplets into the gas stream for materials forming a low viscosity melt layer on their burning surface (liquefying fuels) [43]. The most important consequence of the high regression rate of liquefying fuels is that it becomes possible to design a relatively compact single port high thrust hybrid engine that can be competitive with other kinds of chemical propulsion systems in terms of performance while retaining its simplicity, low cost and safety advantages.

In this research the last solution is considered and an analysis of the liquid layer instability and entrainment processes is performed. In particular, the influence of different paraffin-based fuel compositions, oxidizer mass flows and combustion chamber pressures on the melt layer instability process is investigated with different optical techniques.

1.2 Research Motivation

As previously mentioned, the combustion process in a hybrid rocket engine is extremely complex. It occurs within the turbulent boundary layer over the fuel surface, where the diffusion flame is located. Modelling the kinetics of this kind of flame is not an easy task since it requires the knowledge of the pyrolysis products, as well as their reactions mechanisms with the oxidizer. The analysis becomes even more complex when liquefying fuels, instead of conventional

polymeric fuels, are considered. In this case, the model also needs to include the formation of a melt layer over the fuel surface, its instability mechanism with roll-wave formation, droplets entrainment and droplets combustion. On the other hand, experimental investigation on the hybrid combustion process under real operating conditions is also challenging. High temperatures combined with elevated pressures make it impossible to use in-situ diagnostics. For these reasons, combustion visualizations are a viable solution for studying the burning process within the turbulent boundary layer of a hybrid rocket engine under typical operating conditions. In the framework of this research, optical investigations with a 2D slab burner are performed with the aim of getting insights into the complex combustion phenomena taking place within a hybrid engine. The main focus will be on the visualization and investigation of the combustion flame under different operating conditions, with the intent of studying the liquid layer instability process within a hybrid rocket engine.

1.3 State of the Art of Optical Investigations on Hybrids Combustion Process

The discovery of liquefying hybrid rocket fuels has revitalized researches in hybrid propulsion and, in particular, in optical investigations of the hybrid rocket combustion process, in order to capture the entrainment process. To fully understand this phenomenon, it is necessary to adapt the liquid layer stability theory, extensively studied in the past [18, 14], to the typical operating conditions that are encountered in hybrid combustion. This means that the behaviour of liquid films has to be studied under strong blowing conditions and relatively high liquid Reynolds numbers. The Kelvin-Helmholtz instability (KHI) theory and the liquid layer break up process, which leads to the fuel droplet entrainment, have been well examined in the past [14, 18, 67, 38, 3, 23]. At high Reynolds numbers, a roll wave mechanism for the liquid entrainment is suggested [38]. More recently, Karabeyoglu et al. adapted these theories to the hybrid combustion process. Karabeyoglu's results [43, 44] confirmed those experimental findings. However, the dependence of the entrainment mass transfer on the experimental parameters is different in every study and needs to be assessed on a case-by-case basis. Consequently, many optical investigations on the hybrid combustion process have been performed in recent years.

In 2011, Nakagawa et al. investigated the dependence of the regression rate on the fuel viscosity. They performed optical tests at atmospheric pressure with different paraffin-based fuels and gaseous oxygen. Their images (Fig. 1.3) showed that droplets are generated during the combustion and entrained in the flow [66].

Pelletier investigated the combustion behaviour of paraffin-based fuels. He performed a theoretical film stability analysis and visualized the combustion

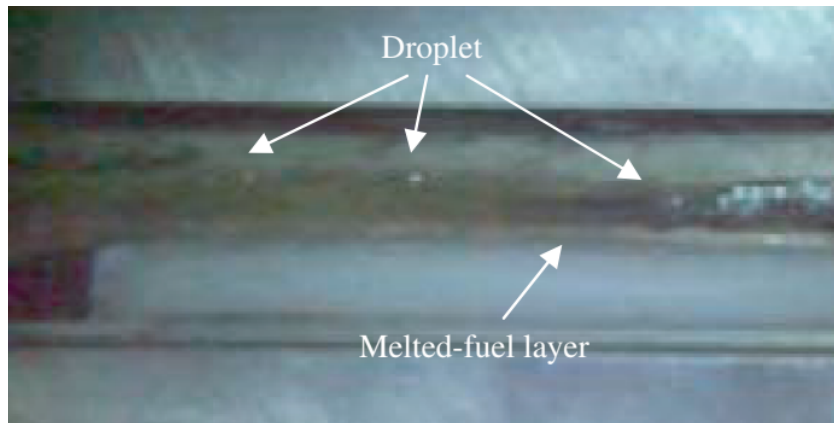


Figure 1.3: Burning fuel image (oxidizer flow from right to left) [66]

of the fuels with the use of an optical chamber. Droplets formation was observed during the tests, but no further correlation between the theory and the experiments is presented [69].

Many optical investigations on the combustion behaviour of both polymeric and paraffin-based hybrid rocket fuels have been done at the Stanford Combustion Visualization facility. In 2012, Chandler et al. investigated the combustion of paraffin-based fuels with gaseous oxygen at both atmospheric and elevated pressures. Their results showed roll waves and droplets in the atmospheric tests and filament-like structures along the sides of the fuel grains in the tests run at elevated pressures. The thickness of the visible flame was also manually measured at both atmospheric and elevated pressures. At higher pressures, they reported a thicker flame, which extends both above and below the fuel slab (see Fig. 1.4) [12]. In 2014-2016, many optical tests were conducted by Jens et al. with the same facility. They performed high-speed videos, Schlieren and OH^* images of the combustion of different classical polymeric and paraffin-based fuels in combination with gaseous oxygen at both atmospheric and elevated pressures [39, 42, 41, 40]. They reported unsteady blowing events of paraffin droplets in the tests at higher pressure, slightly above the critical pressure of their paraffin samples (Fig. 1.5). Schlieren results of their tests reported a thickening boundary layer with increasing pressure [39] (Fig. 1.6). Thanks to the simultaneous recording of Schlieren and OH^* images, they were able to detect from each test both the boundary layer height and the flame location (Fig. 1.7). They concluded that the flame location is decreasing with increasing combustion chamber pressure, for both classical polymeric and paraffin-based fuels [40].

Other experiments on the combustion of paraffin-based hybrid fuels have been also performed at the SPLab (Space Propulsion Laboratory) in Politecnico di Milano. They performed many combustion tests with an optical burner, in order to determine the instantaneous regression rate of different paraffin-based fuel grain samples. Thanks to a mirror set-up, it is possible

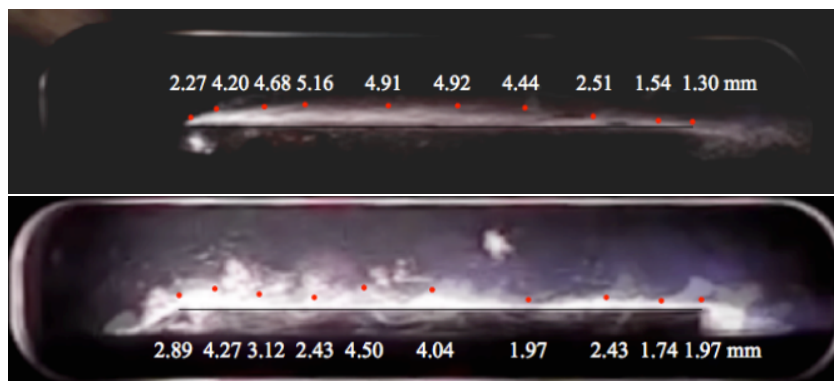


Figure 1.4: Thickness of the visible flame at atmospheric (top) and elevated (bottom) pressures (oxidizer flow from left to right) [12]

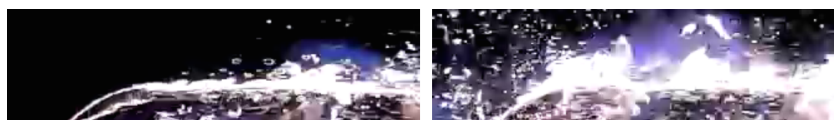


Figure 1.5: Video images taken during combustion at 70 psi: nominal combustion (left) and blowing event (right) (oxidizer flow from left to right) [39]

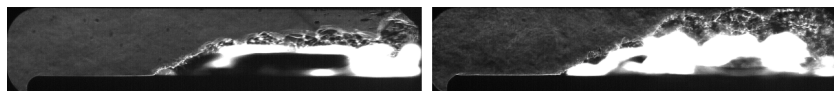


Figure 1.6: Schlieren images taken during combustion at 40 psi (left) and 70 psi (right) (oxidizer flow from left to right) [39]

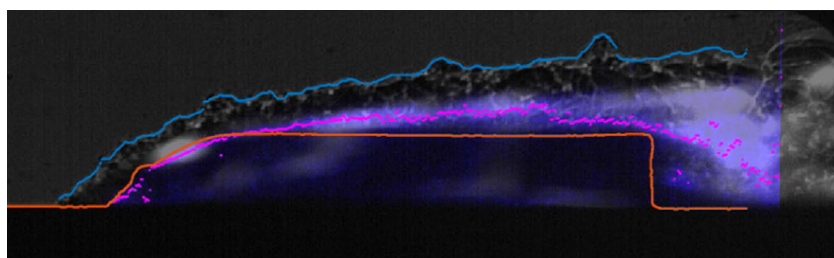


Figure 1.7: Boundary layer edge (blue), flame location (magenta) and original fuel position (orange) overlaid on grayscale Schlieren and OH* images (oxidizer flow from left to right) [40]

to look directly in the port diameter of the fuel grain. This allows them to record and, later, analyse the fuel port regression during the burning time [20]. Moreover, more tests have been also performed with another optical set-up. This consists of a double slab burner with side windows. In this case, space-time averaged regression rate measurements of different paraffin-based fuels have been taken and then compared. The aim was to develop hybrid

fuels combining at the same time good ballistics and mechanical properties [24].

In 2014, Wada et al. visualized the combustion of different polymeric and paraffin fuels at a pressure ranging from 1 up to 20 bar. In contrast to the other mentioned optical experiments, this set-up looks at the combustion of opposing slabs of fuel mounted vertically, see Fig. 1.8. From their observations, they concluded that both the number and size of the entrained droplets are independent of the chamber pressure [79].

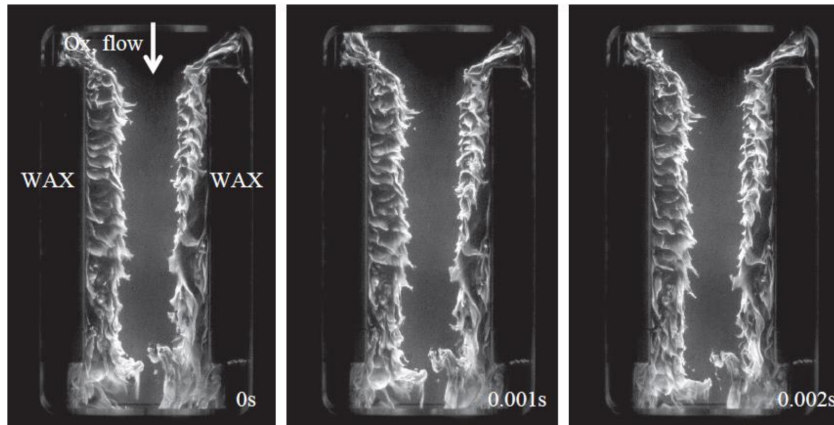


Figure 1.8: Paraffin combustion at 1.9 MPa and 50 kg/m²s [79]

Since 2013, many optical investigations have been conducted at the German Aerospace Center (DLR), Institute of Space Propulsion in Lampoldshausen. Kobald et al. performed visual and Schlieren images of the combustion of paraffin wax and gaseous oxygen at atmospheric pressure. They reported visualization of droplets entrainment during start-up and shut-down transients (Fig. 1.9) [51, 49]. Since 2015, in the framework of the present research, an automated video evaluation routine has been developed in DLR, in order to capture the dominant flow dynamic and combustion behaviour of paraffin-based hybrid rocket fuels during a typical test [54, 50, 71, 70]. This work will present and discuss these results.

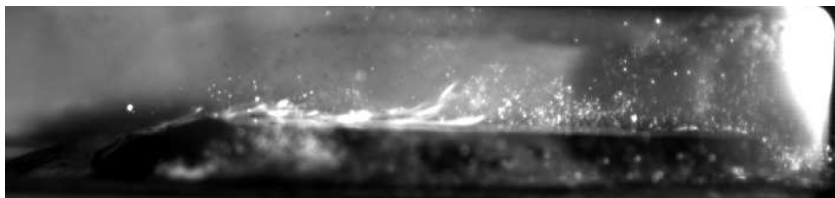


Figure 1.9: Combustion image of paraffin-based fuel during ignition at atmospheric pressure (oxidizer flow from left to right) [53]

An up-to-date overview of the optical studies conducted on hybrid rocket combustion is presented in Tab. 1.2.

Table 1.2: Overview of the optical studies on hybrid combustion

Reference	Fuel Config.	Fuel Comp.	Oxidizer	Pressure	Optical Set-Up	Droplets
Nakagawa et al. [66]	Single slab	Paraffin-based	GOX	1 bar	High-speed video	Yes
Pelletier [69]	Single slab	Paraffin-based			High-speed video	Yes
Chandler et al. [13], [12]	Single slab	Paraffin-based, HDPE, HTPB	GOX	up to 10 bar	High-speed video	Yes No
Jens et al. [42], [39], [40]	Single slab	Paraffin-based, HDPE, HTPB, PMMA	GOX	up to 15 bar	High-speed video, Schlieren images OH* images	Yes No
DeLuca et al. [20]	Single port grain	Paraffin-based, HTPB, isoprene rubber	GOX	up to 30 bar	High-speed video	Yes No
Merotto et al. [65]	Double slabs	Solid and gel wax, HTPB +nano-Al/ MgH_2	GOX	1.5 bar	Regression-rate measurements	
Galfetti et al. [24]	Single and double slabs	Solid and gel wax, HTPB +nano-Al/hydrides +PUF/KER +SEBS/MO/KER	GOX	1.5 bar	Regression-rate measurements	
Wada et al. [79]	Double vertical slabs	Wax, PMMA, GP/LT fuel	GOX	up to 20 bar	High-speed video with infrared filter	No
Kobald et al. [51], [54]	Single slab	Paraffin-based HTPB, HDPE	GOX	1 bar	High-speed video Schlieren images	Yes (during transients)

1.4 Objectives of the Work

As stated before, some hybrid rocket systems suffer from low regression rate, which, in turns, leads to low engine performance. In order to overcome this problem, different solutions have been suggested in the past years, but most of them make the whole engine design more complicated, thus losing one of the biggest advantages of hybrid engines. A simple and effective solution is the use of the so-called liquefying fuels that experience the entrainment phenomenon. These fuels, characterized by low viscosity and surface tension, are able to form along their burning surface a liquid layer, which can become unstable due to the high velocity gas flow in the fuel port. The unstable waves can break-up into droplets, which, in turns, get entrained into the gas flow. The entrainment is an additional regression rate mechanism that works like a spray injection along the length of the motor. This process increases the effective fuel burning area and reduces the blocking effect given from the pyrolysis of the fuel. Unfortunately, the combustion behaviour of this kind of fuels is not yet completely well understood, despite many numerical and experimental works done in the last years. In order to do so, it would be necessary to adapt the well-known liquid layer stability theory to the typical burning conditions in hybrid systems. However, until now, no general theoretical model exists for such a problem and the researchers are still trying to experimentally characterize the entrainment phenomenon on a case-by-case basis. The present study and its attempt to contribute to the knowledge of this process are inserted in this framework.

The main aims of this research are, first of all, to identify the main parameters influencing the entrainment mechanism; second, to understand the dependence of this process on the identified experimental parameters; third, to try to give a general rule that could be applied also to other cases. In order to do so, optical investigations on the combustion behaviour of different paraffin-based 2D fuel slab samples burning with GOX were performed. Various operating conditions and experimental parameters were tested, in order to identify those having a bigger influence on the combustion. The burning process was recorded with a high speed camera and the videos were analyzed with two different decomposition algorithms, which allow to get insights into the main combustion processes. From the results of this analysis, a strong influence of the fuel viscosity and oxidizer mass flow on the entrainment process was actually found. Moreover, a close dependence of the regression rate on the liquid layer instability mechanism was demonstrated.

1.5 Outline

The presentation plan of this work is as follow:

- **Chapter 1:** introduction to this work. A general overview on hybrid rocket engines technology is presented, together with the motivations

that have generated a renewed interest in studying hybrid propulsion. A brief state of the art of optical investigations on hybrids combustion process is also included. Finally, the objectives of the present work are shown.

- **Chapter 2:** explanation of internal ballistics of hybrid systems. A theoretical introduction into the combustion mechanism of hybrid rocket engines is given. The Marxman model for the regression rate of conventional polymeric fuels is presented. The entrainment phenomenon, which characterizes the recently discovered “liquefying fuels”, is also explained. Finally, the extended hybrid theory, which brings together both approaches, is discussed.
- **Chapter 3:** explanation of Kelvin-Helmholtz instability theory and droplets entrainment. In this chapter, the theory about the Kelvin-Helmholtz instability process, which leads to the entrainment process, is discussed. A brief state of the art of shear film instabilities and atomization mechanism of liquid films is also presented.
- **Chapter 4:** the decomposition methods used in this research (Proper Orthogonal Decomposition and Independent Component Analysis) for the analysis of the combustion videos are explained, together with the respective algorithms.
- **Chapter 5:** description of the propellant properties and experimental set-up. The paraffin-based fuels used in this research are presented, together with their properties (dynamic viscosity, surface tension, liquid density). The test-facilities (atmospheric and pressurized) used in this research are described.
- **Chapter 6:** description of the combustion tests analysis. The methodology used for the analysis of the video data is discussed step-by-step, for both high-speed and CH* chemiluminescence videos.
- **Chapter 7:** presentation and discussion of theoretical and experimental results.
- **Chapter 8:** conclusions of the work and discussion of possible future developments.

2 Hybrid Combustion Theory

In this chapter, theoretical models explaining the internal ballistics of hybrid rocket engines are presented. The flame structure and the classical hybrid combustion theory developed by Marxman is presented. The entrainment model of Karabeyoglu is also explained together with the stability analysis of the liquid layer. Finally the extended hybrid theory, which is a generalization of Marxman's model taking into account the entrainment phenomenon, is presented.

2.1 Diffusion Limited Model

The first theoretical model for hybrid combustion was proposed in 1946 by Bartel and Rannie; then, in the 60's, Marxman and colleagues developed the current reference model for the combustion in hybrid rocket engines [64, 63]. The model considers the presence of a turbulent diffusion flame in the zone of the boundary layer, where there is a combustible ratio between the injected oxidizer and the vaporized fuel. The energy released from the flame is transferred to the surface of the solid fuel grain by convection and radiation, allowing the vaporization of the fuel which reacts with the oxidizer in the boundary layer, thus supporting the combustion. The convective flow transports the combustion products downstream and mixes them with the oxidizer over the flame and with the fuel below the flame. So the flame divides the boundary layer into two regions: the first one from the fuel surface to the flame is fuel rich, the second one from the flame to the boundary layer edge is oxidizer rich. Theoretically the flame is assumed to have an infinitesimal thickness and to be a discontinuity for temperature and composition gradients. It is considered as a sheet located where the injected oxidizer and the gasified fuel reach the stoichiometric ratio. Actually, due to interdiffusion effects and to the finite chemical reaction velocity, the flame has a finite thickness and the gradients are continuous. The temperature increases monotonically going from the fuel surface to the flame, where it is roughly equal to the adiabatic flame temperature T_c ; while it monotonically decreases over the flame going to the boundary layer limit. It is important to note that the curvature of the temperature profile can change depending on the thermal model considered. The concentrations of fuel and oxidizer are maximum respectively on the fuel surface and on the upper limit of the boundary layer; then they monotonically decrease towards the flame where they cancel out if there is a stoichiometric ratio. The gaseous velocity, indeed, has the typical

trend of a boundary layer: it monotonically increases from the fuel surface (where it has a null value) to the free stream zone, out of the boundary layer (Fig. 2.1).

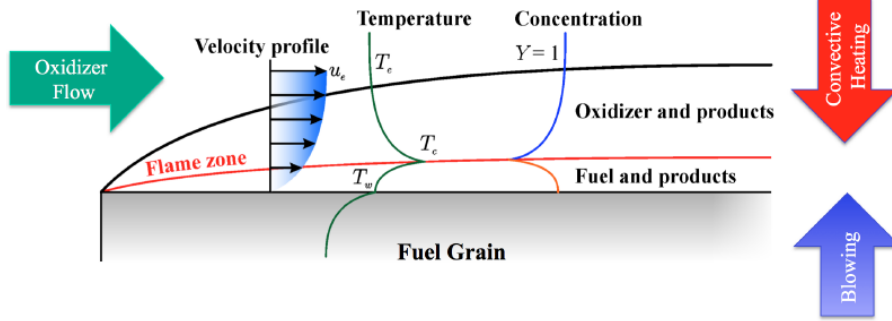


Figure 2.1: Diffusive flame structure in a hybrid rocket engine [10]

A more comprehensive model of the thermodynamic and physical processes near the surface of a conventional hybrid rocket fuel is given by Chiaverini [16] and can be seen in Fig. 2.2.

2.1.1 Hybrid Combustion Model

In order to obtain an expression for the regression rate in a hybrid rocket engine, it is possible to write the energy conservation balance on the fuel surface. Assuming quasi-steady conditions and neglecting the heat fluxes exchanged by radiation and conduction (only convection is considered), the following equation can be written:

$$\dot{q}_{g,s} = \rho_f r_f h_f \quad (2.1)$$

where $\dot{q}_{g,s}$ is the heat flux on the surface coming from the gas side, ρ_f is the fuel density, h_f is the fuel enthalpy of vaporization.

The heat flux evaluated in the boundary layer at the gas side is equal to:

$$\dot{q}_{g,s} = k_g \left. \frac{\partial T}{\partial y} \right|_{y=0} \quad (2.2)$$

where k_g is the gas thermal conductivity and the temperature gradient is computed in the direction normal to the surface of the fuel.

Applying the Reynolds analogy, which states that in a turbulent flow the transfer of enthalpy and momentum are similar, and assuming the hypothesis of boundary layer on a flat plate, the heat exchange coefficient on the surface C_h is linked to the surface friction coefficient C_f through the Prandtl number Pr , according to the following relation:

$$C_h = \frac{\dot{q}_{g,s}}{\rho_e u_e \Delta h} = \frac{Nu_x}{Pr Re_x} = \frac{C_f}{2} Pr^{-\frac{2}{3}} \quad (2.3)$$

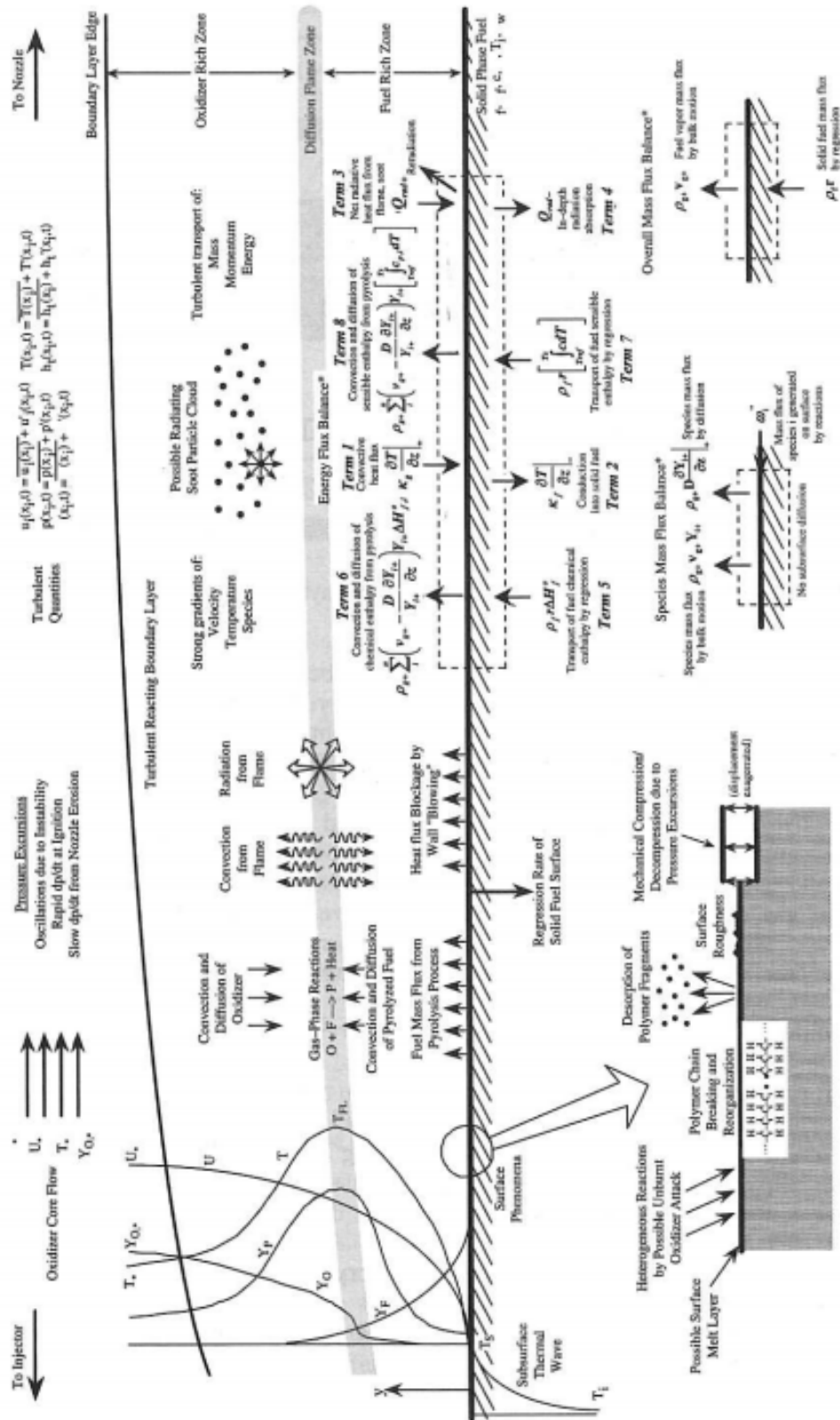


Figure 2.2: Thermo-physical processes near the surface of a conventional hybrid fuel [16]

where ρ_e and u_e are respectively the free stream density and velocity, $\Delta h = c_p \Delta T$ is the enthalpy absorbed in the combustion process computed as the enthalpy difference between the flame zone and the fuel surface, Nu_x , Pr and Re_x are the Nusselt, Prandtl and Reynolds numbers and x is the position along the fuel grain. The non-dimensional numbers are defined in the following equations:

$$C_f \equiv \frac{\tau_w}{\frac{1}{2}\rho_e u_e^2} = \frac{\mu \left(\frac{\partial u}{\partial y} \right)_{y=0}}{\frac{1}{2}\rho_e u_e^2} \quad (2.4)$$

$$C_h \equiv \frac{\dot{q}_{g,s}}{\rho_e u_e \Delta h} = \frac{h}{\rho_e u_e c_p} \quad (2.5)$$

$$Pr \equiv \frac{\nu}{\alpha} = \frac{c_p \mu}{k_g} \quad (2.6)$$

$$Nu_x \equiv \frac{h}{k_g/x} \quad (2.7)$$

$$Re_x \equiv \frac{\rho_e u_e x}{\mu} \quad (2.8)$$

Thus, Eq. 2.1 becomes:

$$\dot{q}_{g,s} = C_h \rho_e u_e \Delta h = \frac{C_f}{2} Pr^{-\frac{2}{3}} \rho_e u_e \Delta h = \rho_f r_f h_f \quad (2.9)$$

So obtaining the following expression for the regression rate r_f :

$$r_f = \frac{C_f \Delta h \rho_e u_e}{2 h_f \rho_f} Pr^{-\frac{2}{3}} \quad (2.10)$$

in which, for a turbulent flow, $Pr \simeq 1$.

Due to the continuous addition of fuel mass from the solid surface caused by its vaporization, it is necessary to consider a blowing boundary layer. This phenomenon causes a “blocking effect” that reduces the convective heat transfer and, consequently, the regression rate. In order to consider this phenomenon, the friction and the heat transfer coefficients, respectively C_f and C_h , must be corrected. Marxman experimentally derived the relationship between the friction coefficients with and without blowing $C_f/C_{f0} = C_h/C_{h0}$, which is called blocking factor:

$$\frac{C_f}{C_{f0}} = \left[\frac{\ln(1+B)}{B} \right]^{0.8} \left[\frac{1 + 1.3B + 0.364B^2}{(1+B/2)^2(1+B)} \right]^{0.2} \quad (2.11)$$

Here, B is the non-dimensional blowing parameter, which evaluates the importance of the mass flux injected transversely in the boundary layer with respect to the axial free stream flux and is defined as:

$$B \equiv \frac{\rho_s u_s}{\frac{C_f}{2} \rho_e u_e} = \frac{\rho_f u_f}{\frac{C_f}{2} G} = \frac{\dot{m}_f}{\frac{C_f}{2} G} \quad (2.12)$$

where $G = G_{Ox} + G_f$ is the total mass flux. Thus, the friction coefficient is related to the blowing parameter, as shown in Fig. 2.3.

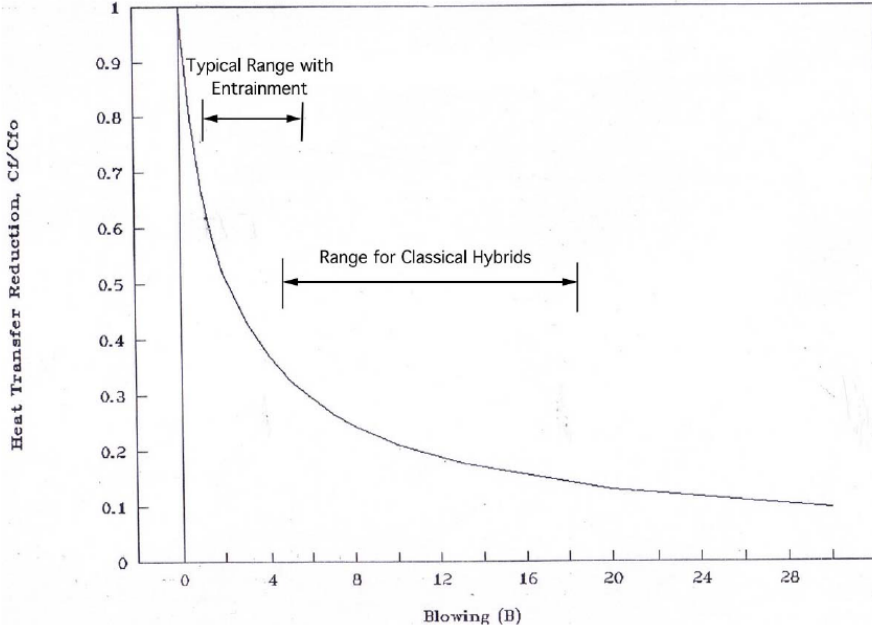


Figure 2.3: Blocking effect dependence on the blowing parameter B [19]

Experimentally it is possible to find that, for $5 \leq B \leq 100$, which is of interest for classical applications in hybrid propulsion (no liquefying fuels), the variation of the friction coefficient with the parameter B can be approximated to:

$$\frac{C_f}{C_{f0}} = 1.27B^{-0.77} \quad (2.13)$$

being C_{f0} (the friction coefficient for a turbulent boundary layer without blowing) expressed according to the following relation:

$$\frac{C_{f0}}{2} = 0.029Re_x^{-0.2} \quad (2.14)$$

Finally, in a turbulent boundary layer without radiation, the blowing parameter B is equal to the transfer mass number B_t , defined as:

$$B_t = \frac{u_e \Delta h}{u_b h_f} \quad (2.15)$$

Thus obtaining:

$$B = B_t \simeq \frac{\Delta h}{h_f} \quad (2.16)$$

So, the regression rate equation for a pure convective model in a turbulent boundary layer ($P_r \simeq 1$) can be expressed as:

$$r_f = 0.036 \frac{G^{0.8}}{\rho_f} \left(\frac{\mu}{x} \right)^{0.2} B^{0.23} \quad (2.17)$$

Considering the more narrow range $5 \leq B \leq 20$, which is typical for classical hybrid rocket engines, the equation can be rewritten as:

$$r_f = 0.036 \frac{G^{0.8}}{\rho_f} \left(\frac{\mu}{x} \right)^{0.2} B^{0.32} \quad (2.18)$$

From this equation it is possible to note the strong dependence of the regression rate on the total mass flux G and the lack of any explicit dependence on the pressure. The fuel thermochemical properties $\Delta h/h_f$ influence the regression rate only through the blowing parameter B .

In practical applications, the expression of the regression rate is replaced by a more compact form where the coefficients are obtained experimentally:

$$r_f = a G^m x^m = a [G_{Ox} + G_f(x)]^n x^m \quad (2.19)$$

Thus, the regression rate can change along the solid grain length because of the variation of the fuel mass flux (by increasing x the addition of fuel mass in the boundary layer increases and, consequently, also the regression rate). But the presence of the x^m term counteracts this effect since, by increasing x , the thickness of the boundary layer also increases and the flame moves away from the fuel surface, thus decreasing the energy feedback to the solid grain and, consequently, the regression rate. So it can be said that r_f is uniform along the solid grain length and a more simple equation can be used for the regression rate:

$$\bar{r}_f = a L_f^m \bar{G}^n \quad (2.20)$$

where \bar{G} is the average total mass flux (total mass flow rate divided by the average port area) and L_f is the solid grain length. It must be noticed that in this relation the regression rate depends on itself through the fuel mass flux $G_f(x) = G_f(r_f(x))$. Thus a simpler relation can be used:

$$\boxed{r_f = a G_{Ox}^n} \quad (2.21)$$

where the coefficients a and n must be evaluated experimentally through combustion tests. This expression is the most used in many experimental works due to its simplicity.

2.1.2 Thermal Radiation Effects

The Marxman's model does not consider the radiation effects even if they are important in some propellant formulations such as those based on metallized fuels. In order to take into account the presence of the radiation, a radiation flux must be added to the energy equation (Eq. 2.1):

$$\dot{q}_{g,s} + \dot{q}_r = \dot{q}_{g,s} + \sigma_{SB} \varepsilon_s (\varepsilon_g T_f^4 - T_s^4) = \rho_f r_f h_f \quad (2.22)$$

where \dot{q}_r is the radiation flux coming from the flame, σ_{SB} is the Stefan-Boltzmann constant, ε_s and T_s are respectively the emissivity coefficient and the temperature of the solid fuel grain, T_f is the flame temperature and ε_g is the emissivity coefficient of the gas phase.

The presence of radiation effects increases the regression rate of the solid fuel grain, but, on the other hand, this addition of heat increases the blocking effect leading to a decrease in the convective heat transfer. Thus, radiation has contrasting effects: it increases the heat transfer in the boundary layer but causes a reduction of the convection due to the increased blowing effect. This means that the benefit on the energy released is damped from the blocking effect on the convective heat flux. In order to take into account this effect, Marxman and colleagues suggested the following correction for the blowing parameter:

$$\frac{B_{rad}}{B} = 1 + \frac{\dot{q}_{rad}}{\dot{q}_{conv}} \left(\frac{B_{rad}}{B} \right)^{0.77} \quad (2.23)$$

So a new expression can be written to take into account both convective and radiative effects:

$$\frac{r_f}{r_{f,conv}} = e^{\left(-0.75 \frac{\dot{q}_{rad}}{\dot{q}_{conv}} \right)} + \frac{\dot{q}_{rad}}{\dot{q}_{conv}} \quad (2.24)$$

where $r_{f,conv}$ and \dot{q}_{conv} are evaluated considering only convective heat transfer.

When the radiation contribution is similar to the convective one there is an increase in the regression rate, but, when the contribution of radiation is small, the increase of the radiative term and the decrease of the convective term are almost equal. It is then possible to conclude that the Marxman's classical model (without radiation) is considered valid if the radiative term is smaller than the convective one.

2.1.3 Chemical Kinetics Effects

The results of the regression rate theory proposed by Marxman are based on the hypothesis that, for typical operating conditions of hybrid rocket engines, the Damköhler number is very high, meaning that the chemical reactions rate is much greater than the mixing rate of the reactants in the turbulent flame. However, in the operating region of very high mass fluxes, this approximation

is not valid anymore because the residence time of the gases in the combustion chamber largely decreases at a high oxidizer injection velocity. Therefore, in this region it is necessary to take into account also the chemical kinetics that causes a reduction of the regression rate. Moreover, the pressure influences the regression rate because the chemical reaction rate becomes higher at increasing pressure. The regression rate dependence on the pressure at very high mass fluxes is caused by two phenomena: the kinetics of the gas-phase reactions between the oxidizer and the pyrolyzed fuel and the kinetics of the heterogeneous reactions between the oxidizer and the solid fuel at the grain surface.

Wooldridge and Marxman derived a normalized regression rate expression dependent on the Damköhler number, which is defined as the ratio between the turbulent time scale and the chemical time scale:

$$Da \equiv \frac{\tau_t}{\tau_c} \gg 1 \quad (2.25)$$

Taking into account the chemical kinetics of both the gas-phase reactions and the heterogeneous reactions, it is possible to obtain:

$$\frac{\dot{r}}{\dot{r}_0} = (2Da)^{0.5} \left\{ 1 - Da \left[1 - \exp\left(-\frac{1}{Da}\right) \right] \right\}^{0.5} \quad (2.26)$$

where the reference regression rate is computed in the region of pressure independence.

The chemical kinetics is the limiting parameter when the Damköhler number is high. This happens when the combustion chamber pressure is low or when the mass flux is high. In this region the previous equation simplifies to:

$$\frac{\dot{r}}{\dot{r}_0} = (2Da)^{0.5} \quad (2.27)$$

If a second-order reaction is considered, the Damköhler number can be approximated as follows:

$$\frac{1}{Da} = c_1 \left(\frac{G^{0.8}}{p_c x^{0.2}} \right) \quad (2.28)$$

where the constant c_1 includes the effects of the blowing parameter, the flame temperature and the gas viscosity. Combining the last two equations it is possible to write:

$$\frac{\dot{r}}{\dot{r}_0} = c_2 \left(\frac{p_c^{0.5} x^{0.1}}{G^{0.4}} \right) \quad (2.29)$$

Substituting the reference regression rate (Eq. 2.17) and absorbing the blowing number into the constant c_2 , it is possible to obtain the expression of the regression rate for the kinetically controlled region:

$$\dot{r} = c_3 p_c^{0.5} G^{0.4} x^{-0.1} \quad (2.30)$$

Even if this correlation has a qualitative meaning, it underlines that in the region of very high mass fluxes the regression rate is more dependent on the pressure and less dependent on the total mass flux (see next section).

2.1.4 Pressure Effects

For most practical applications, the regression rate is considered not dependent on pressure. However, for some ranges of mass fluxes, a dependency of the regression rate on the chamber pressure can be observed. In particular, for low mass fluxes the influence of the radiative heat flux increases because the turbulent convection component of the total wall heat flux is small. In this region, a lower pressure causes a decrease of the regression rate. For high mass fluxes the effect of the chemical kinetics is more important because the residence time of the gases is reduced. In this region a higher pressure increases the regression rate.

2.1.5 Regression Rate Behaviour

All those considerations about the dependency of the regression rate on different parameters can be summarized as shown in Fig. 2.4 [16], which qualitatively represents the correlation between the regression rate and the total mass flux in a logarithmic plot:

- at low mass fluxes, the effect of thermal radiation becomes important due to a lower convective heat transfer. In this region, an increasing regression rate is achieved by metal addition or by increasing the product of the pressure with the port diameter (in both cases the effects of radiation become more prominent). If the mass flux is further decreased, the 'cooking' limit is reached. Here the fuel is expected to melt, char or undergo subsurface decomposition. At this point, the combustion cannot be sustained any further;
- at intermediate mass fluxes, the regression rate is dominated by turbulent heat transfer and shows a power dependence on the flux with an exponential coefficient of 0.8, as predicted by the Marxman's model (see Eq. 2.17 and 2.18). In this regime, neither radiation nor kinetics significantly influences the behaviour of the regression rate with respect to mass flux;
- at high mass fluxes, the effect of chemical kinetics becomes important. In this regime, the regression rates are smaller than predicted by the classical theory, due to heterogeneous reactions and/or polymer decomposition. If the mass flux is further increased, a limit is reached where

the combustion cannot be sustained anymore due to flooding effects of excessive oxidizer in the port.

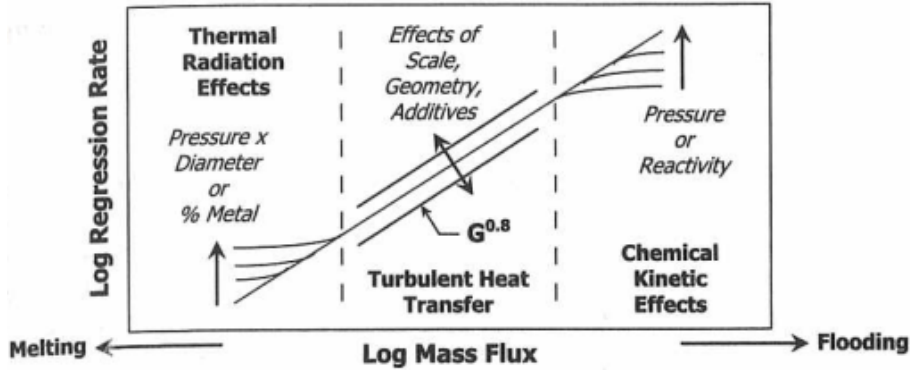


Figure 2.4: Variation of the regression rate with the total mass flux [16]

2.2 Liquefying Hybrid Theory

The Marxman's model is valid only for polymeric fuels such as HTPB. This class of fuels shows a low regression rate due to the diffusion flame characterizing hybrid systems. In fact, the heat and mass transfer from the relatively remote flame zone to the fuel surface limits the vaporization of the solid fuel grain and, consequently, the regression rate and the thrust (with a simple grain geometry).

In order to increase the regression rate various solutions are suggested (see Sec. 1.1), acting both on the fluid dynamics in the combustion chamber and on the fuel grain. One effective method is to use fuels characterized by low viscosity and surface tension, which allow for a different combustion mechanism. The so-called liquefying fuels form a thin liquid layer on the fuel surface during the combustion [43], which becomes unstable under the oxidizer flow. It is expected that the shear forces between the liquid layer and the oxidizer flow are able to trigger the Kelvin-Helmholtz instability process: roll waves are produced in the liquid layer and fuel droplets are forced to separate and entrain into the flow [44], see also Fig. 2.5. Thus, in addition to the classical gasification, these liquefying fuels are interested by a mass transfer mechanism resulting in an increase of the total regression rate. This mechanism works like a spray injection along the length of the motor, which increases the effective fuel burning area and reduces the blocking effect and the effective heat of gasification. This enables simple, single-port fuel grain designs and makes hybrid propulsion a competitive candidate for launch systems and in-space missions. A visualization of the entrainment phenomenon with paraffin-based fuels, obtained in the framework of this research, is shown in Fig. 2.6.

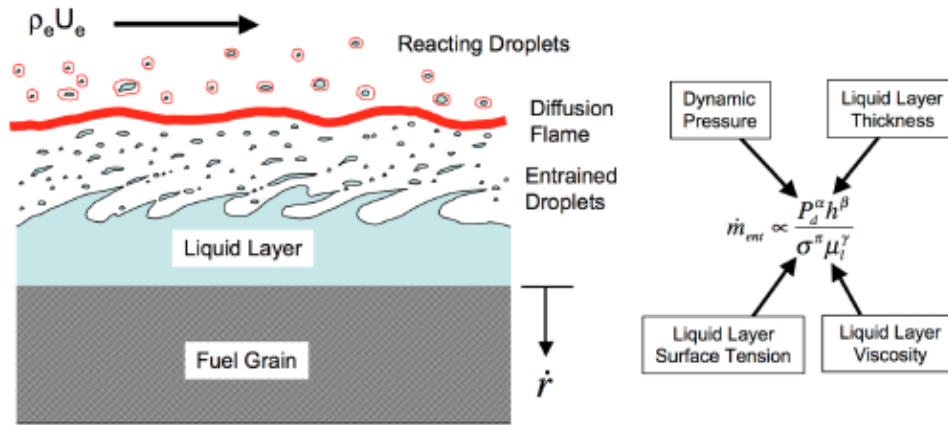


Figure 2.5: Entrainment of droplets from the melt liquid layer in a liquefying fuel [10]

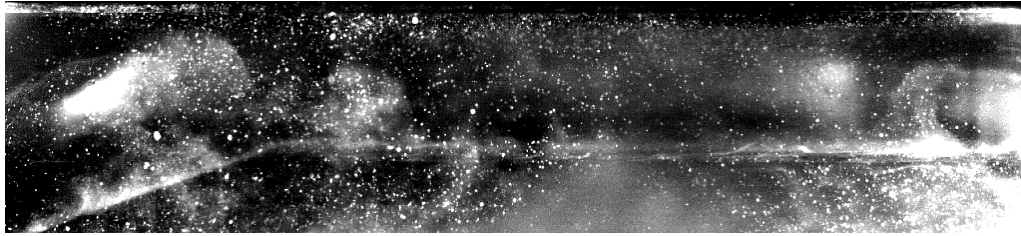


Figure 2.6: Liquefying fuel combustion image created within this research (oxidizer flow from left to right)

Usually the fuels that are able to form a melt layer at the combustion surface are non-polymerized substances that liquefy on heating. Representative fuels of this class are the solid cryogenic hybrids: liquid or gaseous fuels at standard conditions which are frozen to form solid grains. Typical members of this class range from H_2 to liquid amines and hydrocarbons [43]. Nevertheless the use of these fuels adds complications in the design of a hybrid rocket engine due to the need of cryogenic systems that lead to an increase in structural/inert mass of the propulsive system and a loss of performance. Thus, other materials forming a low viscosity melt layer on the combustion surface were studied. The research focused on the members of the homologous series of n-alkanes $C_n H_{2n+2}$. Experiments demonstrated that paraffin and polyethylene waxes, which have a carbon number in the range 25-45, show high rates of entrainment of liquid droplets into the gas stream and so high regression rate (Fig. 2.7).

2.2.1 Entrainment Model

Karabeyoglu and colleagues developed a mathematical formulation of the entrainment [43, 44], which is conceived as an extension of the classic hybrid

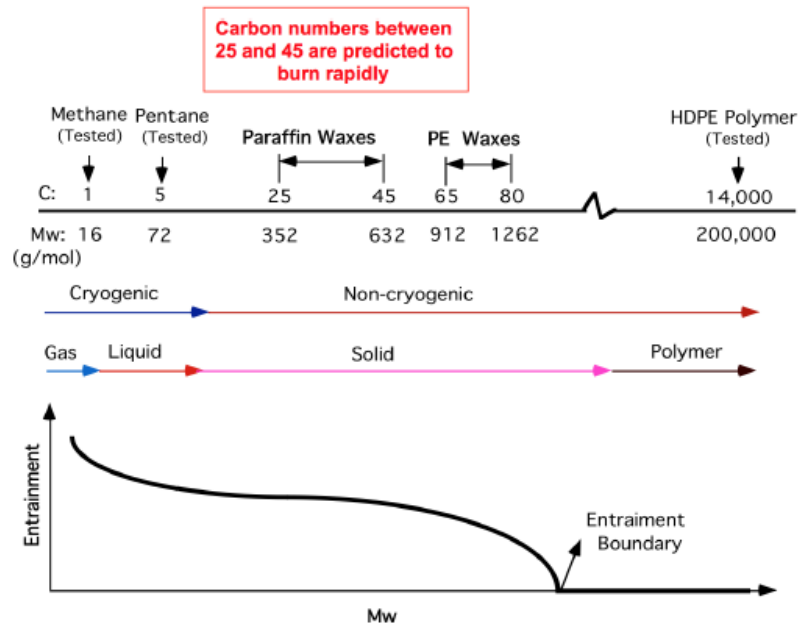


Figure 2.7: Normal alkanes expecting to exhibit high regression rate [10]

combustion theory. In the entrainment model, the liquid layer thickness on a burning slab is determined by considering the convective and radiative heat transfer both in the solid and liquid phases (Fig. 2.8).

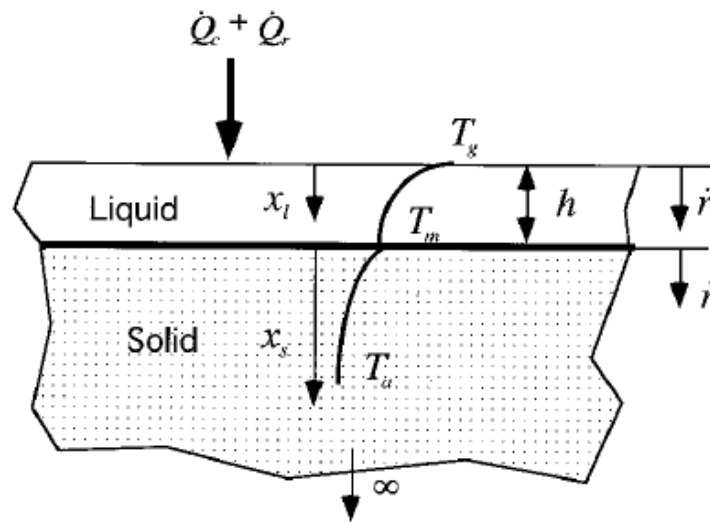


Figure 2.8: Schematic of the thermal model used by Karabeyoglu in the melt layer thickness estimation [43]

In this formulation the following assumptions are made:

- steady-state regression of the fuel slab;

- the velocities of the liquid-gas and the solid-liquid interfaces are assumed to be equal and constant, thus leading to a constant film thickness;
- the thermo-physical properties of the materials both in the liquid and in the solid phases are considered uniform;
- the effect of convection in the liquid layer is ignored due to the small melt layer thickness (low Reynolds number and large temperature gradients);
- the radiative flux field is assumed to be one-dimensional;
- the contribution of radiation emitted by internal material to the radiative intensity is negligible due to the small temperature levels in the slab;
- both the liquid and the solid material are assumed to behave like a grey bodies (the absorption coefficient is independent on the frequency of the impinging radiation).

Under these assumptions the radiative energy flux in the liquid and solid phases are:

$$\dot{q}_{rad}(x_l) = \dot{Q}_{rad} e^{-\alpha_l x_l} \quad (2.31)$$

$$\dot{q}_{rad}(x_s) = \dot{q}_{rad}(h) e^{-\alpha_s x_s} = \dot{Q}_{rad} e^{-\alpha_l h} e^{-\alpha_s x_s} \quad (2.32)$$

where \dot{Q}_{rad} is the total collimated radiative flux impinging on the surface, α_l and α_s are the absorption coefficients of liquid and solid phases respectively. The radiative heating of material at any position can be expressed as the divergence of the radiative flux $-\nabla \cdot q_{rad}$. In a one-dimensional model the radiative heatings in the liquid and solid phases are:

$$-\frac{dq_{rad}}{dx_l} = \alpha_l \dot{Q}_{rad} e^{-\alpha_l x_l} \quad (2.33)$$

$$-\frac{dq_{rad}}{dx_s} = \alpha_s \dot{Q}_{rad} e^{-\alpha_l h} e^{-\alpha_s x_s} \quad (2.34)$$

It can be shown that the total heating of the fuel by radiation is equal to the radiative heat input:

$$\int_0^h \alpha_l \dot{Q}_{rad} e^{-\alpha_l x_l} dx_l + \int_0^\infty \alpha_s \dot{Q}_{rad} e^{-\alpha_l h} e^{-\alpha_s x_s} dx_s = \dot{Q}_{rad} \quad (2.35)$$

In order to write the energy balance equations in the liquid and in the solid phases, the characteristic thermal thickness in the liquid and solid phases has to be defined:

$$\delta_l = \frac{\kappa_l \rho_l}{r_f \rho_s} \quad (2.36)$$

$$\delta_s = \frac{\kappa_s}{r_f} \quad (2.37)$$

where κ_l , κ_s , ρ_l and ρ_s are the thermal diffusivity and density of the liquid and solid phase.

Thus the energy balance equations for the liquid and solid phases are:

$$\frac{d^2 T}{dx_l^2} + \frac{1}{\delta_l} \frac{dT}{dx_l} = -\frac{\alpha_l \dot{Q}_{rad}}{\kappa_l \rho_l c_l} e^{-\alpha_l x_l} \quad (2.38)$$

$$\frac{d^2 T}{dx_s^2} + \frac{1}{\delta_s} \frac{dT}{dx_s} = -\frac{\alpha_s \dot{Q}_{rad}}{\kappa_s \rho_s c_s} e^{-\alpha_s x_s} \quad (2.39)$$

in which c_l and c_s are respectively the specific heats of the two phases.

The boundary conditions, according to Fig. 2.8, are $T(0) = T_g$ and $T(h) = T_m$ for Eq. 2.38, while $T(0) = T_m$ and $T(\infty) = T_a$ for Eq. 2.39. Thus the general solutions for the two linear ordinary differential equations can be found:

$$T(x_l) = c_1 e^{-x_l/\delta_l} + c_2 - \frac{\dot{Q}_{rad}}{\rho_l c_l r_f (\alpha_l \delta_l - 1)} e^{-\alpha_l x_l} \quad (2.40)$$

$$T(x_s) = c_1 e^{-x_s/\delta_s} + c_2 - \frac{\dot{Q}_{rad} e^{-\alpha_l h}}{\rho_s c_s r_f (\alpha_s \delta_s - 1)} e^{-\alpha_s x_s} \quad (2.41)$$

Now it is possible to evaluate the temperature gradients in the two phases and, thus, write the energy balances at the liquid-solid interface and at the gas-liquid interface, which are respectively:

$$-\lambda_l \left. \frac{dT}{dx_l} \right|_{x_l=h} + \lambda_s \left. \frac{dT}{dx_s} \right|_{x_s=0} - h_m \rho_s r_f = 0 \quad (2.42)$$

$$\dot{Q}_{conv} + \lambda_l \left. \frac{dT}{dx_l} \right|_{x_l=0} - h_v \rho_s r_v = 0 \quad (2.43)$$

where h_m is the latent heat of melting of the fuel, λ_l and λ_s are respectively the thermal conductivity in the liquid and solid phase, h_v is the latent heat of vaporization and r_v is the regression rate due to vaporization. In Eq. 2.42 the energy transfer from the liquid to the interface must be equal to the heat conducted into the solid from the interface and the energy required for the phase transformation.

In Eq. 2.43 the convective heat transfer from the gas to the interface must be equal to the conductive heat transfer into the liquid and the heat required for the phase transformation. In this last formula (Eq. 2.43) the possibility

of entrainment mass transfer from the liquid surface is considered other than the mass transfer by vaporization.

Combining Eq. 2.42 and 2.43, it is possible to obtain that the total energy transferred to the wall \dot{Q}_w must be equal to the energy absorbed by the fuel grain, which is composed of the energy required to heat the liquid and solid and the heat required for the phase transformations:

$$\dot{Q}_w = \dot{Q}_{rad} + \dot{Q}_{conv} = h_{ent} \rho_s r_f + h_v \rho_s r_v \quad (2.44)$$

where $h_{ent} = h_m + c_l(T_g - T_m)$ is the total heat of entrainment.

Thus the enthalpy of vaporization for liquefying propellant becomes:

$$h_v = \frac{\dot{Q}_w}{\rho_s r_f} = c_l(T_g - T_m) + c_s(T_m - T_a) + h_m + h_v \frac{r_v}{r_f} \quad (2.45)$$

Eq. 2.45 is different from the typical expression reported in the literature because the heat required to vaporize the fuel transported by means of entrainment is zero.

Finally, substituting the known temperature derivatives into Eq. 2.42, it is possible to write:

$$\Phi = \frac{h_{m,tot}(R_l - 1) + h_{v,tot}(\dot{Q}_{rad}/\dot{Q}_w)\Phi^{R_l}}{h_e(R_l - 1) + h_{v,tot}(\dot{Q}_{rad}/\dot{Q}_w)} \quad (2.46)$$

where $\Phi = e^{-h_L/\delta_l}$, $R_l = \alpha_l \delta_l$, $h_{m,tot}$ and $h_{v,tot}$ are respectively the total heats of melting and vaporization.

An explicit solution for this algebraic non-linear equation (Eq. 2.46) could not be achieved, but it is possible to recognize two limiting cases of interest:

- $R_l \gg 1$: the absorption of the radiation in the liquid layer is high, all of the radiative heat is absorbed at the liquid-gas interface. The thickness of the liquid layer can be written as:

$$h_L = \delta_l \ln \left(1 + \frac{c_l(T_g - T_m)}{h_{m,tot}} \right) \quad (2.47)$$

This case is important for fuel loaded with strongly absorbing materials (for example carbon black).

- $R_l \ll 1$: the absorption of the radiation in the liquid layer is small, all the radiative heat flux is absorbed by the solid. The thickness of the melt layer can be written as:

$$h_L = \delta_l \ln \left(1 + \frac{c_l(T_g - T_m)}{h_{m,tot} - h_{v,tot}(\dot{Q}_{rad}/\dot{Q}_w)} \right) \quad (2.48)$$

An important common property of Eq. 2.47 and 2.48 is that the melt layer thickness h_L is proportional to the characteristic thermal length of the liquid phase δ_l and, thus, inversely proportional to the regression rate:

$$h_L \propto \frac{1}{r_f} \quad (2.49)$$

Another important parameter affecting the thickness of the melt layer is the ambient temperature of the fuel T_a . If the ambient temperature increases, the melt layer thickness also increases until reaching a maximum value for a given regression rate which is attained when the ambient temperature is equal to the melting temperature (Fig. 2.9).

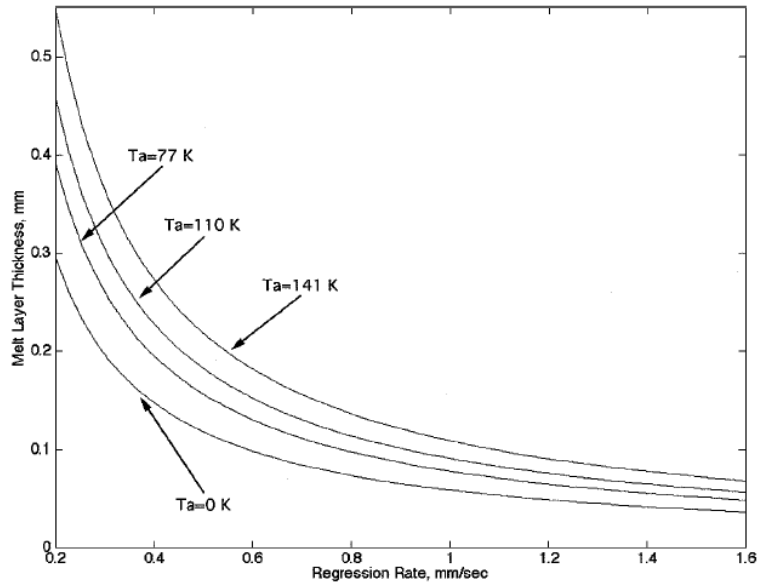


Figure 2.9: Effect of regression rate and slab temperature on the melt layer thickness for pentane [43]

2.2.2 Liquid Layer Stability

Karabeyoglu et al. [44] have also performed the stability analysis of liquid films under the conditions encountered in hybrid rocket engines. A schematic of the liquid layer stability model is shown in Fig. 2.10.

In order to simplify the problem, the following assumptions are made:

- the liquid layer has a laminar nature ($Re_L < 300$);
- the fluids have constant physical properties;
- steady-state analysis (i.e. the amount of liquid injected at the solid-liquid interface is equal to the amount removed at the liquid-gas interface);

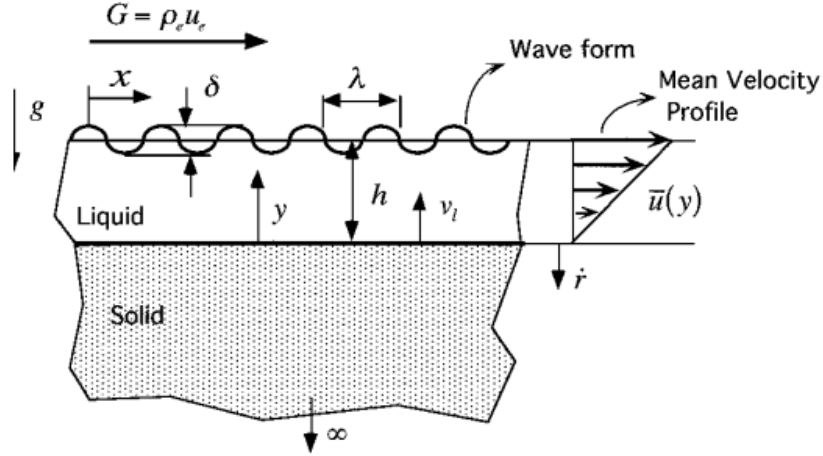


Figure 2.10: Schematic of the stability model [44]

- the frame of reference is fixed to the moving interfaces, which are translated at a constant speed with respect to the rocket frame;
- incompressible flow;
- uniform pressure in space.

Incompressible Navier-Stokes equations are written and coupled with a no-slip condition at the wall and the shear force balance at the gas-liquid interface. An expression for the mean axial component of the liquid flow velocity is obtained. In the limit case of zero liquid blowing, the linear velocity profile of the standard Couette flow is obtained. For little injection (for typical hybrid conditions, the liquid blowing parameter b falls in the range of 0.1-1), a corrected linear profile can be a good approximation of the exact velocity profile. Thus, for small blowing parameters (usually for $b < 0.8$), the mean axial velocity profile of the liquid is given from Eq. 2.50.

$$U_0(y) = U_l^0 \left[\frac{e^b - 1}{b} e^b \right] (y/h) \quad (2.50)$$

where U_l^0 is the mean axial velocity of the liquid at the interface without blowing.

In order to study the stability of the harmonic surface waves, the base flow is perturbed and the Navier-Stokes equations for the base flow and the perturbation components are written. Simplifications and first order approximations allow to obtain a set of linear equations in terms of pressure and velocities or stream functions. In particular, the introduction of the stream function $\varphi(x, y, t)$ leads to the Orr-Sommerfeld equation governing the stability of a film layer (Eq. 2.51).

$$\phi^{IV} - 2\alpha^2 \phi'' + \alpha^4 \phi - b(\phi''' - \alpha^2 \phi') = i\alpha Re(\bar{y} - \beta/\alpha)(\phi'' - \alpha^2 \phi) \quad (2.51)$$

where ϕ is the y component of the liquid-phase stream function $\varphi(x, y, t)$, α is the non dimensional wave number and β is the amplification parameter. This is a fourth-order differential equation with five boundary conditions: no slip condition at the solid wall, steady slab regression rate, kinematic condition at the liquid-gas interface, shear and normal force balances at the liquid surface. Therefore, this is an over-posed boundary value problem, solved by Karabeyoglu et al. who developed an analytical solution. The linear stability problem requires the gas-phase response as input. Some assumptions about the gas-phase are made:

- the gas flow is parallel to the surface waves;
- turbulence does not interact with waves;
- chemical reactions and gas property variations across the boundary layer are ignored;
- viscosity acts in a confined region called wall friction layer;
- the gas velocity in the center of the port is much higher than the liquid velocity;
- the wavelength of the disturbances has to be smaller compared to the port diameter and the thickness of the wall friction layer.

All these conditions seem to be satisfied for the typical hybrid operating conditions.

One of the most interesting results of this linear theory is that, even at very small film thickness, there exist a finite range of amplified wave numbers. This means that the layer is unstable over a finite range of wave numbers. These kind of instabilities were already discovered for thin water films in a wind tunnel by Craik [18], and they are called slow waves. These are generated by the interaction of the gas-phase shear stresses acting on the liquid surface with the slope of the liquid layer surface. The maximum in the range of unstable wave numbers is the most amplified wave number. The corresponding wavelength is expected to be the observed size of the disturbance in the actual flow system. Intuitively, the most important parameter linking the linear stability theory to the entrainment rate of the liquid from the surface is the amplification rate of disturbances. Its value can be influenced by many parameters:

1. the liquid Reynolds number, it has a not stabilizing effect on the liquid layer. As it increases, the amplification rate increases;
2. the liquid blowing parameter b , it has a slightly stabilizing effect on the film. As it increases, the amplification rate decreases;

3. the surface tension and viscosity of the liquid, they have a stabilizing effect on the liquid film. These two parameters play a major role in determining which fuel is more likely to show instabilities and potentially entrain droplets into the gas stream. Fuels with higher viscosity and surface tension values, such as isopropanol and HFI (mixture of hydrocarbons: 60% isopropanol, 30% hexane, 10% tetrahydrofuran), are less likely to sustain liquid layer instabilities than those having small viscosity values (see Fig. 2.11).

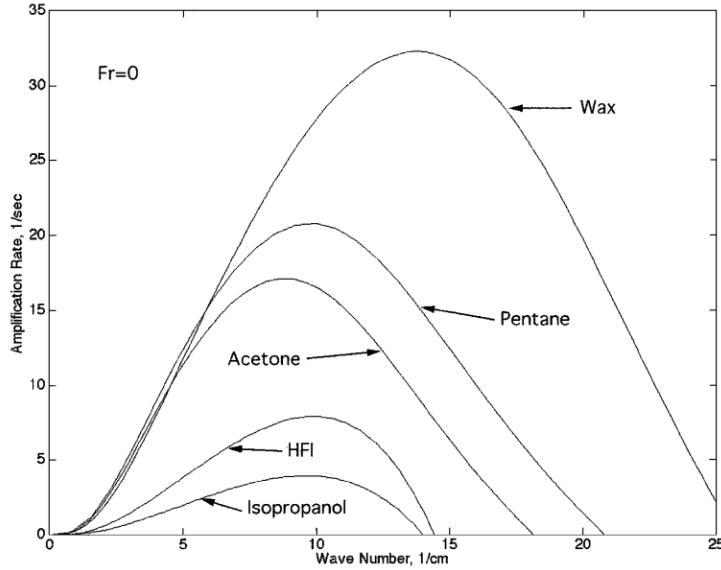


Figure 2.11: Amplification curves for various liquids for $G_{Ox} = 80 \text{ kg}/(\text{m}^2\text{s})$, $r_f = 1 \text{ mm}$ and $h_L = 0.15 \text{ mm}$ (body force is assumed to be zero) [44]

The linear stability theory can be also applied to classical hybrid fuels that form a liquid layer on their burning surfaces, such as HDPE. Its melt layer is four orders of magnitude more viscous than pentane and the linear stability theory predicts that, at such high viscosity levels, it will be stable at the mass fluxes typical of hybrid engines. This means, that the linear instability of the liquid film is a necessary but not a sufficient condition for the onset of entrainment. For a rigorous treatment of the entrainment process, a fully non linear investigation is required.

Finally, taking into account the results of the theory and experiments, Karabeyoglu et al. [43] suggested the following empirical expression for the entrainment rate of liquid droplets in terms of the relevant properties of the hybrid engine:

$$\dot{m}_{ent} \propto \frac{P_d^\delta h^\theta}{\mu_l^\gamma \sigma^\pi} \quad (2.52)$$

where δ , θ , γ , π are experimental parameters.

This relation shows that the entrainment phenomenon is mainly favoured by low values of surface tension and viscosity. Moreover, Karabeyoglu and colleagues believe that, under the conditions of hybrid rocket applications, the melt layer viscosity plays a more important role compared to the surface tension in establishing the entrainment mass transfer rate ($\gamma > \pi$) [43].

Finally, it has to be highlighted that all these results come from a linear theory. Linear instability is a necessary but not sufficient condition for the onset of entrainment. This means that it can suggest if the melt layer of a fuel is more or less stable, but it cannot directly predict if the entrainment occurs. In practice, the hidden assumption is that the amplification rate gives a direct measure for the entrainment.

2.3 Extended Hybrid Theory

In the light of the liquid layer theory and the entrainment model elaborated at Stanford University by Karabeyoglu et al. [43, 44], the classical hybrid theory of Marxman can be modified in order to take into account the entrainment phenomenon. Three main modifications have to be done:

1. The ratio of the enthalpy difference between the flame and the surface to the total effective heat of gasification ($\Delta h/h_{v,tot}$) that appears in the thermal blowing parameter (Eq. 2.16) is modified. The effective heat of gasification is reduced since the mechanical entrainment of the liquid decreases the evaporation energy required for the fuel mass transfer from the surface. Also, the enthalpy difference between the flame and the fuel surface is reduced since some of the reactants are now in liquid phase. Karabeyoglu and colleagues estimated that the reduction in the effective heat of gasification is higher than that in the enthalpy difference.
2. The blocking factor $C_f/C_{f0} = C_h/C_{h0}$ is modified due to the presence of the two-phase flow. Ignoring the effect of the liquid droplets on the momentum and energy transfer and assuming that evaporation of droplets released into the gas stream does not take place beneath the flame sheet (which is reasonable for typical hybrid operating conditions), it is possible to express the blocking factor as a function of the evaporation blowing parameter (Fig. 2.12):

$$\frac{C_h}{C_{h0}} = f(B_g) \quad (2.53)$$

3. The liquid layer surface shows some ripples that increase the surface roughness and the heat transfer from the flame front to the surface.

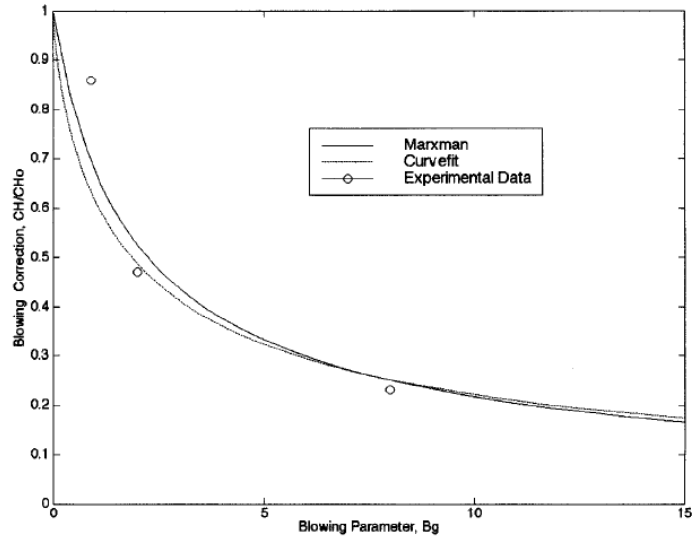


Figure 2.12: Blocking factor correction as a function of the blowing parameter [43]

Finally, the total regression rate of a hybrid motor can be written as a sum of the evaporation regression rate r_v , generated by the vaporization of the liquid into the gas stream, and the entrainment regression rate r_{ent} , caused by the mechanical mass transfer from the liquid surface due to the unstable melt layer interacting with the oxidizer flow (Fig. 2.13):

$$r_f = r_v + r_{ent} \quad (2.54)$$

It can be concluded that fuels having low viscosity and surface tension show higher regression rate with respect to those having high viscosity, due to the entrainment phenomenon. The liquefying fuels form a thin melt layer on the combustion surface which can become unstable under hybrid operating conditions. The instabilities cause the entrainment of droplets into the gas stream. This extra mass transfer mechanism can increase the regression rate from three to four times with respect to that estimated from the classical theory (Fig. 2.14). This is mainly due to the reduced effective heat of gasification, decreased blocking factor in the boundary layer and increased surface roughness. Ideally, the maximum regression rate occurs when there is no vaporization at the surface: in this case, under the assumptions of the liquid stability theory [43], the blocking factor becomes unity.

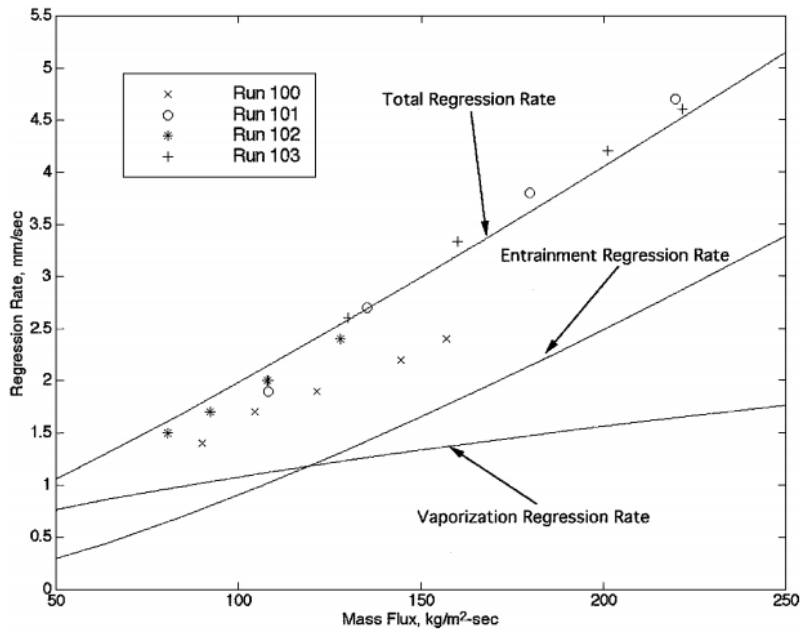


Figure 2.13: Liquid layer theory predictions for vaporization, entrainment and total regression rates for four pentane tests [43]

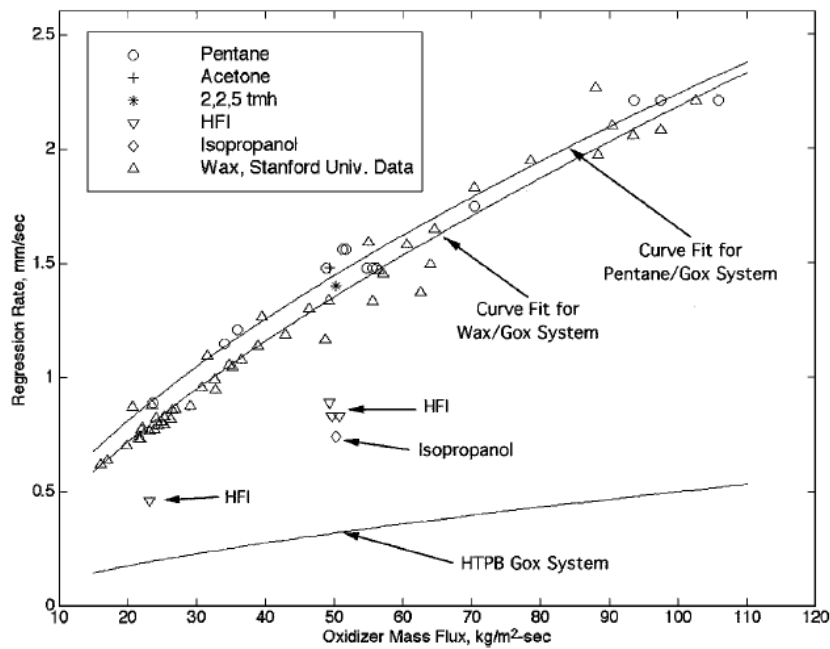


Figure 2.14: Space-time averaged regression rate vs. average oxidizer mass flux for various liquefying materials and HTPB [43]

3 Kelvin-Helmholtz Instability and Droplets Entrainment

In this chapter, the Kelvin-Helmholtz instability theory and the liquid layer break up process, which lead to the fuel droplet entrainment, are presented. A brief state of the art about droplets entrainment inception criteria and liquid layer instability theory is introduced. The Kelvin-Helmholtz instability process has been well understood in the past and explained in the literature, but almost nothing has been done under operating conditions encountered in hybrid engines combustion. Theoretical models for the Kelvin-Helmholtz instability exist in literature and are also presented here.

3.1 Mechanism of Liquid Film Destabilization

The appearance of roll waves is a key event in droplets formation and is considered the entrainment onset point. Hydrodynamic and surface tension forces govern the motion and deformation of the wave crests. Under certain conditions, these forces lead to a deformation of the interface which results in the formation of axial waves, also called primary Kelvin-Helmholtz instabilities. When amplified, they give birth to ligaments (second instability) at a distance equal to the transversal wavelength. Ligaments are, in turn, subjected to shear and torsional stresses due to the rotational nature of the gas flow. This results in a break-up of the unstable liquid film into several droplets by the Plateau-Rayleigh instability mechanism (primary breakup). According to Kuo and Houim [57], droplets entrainment occurs from the unstable waves when the surface tension force in the waves is smaller than the interfacial shear force between the gas flow and the waves. Droplets are then accelerated by the gas flow and eventually rebound or break into droplets of smaller size (secondary breakup). The development of the instability that leads to the primary breaking of the liquid film is shown in Fig. 3.1.

This work focuses on the first stage of destabilization of the liquid film, i.e. the primary Kelvin-Helmholtz instability. It generates stratified fluids characterized by different densities and moving at different speeds, due to perturbations in pressure and/or velocity. This changes the pressure distribution over the wave, causing tightening and spacing of the streamlines, respectively at the crests and at the troughs. In particular, at the wave crest, the fluid velocity is higher, which corresponds to a lower pressure, according to the Bernoulli theorem. On the other hand, at the wave trough, the lower

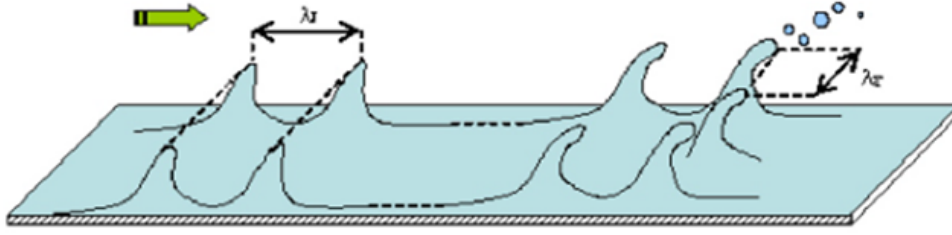


Figure 3.1: Mechanism of liquid film destabilization and breakup: (a) primary instability, (b) secondary instability and primary breakup [69]

fluid velocity results in a higher pressure. As a result, the fluid will accelerate or slowdown and the regions of overpressure/depression accentuate. When the film is unstable, the dominant waves to appear are those having the maximum growth factor. It is important to underline that the appearance of the Kelvin-Helmholtz instability is a necessary but not a sufficient condition for the droplets entrainment, since it describes only the formation of waves on the liquid surface.

3.2 State of the Art of Flow Instabilities and Droplets Entrainment

Instabilities arising in gas-liquid film flows and inception criteria for liquid break-up processes and droplets entrainment have been studied since the late 50s. Understanding the conditions leading to entrainment and atomization of a liquid film by a gas flow is of great importance for heat and mass transfer processes in two-phase flow systems. This topic is, for example, particularly important in the field of cooling systems in nuclear reactors and in jet and rocket engines, since the cooling performance can be significantly affected by the entrainment of the liquid film.

3.2.1 Atomization Mechanism of a Liquid Film

Many experiments have been performed in the past and many empirical correlations have been found for the roll wave formation and entrainment onset criteria [78, 82, 58]. In particular, it has been shown that there are several possible mechanisms of droplet entrainment by a high velocity gas flow in a concurrent two-phase film flow system. At relatively high film Reynolds number regimes, the mechanism of shearing-off of roll wave crests has been predicted. The critical velocity for the entrainment onset depends on the liquid viscosity and film Reynolds number. However, at really high film Reynolds number regimes (completely rough turbulent flow for $Re_f > 1650$), the entrainment onset seems to be independent from the Reynolds number. On the contrary,

in the lower film Reynolds number regime, the entrainment mechanism based on the wave undercutting by a turbulent gas flow has been postulated. Unfortunately, a physical understanding of the initiation of entrainment could not be obtained from these empirical correlations and the generality of some of them was also not proofed [38]. In Fig. 3.2, a summary of the correlations between the liquid Reynolds number and the onset of entrainment present in literature is shown. Many discrepancies can be noticed among them. These differences derive from several completely different methods of defining the experimental point of entrainment inception.

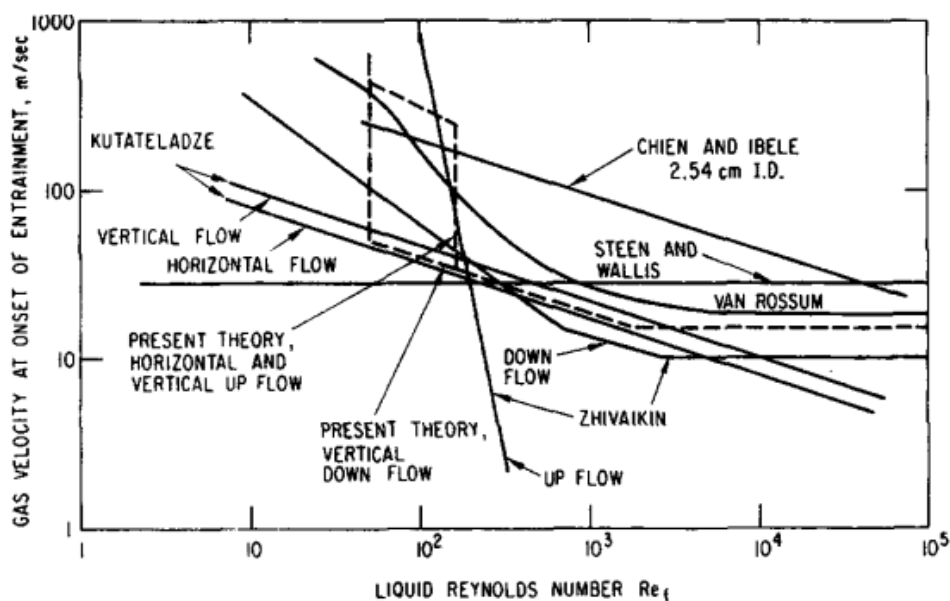


Figure 3.2: Comparison of various entrainment correlations for water-airflow at 15 °C [38]

The first analytical study on roll wave formation and stability analysis (consistent with Kelvin-Helmholtz type instability) to determine a roll wave formation criteria was performed by Hanratty et al. [29]. The stabilizing effect of surface tension was ignored in favour of gravity stabilization. The study showed that film instability occurs when the destabilizing effects of inertia outweigh the stabilizing effects of gravity. This model incorrectly predicts that all films are unstable above a critical gas Reynolds number, rather than a film Reynolds number (which considers the film thickness).

In 1969, Woodmansee and Hanratty [80] proposed that the droplets formation is not due to the destabilization of the roll waves, but of smaller structures. In particular, droplet entrainment comes from acceleration, lifting and breaking of wavelets on the ligaments, see Fig. 3.3. In fact, since the wave speed is proportional to the square root of the wave number, the wavelets travels on the liquid layer at a higher speed than the roll waves. This causes a ripple to take-off at the end of the ridge and, therefore, to form the

ligament, which will break according to the mechanism of Rayleigh instability (see Fig. 3.4).

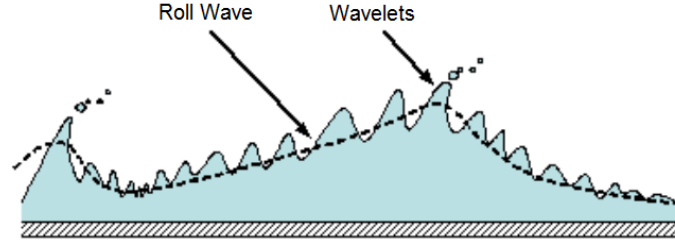


Figure 3.3: Wavelets atomization mechanism [80]

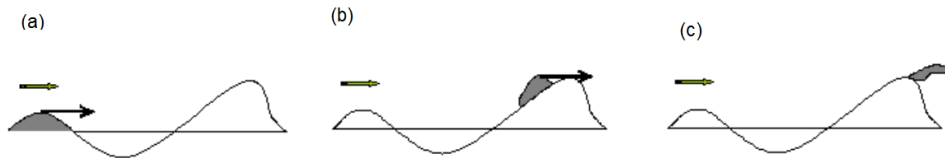


Figure 3.4: Wavelets displacement: a) wavelet formation; b) ripple formation; c) ligament formation [80]

In 1975, Ishii and Grolmes tried to obtain an entrainment inception criterion based upon physical modelling, in order to provide a better understanding of the entrainment process and reliable design rule. In particular, they studied the various entrainment mechanisms described in the literature [38]. A wavy liquid film can be entrained into a gas flow in a number of different ways, depending on the hydrodynamic and surface tension forces acting on it (see Fig. 3.5). The first type of entrainment is characterized by roll waves being sheared-off from the wave crests by the turbulent gas flow. The second type is caused by undercutting the liquid film by a gas flow. The third type is related to the bursting of gas bubbles rising to the liquid film surface. The fourth type of entrainment is caused by the impingement of the liquid drops to the film interface.

By examining the existing experimental data, it is possible to note that there exist at least three different regimes for each fluid, as shown in Fig. 3.6. At large film Reynolds numbers ($Re_f > 1600$), the critical gas velocity becomes constant. This corresponds to the minimum velocity below which no entrainment takes place, regardless of the film Reynolds number. In this regime, the film is in the completely rough turbulent flow regime where the hydrodynamics of the film is mostly governed by the interfacial conditions. The onset of entrainment is based, in this case, on the roll wave mechanism. In the region between point A and B shown in Fig. 3.6 ($160 < Re_f < 1600$), the critical gas velocity for the onset of entrainment

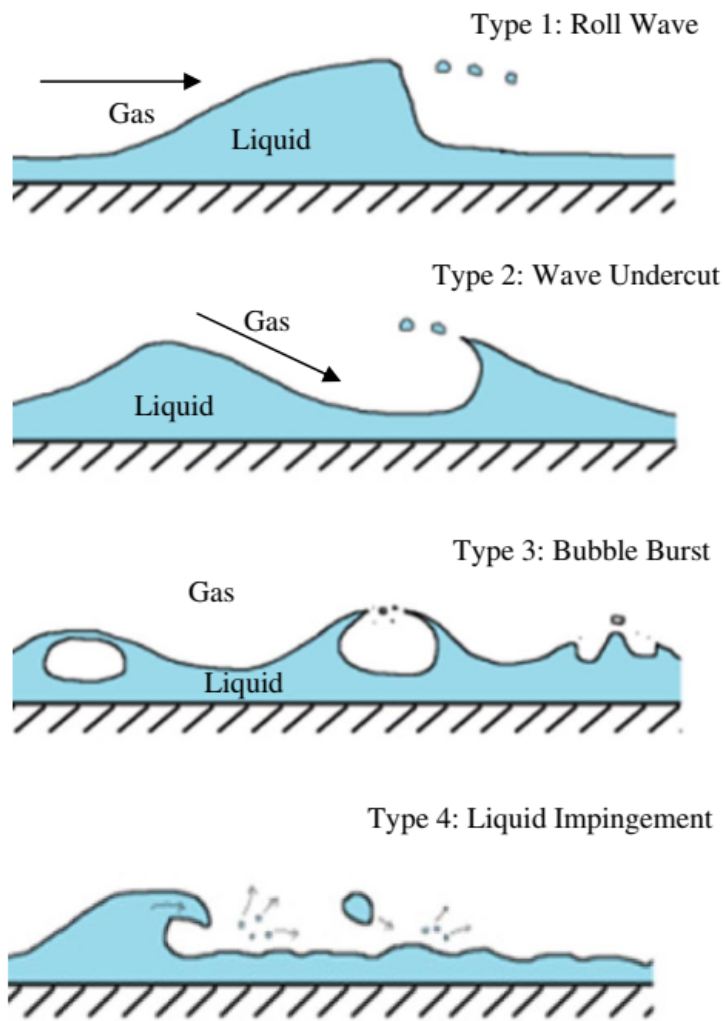


Figure 3.5: Various entrainment mechanism [38]

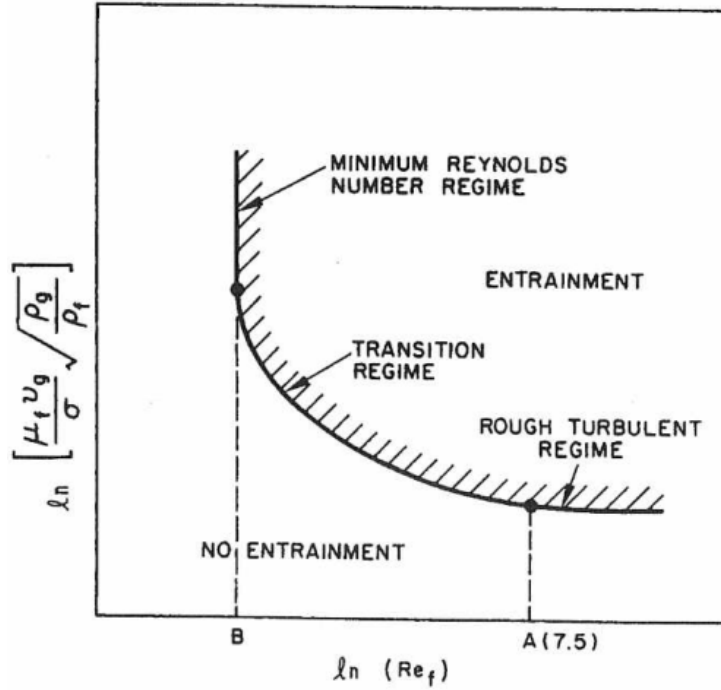


Figure 3.6: Schematic inception boundary for a particular combination of liquid and gas [38]

becomes a function of the film Reynolds number. This region is also characterized by the laminar-turbulent transition regime. The entrainment inception criterion is based on the shearing-off of roll wave crests. At low film Reynolds numbers ($Re_f < 160$), the entrainment mechanism shifts to the one based on the wave undercutting mechanism. In this region, the critical gas velocity starts to increase very rapidly, until it reaches a minimum Reynolds numbers below which no entrainment is possible, independently of the gas velocity. The minimum Reynolds number can be computed with the following formula, proposed by Ishii and Grolmes [38]:

$$(Re_f)_{min} = \left(\frac{y^+}{0.347} \right)^{3/2} \left(\frac{\rho_f}{\rho_g} \right)^{3/4} \left(\frac{\mu_g}{\mu_f} \right)^{3/2} \quad (3.1)$$

where $y^+ = \frac{y u_T}{\nu} \simeq 10$ represents the dimensionless distance from the wall based on the shear velocity.

The model of Ishii and Grolmes accurately predicts the entrainment onset for a variety of fluid combinations, including alkanes similar to paraffin. For this reason, this model is often used to predict entrainment onset for paraffin fuels.

3.2.2 Shear Flow Instabilities

Flow instabilities arising at the interface between two fluids and the Kelvin-Helmholtz instability have been well studied in the past [14, 18, 67, 38, 3, 23].

In 1965, Chang and Russell [14] analysed the stability of a liquid layer in presence of a compressible high speed gas flowing over it. The effects of viscosity, surface tension at the gas-liquid interface and gravitational force are included in the analysis. The equations of motion for small perturbations are linearised at the equilibrium configuration. They found out that at small Mach numbers the stability conditions do not differ significantly from those for incompressible gas flows. If the acceleration of the system is directed from the gas to the liquid, their results show two cut-off wave numbers, which represent the stability limit for the system: for disturbances with wave numbers lying between these two limits, the system is unstable. If the acceleration is directed from the liquid to the gas, there exists only one cut-off wave number: the system is stable for disturbances with wave numbers larger than the cut-off value and unstable otherwise. These criteria remain the same even if the liquid is highly viscous, except that the rate of damping of the disturbances increases. On the other hand, at higher Mach numbers, the compressibility of the gas has an appreciable effect on the stability. In particular, if the relative velocity component between the gas flow and the wave front exceeds the sonic velocity, the system will be always unstable, unless the liquid is highly viscous. In this case, there are again cut-off wave numbers for stability, similar to the subsonic case.

In 1971, Nayfeh and Saric [67] performed a non-linear analysis for the stability of a liquid film adjacent to a compressible gas and under the influence of body forces. The effect of the liquid surface tension is also considered. For a subsonic external flow, it was found that the cut-off wave number is amplitude dependent in the inviscid case and amplitude independent in the viscous case, contrary to the linearised theory of Chang and Russel [14]. They also showed that the non-linear motion of the gas may be stabilizing or destabilizing, whereas the non-linear motion of the liquid is found to be stabilizing in the viscous case. For a supersonic external flow and a viscous liquid, the cut-off wave number is amplitude dependent. Moreover, unstable disturbances with wave numbers near the cut-off value do not grow indefinitely with time but achieve a steady-state amplitude.

In 1967, Yih has been the first one to make a significant study on two-fluid shear-flow stability between two parallel plates [81]. Considering waves much longer than the thickness of the upper layer, he found out that a jump in viscosity across the interface can lead to instability. Hooper [31] confirmed this result for an only-upper-unbounded configuration. His results show that when the thinner layer is the less viscous fluid, stability is granted. On the other hand, when the thinner layer is the more viscous, instability arises. This is the so-called thin layer effect. Hooper and Boyd [32] investigated also the unbounded case where each fluid occupies a half plane. They showed

that this fluid can be unstable in the short wave range. Hinch [30] explained this short wave instability mechanism: as the interface is perturbed, the more viscous fluid is slower with respect to the undisturbed velocity, whereas the less viscous one is faster. To satisfy the continuity of velocity at the interface, some velocity disturbances must develop. This means that there will be positive vortices at the peaks and negative at the troughs. In the short wave range, viscosity dominates inertia, thus allowing an easy diffusion of the vorticity. Advection by the base flow creates small out-of-phase components of vorticity, which in turn induce a flow that amplifies the initial perturbation (see Fig. 3.7, 3.8).

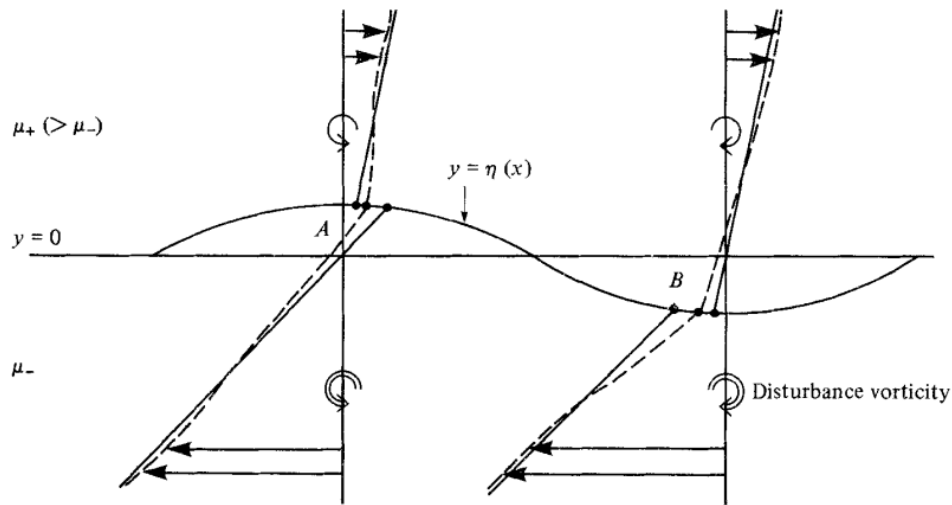


Figure 3.7: Horizontal velocity profiles: the continuous curves are the undisturbed profiles, the dotted curves are the disturbed profiles [30]

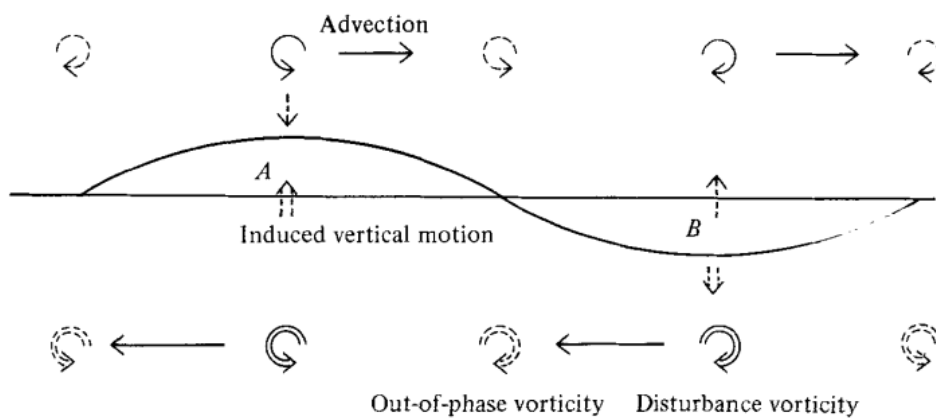


Figure 3.8: Induced vertical motion at the interface: the disturbance vorticity (continuous) is advected by the mean shear to produce small out-of-phase components of vorticity (dotted), which induce the vertical motion of the interface [30]

Moreover, Hooper and Boyd [32] investigated instabilities arising from a shear mode. This kind of instability is related to the viscous effects at the walls and within the critical layer, which takes place when the Reynolds number is sufficiently large. This is the typical instability taking place when a fluid flows in a channel and its speed exceeds a certain value.

Funada and Joseph [23], studied the stability of a stratified gas-liquid flow in a horizontal rectangular channel, considering a viscous potential flow. The effects of viscosity and surface tension are considered. The main result of this analysis is the presence of a critical value of velocity, below which no instability arises (see Sec. 3.4 for more details).

As it is possible to notice, no studies about the stability of liquid films under hybrid combustion conditions have been done until this point. Karabeyoglu et al. [43], [44] have been the first ones to investigate the linear stability of a liquid layer with strong blowing under the effect of shear forces generated by the high-speed gas flow in the port. They derived an Orr-Sommerfeld equation for the linear stability of the liquid-gas interface and found an exact solution for a linear base velocity profile. This solution for the liquid phase was coupled with the linearized gas-phase response with appropriate boundary conditions at the interface to give an eigenvalue problem for the linear stability of the liquid layer. The results for film Reynolds numbers of practical interest ($Re_f = 50 - 300$) show the existence of a range of unstable wave numbers. Both the most amplified wave number and the maximum amplification increase with the film Reynolds number (see Fig. 3.9). It was also showed that the surface tension and the liquid viscosity have a stabilizing effect on the film (see Fig. 2.11). That is why fuels with highly viscous melt layer, such as HDPE, cannot sustain thin film instabilities.

Adachi and Shimada [1] numerically investigated the stability of liquid films under super-critical operating conditions. Numerical simulations were performed considering methane as fuel. A linear instability analysis was conducted by imposing a very small perturbation on the steady-state solution and it showed that an amplification rate has a peak at a certain wave number of initial perturbations. The perturbation becomes unstable as the Reynolds number and the chamber pressure increase (see Fig. 3.10). A non linear instability analysis was also performed and a limit cycle of the amplitude of perturbations was observed at low-Reynolds-number flows. Entrainment phenomena at high-Reynolds-number-flows were also observed. They suggested that the perturbation with the peak value of the amplification rate finally dominates in a hybrid rocket engine.

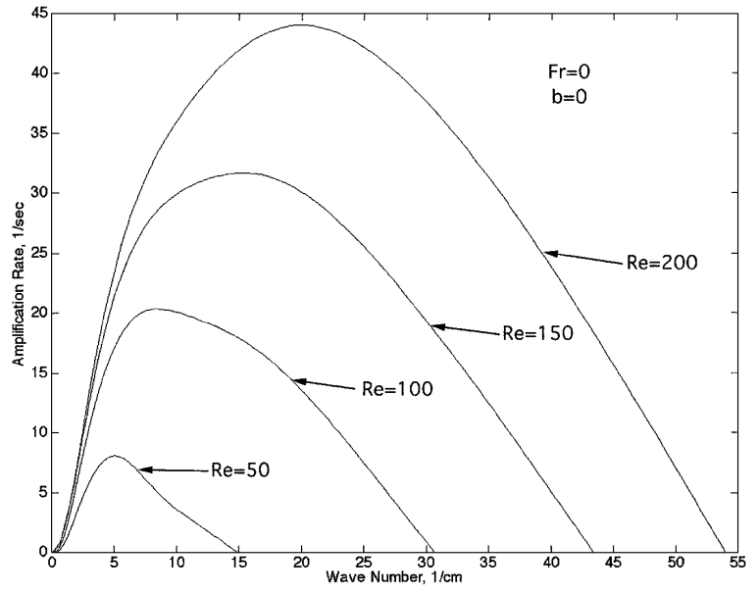


Figure 3.9: Amplification curves for various film Reynolds numbers for a pentane film with $h_L = 0.3$ mm (body force and regression rate are assumed to be zero) [44]

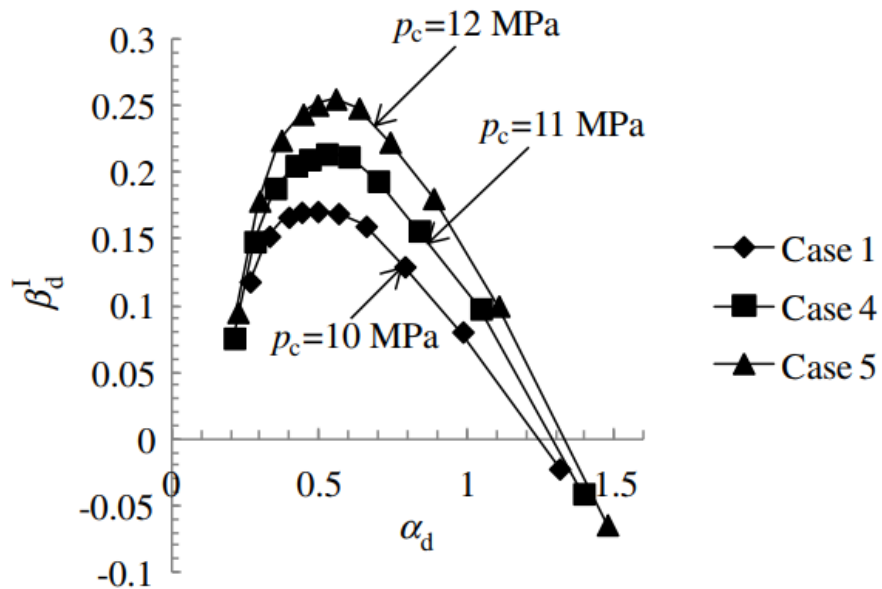


Figure 3.10: Non-dimensional amplification rate as a function of wave number (Case 1: $Re_f = 118$, Case 2: $Re_f = 120$, Case 3 $Re_f = 122$) [1]

3.3 Parameters Affecting Kelvin-Helmholtz Instability

Kelvin-Helmholtz instability produces mixing of the two fluids both mechanically (through the roll-up of the waves) and diffusively (due to density gradients). Therefore, intuitively it is possible to state that:

- velocity gradient promotes the mixing, since the faster fluid will tend to “grab” the slower one forcing it to move;
- buoyancy force works against the mixing, because the two fluids will tend to separate so that the lighter one stays on the top and the heavier remains at the bottom;
- viscosity and surface tension tend to damp instability, because the liquid acts against the deformation trying to retain the initial stability of the liquid sheet;
- gravity has a stabilizing effect when directed from the less dense fluid to the denser one, like in the present analysis.

According to the previously discussed analysis (see Sec. 3.2.2), the following conclusions can be drawn:

- **Disturbance wave number:** the behaviour of the liquid film depends on the disturbance wave number and two cut-off values limit the stable/unstable region. In general, there is a broad unstable frequency range for low wave number disturbances; on the other hand, instability appears at a specific frequency for high wave number disturbances.
- **Surface tension:** the presence of the surface tension broadens the stability region, stabilizing the short waves.
- **Gas speed:** for low gas speed at the interface, the film tends to be stable because of the low shear stresses and limited energy transfer from the gas to the liquid. Higher gas velocities promote instability at any wave number.
- **Film thickness:** a thinner liquid film is more prone to be unstable.
- **Gravity:** the gravitational force has a stabilizing effect on the liquid film, which is more important at high wave numbers.
- **Viscosity:** it limits the development of shear instabilities, by reducing the energy available for the interface deformation. Therefore, the more viscous the liquid, the lower the growth rate and the higher the critical speed. This means that the minimum gas speed required for the onset of instability increases. If the two fluids have different thicknesses and the thinner one is the more viscous (as in hybrid rocket engines), the thin layer effect causes instability in the long wave range [31].

3.4 Theoretical Models

In this section a mathematical formulation of the instabilities arising at the interface between two fluids is provided. The stability of stratified gas-liquid flow is studied in a 2D domain. This assumption is justified by the Squire's Theorem that states that a two-dimensional system is always more unstable than any equivalent three-dimensional system. Moreover, a long-wave assumption is considered. This approximation is valid when the dimensionless aspect ratio, defined as the thickness of the fluid divided by either the wavelength or the channel width in a bounded case, is much smaller than one. For liquefying hybrid fuels, the liquid layer thickness is assumed to be on the order of tenths of millimeters [43], thus the long-wave assumption is justified. Gravity, surface tension and viscosity are considered. In particular, the effect of the viscosity on the shear stress is neglected, while it contributes to the normal stress balance at the interface. Two analysis domains have been considered for the investigation of the Kelvin-Helmholtz instability: an unbounded model represented in Fig. 3.11, taken from [4] and a bounded model represented in Fig. 3.12, taken from [23]. In this last case, the coordinate y was neglected, so that a 2D bounded model could be studied.

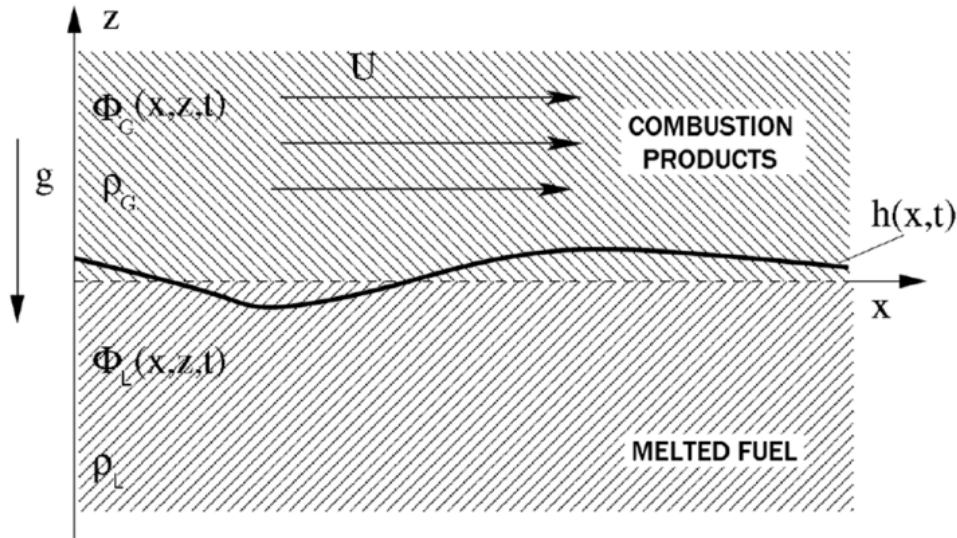


Figure 3.11: Representation of the 2D unbounded model [4]

The governing equations describing the Kelvin-Helmholtz instability problem are the Navier-Stokes and the continuity equations for viscous Newtonian fluids. The fuel liquid layer is considered at rest and the combustion products gas flow is moving at a fixed velocity. The only considered external force is the gravitational one. The effect of viscosity on shear stress is neglected and both fluids are considered homogeneous and irrotational. Boundary conditions are added to the governing equations:

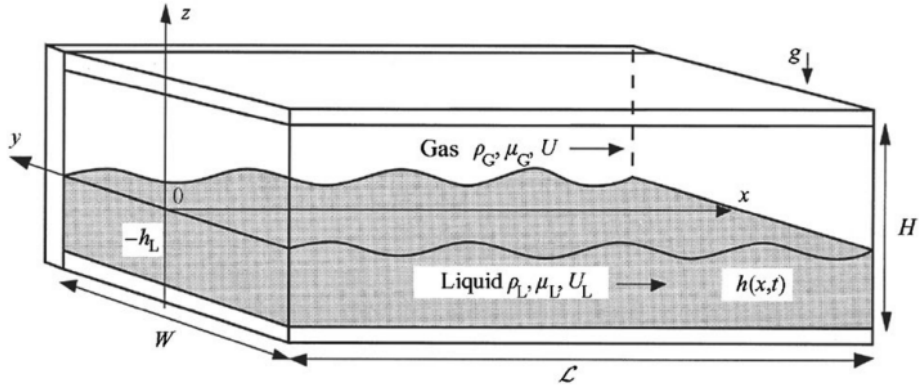


Figure 3.12: Representation of the 2D bounded model [23] (the y coordinate is neglected in this analysis)

- conditions at infinity, for the unbounded model: far from the interface the liquid remains undisturbed and the speed of the gas is the external one;
- conditions at the wall, for the bounded model: no-slip conditions;
- conditions at the interface, for both models: kinematic conditions and normal stress-balance conditions.

The equations are then linearised and sinusoidal solutions are applied [54]. A small sinusoidal perturbation h is introduced at the interface between the gas and the liquid:

$$h(x, t) = Ae^{i\kappa x - i\omega t} \quad (3.2)$$

Here the complex wave frequency ω gives information about the temporal stability, while the complex wave number κ gives information about the spatial stability. For $\omega_I = 0$ neutral temporal stability is achieved, $\omega_I > 0$ indicates temporal instability, while $\omega_I < 0$ indicates temporal stability. In the same way, spatial instability is achieved for $\kappa_I < 0$, stability for $\kappa_I > 0$ and neutral stability for $\kappa_I = 0$.

Solving the equations leads to the **dispersion relation**:

$$\boxed{K_0\omega^2 + 2K_1\omega + K_2 = 0} \quad (3.3)$$

This equation represents a relation between κ and ω and gives the stability criterion and interval for the Kelvin-Helmholtz instability. If the gas velocity is below a so-called critical value, no instability is triggered. Three different cases have been analysed:

- **inviscid unbounded model**, where:
 $K_0 = (1 + \rho)$;

$$K_1 = -U \rho \kappa;$$

$$K_2 = -\{(\beta^2 \kappa^2 + 1 - \rho) g_0 - U^2 \rho \kappa\} \kappa$$

- **inviscid bounded model**, where:

$$K_0 = a_g \rho_g + a_l \rho_l;$$

$$K_1 = -\kappa U a_g \rho_g;$$

$$K_2 = [U^2 \kappa^2 a_g \rho_g - \kappa g_0 (\rho_l - \rho_g) - \sigma \kappa^3]$$

- **viscous bounded model**, where:

$$K_0 = a_g \rho_g + a_l \rho_l;$$

$$K_1 = -\kappa U a_g \rho_g + i \kappa^2 (a_g \mu_g + a_l \mu_l);$$

$$K_2 = [U^2 \kappa^2 a_g \rho_g - \kappa g_0 (\rho_l - \rho_g) - \sigma \kappa^3] - 2 i U a_g \mu_g \kappa^3$$

with $a_l = \coth(\kappa h_l)$; $a_g = \coth(\kappa h_g)$; $\rho = \frac{\rho_g}{\rho_l}$; $\beta = \sqrt{\frac{\sigma}{g_0 \rho_l}}$.

In order to find the neutral curve for each case, it is necessary to search for those values of the parameters for which the roots of the dispersion relation (3.3) are real (note that $\omega = \omega_R + i \omega_I$). By manipulating the dispersion relation and solving it with respect to the gas flow speed U , the neutral curve for each model is obtained:

- **inviscid unbounded model**:

$$U^2 = g_0 \frac{(1 + \rho)}{\rho} \left(\beta^2 \kappa + \frac{1 - \rho}{\kappa} \right)$$

- **inviscid bounded model**:

$$U^2 = g_0 \left(\frac{1}{a_l} + \frac{1}{\rho a_g} \right) \left(\beta^2 \kappa + \frac{1 - \rho}{\kappa} \right)$$

- **viscous bounded model**:

$$U^2 = g_0 \frac{(a_l \mu_l + a_g \mu_g)^2}{a_l a_g^2 \mu_g^2 + \rho a_g a_l^2 \mu_l^2} \left(\beta^2 \kappa + \frac{1 - \rho}{\kappa} \right)$$

4 Decomposition Methods

In this chapter, the two decomposition methods used in the analysis of the combustion videos are introduced. Features and differences between the two methods are discussed, together with advantages and disadvantages of each technique. Both methods are used in the video analysis in order to find the most excited frequencies and wavelengths characterizing the fuel melt layer.

The development of faster and more precise measurement and video techniques allows the collection of a huge amount of data, which needs to be accurately analyzed. In order to reduce the order of the problem, decomposition techniques are usually applied to the analysis of complicated turbulent fluid flows. In this way, a computationally affordable dynamical system is obtained and a reduced model of the flow field is provided. This can be, in turn, used for analysis or inspection purposes in order to find coherent structures that yield insight in terms of physical events involved within the flow of interest.

In the framework of this research, two decomposition techniques have been used in order to reduce the order of the problem and find the most important structures characterizing the flow field. The Proper Orthogonal Decomposition (POD) is able to find the most coherent and energetic structures of the dynamic field. The Independent Component Analysis (ICA) is able to recognize the essential and independent structures characterizing the flow field. Both techniques are able to separate the complex spatio-temporal flow field into sets of spatial modes and the corresponding temporal coefficients.

4.1 Proper Orthogonal Decomposition

4.1.1 Motivation

The POD (Proper Orthogonal Decomposition), also known as Principal Component Analysis (PCA), Karhunen-Loève decomposition and Singular Value Decomposition (SVD), has been used in diverse area of research to obtain approximate, low-dimensional descriptions of turbulent fluid flows, structural vibrations and dynamical systems. It has also been extensively used in image processing, signal analysis and data compression [15]. For example, Arienti et al. [2] used POD to investigate the dynamics of fluid jets. Bizon et al. [7] applied POD in internal combustion engines to investigate the scalar field of luminosity, thus receiving information about the flame dynamics.

Turbulent flows are characterized by organized motions, commonly referred to as coherent structures, within which most of the essential flow physics is believed to be buried. Understanding their dynamics and interactions with other coherent structures in the flow will lead to an increased understanding of turbulence and its control. The process of identifying flow patterns in experimental and computer-generated data is still a trivial task, since they are hidden amongst the incoherent turbulent motions. In addition, the volume of the data can be so large that it must be summarized in a concise manner so that the most useful information about the physical processes may be extracted. POD has proved to be an effective method for identifying dominant features and events in experimental and numerical data. When performing a POD of a flow, the fluid motions that contribute most to the energy of the flow are searched. The decomposition results in a set of modes that represent an average spatial description of structures containing most of the energy and that are predominantly associated with large-scale structures. They do not necessarily have to correspond to coherent structures. The modes may also correspond to events in the flow that contribute the most, in a statistical sense, to the energy of the flow. The POD modes represent the most common events occurring in the “fluctuating” velocity/vorticity/luminosity fields. A conceptual aid used in interpreting their physical meaning is to consider them being superimposed upon a mean flow.

The most appealing properties of POD are [47]:

- POD is the optimal linear algorithm, since it minimizes the average square distance between the original signal and its reduced linear representation;
- POD gives an energy criterion that enables us to retain only the dominant modes and to filter out the presence of the measurement noise;
- POD modes provide a good characterization of the dynamics of the problem;
- spatial and time information is explicitly separated.

The application of POD has also limitations [56, 47]:

- the less deterministic a flow is, the less efficiently it will be represented by the POD modes;
- the analysis de-emphasizes infrequent events, although they may be dynamically important;
- since the technique is based on time averaged correlations, the POD modes only represent time average information about the flow structures;
- the linear nature of the method can be a restriction for some data sets;

- POD tries to describe all the data using the same global features (the use of local features would be better for an efficient representation of qualitatively different domains of the data);
- since the POD removes linear correlations among variables (i.e. diagonalizes the covariance matrix), it is only sensitive to second-order statistics. This means that this method is able to find only uncorrelated variables.

From a mathematical point of view, POD is a statistical method where an orthogonal transformation is used to convert a set of data into a set of linearly uncorrelated variables. They are called principal components. Their number is less than or equal to the number of the original variables. This transformation is performed so that the first principal component has the largest variance and each succeeding component has the highest variance possible. This is done under the constraint that each component has to be orthogonal to the preceding ones, thereby being uncorrelated. An orthogonal transformation to the basis of the eigenvectors of the sample covariance matrix is performed, and the data are projected onto the subspace spanned by the eigenvectors corresponding to the largest eigenvalues (most energetic modes). This transformation decorrelates the signal components and maximizes the variance. Therefore, POD gives an orthogonal basis that ranks modes according to an energy criterion [9].

Suppose to approximate a function $z(x, t)$ over some domain of interest as a finite sum in the variables-separated form:

$$z(x, t) \approx \sum_{k=1}^M a_k(t) \phi_k(x) \quad (4.1)$$

with the approximation becoming exact in the limit as M approaches infinity. The representation of Eq. 4.1 is not unique: for each choice of a sequence $\phi_k(x)$ that forms a basis for some suitable class of functions $z(x, t)$, the sequence of time functions $a_k(t)$ is different. The POD is concerned with one possible choice of the functions $\phi_k(x)$.

If orthonormal basis function are chosen, i.e.

$$\int_x \phi_{k_1}(x) \phi_{k_2}(x) dx = \begin{cases} 1, & \text{if } k_1 = k_2 \\ 0, & \text{otherwise} \end{cases} \quad (4.2)$$

then

$$a_k(t) = \int_x z(x, t) \phi_k(x) dx \quad (4.3)$$

i.e. for orthonormal basis functions the determination of the coefficient function $a_k(t)$ depends only on $\phi_k(x)$ and not on others ϕ . In order to select the

functions ϕ_k , it is useful to choose them orthonormal and in such a way that the approximation for each M is as good as possible in a least squares sense. This means that it is useful to find a sequence of orthonormal functions $\phi_k(x)$ such that the first two of these functions give the best possible two-terms approximation, the first seven give the best possible seven-term approximation, and so on. These special, ordered, orthonormal functions are called the proper orthogonal modes for the function $z(x, t)$. With these functions, the expression in Eq. 4.1 is called the POD of $z(x, t)$ [15].

In this research, the POD is applied to the analysis of the luminosity field of images (scalar field) in a reactive flow. This allows for an analysis of the considered scalar field by decomposing it into mean, coherent and incoherent parts via statistical methods and to visualize the relevant flow morphologies. In general, the coherent part includes all fluctuations possessing a somehow structured feature over the burning process. The incoherent part should include all fluctuations for which no pattern can be identified over the burning process. It is commonly thought that the first few modes correspond to the average structure of the data, while higher order modes contain information about fluctuations [7]. The Nonlinear Iterative Partial Least Squares (NIPALS) algorithm is used for the principal component analysis in the POD method (see Risvik [72]). The PSD of the temporal and spatial coefficients is performed at the end of the algorithm in order to obtain the excited frequencies and wavelengths during the combustion.

4.1.2 NIPALS Algorithm

The Non-linear Iterative Partial Least Square Algorithm (NIPALS) is a widely used method to compute the principal components of a data set. It gives more accurate results with respect to more traditional methods (such as Singular Value Decomposition SVD) and it is more efficient in terms of time and memory.

The data set is organized in a matrix \mathbf{X} ($IJ \times N$), whose columns are the known data:

$$\mathbf{X} = (\mathbf{x}_1 | \dots | \mathbf{x}_n | \dots | \mathbf{x}_N) = x_{\alpha n} \quad (4.4)$$

so that each snapshot is a $I \times J$ array of points (pixels) and N is the total amount of considered frames at the discrete times t_1, \dots, t_N .

The aim is to decompose the data matrix into a structure part $\mathbf{T}\mathbf{P}^T$, which includes the principal components, and a noise part \mathbf{E} :

$$\mathbf{X} = \mathbf{T}\mathbf{P}^T + \mathbf{E} \quad (4.5)$$

with \mathbf{T} and \mathbf{P} being, respectively, the scores and loadings matrices. The matrix \mathbf{T} contains the projections of the data on the principal component direction and the orthonormal matrix \mathbf{P} contains the direction cosines of the

data (it acts like a rotation for aligning the data with the direction of maximal variance), see Fig. 4.1 and 4.2.

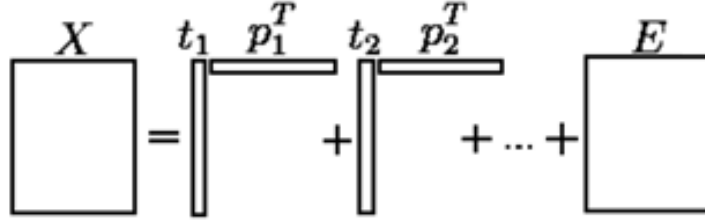


Figure 4.1: Decomposition process: collection of scores and loadings [72]

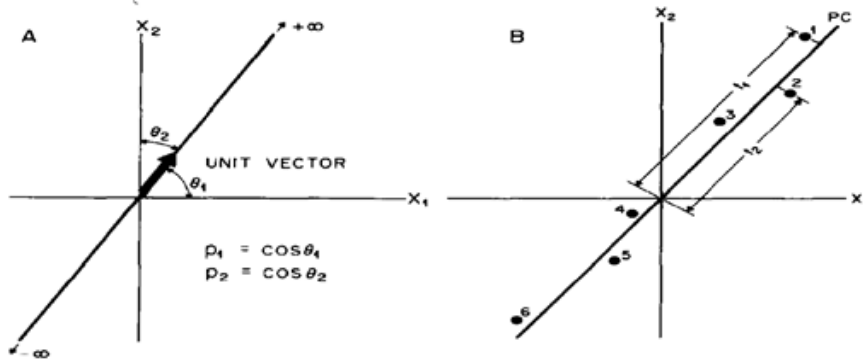


Figure 4.2: Principal components in the case of two variables [26]

NIPALS does not calculate all principal components at once: at every iteration, only one pair of loading and score is calculated and subtracted to the data matrix. The residual matrix can be used to compute the next pair in the consecutive iteration. At the end, the POD basis and the corresponding time coefficients can be computed, as follows:

$$\underline{\varphi}_s = \frac{\mathbf{X}P_s}{\|\mathbf{X}P_s\|} \quad (4.6)$$

$$\underline{a}_s = \mathbf{X}^T \underline{\varphi}_s \quad (4.7)$$

being $s = [1, \dots, M]$ the number of principal components found. Finally, the following decomposition is obtained:

$$\mathbf{X} = \phi \mathbf{A} + \mathbf{E} \quad (4.8)$$

where:

$\phi_{IJ \times M} = (\varphi_1 | \dots | \varphi_M)$ is the matrix whose columns are the POD modes;

$\mathbf{A}_{N \times M} = (\underline{a}_1 | \dots | \underline{a}_M)$ is the matrix whose columns are the time series of the mode φ_s ;

$\mathbf{E}_{IJ \times N} = (\underline{e}_1 | \dots | \underline{e}_N)$ is the matrix whose columns are the errors.

4.2 Independent Component Analysis

4.2.1 Motivation

The ICA (Independent Component Analysis) is a statistical signal processing technique whose main applications are blind source separation, blind deconvolution and feature extraction [34]. One application with combustion was demonstrated by Bizon et al. [8], [6]. They applied ICA to 2D images of combustion-related luminosity, in order to identify leading independent structures.

Imagine to be in a room where two people are speaking simultaneously. The two voice signals are recorded by two microphones hold in different locations. Each of the two recorded signals $x_1(t)$ and $x_2(t)$ is a weighted sum of the speech signals emitted by the two speakers $s_1(t)$ and $s_2(t)$. They can be represented with the linear equations:

$$x_1(t) = a_{11}s_1 + a_{12}s_2 \quad (4.9)$$

$$x_2(t) = a_{21}s_1 + a_{22}s_2 \quad (4.10)$$

where a_{11} , a_{12} , a_{21} , a_{22} are some parameters that depend on the distances of the microphones from the speakers. It would be useful to estimate the two original speech signals $s_1(t)$ and $s_2(t)$, using only the recorded signals $x_1(t)$ and $x_2(t)$ without knowing the parameters a_{ij} . This is the so-called *cocktail-party problem*. One approach to solve this problem is to use some information on the statistical properties of the signals $s_i(t)$ to estimate a_{ij} . It turns out that it is enough to assume that the two speech signals $s_1(t)$ and $s_2(t)$ are statistically independent at each time instant t . This is not an unrealistic assumption in many cases and it does not need to be exactly true in practice. The Independent Component Analysis or ICA is able to separate the two original source signals $s_1(t)$ and $s_2(t)$ from their mixtures $x_1(t)$ and $x_2(t)$, based on the information that the two original signals are independent.

To rigorously define ICA, a “latent variables” model can be used. Assume to observe n linear mixtures $x_1(t), \dots, x_n(t)$ of n independent components

$$x_j(t) = a_{j1}s_1 + a_{j2}s_2 + \dots + a_{jn}s_n \quad \text{for all } j \quad (4.11)$$

Let us denote \mathbf{x} as the random column vector whose elements are the mixtures x_1, \dots, x_n , \mathbf{s} as the random column vector with elements s_1, \dots, s_n and \mathbf{A} as the matrix with elements a_{ij} . Using this vector-matrix notation, the above mixing model is written as:

$$\mathbf{x} = \mathbf{A}\mathbf{s} \quad (4.12)$$

The model in Eq. 4.12 is called independent component analysis or ICA model. This model is a generative model, meaning that it describes how the

observed data are generated by a process of mixing the components s_i . The independent components s_i are latent variables, meaning that they cannot be directly observed. They are supposed to be the underlying components that describe the essential structure of the data and that correspond to some physical causes involved in the process. Also the mixing matrix is supposed to be unknown. Only the vector \mathbf{x} can be observed; \mathbf{A} and \mathbf{s} must be estimated by using it, under the most general possible assumptions. The basic assumption of ICA is that the components s_i are statistically independent and they have a non-gaussian distribution. In this way, after estimating the matrix \mathbf{A} , it is possible to compute its inverse and obtain the estimated independent components:

$$\mathbf{s} = \mathbf{W}\mathbf{x} \quad (4.13)$$

which can be solved by computing the matrix $\mathbf{W} = \mathbf{A}^{-1}$ in such a way that a linear combination $\mathbf{y} = \mathbf{W}\mathbf{x}$ is the optimal estimation of the independent source signals \mathbf{s} . Under the assumption of statistical independence of the components, each of whom characterized by a non-Gaussian distribution, the basic ICA problem given by Eq. 4.12 and 4.13 can be solved by maximization of the statistical independence of the estimates \mathbf{y} . Depending on the definition of statistical independence, the most popular ICA algorithms are based on the minimization of mutual information (which minimizes the dependence between random variables), maximization of likelihood estimation (which finds an unmixed matrix \mathbf{W} that yields extracted signals \mathbf{y} whose joint probability distribution functions (PDF) is as similar as possible to the joint PDFs of the unknown source signals) and maximization of non-gaussianity. The latter consists in finding the local maxima or minima of some measures of non-Gaussianity, such as kurtosis, negentropy or higher order cumulants, of a linear combination of the x_i $y = w^T x = \sum w_i x_i$, under the constraint that the variance of \mathbf{y} is constant. Each local maximum or minimum gives one independent component. In this work, a FastICA algorithm [37] is employed, which, by means of a gradient method, maximizes non-gaussianity as a measure of statistical independence. The algorithm is applied on centered and whitened image data, by using the transformation:

$$\mathbf{x} = \mathbf{D}^{-0.5} \mathbf{E}^T (\mathbf{x}' - E\{\mathbf{x}'\}) \quad (4.14)$$

where \mathbf{x}' is the raw data, \mathbf{E} is the $n \times n$ matrix made of POD eigenvectors, \mathbf{D} is the diagonal matrix made of POD eigenvalues and $E\{\cdot\}$ is the ensemble average. It must be noted that often the number n of ICs to be determined is smaller than the number m of available signal mixtures. In this case, the plain application of the basic ICA would lead to a non-square $m \times n$ mixing matrix \mathbf{A} , whose inverse cannot be determined. One solution is to reduce the rank of the data during the whitening phase, by projecting the observed mixture onto its POD modes and truncating to the few most significant. In this case, \mathbf{E} is the rectangular matrix made of the leading n POD eigenvectors and \mathbf{D}

contains the corresponding POD eigenvalues. This preprocessing assures that the algorithm still operates on a square $n \times n$ matrix and, additionally, allows to reduce the noise present in the data [33].

The ICA is a much more powerful method with respect to POD. The basis functions found by POD, which reflect the directions of the most prominent variances in the data, are uncorrelated but not statistically independent. This means that higher order dependencies still exist and, therefore, they are not properly separated. In other words, all POD modes contain some element of all structures found in all of the fields [8]. On the other hand, ICA is able to search for basis functions that are statistically independent or as independent as possible, increasing the independence to higher statistical orders. ICA minimizes the statistical dependence between basis functions and searches for a linear transformation \mathbf{W} that is able to express a set of features \mathbf{x} as a linear combination of statistically independent basis functions \mathbf{s} , so that the transformed components \mathbf{y} are independent. When deriving these components, the data are separated into either spatially (sICA) or temporally (tICA) independent components; each choice yields corresponding statistically independent images or time courses. In particular, tICA produces a set of mutually independent temporal sequences and a corresponding set of unconstrained images; sICA determines mutually independent images and a corresponding set of unconstrained temporal sequences [6], [22], see also Fig. 4.3.

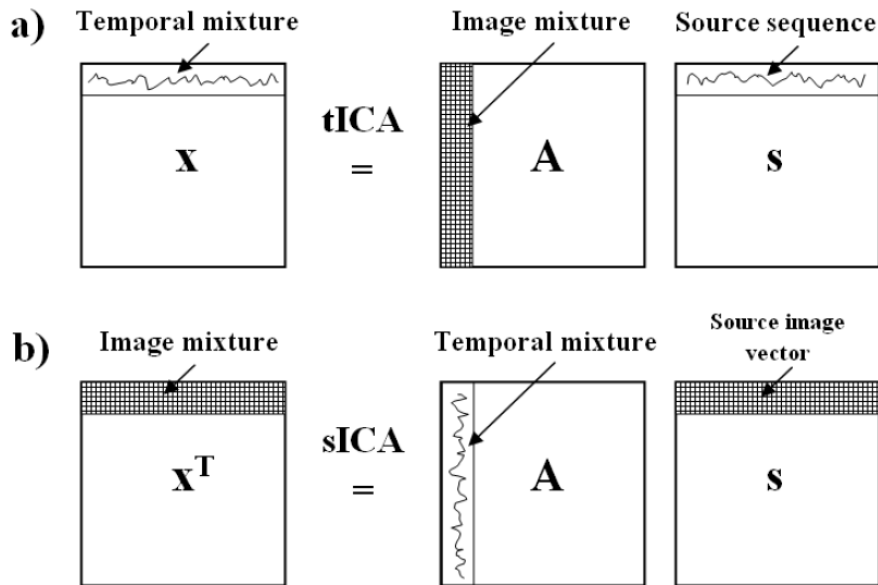


Figure 4.3: Vector matrix representation of the mixing process for tICA and sICA [76]

Some weak points have to be highlighted also for ICA: unlike for the principal components of the data, which are ordered according to their variance, no

intrinsic order exists for the independent components. In fact, any ordinary method of optimization tends to first find maxima/minima that have large basins of attraction. It is not possible to determine with certainty this order, but a suitable choice of the maximization function means that independent components with certain distributions tend to be found first. This is, however, so application-dependent that it is not possible to say much in general. Also the amplitudes of the rows of \mathbf{y} can be varied without affecting \mathbf{x} by scaling \mathbf{A} accordingly. This is the reason why ICA provides a solution only up to a multiplicative constant. In other words, the order, the signs and the scaling of the independent components cannot be determined: indeterminacy is an inherent property of this analysis [37].

The aim of the present work is to identify independent spatial structures evolving in time. Therefore, the spatial ICA is applied to the analysis of the luminosity field of the combustion process in a hybrid engine. This allows the identification of the leading independent structures during the burning process. The FastICA algorithm [37] is employed. It maximizes non-gaussianity by means of a gradient method, estimated by the absolute value of kurtosis, as a measure of statistical independence. The PSD of the temporal and spatial coefficients is performed at the end of the algorithm in order to obtain the excited frequencies and wavelengths during the combustion.

4.2.2 FastICA Algorithm

The data matrix \mathbf{X} is considered to be a linear combination of non-Gaussian (independent) components \mathbf{S} , according to 4.12. Under this generative model, the measured signals \mathbf{X} will tend to be “more Gaussian” than the source components \mathbf{S} , due to the Central Limit Theorem. Thus, in order to extract the independent components, an un-mixing matrix \mathbf{W} that maximizes the non-gaussianity of the sources has to be found.

Before starting to compute the independent components, the data are centered by subtracting the mean of each column of the data matrix \mathbf{X} . This is then whitened by projecting the data onto its principal component directions, as already explained in the previous subsection (see Eq. 4.14). The number of the principal components can be specified by the user, according to an energy criterion (as already done for computing the POD modes). The algorithm then estimates the un-mixing matrix \mathbf{W} , by maximizing the negentropy approximation under the constraints that \mathbf{W} is an orthonormal matrix. This ensures that the estimated components are uncorrelated. The algorithm is based on a fixed-point iteration scheme for maximizing the negentropy [5, 36].

In FastICA, non-gaussianity is measured using approximations of negentropy (J), which are more robust than kurtosis-based measures and faster to compute [35]. Practically, any non-quadratic, well-behaving even function can be used to construct a contrast function. Such a general contrast function can be defined as:

$$J(y) = [E\{G(y)\} - E\{G(v)\}]^2 \quad (4.15)$$

where G is any non-quadratic function and v is a Gaussian variable of zero mean and unit variance (i.e. standardized). The random variables y are also assumed to be standardized. Different choices of the function G can be done, depending on the problem. It is highly preferable that the estimator given by the contrast function is robust against outliers. The more slowly G grows as its argument increases, the more robust is the estimator [5]. Moreover, the contrast function should be fast to compute. Finally, the choice of the contrast function can influence the order in which the components are estimated. In fact, any ordinary optimization method tends to first find maxima that have large basins of attraction. Of course, as already said in the previous section, it is not possible to determine with certainty this order, but a suitable choice of the contrast function means that independent components with certain distributions tend to be found first [35]. In the FastICA algorithm, four contrast functions can be chosen:

$$\begin{aligned} G_1(u) &= \frac{1}{a_1} \text{logcosh}(a_1 u) \\ G_2(u) &= -\frac{1}{a_2} \exp(-a_2 u^2/2) \\ G_3(u) &= \frac{1}{4} u^4 \\ G_4(u) &= \frac{1}{3} u^3 \end{aligned} \quad (4.16)$$

where $1 \leq a_1 \leq 2$, $a_2 \approx 1$ are constants. In general, G_1 is a good general-purpose contrast function; G_2 may be better when the independent components are highly super-Gaussian, or when robustness is very important; G_3 and G_4 are justified on statistical grounds for estimating sub-Gaussian independent components when there are no outliers. Anyway, the estimators provided by this algorithm work for any distribution of the independent components and for any choice of the contrast function. The choice of the contrast function is only important for optimizing the performance of the method.

To find one independent component $y_i = \mathbf{w}^T \mathbf{x}$, it is necessary to maximize the function J_G , given by:

$$J_G(\mathbf{w}) = [E\{G(\mathbf{w}^T \mathbf{x})\} - E\{G(v)\}]^2 \quad (4.17)$$

where \mathbf{w} is an m -dimensional (weight) vector constrained so that the condition $E\{(\mathbf{w}^T \mathbf{x})^2\} = 1$ is true. Several independent components can be then estimated one-by-one using a deflation scheme. According to the Kuhn-Tucker conditions [59], the optima of $E\{G(\mathbf{w}^T \mathbf{x})\}$ under the constraint $E\{(\mathbf{w}^T \mathbf{x})^2\} = 1$ are obtained at points where

$$E\{\mathbf{x}g(\mathbf{w}^T \mathbf{x})\} - \beta \mathbf{w} = 0 \quad (4.18)$$

where β is a constant that can be evaluated to give $\beta = E\{\mathbf{w}_0^T \mathbf{x} g(\mathbf{w}_0^T \mathbf{x})\}$ and \mathbf{w}_0 is the value of \mathbf{w} at the optimum. The fixed-point iteration scheme for one unit used for maximizing the function J_G is:

$$\begin{aligned}\mathbf{w}^+ &= E\{\mathbf{x}g(\mathbf{w}^T \mathbf{x})\} - E\{g'(\mathbf{w}^T \mathbf{x})\}\mathbf{w} \\ \mathbf{w}^* &= \mathbf{w}^+ / \|\mathbf{w}^+\|\end{aligned}\tag{4.19}$$

To estimate all the independent components, the outputs $\mathbf{w}_1^T \mathbf{x}, \dots, \mathbf{w}_n^T \mathbf{x}$ need to be decorrelated after every iteration, in order to prevent them from converging to the same maxima.

4.3 A Practical Example

In order to check the performance of both decomposition algorithms before applying them to the combustion video data, an easy but representative example was performed.

4.3.1 POD vs. ICA

First of all, three sinusoidal periodic signals with frequencies of 0.5, 2 and 4 Hz are produced (see Fig. 4.4). Second, the source signals are linearly mixed together and three secondary signals are created: these are the “observed” signals (see the first plot in Fig. 4.5). The aim is to reconstruct the original signals with the only knowledge of the mixed ones. At this point it is important to remind that, in order to be able to do the reconstruction, the number of the “observed” signals must be the same (like in this case) or higher than the number of the source signals. Finally, the two decomposition techniques POD (or PCA) and ICA are applied to the mixed signals and their components, respectively principal and independent, are plotted in Fig. 4.5. Also, the PSD of the signals found by the algorithms is performed and the results are shown in Fig. 4.6 and 4.7.

From the PSD plots, it is clear that both algorithms are able to catch the right original frequencies. However, POD is not able to separate the frequencies in the different signals: each component contains frequencies that are also present in other components. On the other hand, ICA clearly separates each frequency in each signal and correctly reconstructs the original source signals. As previously said in Sec. 4.2, the weak point of ICA is that it is not able to correctly catch the amplitude and the order of the original signals due to its indeterminacy, as it can be noticed in Fig. 4.5.

The original signals are then non-linearly mixed in other three secondary signals (see first plot in Fig. 4.8) and the same decomposition and reconstruction procedures as before are applied to them. The three reconstructed signals coming from the POD and the ICA are plotted in Fig. 4.8. The PSD of the principal and independent components are shown in Fig. 4.9 and 4.10. From these plots, it is directly visible that both algorithms fail in finding the

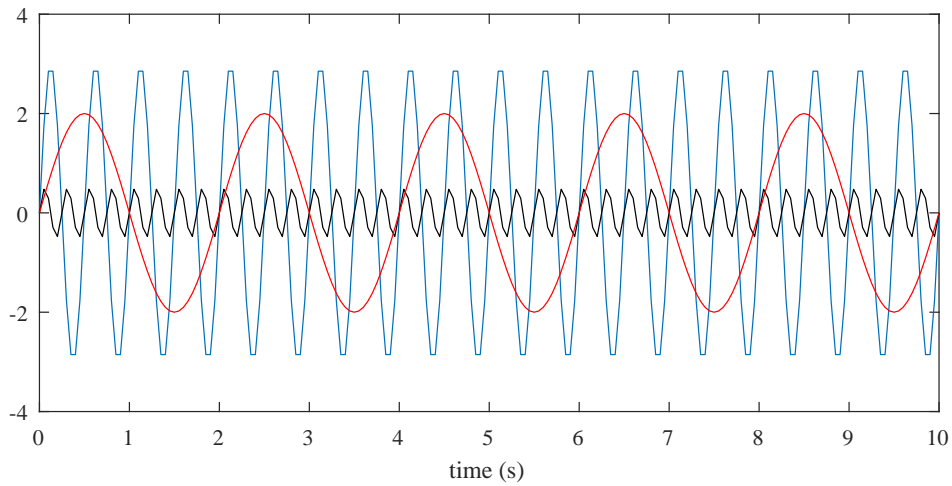


Figure 4.4: Source signals

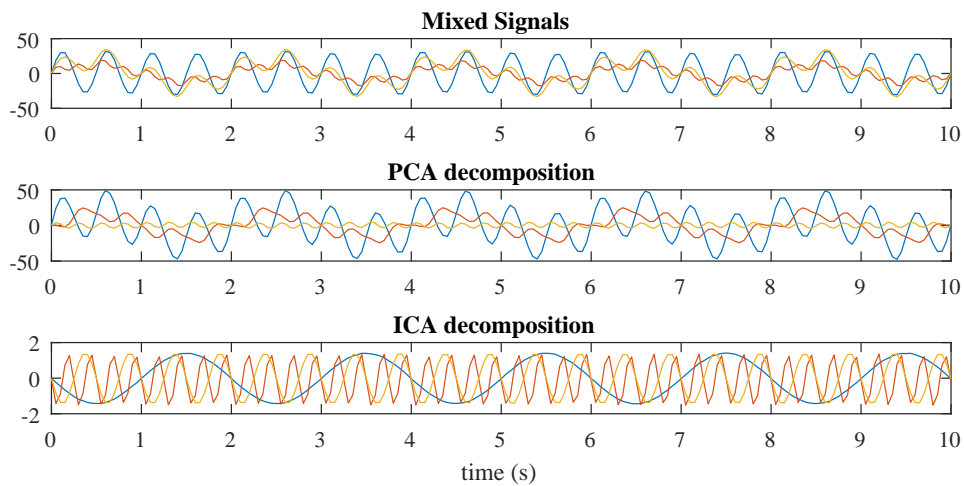


Figure 4.5: Linearly mixed signals (top) and computed source signals with PCA (middle) and ICA (bottom)

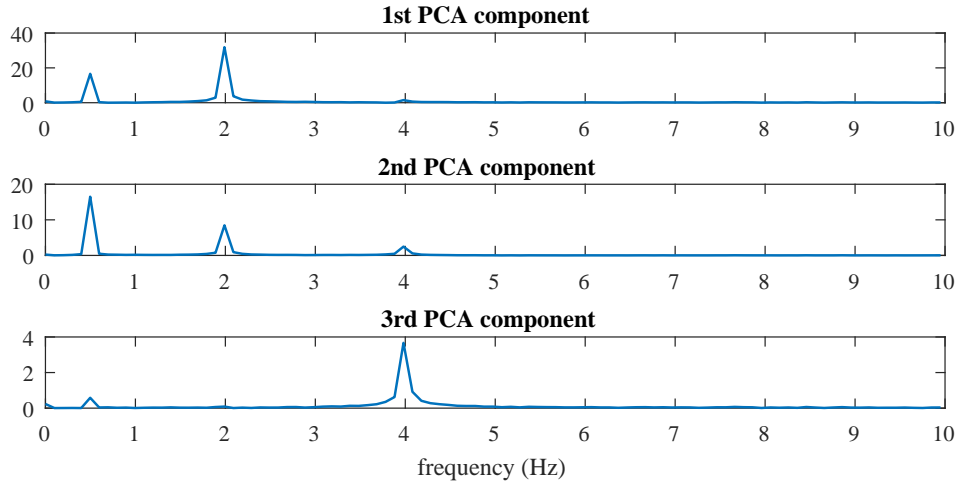


Figure 4.6: PSD of the principal components (PCA) of the linearly mixed signals

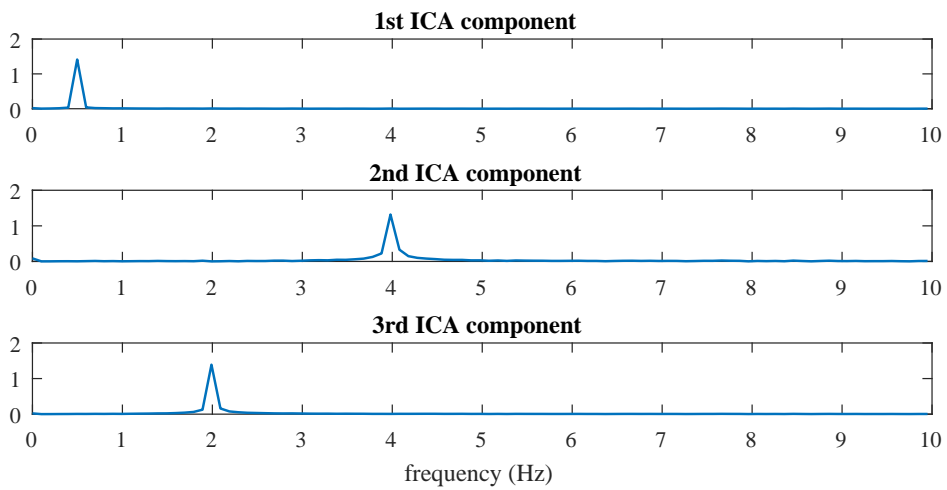


Figure 4.7: PSD of the independent components (ICA) of the linearly mixed signals, computed with G_3

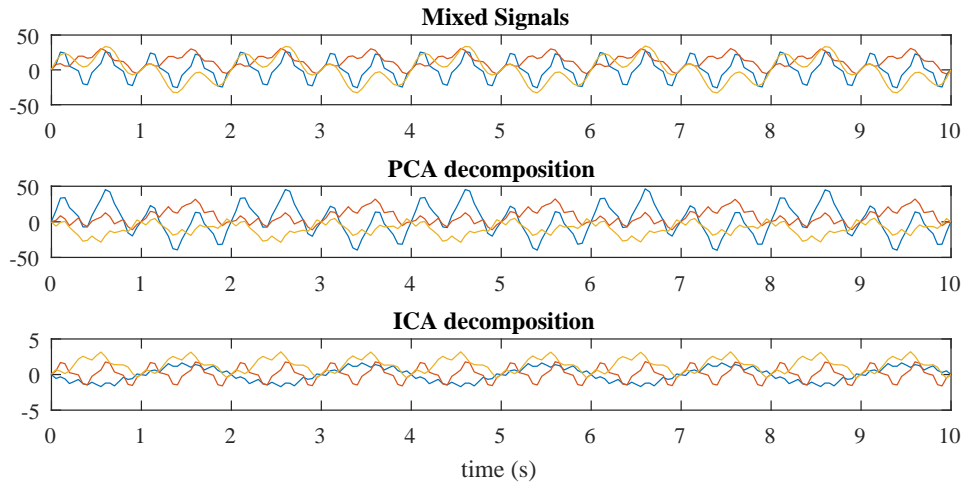


Figure 4.8: Non-linearly mixed signals (top) and computed source signals with PCA (middle) and ICA (bottom)

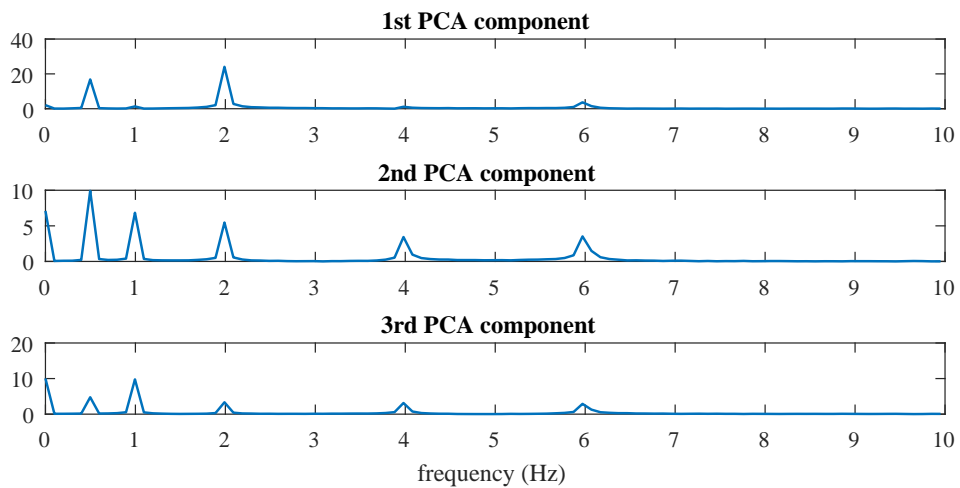


Figure 4.9: PSD of the principal components (PCA) of the non-linearly mixed signals

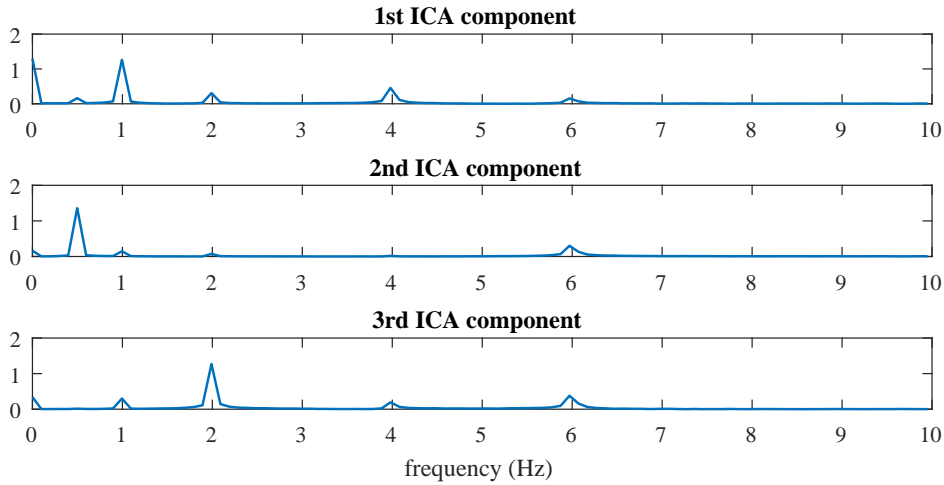


Figure 4.10: PSD of the independent components (ICA) of the non-linearly mixed signals, computed with G_3

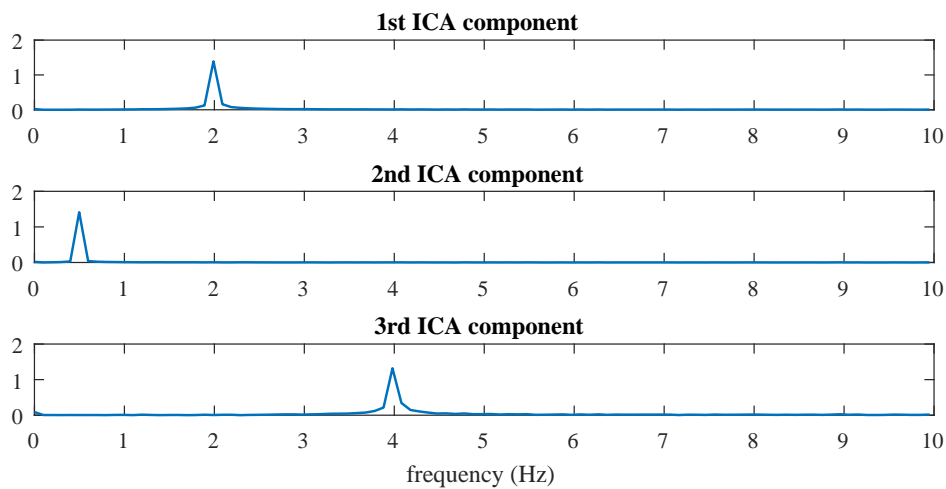
original signals. A wider range of frequencies is found in this case and none of the techniques is able to separate them. Despite this, the right frequencies can be recognized, among some other noisy and “spurious” signals.

From these two examples, it is possible to state that the decomposition methods, being both based on linear algorithms, work as expected in the case of linearly mixed signals. This means that POD or PCA is able to correctly predict the main components of a flow field (those that contribute the most to the energy of the flow), but not to correctly separate them. On the other hand, ICA is able to identify the independent components of the flow, but not to predict their order and scale. In the case of non-linearly mixed signals, such those that can be found in a real situation, both algorithms find not only the original components, but also some “spurious” signals. A whole range of frequencies, among which the original ones can also be recognized, are found. This is the case of the combustion video data. The main events happening in the combustor are obviously not linearly correlated and not independent from each other. Consequently, the decomposition methods are still able to recognize the main signals, but these will not be well separated from other noisy or “spurious” signals. That is why an accurate analysis and interpretation of the results will be necessary.

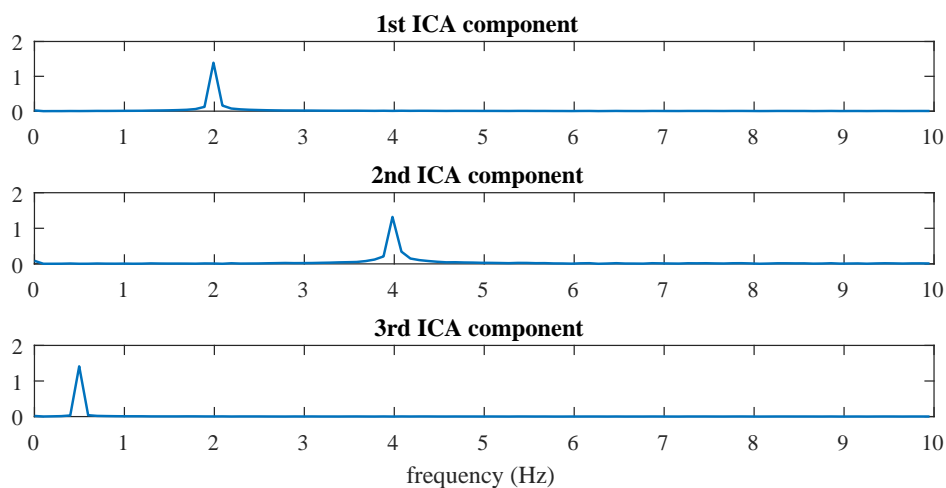
4.3.2 Choice of the contrast functions for ICA

The same example was used to evaluate the different contrast function provided by the FastICA algorithm. For the linearly mixed signals, the contrast functions G_1 , G_2 and G_3 (see Sec. 4.2) all work well and give the same results in terms of frequencies and signal separation. The order of the components is, of course, different, since the basins of attraction of the contrast func-

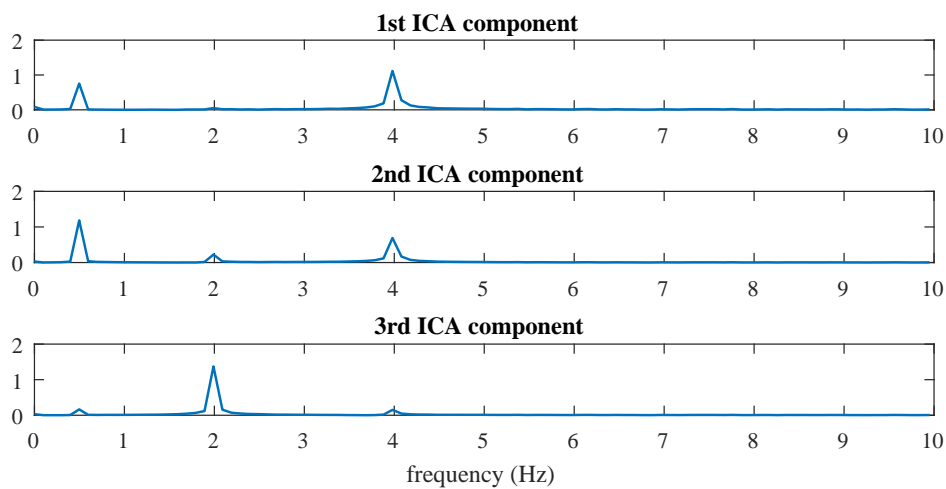
tions have different sizes. The function G_4 finds the right frequencies but does not separate them correctly. Like in the PCA, each signal has traces of frequencies of the other signals. Moreover, during the computation of the components, the algorithm had problems to converge, unlike with the other contrast functions. The PSD of the independent components found by using the different contrast function can be seen in Fig. 4.11 (the PSD of the independent components of the linearly mixed signals computed with G_3 is shown in Fig. 4.7). For the non-linearly mixed signals, all functions find the right frequencies together with “spurious” ones. Their PSD can be seen in Fig. 4.12 (the PSD of the independent components of the non-linearly mixed signals computed with G_3 is shown in Fig. 4.10).



(a) Independent Component computed with G_1

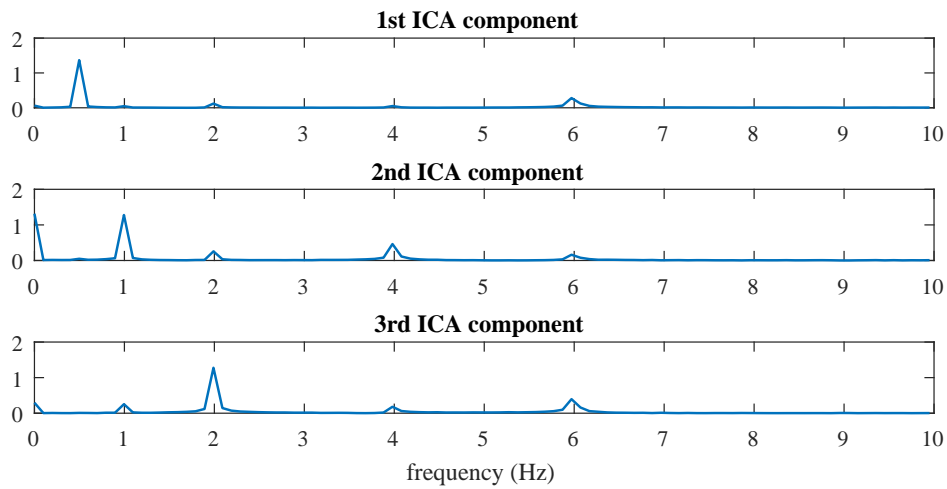


(b) Independent Component computed with G_2

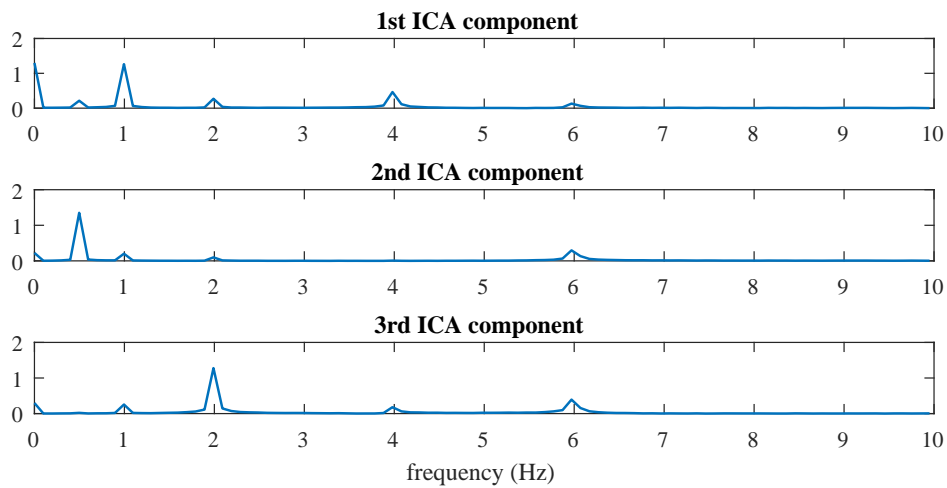


(c) Independent Component computed with G_4

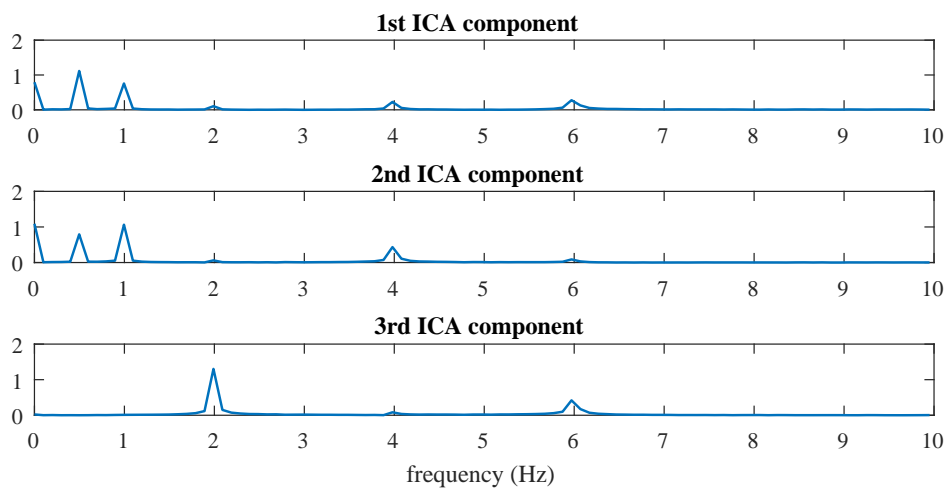
Figure 4.11: PSD of the independent components of the linearly mixed signals, computed with different contrast functions



(a) Independent Component computed with G_1



(b) Independent Component computed with G_2



(c) Independent Component computed with G_4

Figure 4.12: PSD of the independent components of the non-linearly mixed signals, computed with different contrast functions

5 Experimental Activity Set-Up

In this chapter, the propellants used in this research and the experimental set-ups are presented. In particular, the investigated paraffin-based fuels and their properties are described. The atmospheric and pressurized combustion facilities are introduced, together with the test sequence.

5.1 Paraffin-Based Fuels Properties

Paraffins (or alkanes) are saturated hydrocarbons having the general chemical formula C_nH_{2n+2} . Carbon and hydrogen atoms are linked by single bonds in an open chain. The number of carbon atoms n affects the physical, thermal and transport properties. For normal alkanes, the molecular weight increases with increasing carbon atoms number n . Consequently, the viscosity increases and melting and boiling points get higher. For an intermediate range of carbon numbers (25-45), which corresponds to waxes (see Fig. 2.7), the increase in viscosity caused by the increased molecular weight is counter-balanced by its decrease due to a higher melt layer temperature. For these reasons, paraffin waxes are the ideal fuels for the onset of the entrainment mechanism. Also critical properties depend on the carbon number n : normal alkanes with moderate to high carbon number, such as paraffin waxes, have low critical pressures and temperatures. For all practical engine operating conditions, paraffin waxes work under super-critical pressure and temperature conditions. In this case, no surface separates the liquid from the vapour phase, thus there is no clear definition for the surface tension.

The paraffin waxes that are typically used in hybrid rocket engine applications are a mixture of hydrocarbons, thus n represents the average carbon number. They appear as a white or colourless, odourless and tasteless materials, which are solid at room temperature. Typical values for melting point are about 45-70 °C, density is around 900 kg/m³ and boiling point above 370 °C. They are insoluble in water and they burn with a heat of combustion around 200-220 J/g. Their specific heat capacity is around 2.14-2.9 J/(gK).

5.1.1 Investigated Paraffin-Based Fuels

Four different paraffin-based fuels have been investigated in the framework of this research. The wax that has been used as a baseline for all the fuels is type 6805 from the manufacturer Sasol Wax. It has been chosen because of its viscosity and surface tension values, which are the two fuel parameters

that are expected to have the biggest influence on the entrainment process (see also Fig. 2.5). Detailed laboratory experiments have been performed before, in order to measure these two parameters for the different fuels (see Sec. 5.2). All samples for the ballistic tests have been blackened by additives during fabrication to limit radiation effects during combustion to the fuel surface. Generally, the amount of blackening additive was less than 1% and has therefore negligible impact on the performance [53]. Three different percentages of a commonly available polymer with the general chemical formula $(C_2H_4)_n$ have also been added to the paraffin samples, in order to have different viscosity values. In this way it was possible to study the influence of this parameter on the entrainment process. Moreover, the addition of polymer increases the mechanical properties of the paraffin, thus increasing also the quality of the combustion visualizations (less polluted window). Three different fuel configurations have been investigated. Combustion tests with fuel slabs with 5°, 20° and 90° forward facing ramp (FFR) angle have been performed (see Fig. 5.1) and the influence of the fuel configurations on the combustion and entrainment process has been investigated. All fuel slabs, produced and machined according to the same procedure, are 200 mm long, 100 mm wide and 20 mm high. A photo of a fuel slab before and after the combustion is shown in Fig. 5.2. A wavy fuel surface can be recognized after the burning process, thus confirming the formation of a melt layer on the slab surface during combustion.

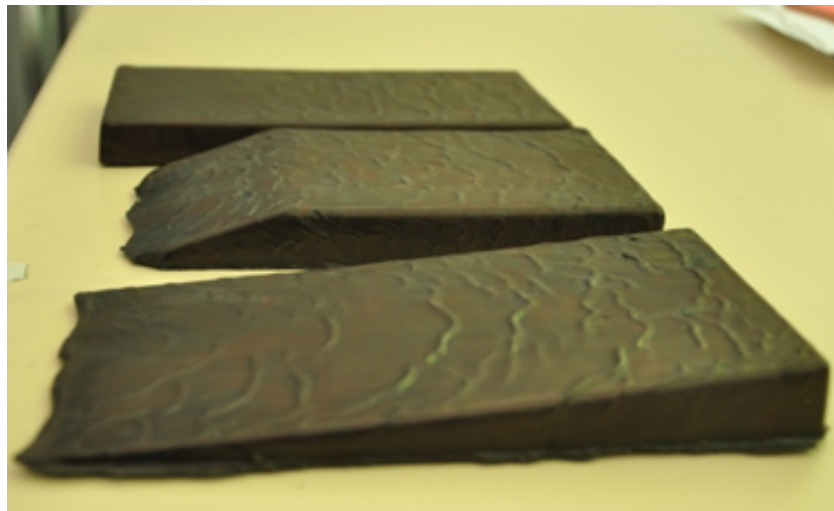


Figure 5.1: Different fuel configurations used in this research

5.2 Paraffin-Based Fuels Characterization

Characterization of the paraffin samples is necessary, since the entrainment process strongly depends on the fuel properties. Analytical formula for mate-



Figure 5.2: 20° FFR fuel slab before (top) and after (bottom) combustion test

rial properties, like surface tension and viscosity of paraffin waxes, are available in different publications, such as in Marano et al. [60, 61, 62]. Unfortunately, these are often only valid for straight paraffin with distinct carbon numbers. Therefore, they cannot be applied for most of the samples used in this research, as well as for paraffin-based mixtures.

Viscosity, liquid density and surface tension measurements of the four types of paraffin-based fuels used in this research were performed in the M3 chemical laboratory at the DLR Lampoldshausen.

5.2.1 Viscosity Measurements

The viscosity of a fluid defines its resistance to deformation by external forces, such as shear stress or tensile stress. It is expected to have the biggest influence on \dot{m}_{entr} [43]. For this reason, it was fundamental to evaluate the viscosities of the fuel mixtures used in this work and to connect them to the entrainment process. The viscosity measurements were performed with the rotational rheometer Thermo Haake RheoStress 6000. A cone-plate geometry with a cone angle of 2° was used in this study (see Fig. 5.3). For more details about the instrument see Appendix A.

Early viscosity measurements at different shear rates performed with the same instrument by Kobald et al. [52] showed that all the paraffin-based samples have a Newtonian behaviour, except for the paraffin with nanoclay particles. Therefore, the viscosity of the paraffin with polymer does not depend on the shear rate. Consequently, for these viscosity measurements, it was decided to consider a constant shear rate of 200 1/s and to vary only the fuel temperature. The measurements of the viscosity of the samples at different temperatures are shown in Fig. 5.4. Each curve represents the average of four curves obtained for each fuel formulation. The standard deviation is around 10% of the average values at each measurement point. It can be noticed that the viscosity increases significantly with increasing polymer ad-



Figure 5.3: Rotational rheometer and cone-plate geometry used in the framework of this research

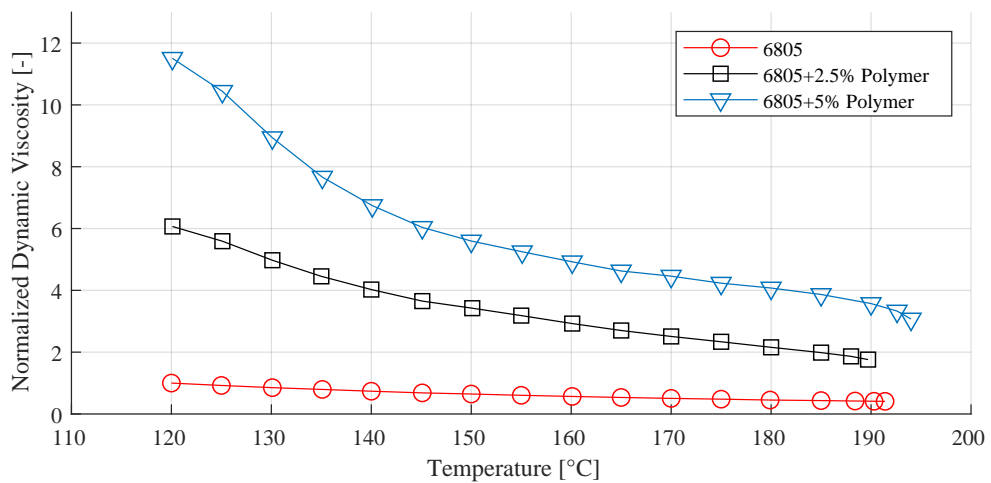


Figure 5.4: Viscosity of paraffin 6805 with different additives at a constant shear rate (values are normalized to the 6805 viscosity value at 120 °C)

diction. Moreover, with increasing temperature, the viscosities of the three blends tend to decrease faster than that of pure paraffin. Quantitative values are presented in Tab. 5.1.

Table 5.1: Measured viscosity values at different temperatures (for each temperature, data are compared to the pure paraffin viscosity value)

Fuel	T [°C]	μ [mPa s]	$\Delta\mu$ [-]
6805	120	3.9	0
6805+2.5% polymer	120.1	23.5	5
6805+5% polymer	120.1	44.6	10.5
6805	140	2.8	0
6805+2.5% polymer	140	15.6	4.5
6805+5% polymer	140.1	26.1	8.15
6805	160.1	2.2	0
6805+2.5% polymer	160.1	11.3	4.15
6805+5% polymer	160.1	19.1	7.7
6805	179.9	1.7	0
6805+2.5% polymer	180	8.3	3.8
6805+5% polymer	180	15.8	8

5.2.2 Surface Tension and Liquid Density Measurements

Surface tension is the property of a liquid to resist against an external force applied to it and results from the attraction of liquid molecules to each other. Surface tension and liquid density depend strongly on the temperature. Both properties were measured with the EasyDyne tensiometer with an accuracy of ± 0.1 mN/m (see Fig. 5.5). Further details about the instrument are given in Appendix A.

The measurements of the two properties of the samples at different temperatures are shown in Fig. 5.6 and 5.7. In this case, each point corresponds to one single measurement performed on different samples for each fuel formulation. Around 25-30 measurements are taken for each sample at decreasing temperature. The starting measuring temperatures are approximately 140-150 °, depending on the fuel formulation. Then, measurements are taken while the samples are cooling down, until they start to solidify. The curves are the best-fit interpolation of those points. The standard deviation, given by the instrument, on the single point is less than 1% and the R^2 for the interpolation curves is ranging from 0.93 to 0.98. As expected, the surface tension is increasing with increasing amount of polymer addition and decreasing temperature. On the other hand, the liquid density is increasing with decreasing

amount of polymer addition and decreasing temperature. Quantitative values can be found in Tab. 5.2 and 5.3.



Figure 5.5: Tensiometer used in the framework of this research

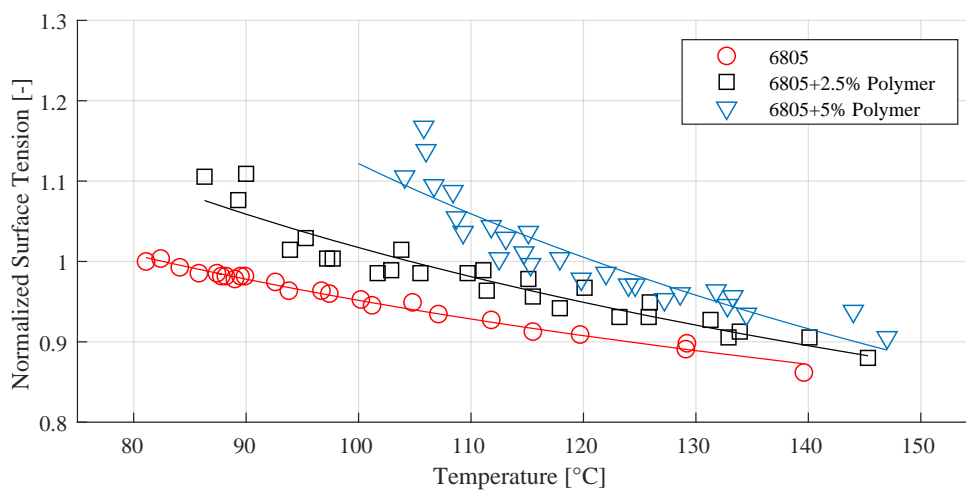


Figure 5.6: Surface tension of paraffin 6805 with different additives (values are normalized to the 6805 surface tension value at 80 °C)

Table 5.2: Measured surface tension values at different temperatures (for each temperature, data are compared to the pure paraffin surface tension value)

Fuel	T [°C]	σ [mN/m]	$\Delta\sigma$ [%]
6805	111.8	25.5	0
6805+2.5% polymer	111.4	26.5	3.9
6805+5% polymer	111.8	28.7	12.5
6805	119.7	25	0
6805+2.5% polymer	120.1	25.9	3.6
6805+5% polymer	119.8	26.9	7.6
6805	129.2	24.7	0
6805+2.5% polymer	131.3	25.5	3.2
6805+5% polymer	131.8	26.5	7.3
6805	139.6	23.8	0
6805+2.5% polymer	140.1	24.5	2.9
6805+5% polymer	140	25	5

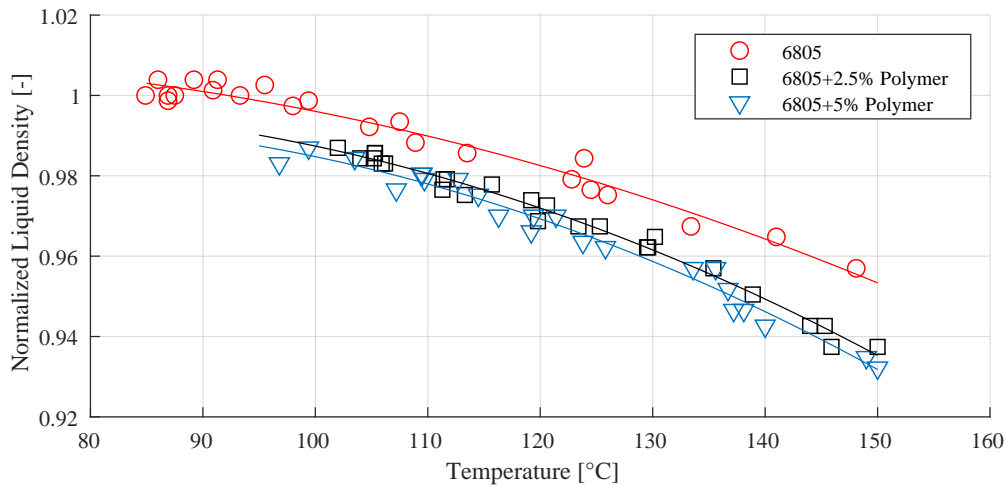


Figure 5.7: Liquid density of paraffin 6805 with different additives (values are normalized to the 6805 liquid density value at 85 °C)

Table 5.3: Measured liquid density values at different temperatures (for each temperature, data are compared to the pure paraffin liquid density value)

Fuel	T [°C]	ρ [g/ml]	$\Delta\rho$ [%]
6805	110.8	0.758	0
6805+2.5% polymer	111.3	0.749	-1.2
6805+5% polymer	109.7	0.751	-0.92
6805	122.8	0.751	0
6805+2.5% polymer	120.6	0.746	-0.67
6805+5% polymer	121.4	0.744	-0.93
6805	133.4	0.742	0
6805+2.5% polymer	130.2	0.74	-0.27
6805+5% polymer	133.6	0.734	-1.1
6805	141	0.74	0
6805+2.5% polymer	138.9	0.729	-1.5
6805+5% polymer	140	0.723	-2.3

5.2.3 Thermogravimetric Analysis and Differential Scanning Calorimetry

The thermogravimetric analysis (TGA) is a method of thermal analysis where the mass of a sample is measured over time as the temperature changes. This measurement provides information about physical phenomena, such as phase transitions, absorption and desorption, as well as chemical phenomena including thermal decomposition and solid-gas reactions (e.g. oxidation or reduction). The differential scanning calorimetry (DSC) is a thermal analysis in which the difference in the amount of heat required to increase the temperature of a sample and a reference is measured as a function of temperature. Both the sample and the reference are maintained at nearly the same temperature throughout the experiment. Since this analysis is based on a comparative method, the reference sample should have a well-defined heat capacity over the range of investigated temperatures. In this way, it is possible to detect phase transitions of the sample depending on if more or less heat is required to flow to the sample than to the reference, in order to maintain both at the same temperature. The amount of heat required depends on whether the process is exothermic or endothermic. Therefore, by observing the difference in heat flow between the sample and the reference, DSC is able to measure the amount of heat absorbed or released during such transitions. The TGA and DSC measurements were performed with the simultaneous thermal analyzer NETZSCH STA 449 F3 Jupiter (see Fig. 5.8). For all the

analysis, nitrogen was used as reference sample. The measurements were obtained by setting a dynamic temperature ramp, starting at 30 °C and ending at 1000 °C with a heating rate of 2 K/min. Further details about the instrument are given in Appendix A. The results for the pure paraffin and the fuel blend with 5% polymer are shown respectively in Fig. 5.9 and 5.10. It must be noted that, after the last endothermic peak, where all the remaining fuel vaporizes, nothing more is happening. This is why the plots are cut at 700 °C.



Figure 5.8: Thermal analyzer used in the framework of this research

In Fig. 5.9, at around 70 °C a strong endothermic peak can be seen in the DSC plot, but no mass change is visible in the TGA plot. This temperature corresponds to the melting point of the pure paraffin. The boiling point and the consequent vaporization of the paraffin can be clearly recognized at around 415 °C. At this temperature, another endothermic peak and a strong mass loss of almost 100 % are visible respectively in the DSC and TGA plots. After reaching this temperature, the sample is completely vaporized.

A similar trend can be seen in Fig. 5.10. In this case, four endothermic peaks can be recognized. The first one, at around 70 °C, corresponds exactly to the melting point of the pure paraffin. The second one, at around 110 °C, represents the melting temperature of the polymer. Also in this case, no mass losses can be seen in correspondence with the two endothermic peaks. The paraffin vaporizes endothermically at around 400 °C. After this temperature

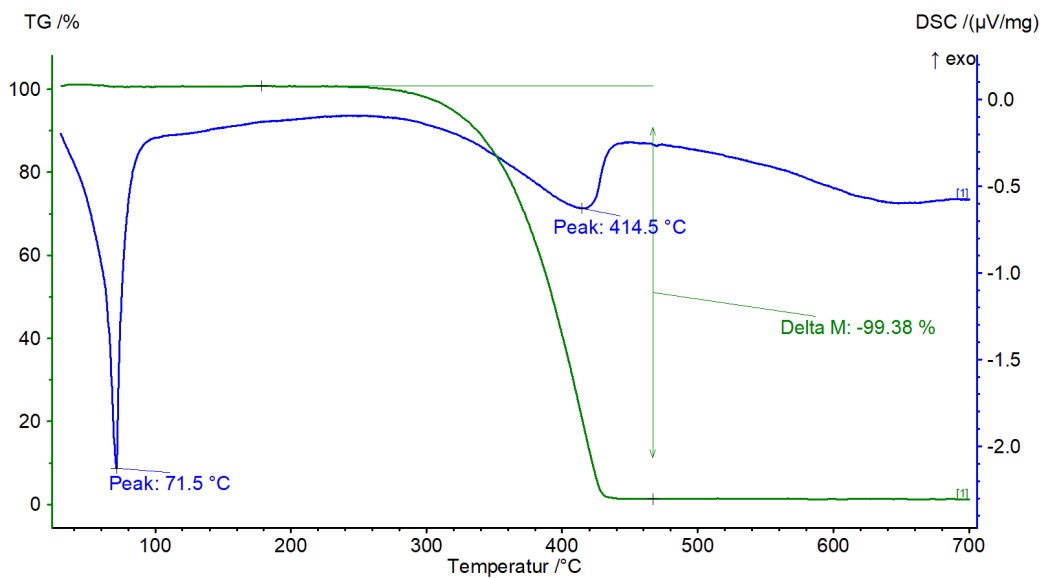


Figure 5.9: TGA and DSC measurements of pure paraffin 6805

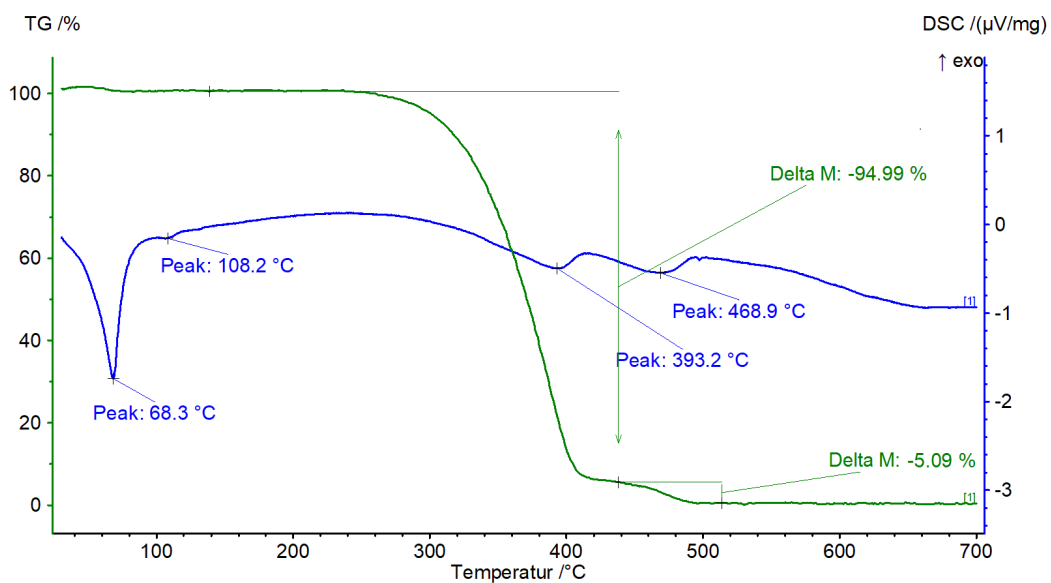


Figure 5.10: TGA and DSC measurements of 6805+5%polymer

peak, the sample loses almost 95% of its mass (as it can be seen in the TGA measurement), which exactly corresponds to the amount of paraffin mass in the sample. Finally, the last temperature peak at around 470 °C corresponds to a further polymer decomposition and subsequent vaporization. After this peak, the TGA measurement shows a mass loss of about 5%, which corresponds to the percentage of polymer added to the sample.

5.3 Experimental Set-Up and Data Acquisition

The experimental tests were performed at the Institute of Space Propulsion at the DLR Lampoldshausen at the test complex M11. The test facility at M11.3 was used for both atmospheric and pressurized combustion tests.

5.3.1 Atmospheric Combustion Facility

An already existing modular combustion chamber, used in the past to investigate the combustion behaviour of solid fuel ramjets, was adjusted and used for the test campaigns [17]. With this set-up, it is possible to perform tests both with and without a facing step placed before the fuel grain, which provides adequate flame holding and assures combustion stability. Tests performed in the framework of this research were all done without the flame holding step. A side view of the whole combustion chamber set-up is shown in Fig. 5.11. It consists of a planar single-slab combustor with a rectangular section of 150x90 mm. The flow straighteners with the pre-chamber, the optically accessible combustion chamber and the post-chamber are, respectively, 450 mm, 400 mm and 150 mm long. The oxidizer main flow is entering the combustion chamber from the left, after having passed the two flow straighteners. Its mass flow rate is adjusted by a flow control valve and it is measured with a Coriolis flow meter with accuracy higher than 0.35% and a repeatability higher than 0.2% of the mean flow rate. Nitrogen is used for purging. A high frequency static pressure sensor is mounted in the combustion chamber. Signals from the pressure transducer are recorded at 20000 Hz, in order to be able to analyze also transient phenomena. Ignition is done by an oxygen/hydrogen torch igniter attached at the bottom of the chamber. The two windows, one at each side, enable several different optical diagnostic tools. A photo of the high-speed video imaging set-up is shown in Fig. 5.12.

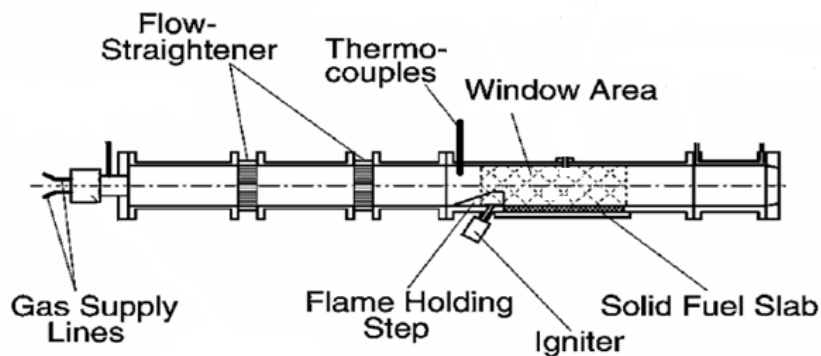


Figure 5.11: Sideview of the atmospheric combustion chamber set-up [77]

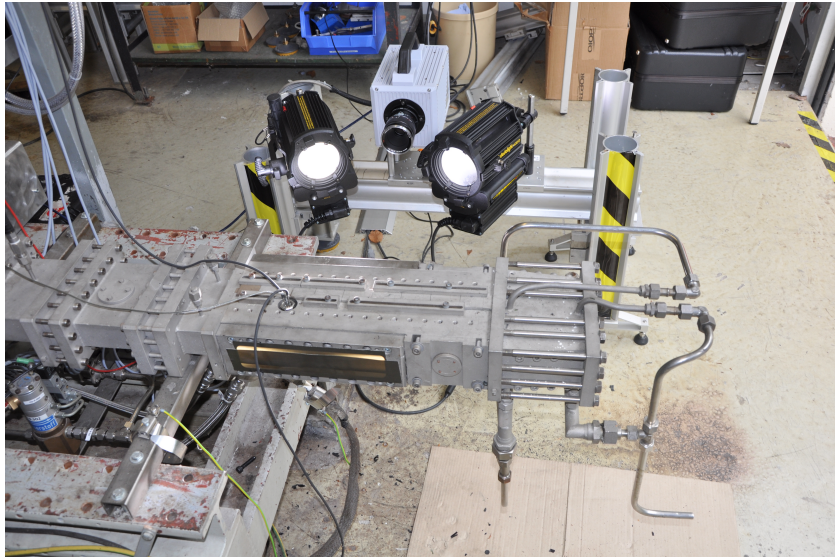


Figure 5.12: Combustion chamber set-up with optical diagnostic

5.3.2 Pressurized Combustion Facility

Another combustion chamber, which allows to perform tests at higher pressures (until 50 bar), can be used at the same test bench. In order to do so, some modifications to the test facility have been done. First of all, in order to better sustain higher pressures and avoid stress concentrations, the shape of the combustion chamber has been changed from a rectangular to a rounded one. The main combustion chamber body was machined out of a stainless steel cylinder with an internal diameter of 45 mm. The two quartz windows have also been adapted in size and shape to the new combustion chamber. In particular, a simpler design is used in order to reduce potential stress concentrations and costs. The two windows are also positioned further from the flame. Moreover, in order to minimize the interaction between the quartz window and the aluminum frame, more play is left between these two elements. Graphite gaskets are used to seal the windows and to further minimize the contact between the glass and the metal surfaces. The fuel slab width has been reduced to the half (around 50 mm), in order to decrease 3D effects along the width. The fuel grains are placed on a brass support in the combustion chamber. Ignition is realized, like in the tests at atmospheric pressure, with an oxygen/hydrogen torch igniter placed at the fore head of the combustion chamber. A shower head injector is used to bring the gaseous oxygen into the combustion chamber. The system can be run at variable pressures, up to around 40 bar by using different nozzle throat inserts having different diameters. The supply system has been left like in the tests at atmospheric pressures. This means that it is still possible to change the oxidizer mass flow by adjusting a flow control valve. The same Coriolis flow meter is used to measure the oxidizer properties. Pressure sensors are placed before

and after the injector (one on the feed line and one in the fore head of the combustion chamber), in order to measure injection and combustion chamber pressures. The test sequence has also been adapted to the pressurized facility. A side view and a picture of the new experimental set-up are shown in Fig. 5.13 and 5.14.

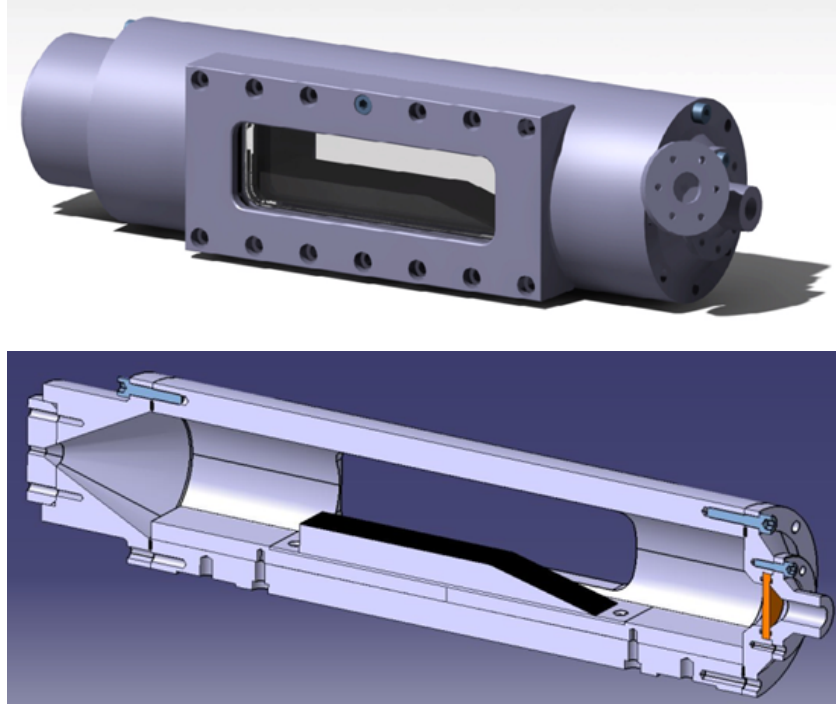


Figure 5.13: Sideview of the pressurized combustion chamber set-up

5.3.3 Test Bench Control System and Test Sequence

The test bench M11 is operated by a control system from Siemens based on Programmable Logic Controllers (SPS). The SPS controls the timing and operation of all the valves and hardware of the test bench. A supply of GH_2 , GN_2 and GOX , stored at a maximum pressure of 200 bar, is available at the test bench. Dome pressure regulators for each line regulate the incoming gas supply and set the required pressure in the system. In order to set and control the oxidizer flow, a flow control valve is installed in the oxygen main line. Pressure transmitters, thermocouples and Coriolis mass flow meter are connected directly to the SPS and provide feedback to control the tests. The scheme of the feed-line is shown in Fig. 5.15. A test sequence, reported in Tab. 5.4, is programmed before the test and is run automatically by the test bench control system. An ADwin measurement system by the company Jäger Messtechnik is used for data acquisition, programmed by the proprietary software named ADbasic. All data are low-pass filtered via Dewetron signal amplifiers before being acquired. Measured data are routed from ADwin via

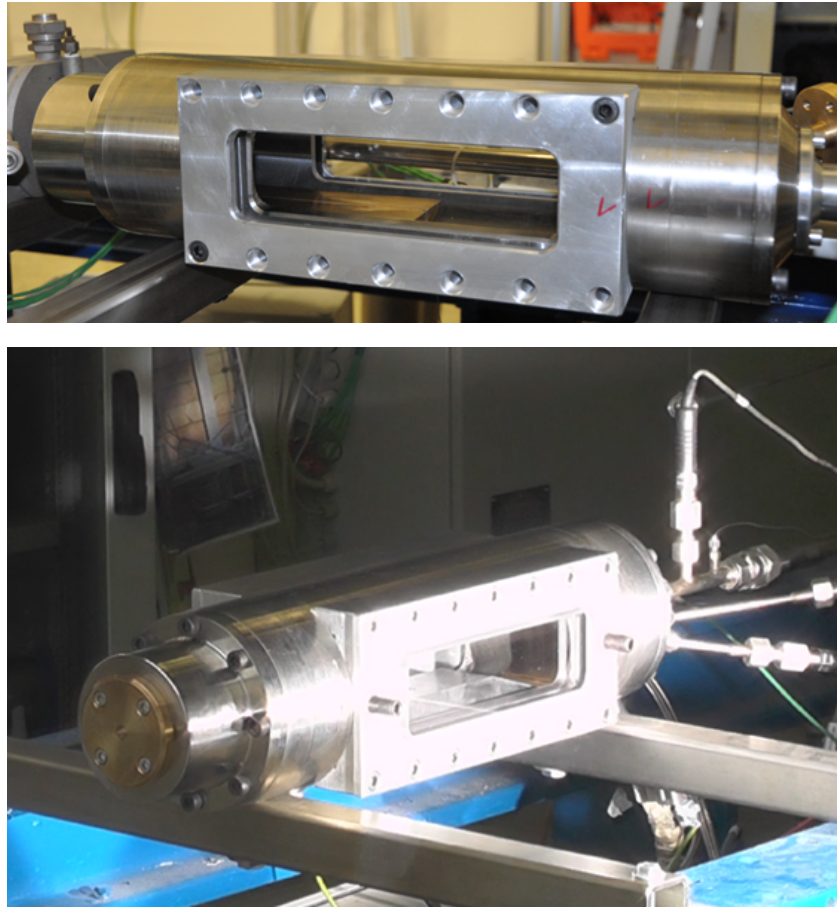


Figure 5.14: Pressurized combustion chamber set-up

Ethernet to a second computer that handles the saving routines by a Labview program. More information about the measurement data acquisition and test bench control system can be found in [48].

5.3.4 Combustion Tests Set-Up

In the framework of this research, combustion tests were performed using a single-slab paraffin-based fuel in combination with gaseous oxygen. Three fuel slab configurations with different forward facing ramp angle were tested (see Sec. 5.1.1). Burning time was 3 seconds for each test. The oxidizer mass flow was varied between 10 and 120 g/s. Tests were performed at both atmospheric and elevated combustion pressures.

For video data acquisition a black and white Photron Fastcam SA 1.1 and a colour Photron Fastcam SA X2 high speed video cameras were used with a maximum resolution of 1024x1024 pixel. The resolution and shutter times of the camera were adjusted for each test, according to the test conditions and position of the camera. Video recording frequency was set at 10000 frames per second (fps) for all the tests. Further details of the cameras are listed

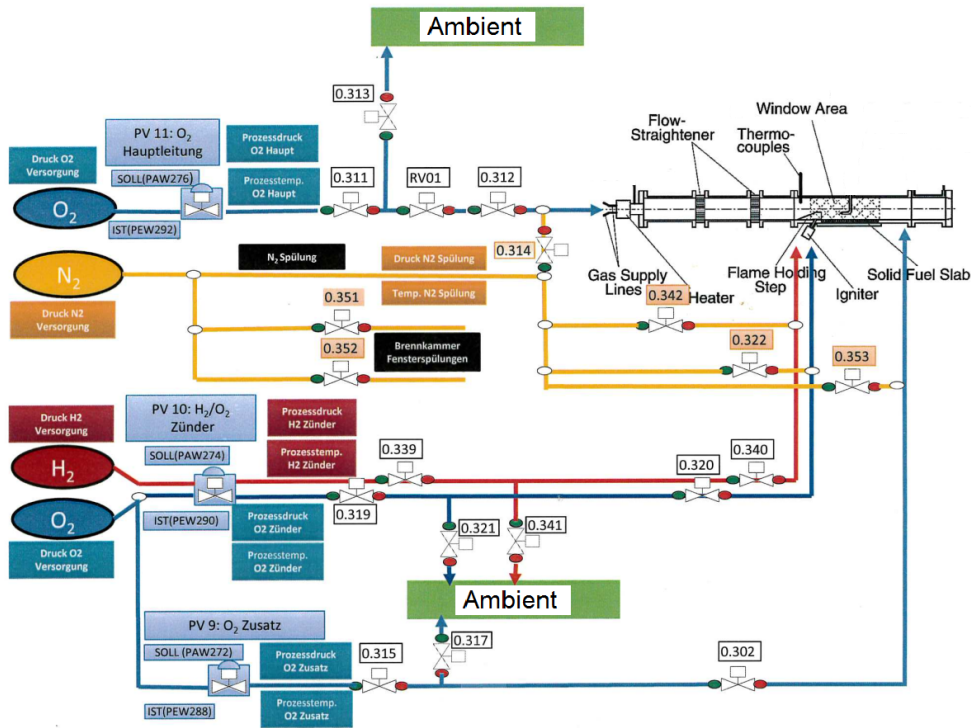


Figure 5.15: Feed-line scheme of the test bench M11.3

Table 5.4: Automatic test sequence

Time [s]	Action
T-30	Start of the sequence
T-29	Commanding control valve
T-15	Set dome regulator pressure
T-3	Start of the data acquisition
T-1	Start spark plug
T-0.2	Open ignition valve
T0	Open oxidizer main valve, start high-speed camera
T+0.3	Close ignition valve
T+3	Close oxidizer main valve, start nitrogen purge
T+10	End of the sequence

in Appendix A. For the CH^* chemiluminescence imaging a band-pass filter centered around 431 nm was placed in front of the camera. The excited CH^* molecules emit photons around this wavelength, when they relax back to a lower energy state. Since high CH^* concentration exists only in the main reaction zone, the resulting images provide a good indication of the instantaneous flame sheet location and topology.

6 Combustion Tests Analysis

In this chapter, the methodology adopted for analyzing the combustion video and test data is presented and discussed. Particular attention must be paid during the video pre-processing phase, since it has a great influence on the results. The post-processing, visualization and interpretation of the results is also discussed. At the end, challenges and limitations of this analysis are presented and commented.

6.1 Combustion Video Analysis

6.1.1 High-Speed Videos

The combustion high-speed videos are analyzed with a Matlab® routine, which decomposes the high-dimensional video data and returns as results the most excited frequencies and wavelengths characterizing the liquid melt layer, as well as the imaging representation of the different components (principal and independent, depending on the decomposition technique used) of the flame and flow field in the combustor. The video analysis is divided into three main phases:

- *video pre-processing*: the video is modified and the matrix containing the video data (Snapshot Matrix) is created;
- *decomposition* of the Snapshot Matrix into the spatial and temporal coefficients matrices with the two methods: Proper Orthogonal Decomposition (POD) and Independent Component Analysis (ICA);
- *data post-processing*: the Power Spectral Density (PSD) of spatial and temporal coefficients coming from the decomposition methods is performed.

As first step, a video pre-processing is performed, see Fig. 6.1. During this phase, the images are exported from the video and cropped with the Software VirtualDub. Usually filters are added, to adjust the brightness and the contrast of the images. The function sharpen is also used to enhance the contrast of adjacent elements. There exists lateral burning at the sides of the fuel, thus the bottom of the fuel is cropped just up to the solid fuel surface, in order to reduce noise and errors. Yet, the size of the area of interest is kept as large as possible in order to capture the flow dynamics

on the whole upper surface of the fuel slab. The angled front and the rear end, where further vortices are created, are not included in the frames. It is important to underline that the analyzed window has the same size in all the videos (500x60 pixel) and it is able to catch all the phenomena it is worth to analyze, still leaving out sources of noise and errors (such as the aft and rear end of the slab and the bottom of the fuel). The images are then exported into Matlab® and converted from true-color RGB to binary data images, based on a luminance threshold. The background noise, which usually consists of small light spots (most likely burning paraffin droplets), is removed. Finally, the waves edge is automatically detected with the Canny method, which is able to detect both strong and weak edges, and a sparse matrix is created. Each frame is then rearranged as a column vector and the Snapshot Matrix, which contains all the frames to analyze, is created. It has to be noticed that the recorded video data is a line of sight measurement. Thus, the data in the analysis represent an integrated measurement over the whole fuel slab width.

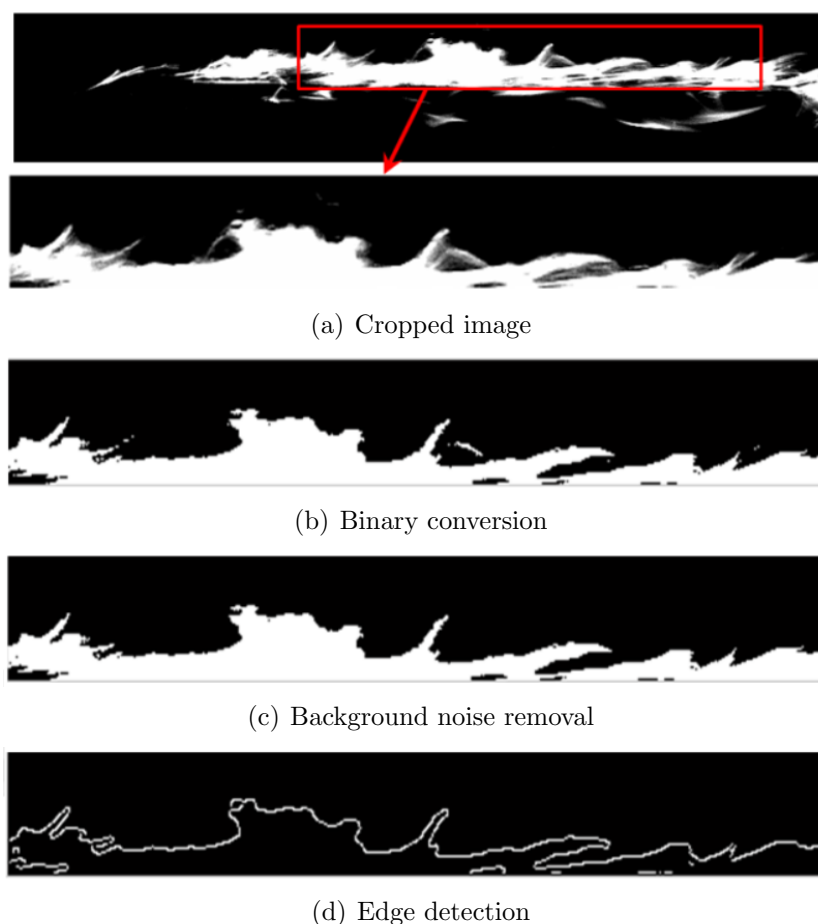


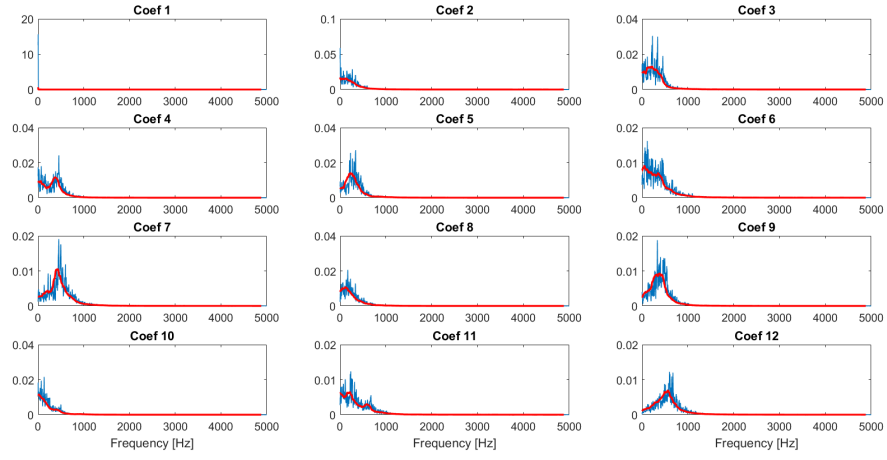
Figure 6.1: Video pre-processing steps

In a second step, the Snapshot Matrix is first tailored by auto-scaling with mean centering and standardization and then decomposed with both tech-

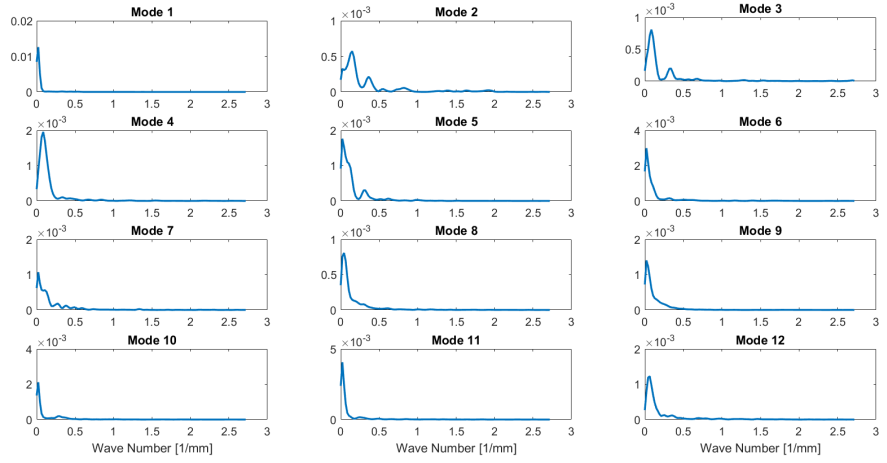
niques, POD and ICA, into two matrices containing spatial and temporal coefficients. The algorithms used for the decomposition, respectively NIPALS and FastICA, are presented in Chap. 4. Both decomposition algorithms are applied to the analysis of the luminosity field of images (scalar field) in a reactive flow. With POD, the most energetic flow structures are searched via statistical methods. The corresponding modes represent an average spatial description of structures containing most of the energy and that are predominantly associated with large-scale structures. They do not necessarily have to correspond to coherent structures. The POD modes represent the most common events occurring in the “fluctuating” luminosity field. It is commonly thought that the first few modes correspond to the average structure of the data, while higher order modes contain information about fluctuations [7]. For what concerns ICA, since the aim of the present work is to identify independent spatial structures evolving in time, the spatial ICA is applied to the analysis of the luminosity field of the combustion process in a hybrid engine. This allows the identification of the leading spatial independent structures during the burning process.

At the end of both algorithms, the Power Spectral Density (PSD) of the temporal and spatial coefficients is performed, in order to obtain the most excited frequencies and wavelengths during the combustion. The PSD of the temporal coefficients reveals whether there are dominant harmonics in the signal. The PSD of the spatial coefficients reveals the dominant wavelengths describing the change in luminosity in the horizontal or vertical direction. The column-wise spectral content of the spatial coefficients is related to the wavelength of the longitudinal waves, which are mainly moving in the horizontal direction. The row-wise spectral content is related to the position of the main flame above the fuel slab. In this case, the PSD peaks are much more spread out and less marked with respect to the peaks of the column-wise spatial coefficients. This happens because the analysis is carried out onto a rectangular grid with luminosity changing mainly in the horizontal direction. Typical results obtained from the PSD of the time and space coefficients coming from the first 12 POD and ICA modes are shown respectively in Fig. 6.2 and 6.3.

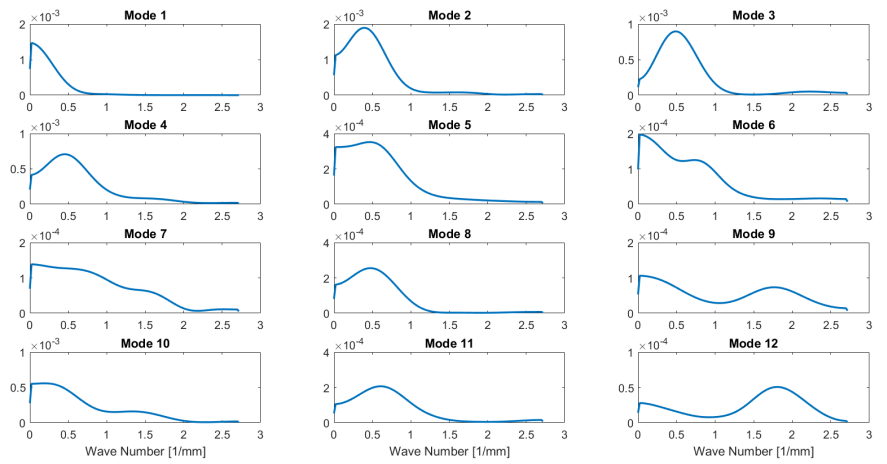
It is important to underline that all the tests were analyzed with both decomposition methods. A comparison of the results given by the two techniques was necessary in order to better characterize the dynamic of the process. In fact, both methods yield a whole range of different frequencies and wavelengths, which are amplified during the combustion. Some of them are related to the main dynamics of the combustion process, others are just random appearing vortices or not very energetic periodic signals (such as noise). In order to understand which frequencies and wavelengths are actually related to the main combustion events, it was necessary to compare the results of the two methods. If a frequency peak appears only in the POD, this is most likely related to a random energetic vortex (POD recognizes the most



(a) PSD of the time coefficients

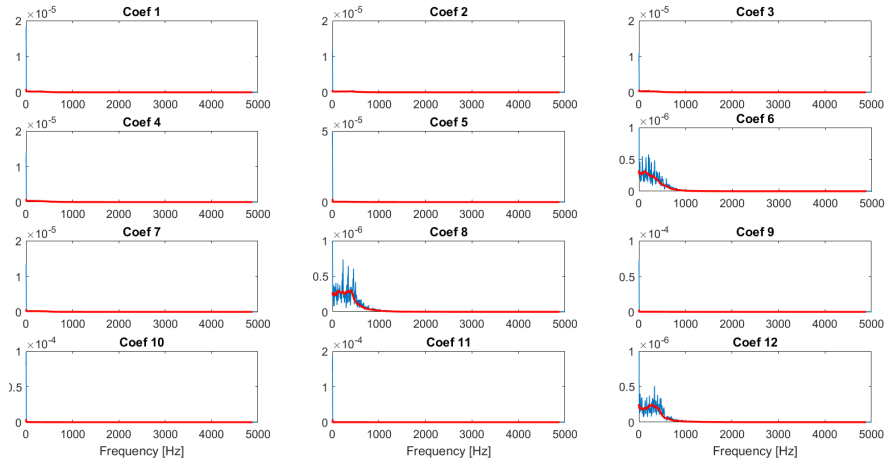


(b) PSD of the column-wise content of the space coefficients

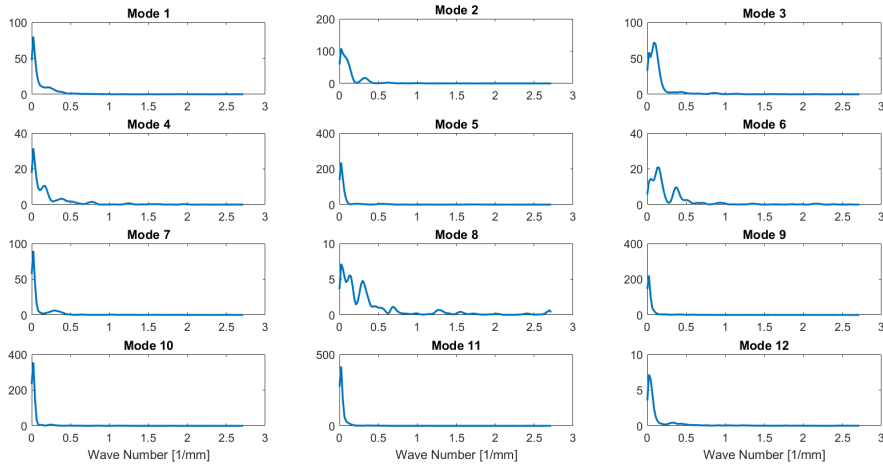


(c) PSD of the row-wise content of the space coefficients

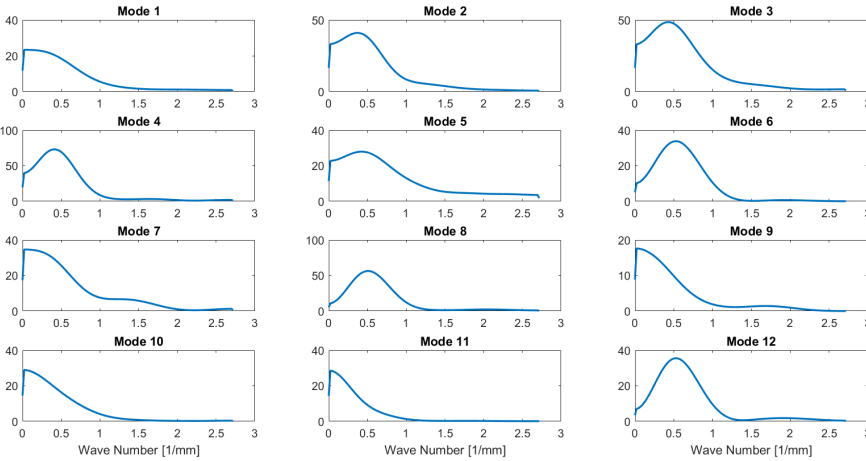
Figure 6.2: PSD of time and space coefficients coming from the POD



(a) PSD of the time coefficients



(b) PSD of the column-wise content of the space coefficients



(c) PSD of the row-wise content of the space coefficients

Figure 6.3: PSD of time and space coefficients coming from the sICA

energetic structures in the flow field). On the other hand, if a frequency peak appears only in the ICA, this is most likely a periodic but not energetic signal (ICA recognizes periodic independent structures). Those peaks that appear in both methods are periodic and energetic signals, thus related to the main events during the combustion process. So, at the end, only those frequencies and wavelengths appearing in both methods were considered.

In order to visually represent the dynamics of the flow field, contour plots of the spatial coefficients of the POD modes and independent components are plotted in the post-processing phase. When this analysis is performed, the pre-processing phase is slightly modified. In fact, since the focus is now on the whole flame intensity field, the same cropping window as in the previous analysis is used, but no binary conversion is performed. The RGB images are converted to greyscale ones, so that the information on the flame luminosity field is not lost. Consequently, no edge detection is applied. Again, a Snapshot Matrix (which, in this case, is not sparse) containing the luminosity information of the frames is created and the two decomposition techniques are applied to it. Two matrices containing temporal and spatial coefficients are found and the contour plots of the spatial coefficients, which represent the intensity of the flame luminosity, are created. In this way, the dynamics of the flame, such as flame oscillations or vortices appearing at the forward-facing ramp, can be visualized, independently from the time. Typical contour plots obtained by plotting the space coefficients coming from the first 3 POD modes are shown in Fig. 6.4. It is clearly visible that the first POD mode represents the typical profile of a boundary layer combustion flame. Even entrained fuel droplets detaching from the flame can be detected. Higher modes show combustion fluctuations and more fragmented structures. Similar results can be found observing the contour plots coming from the sICA.

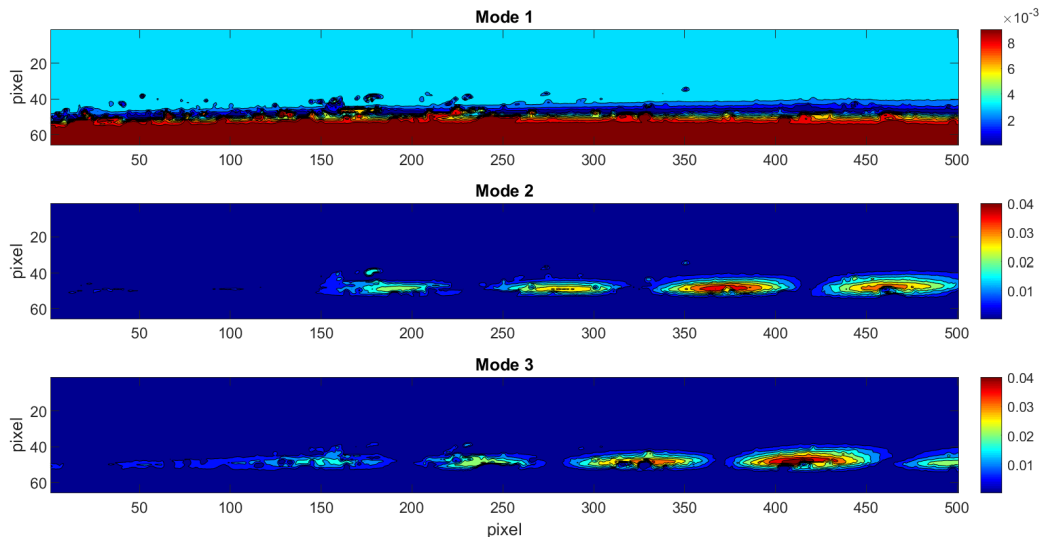


Figure 6.4: Contour plots of the space coefficients coming from the POD applied to high-speed videos (oxidizer flow from left to right)

6.1.2 CH* Chemiluminescence Videos

It is generally recognized (see [21, 74]) that the primary species contributing to flame luminescence are the electronically excited species CH*, C2* and OH*. All three species show a close correspondence across the main reaction zone and are thus equally suitable as markers for the flame zone location. In particular, the concentrations of CH* increase rapidly to a maximum within the flame and then decay rapidly downstream of the reaction zone [73]. Therefore, the CH* images give a good representation of the main flame location.

For the CH* chemiluminescence videos investigation, the flame zone is analyzed with the decomposition algorithms. The same procedure as for the high-speed video imaging is applied. However, the pre and post-processing are slightly modified, since the focus is now not on the frequencies and wavelengths peaks anymore. In particular, in the pre-processing, the same cropping window as in the high-speed video frames is used, but no binary conversion is performed. The RGB images are converted to greyscale ones, so that the information on the flame luminosity field is not lost. Consequently, no edge detection is applied. Each frame is then rearranged as a column vector and the Snapshot Matrix, which contains all the frames to analyze, is created. The data matrix is decomposed with both techniques, POD and ICA, into two matrices containing spatial and temporal coefficients, like already explained for the high-speed videos. In the post-processing, the PSD of the temporal and spatial coefficients is replaced by the contour plots of the spatial coefficients (of both POD modes and independent components), which represent the intensity of the flame luminosity on a colour map. In this way, it is possible to detect, within the flame zone, those areas where the reactions are more concentrated, independently from the time.

Typical contour plots obtained by plotting the space coefficients coming from the first 3 POD modes are shown in Fig. 6.5. It is clearly visible, like in the contour plots of the high-speed videos, that the first POD mode represents the profile of the boundary layer flame. However, in this case, the flame zone and its thickness are clearly detectable, as well as the boundary layer profile. In fact, 3 main regions can be seen in this plot. The first one, closer to the fuel surface, is characterized by a higher luminosity intensity: this is the fuel-rich region, where a large number of CH* molecules is emitted. The middle region is characterized by the lowest luminosity intensity: this is the flame zone, where an almost stoichiometric mixture ratio is achieved and the highest temperature (flame temperature) inside the boundary layer is reached. At this point, it is important to remember that the CH* radicals are more likely to be released where the temperature is not too high. In fact, at higher temperatures, they are further reacting (the most likely reaction is: $\text{CH}^* + \text{O}_2 = \text{CO} + \text{OH}^*$) and, therefore, their concentration decreases in favour of the OH* radicals. The third region is characterized by a medium luminosity intensity: this is the oxidizer-rich region that delimits the boundary layer,

where the still-unburned fuel mass is further reacting with the oxidizer. The CH^* videos are, therefore, a powerful tool to visualize the combustion flame zone and give information about the flame thickness.

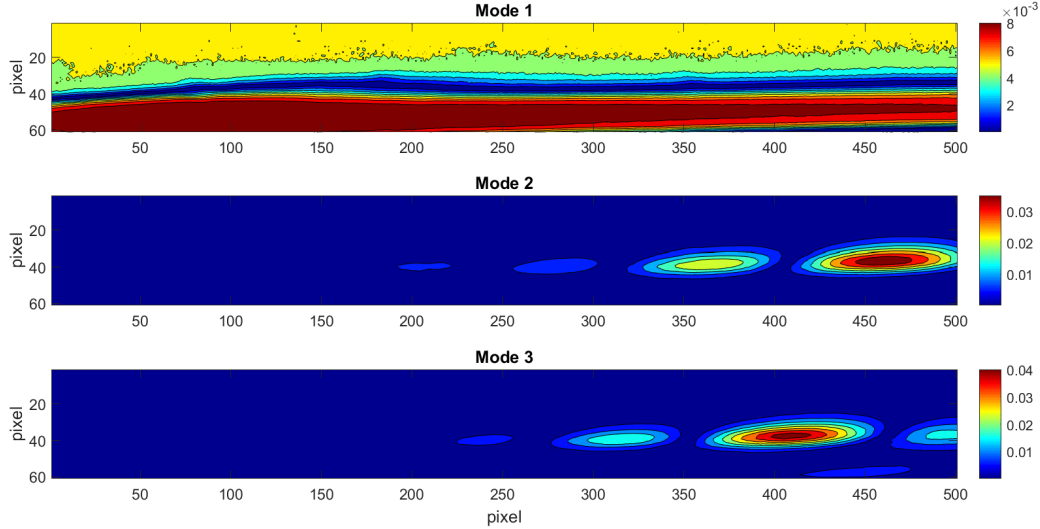


Figure 6.5: Contour plots of the space coefficients coming from the POD applied to CH^* videos (oxidizer flow from left to right)

6.2 Test Data Analysis

After each combustion test, the measurement data recorded by the sensors are analyzed with Matlab®. The evolution of the injector and combustion chamber pressures in time are obtained from the measurements of the static pressure sensors (see Fig. 6.6, top). Instantaneous data of the oxidizer mass flow are given by the Coriolis (see Fig. 6.6, bottom). Before and after each burning test, the fuel slabs are weighted and their dimensions are measured with a caliper. In this way, a space-time averaged regression rate can be computed and the experimental parameters a and n (see Eq. 2.21) can be determined. Obviously, in this particular case, the computed regression rate values are not representative of a typical hybrid rocket engine. In fact, the operating conditions of the experimental set-up used for the combustion tests are different from those of a real engine, even in the pressurized facility. The main difference consists in the fuel configuration: the flow field in the combustion chamber with the 2D fuel slab is different from the 2D radial fuel grain. This causes the convection and diffusion processes inside the chamber, as well as the thermal exchanges, to be different from the real hybrid rockets conditions. Moreover, the interactions between the oxidizer flow and the side walls, as well as the effects of side burning, are further influencing the regression rate values. However, these differences are not an issue for studying the liquid layer instability process, which is the focus of this work. In fact,

the obtained results can be expressed as a function of the flow speed (or mass flow) and mass flux in the combustion chamber and applied, to some extent, also to other operational cases (small differences can be caused by deviations in the combustion chamber temperature).

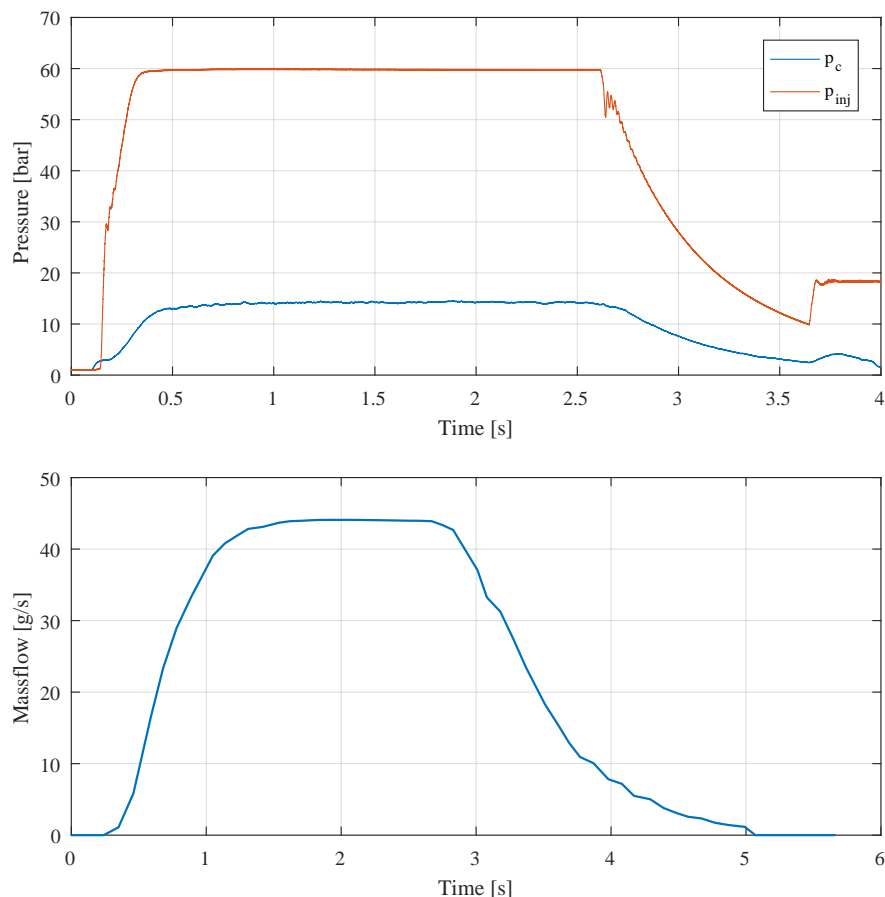


Figure 6.6: Typical pressure (top) and oxidizer mass flow (bottom) time traces from combustion test

6.3 Challenges and Limitations of the Analysis

The optical analysis and methodology proposed in this research aim to automatically detect and investigate the main flow structures characterizing the combustion process of hybrid rocket engines. The results collected in this work provide many insights into the main combustion phenomena and turbulent diffusion flame above a 2D solid fuel slab burning with gaseous oxygen. They find a direct application in the hybrid combustion theory and can help with the design of a hybrid rocket engine. However, some limitations in this analysis must be taken into account and it must be highlighted that the test set-up has some differences with respect to a standard hybrid engine.

For what concerns the optical set-up, the fuel configuration and the whole combustion chamber result in a large empty volume with respect to a standard cylindrical combustion chamber. This causes a different temperature field inside the chamber, since most of the heat is dispersed through the walls, which are not protected from the fuel grain (such as in a standard engine). However, the temperature in the flame and in the boundary layer should not be affected by the different temperature distribution in the chamber. Moreover, the small size of the fuel slab with respect to the large combustion chamber volume also results in a higher mixture ratio than that of a typical engine. Nevertheless, this is not expected to have significant impact on the results found in this study, since they are more focused on the local combustion phenomena that are not affected by the large volume of the oxygen flow. The larger OF only implies a lower combustion efficiency, which results in a higher mass of unburned oxidizer exiting the combustion chamber. Furthermore, the use of a 2D slab instead of a fuel grain causes a different flow pattern inside the combustion chamber, which could also bring to differences in the thermo-fluid dynamics processes. This is expected to have a secondary effect on the results of this research, but still it should be further investigated. Finally, the uniform oxidizer flow entering the optical combustion chamber is not really representative of the injection in a typical engine. This could result in an unstable flame that needs to be stabilized with a forward-facing ramp. A study on the influence of the slab leading edge on the combustion stability was performed in the framework of this work.

For what concerns the analysis, the whole study is based on a 2D approach, which neglects 3D effects coming from the flow pattern and the combustion chamber geometry. In the attempt to reduce these effects, the combustion chamber and fuel slab designs were optimized. In particular, the space between the windows and the fuel slab was reduced and the effects of the fuel leading edge were investigated. Moreover, it has to be noticed that the recorded video data is a line of sight measurement. Thus, the data in the analysis represent an integrated measurement over the whole fuel slab width. Furthermore, it must be also taken into account that the waves on the fuel surface do not always move straight in the longitudinal direction, but they might have a transversal velocity component. This might alter the values of the longitudinal wavelengths computed with the decomposition methods. The brightness of the flame and the pollution of the windows, due to condensed combustion products and soot, make the optical measurements and the analysis even more complicated. However, this problem could be solved by using a bright external lighting source and by choosing the right shutter times of the video camera for each test, according to the burning conditions (i.e. flame brightness). Additionally, during the pre-processing of the burning videos, brightness and contrast were further adjusted, in order to visualize and resolve also darker and smaller scale structures. Moreover, the whole theoretical analysis is based on a linear theory: linear stability is a necessary

but not sufficient condition for the onset of the unstable waves that lead to the entrainment. Finally, the presented research studies the instability of a liquid layer whose thickness is not observable. However, for high rates of entrainment and high flow speed (i.e. when the flame is near the fuel surface), it can be assumed that the flame follows the liquid layer. This assumption is considered valid during the whole analysis.

7 Results and Discussion

In this chapter, the main results of this research are presented and discussed. It is divided in four main parts: first, the theoretical results of the Kelvin-Helmholtz instability models are presented and compared, together with some considerations on the boundary layer thickness and flame position coming from the Marxman's theory; second, the work performed to correctly configure the decomposition algorithms is discussed; finally, two sections are dedicated to the experimental results obtained with the atmospheric and pressurized combustion chamber set-ups.

7.1 Theoretical Results

7.1.1 Kelvin-Helmholtz Instability Onset

In this section, the Kelvin-Helmholtz instability theory presented in Chap. 3 is applied to the paraffin-based fuels used in this work. The values of liquid fuel density, surface tension and viscosity are taken from the measurements performed in the chemical laboratory (see Sec. 5.2). A liquid layer temperature of around 300°C is considered (averaged temperature between melting and boiling points). The gas density and viscosity values for each mixture ratio OF at optimum conditions are given by the software NASA CEA (Chemical Equilibrium with Applications) [27, 28]. The neutral curves for each KHI model are plotted and discussed. The local minimum of each curve shows the critical wavelength and the corresponding gas velocity. The critical wavelength is the first unstable wave that is excited and it appears when the critical gas speed is reached. For gas speed below the critical one no instability is achieved. The critical values are changing depending on the chosen theoretical model, mixture ratio OF and liquid fuel properties.

Inviscid Unbounded Model

In this case, since the liquid layer is considered inviscid, no big difference can be seen between the two paraffin-based fuels. Small deviations of the critical gas flow speed values are due to the slightly different density and surface tension of the two fuels. On the other hand, an influence of the mixture ratio OF and, consequently, of the combustion temperature on the critical gas flow speed can be observed (see Fig. 7.1 and 7.2). The differences between the two fuels are only due to the different densities of the combustion products. Numerical values are reported in Tab. 7.1.

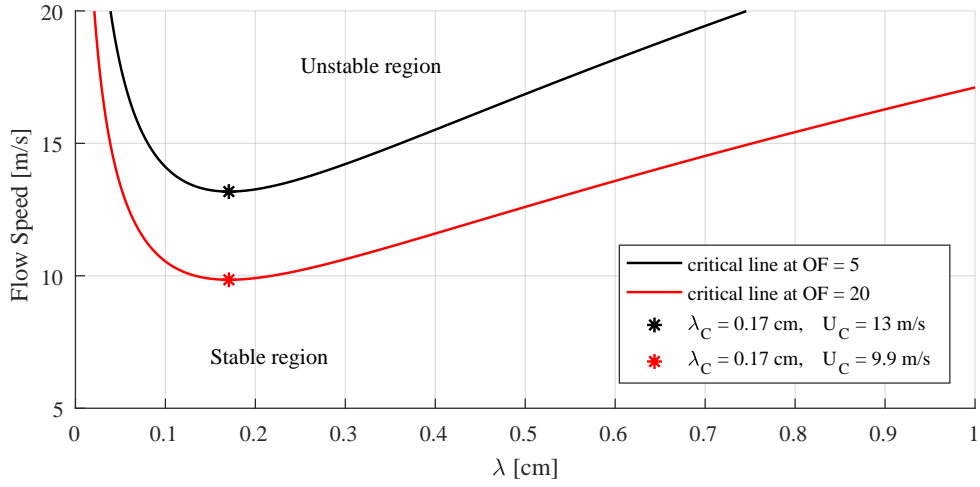


Figure 7.1: Neutral curve of pure paraffin 6805 for the inviscid unbounded model

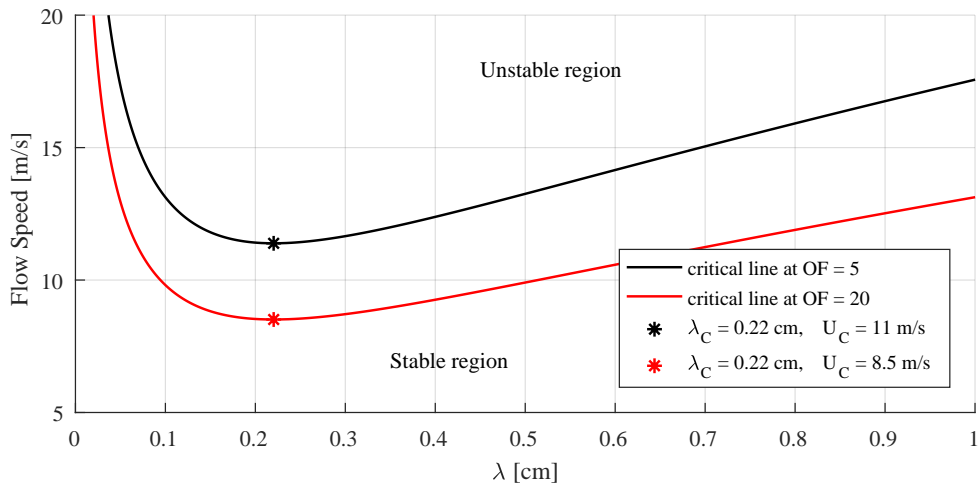


Figure 7.2: Neutral curve of 6805+5%polymer for the inviscid unbounded model

Table 7.1: Critical values for different fuels at different OF (inviscid unbounded model)

Fuel	OF	λ_c [cm]	U_c [m/s]
6805	5	0.17	13
	20	0.17	9.9
6805+5%polymer	5	0.22	11
	20	0.22	8.5

Viscous Bounded Model

In this model, the fuel viscosity is taken into account and a big difference in the results for the two fuels can be seen. In particular, the critical gas flow speeds of the pure paraffin are lower than those of the paraffin blend. Moreover, smaller critical wavelengths are excited for the pure paraffin with respect to the paraffin-based mixture. This is in agreement with the Kelvin-Helmholtz instability theory: the range of unstable wave numbers for each gas flow speed is broader for lower liquid layer viscosities (see Fig. 7.3 and 7.4). An influence of the OF on the critical values can be observed also in this case. However, a different trend in the dependence of the gas speed from the OF can be noticed between the two fuels (see Fig. 7.5). This is due to a different dependence of the densities and viscosities of the combustion gases from the mixture ratio. Numerical values are reported in Tab. 7.2.

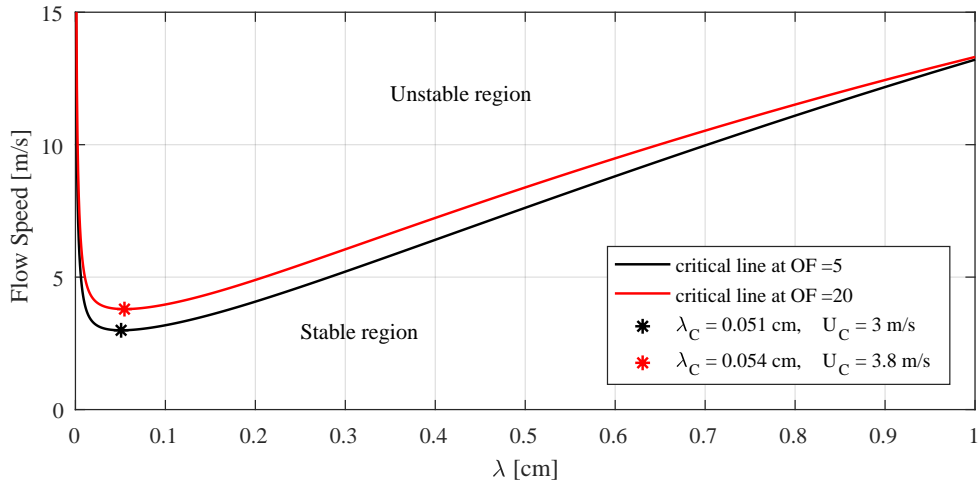


Figure 7.3: Neutral curve of pure paraffin 6805 for the viscous bounded model

Model Comparison

In this section, a comparison of the theoretical models is performed. Fig. 7.6 shows the neutral curves for pure paraffin 6805 at mixture ratio $OF = 2$ for each model. It can be noticed that, in the inviscid case, the confinement of the bounded model affects the stability of the liquid layer only in the long wave range. In fact, the two models show the same critical wave numbers and gas flow speeds. An asymptote can be noted for smaller wave number (longer waves): if the gas speed exceeds this value, there is no longer a lower stability limit in the long wave range. On the other hand, a big influence on the neutral curves can be observed if the viscosity is considered, especially in the short wave range. The liquid layer viscosity has the effect to decrease the critical values and to expand the instability range at each gas flow speed. The lower

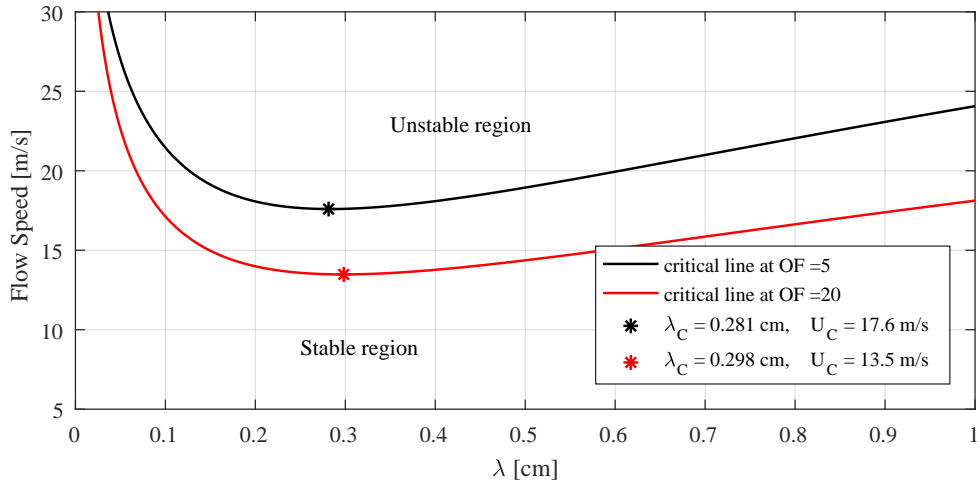


Figure 7.4: Neutral curve of 6805+5%polymer for the viscous bounded model

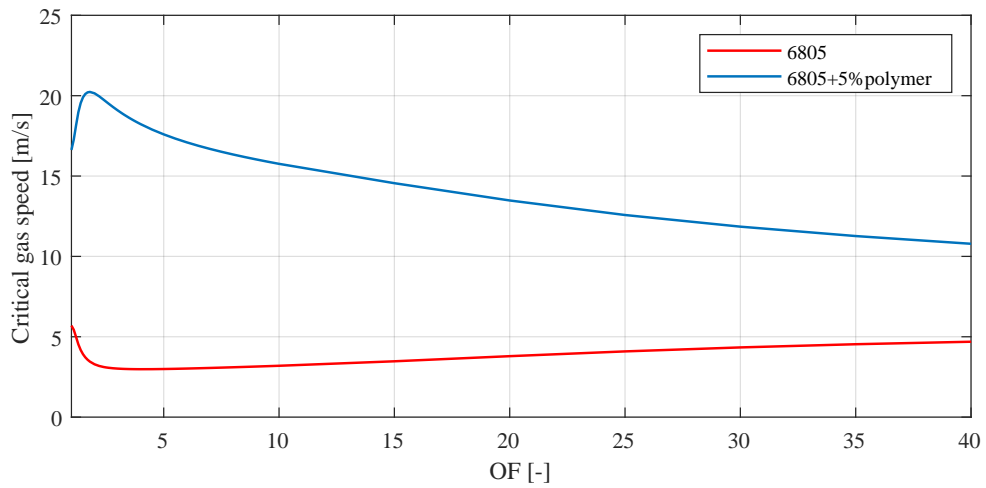


Figure 7.5: Influence of OF and fuel viscosity on the critical gas speed (viscous bounded model)

Table 7.2: Critical values for different fuels at different OF (viscous bounded model)

Fuel	OF	λ_c [cm]	U_c [m/s]
6805	5	0.051	3
	20	0.054	3.8
6805+5%polymer	5	0.281	17.6
	20	0.298	13.5

the viscosity, the broader the unstable region. An influence of the mixture ratio OF on the critical values can be also seen in Fig. 7.7. As previously said, no difference in the critical gas speed is found between the unbounded and the bounded models in the inviscid case (the two curves are perfectly overlapped). On the other hand, a big difference in the critical values and in their dependence from the OF can be noted between the inviscid and the viscous models. Obviously, this is caused by the introduction of the viscosity value of the burning gases, whose dependence on the combustion temperature is inverse to the one on the density, thus having a compensating effect.

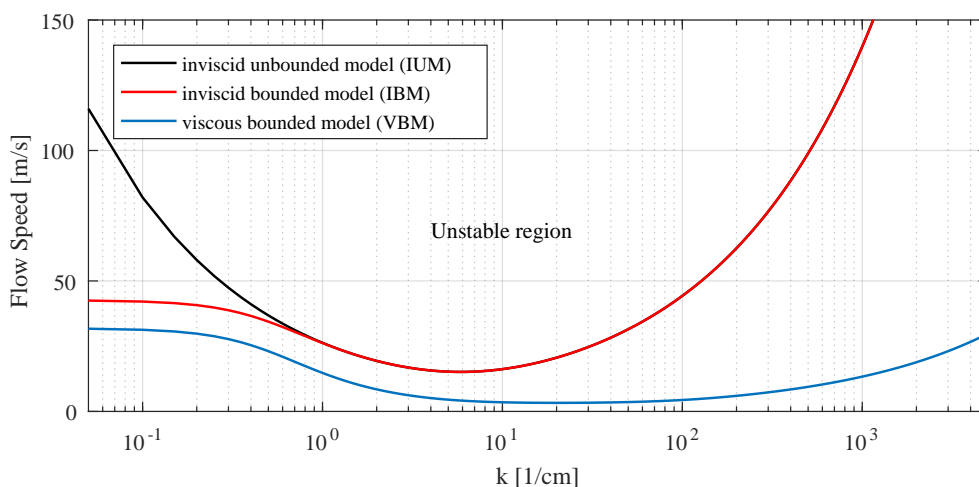


Figure 7.6: Neutral curve of pure paraffin 6805 at $OF = 2$ (for each model, the unstable region is for speeds above the corresponding curve; the stable region is below each curve)

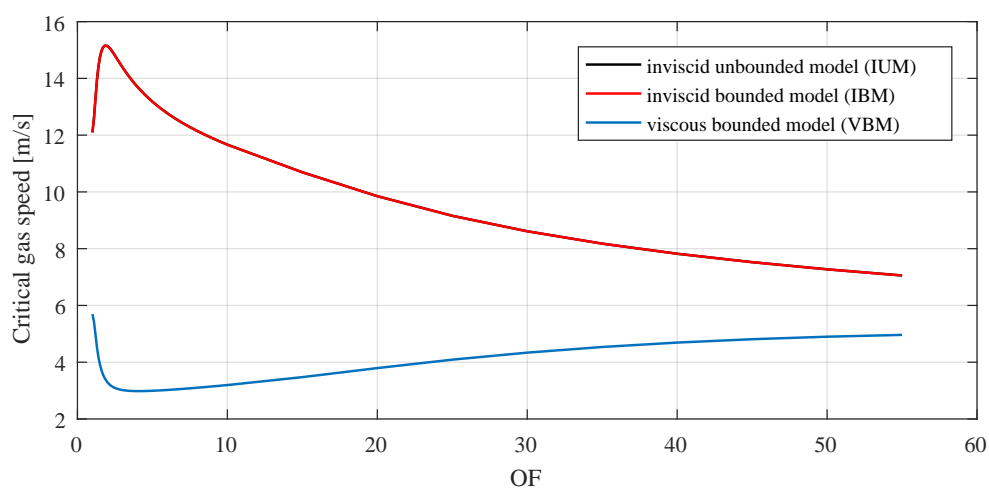


Figure 7.7: Influence of OF on the critical gas speed for pure paraffin 6805

7.1.2 Boundary Layer Thickness and Flame Position

In a boundary layer without combustion or blowing, the transition from laminar to turbulent flow occurs when the Reynolds number based on the distance from the leading edge is $10^5 - 10^6$. The presence of ordinary evaporation may reduce the transition Reynolds number to 10^4 . This effect is greatly magnified in the hybrid system, due to the combustion and extensive fuel sublimation at the surface. Therefore, the hybrid boundary layer is expected to be turbulent over most of its length [63]. According to Marxman [63], the turbulent boundary layer thickness δ can be expressed as a function of the dimensionless blowing parameter B and the free-stream Reynolds number $Re_x = \frac{\rho_e u_e x}{\mu_e}$:

$$\delta = x \{ (0.0281/I)(1+B)[\ln(1+B)/B] \}^{0.8} Re_x^{-0.2} \quad (7.1)$$

where,

$$I = \frac{7(1 + 13B/10 + 4B^2/11)}{72(1 + B/2)^2} \quad (7.2)$$

The Marxman's theory and, therefore, Eq. 7.1 is valid for blowing parameters up to $B = 100$. However, typical values of B for conventional hybrids applications range between 2 and 30. In particular, for liquefying fuel, the blowing parameter is even lower (approximately between 2 and 5) due to the increased fuel mass transfer through the entrainment process (see Chapter 2 and Fig. 2.3). By using Eq. 7.1 and considering the free-stream density and viscosity taken from the values given by the software NASA CEA (Chemical Equilibrium with Applications) at optimum conditions, it is possible to obtain the theoretical boundary layer thickness δ as a function of the longitudinal distance x . In particular, Fig. 7.8 shows the dependence of δ from the blowing parameter B at a constant average oxidizer mass flow of $\dot{m}_{O_x} = 50$ g/s, while Fig. 7.9 represents the dependence of δ from the oxidizer mass flow at $B = 5$. As expected, the boundary layer thickness is increasing as the blowing parameter B (i.e. the fuel mass injection at the surface) increases and is decreasing as the oxidizer mass flow increases.

The diffusion combustion flame is located inside the boundary layer, where the oxidizer and the fuel mass fluxes meet in the proportions required for combustion to occur. Ideally, this mass fraction of oxidizer to fuel would be near the stoichiometric mixture ratio, but hybrid combustion usually occurs at a local fuel-rich mixture ratio. Assuming a "flame sheet" combustion model (which is acceptable since the chemical kinetics times are much faster than the thermo-fluid dynamics ones) and considering a stoichiometric mixture ratio in the flame region, Marxman found that the flame height above the surface should be approximately in the range of 10% to 20% of the boundary layer thickness, depending on the operating conditions [63]. In reality, due to the fuel-rich combustion region, the flame temperature results lower than

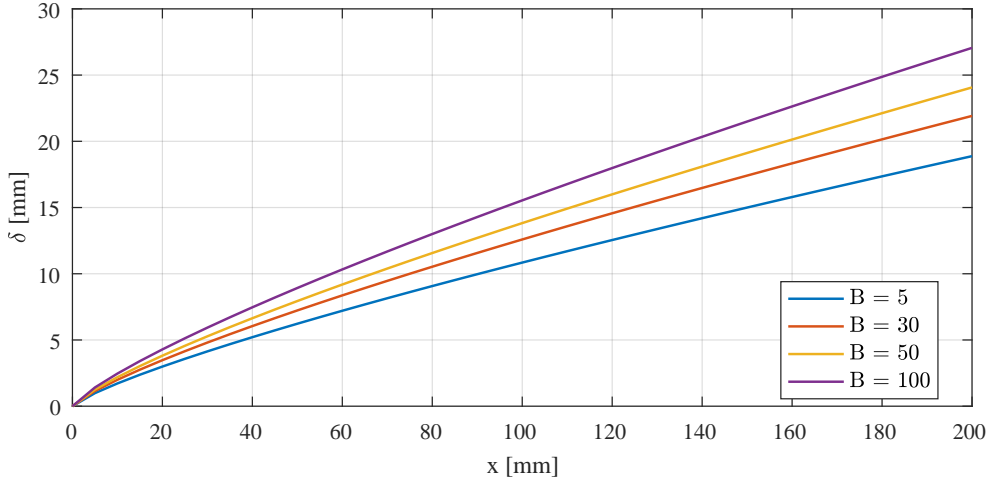


Figure 7.8: Boundary layer thickness δ versus distance x for various values of B ($\dot{m}_{O_x} = 50$ g/s)

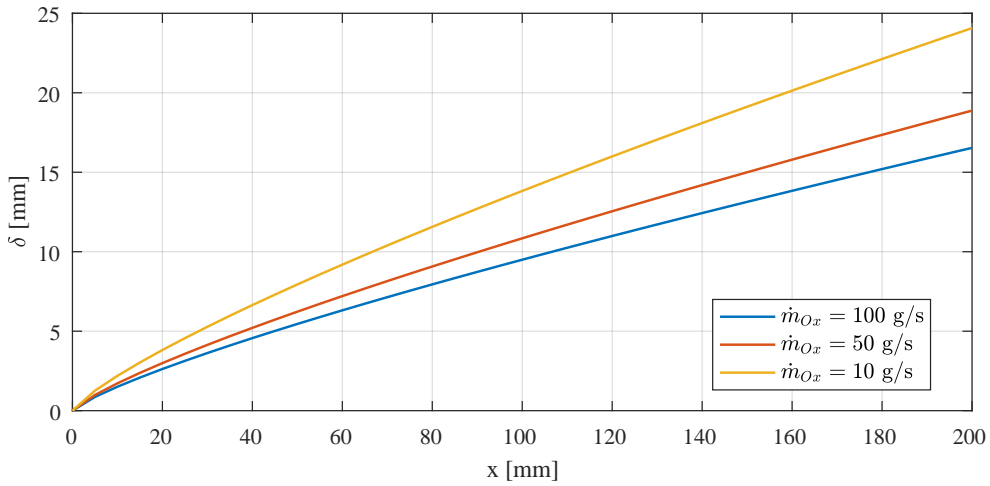


Figure 7.9: Boundary layer thickness δ versus distance x for various values of \dot{m}_{O_x} ($B = 5$)

expected and the flame is closer to the fuel surface. Furthermore, the flame position relative to the boundary layer thickness does not change drastically for a given fuel and oxidizer.

7.2 Algorithms Configuration

In the framework of this work, the decomposition into principal and independent components of the flame luminosity field in a hybrid rocket combustion chamber was performed. This allowed to recognize the main energetic (with POD) and independent (with ICA) structures characterizing the hybrid com-

bustion flame, depending on the fuel composition and configuration, oxidizer mass flow and combustion chamber pressure (see Sec. 7.3.1). In order to be sure to obtain meaningful results, a study on the decomposition algorithms was necessary at the beginning of the study. This allowed to choose the right settings (number of components, function to use as approximation of negentropy, etc.) and variables for POD and ICA. In this section, the configuration of the NIPALS and FastICA algorithms (see Chap. 4) is discussed in details.

7.2.1 Choice of the Components Number

In order to prove the validity of the decomposition methods, a modes reconstruction of the hybrid flame was performed at the beginning of this study. To do so, one combustion test was chosen (fuel: 6805+5%polymer; $\dot{m}_{O_2} = 50$ g/s) and 100 frames (corresponding to 0.01 seconds of burning) taken from its steady-state phase were considered. First, these frames were decomposed into their principal and independent components with POD and ICA. In particular, different numbers of modes were computed, since this parameter has a great influence on the results. Finally, a flame reconstruction using the principal and independent components computed in the first step was performed.

The results show that the output of the reconstruction gives a good representation of the main hybrid combustion flame. This means that the low-dimensional modes representation is an efficient way to describe big dataset, since it is able to capture the main dynamics of the observed phenomenon, without losing important information but filtering out possible noise sources.

POD Reconstruction

As said in Chap. 4, POD is basically an eigenvalue decomposition where the data are projected onto the subspace spanned by the eigenvectors corresponding to the largest eigenvalues. Therefore, this method is able to retain the most energetic and dominant modes. In this study, the minimum number of modes to consider in order to correctly describe the dynamics of the phenomenon was computed, according to an energy criterion. In Fig. 7.10 and 7.11, it is possible to notice that the first eigenvalue carries already almost 90% of the whole energy content of the dataset. Moreover, with only 20 modes, 98% of the total energy has already been retained. This means that it is possible to efficiently describe the dynamics of the combustion with just 20 modes (note that the maximum modes number is equal to the system dimension, which, in this study, corresponds to the frame number, namely 100). In order to prove this, 10, 25, 50 and 100 modes were considered in this study, for both the decomposition and the reconstruction.

From the results of the decomposition, it is shown that the average flame structure is already well described by the first mode (see Fig. 7.12). In fact, no difference can be noticed when 1 or 100 modes are considered. Only

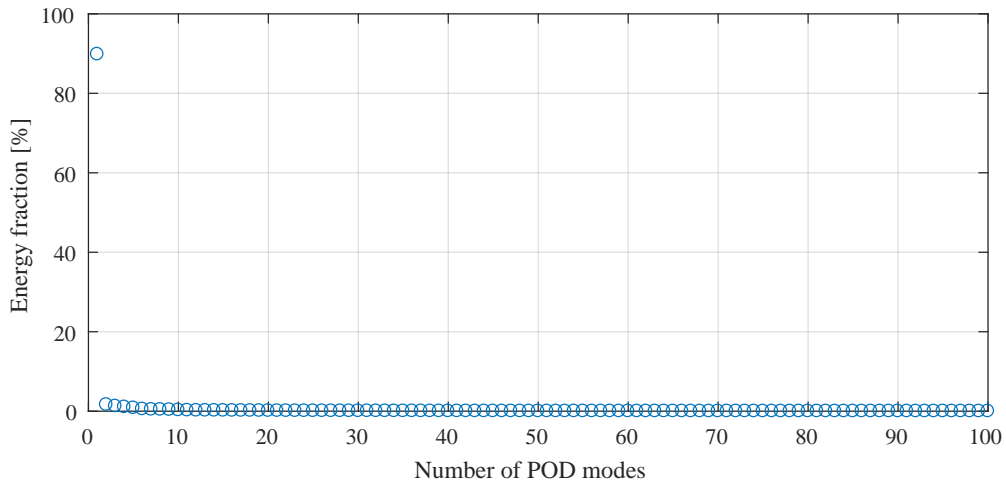


Figure 7.10: Energy fraction associated to each POD mode

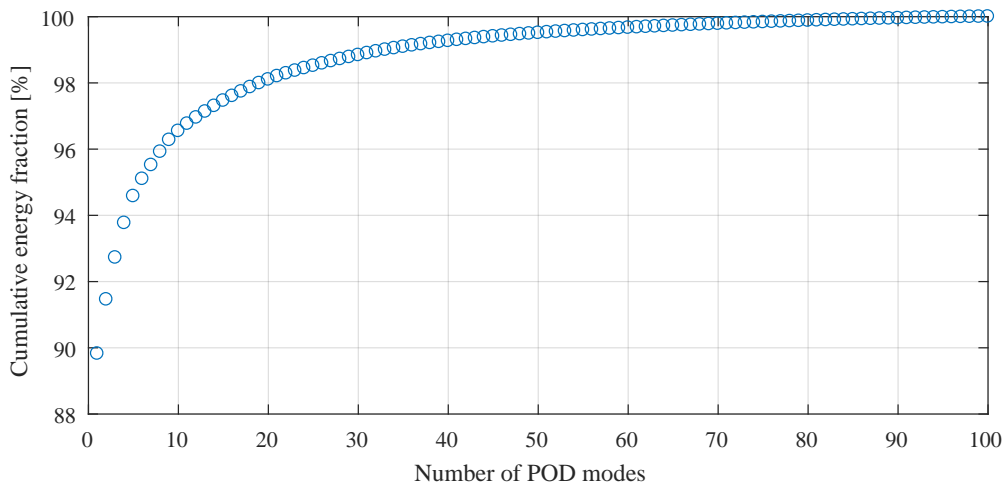


Figure 7.11: Cumulative energy fraction associated to each POD mode

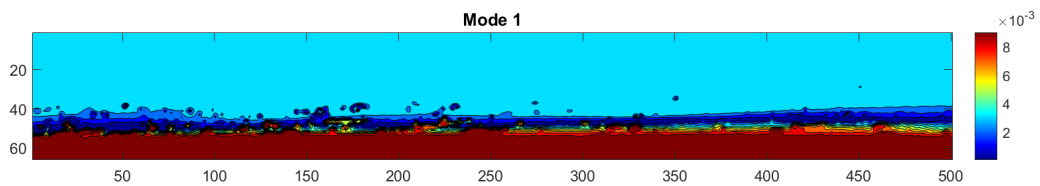


Figure 7.12: First POD mode, representing the average flame structure (the two axes are in pixel; oxidizer flow from left to right)

smaller turbulent structures and fluctuations, corresponding to higher modes, are better described when more modes are computed. On the other hand, looking at the results of the reconstruction (Fig. 7.13), it is possible to notice



(a) Frame 20001: original



(b) Frame 20001: reconstructed with 1 POD mode



(c) Frame 20001: reconstructed with 10 POD modes



(d) Frame 20001: reconstructed with 25 POD modes



(e) Frame 20001: reconstructed with 50 POD modes



(f) Frame 20001: reconstructed with 100 POD modes

Figure 7.13: Frame 20001 of test 203, original and reconstructed (oxidizer flow from left to right)

that some differences are visible, depending on the number of modes considered. Of course, when just 1 mode is computed, only the average flame can be reconstructed. All the information about fluctuations, smaller turbulent structures, random appearing vortices and noise are filtered out. If 10 modes are considered, the main flame behaviour and its leading structures are well reproduced, but the flame appears to be flatter than in the original frames. The information about shorter waves are lost: some of them are merged with longer waves, others are levelled with the main flame. The results look better already with 25 modes. In this case, shorter waves are more clearly detected, but some small waves are still merged together, if they are close to each

other. No differences are observed between the reconstructions with 50 and 100 modes. In both cases, all waves are clearly recognized and the dynamics is well reproduced. Even droplets are correctly detected and reconstructed.

The obtained results show that 10 modes are already enough to correctly describe the main flame dynamics, like average flame shape and height. In fact, 10 modes already retains 97% of the total energy content of the combustion data. If smaller structures (such as shorter waves or droplets) or random appearing dynamics have to be detected, a higher number of modes needs to be considered. In any case, the reconstruction of the POD modes shows that the principal components decomposition is an efficient way to represent the main dynamics and the leading structures of the hybrid combustion process.

ICA Reconstruction

The ICA is a statistical technique used to reveal the independent components, hidden in the observed data. This allows the identification of the leading independent structures appearing during the burning process and representing some physical processes involved in the observed phenomenon. As said in Chap. 4, before applying the ICA algorithm, the video data are first projected onto their POD modes, in order to operate on a lower-dimensional dataset that still retains the most important information and has a higher signal-to-noise ratio. According to the previous study on the energy fraction carried by each eigenvalue (see Fig. 7.10 and 7.11), it is possible to state that no big differences on the main process dynamics are observed when 25, 50 or 100 modes are considered (see Sec. 7.2.1). On the other hand, when the ICA is performed, important differences are found when the data are projected onto 10, 25, 50 or 100 POD modes and the same number of independent components is computed. In particular, the more the data are filtered (which means the lower the number of retained POD modes), the better the main features of the combustion process are described. This is due to the fact that samples of observations of random variables converge to a Gaussian distribution when the number of observation is sufficiently large. This means that, the larger the dataset, the more Gaussian the variables. Since the ICA technique starts from the assumption that the analyzed variables need to be non-Gaussian, the algorithm works better when applied on a lower dimensional and less noisy dataset. In order to prove this, the video data were projected onto 10 and 100 POD modes, before computing 10 independent components. The results show that, in the first case (10 POD modes, 10 ICs), the average flame structure is recovered, while, in the second case (100 POD modes, 10 ICs) only spurious fluctuations are found, see Fig. 7.14. This means that either the original signal is too noisy (thus, the dataset has to be reduced to a lower dimensional system) or 10 ICs are too few to describe such a big dataset.

Obviously, it is necessary to find a good balance between the right number of POD modes and ICs to compute. In fact, 10 POD modes could be enough



(a) Frame 20001: original



(b) Frame 20001: reconstructed with 10 POD modes and 10 ICs



(c) Frame 20001: reconstructed with 100 POD modes and 10 ICs

Figure 7.14: Frame 20001 of test 203, original and reconstructed (oxidizer flow from left to right)

to represent the average flame behaviour, but 10 ICs are probably too few to correctly describe the phenomenon (clearly, the number of ICs cannot be higher than the number of POD modes). Therefore, a study on the correct number of ICs was performed. When the complete dataset is considered (100 POD modes) and a different number of ICs is computed, it is noticed that the results are getting closer to the original data if more ICs are computed. In this case, incoherent and filament-like structures are found when only 10 ICs are considered, while the main average flame structure is reconstructed with 100 ICs (see Fig. 7.15). It is also noticed that the higher the number of ICs, the flatter the flame. More fluctuations and smaller roll-waves are visible with a lower number of ICs. Unfortunately, looking at the original frame, it is possible to observe that these features are not present in the original video data. These are, most likely, spurious and noisy signals coming from the algorithm itself. This could be due to the fact that, as previously underline, the original signal is not really non-Gaussian and the different spatial components contained in the dataset are not totally independent from each other. Moreover, as already said in Sec. 4.2, the ICA is not able to order its components according to a defined criterion (like the POD) and it provides a solution only up to a multiplicative constant. Therefore, it is not said that the first 10 ICs are the most important sources for describing the dynamics of the process. This means that it is better to first reduce the dimension of the problem by using the POD projection, thus being sure that only the most energetic components are retained and that the noise is filtered out. Afterwards, the maximum possible number of ICs of the system (which corresponds to the retained POD modes) should be computed, so that all the

ICs are considered (from the most to the less important). Alternatively, if the POD modes projection is not performed, it is recommended to compute as many ICs as possible and to choose a posteriori which component needs to be retained and which not.



(a) Frame 20001: original



(b) Frame 20001: reconstructed with 100 POD modes and 10 ICs



(c) Frame 20001: reconstructed with 100 POD modes and 25 ICs



(d) Frame 20001: reconstructed with 100 POD modes and 50 ICs



(e) Frame 20001: reconstructed with 100 POD modes and 100 ICs

Figure 7.15: Frame 20001 of test 203, original and reconstructed (oxidizer flow from left to right)

7.2.2 Choice of the Contrast Function for ICA

As already explained in Sec. 4.2, four different contrast functions can be chosen in the FastICA algorithm, depending on the problem. In the example presented in Sec. 4.3, it was already shown that, for linearly mixed signals, the contrast functions G_1 , G_2 and G_3 all work well and give the same results in terms of frequencies. On the other hand, the function G_4 finds the right frequencies but does not separate them correctly. On the contrary, for non-linearly mixed signals (which is more the real case), all the functions find some “spurious” frequencies. Moreover, during the computation of the components,

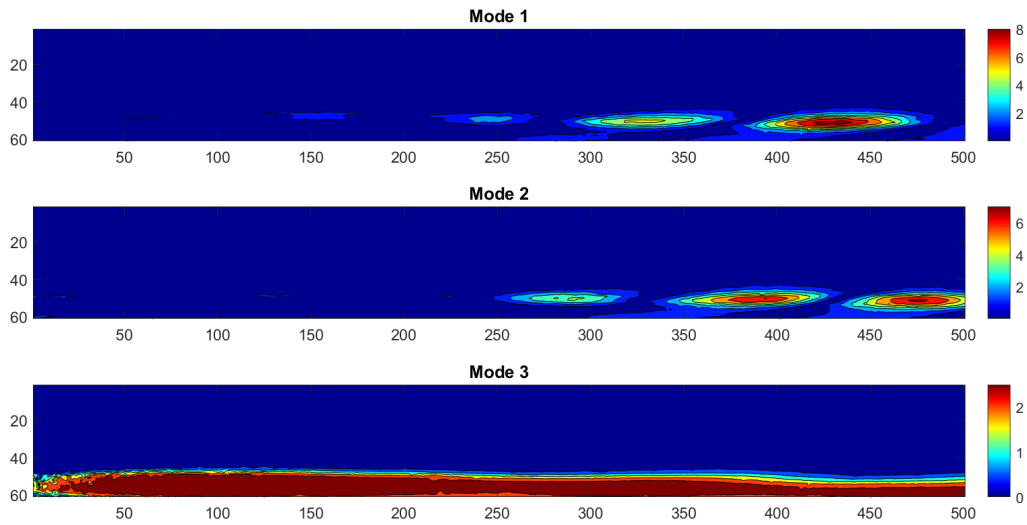
the algorithm had problems to converge when using G_4 , unlike with the other contrast functions. However, this example only considered periodic signals in time. Therefore, before starting the analysis of the combustion videos, it was necessary to test the different contrast functions on a real case. For this reason, the FastICA algorithm was applied to 1000 frames (corresponding to 0.1 seconds of burning) taken from the steady-state phase of a combustion video and only 3 spatial independent components were computed with the sICA. Four runs were performed, one for each contrast function, and the results compared. The contour plots of the space coefficients and the PSD of the time coefficients are shown in Fig. 7.16, 7.17, 7.18 and 7.19.

From these figures, it can be noticed that with the functions G_1 , G_2 and G_3 the same results in terms of contour plots and frequency peaks are obtained. On the other hand, different results in terms of frequency peak intensity and average flame contour plot are shown when using the function G_4 . Moreover, also in this case, some difficulties in the convergence of the algorithm were observed when using G_4 with respect to the other functions. Therefore, the same conclusion of the previous example (see Sec. 4.3) are drawn: the functions G_1 , G_2 and G_3 work well for any distribution of the independent components and for any choice of the contrast function. The choice of one function rather than another one is only important for optimizing the performance of the method. In this work, from now on, the contrast function G_3 will be used to compute the independent components because of the lower computational time.

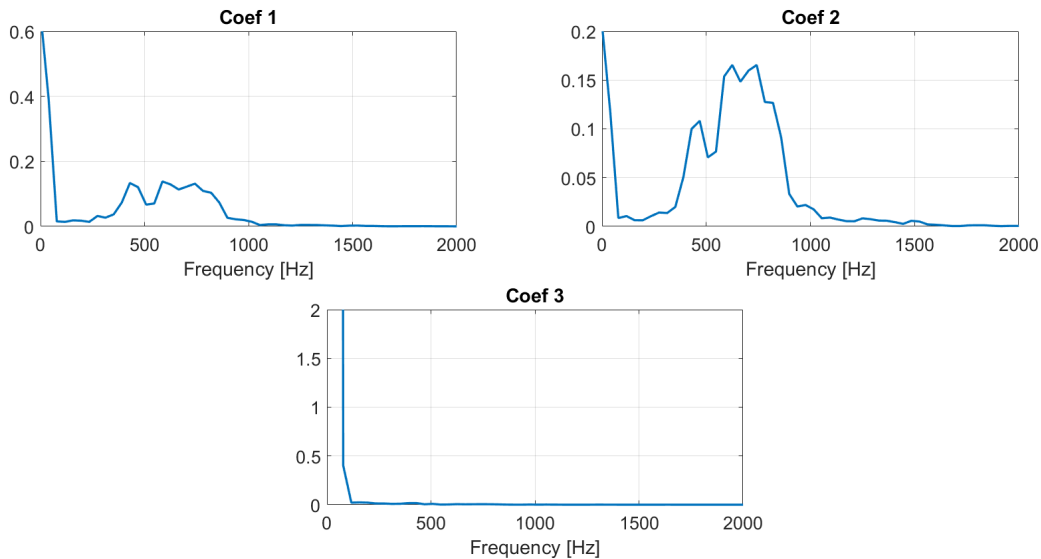
7.2.3 Interpretation of the Components

In order to better understand and interpret the results given by the two decomposition methods, an analysis was performed by applying the NIPALS and FastICA algorithms to 1000 frames (corresponding to 0.1 seconds of burning) taken from the steady-state phase of one of the combustion video. The first 3 principal components and 3 spatial and temporal independent components were computed, respectively, with POD, sICA and tICA and the results compared. The same algorithm (FastICA) was used for sICA and tICA, but tICA is computationally more demanding than sICA, due to the higher spatial compared to temporal resolution [6]. The contour plots of the space coefficients and the PSD of the time coefficients for each decomposition technique are shown in Fig. 7.20, 7.21 and 7.22.

From these figures, it is possible to notice that the same frequency peaks are found with the three methods. However, the peaks in both sICA and tICA are less marked than those in the POD. On the other hand, some differences can be seen in the contour plots of the space coefficients. The first POD mode shows the typical profile of a combustion flame over a flat fuel surface with a turbulent boundary layer. This was consistent for the different fuels and tests that have been investigated. Contour plots of higher modes show effects of the boundary conditions, combustion fluctuations and more



(a) Contour plots of the space coefficients (axes are in pixel; oxidizer flow from left to right)

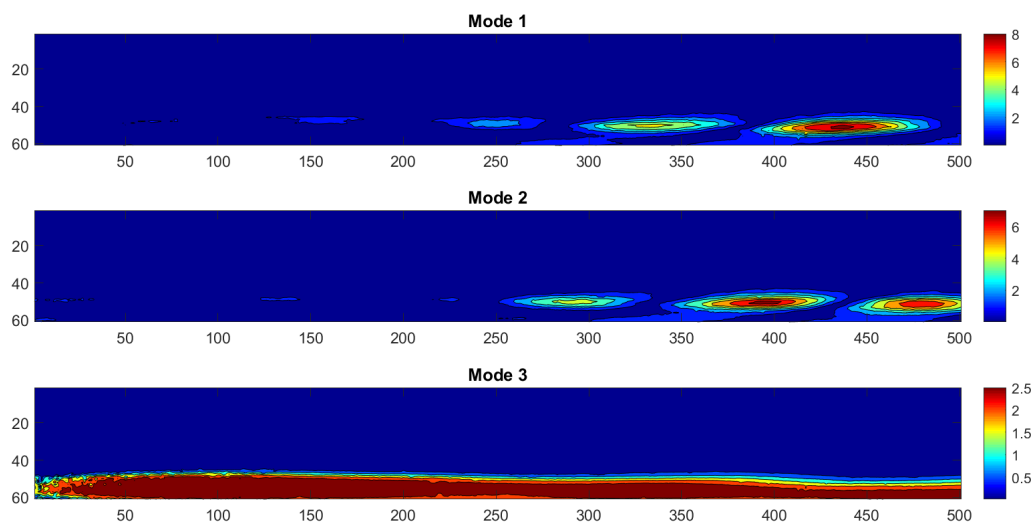


(b) PSD of the time coefficients

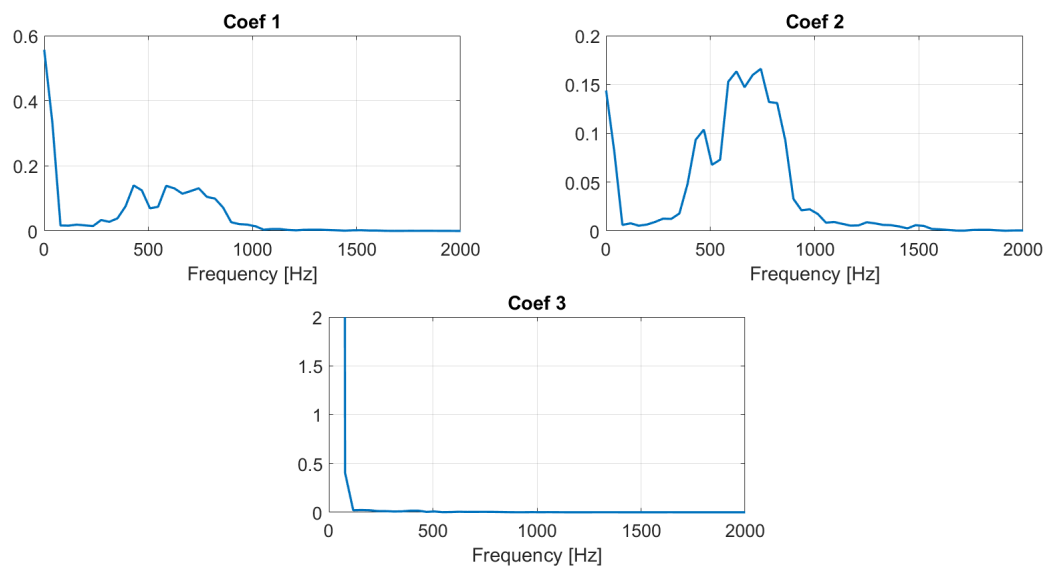
Figure 7.16: Contour plots and PSD of the first 3 spatial independent components (sICA) of test 233, computed with G_1

fragmented structures, as it can be noticed from the increased intensity and variations of the flame. The contour plots of the spatial independent components show more or less the same characteristics of the principal components, just in a different order (remember that the independent components cannot be ordered according to any criteria). The first two components represent the combustion fluctuations, while the last one is closer to the boundary layer flame over the fuel surface. This small difference in the results between POD and sICA suggests that 3 components are not enough to describe the

dynamics of the combustion. Therefore principal and independent components almost coincide. On the other hand, the contour plots of the temporal independent components do not show any average flame profile, but only fluctuations and smaller scale structures. It is important to notice that with all the three methods the luminosity variations and fluctuations are higher in the rear part of the fuel slab, where a higher turbulence level is reached.

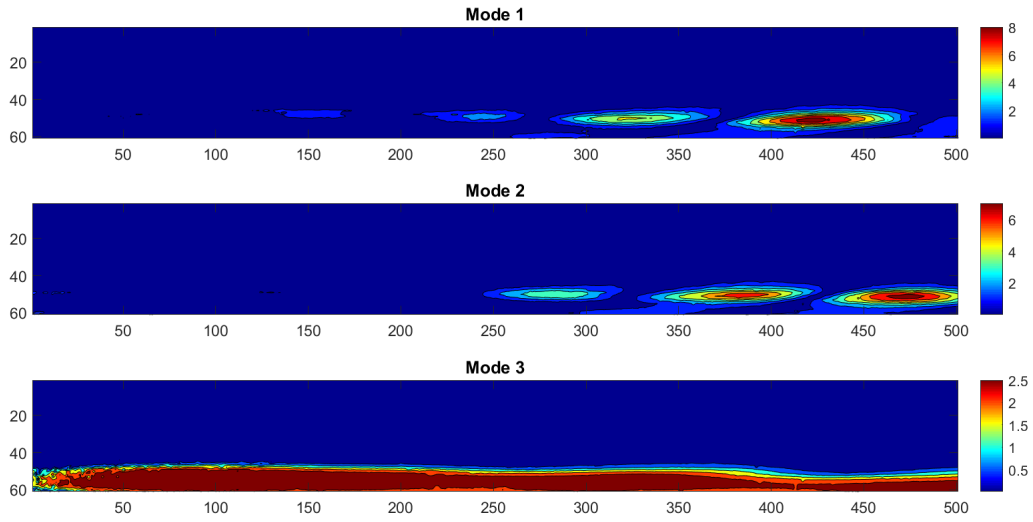


(a) Contour plots of the space coefficients (axes are in pixel; oxidizer flow from left to right)

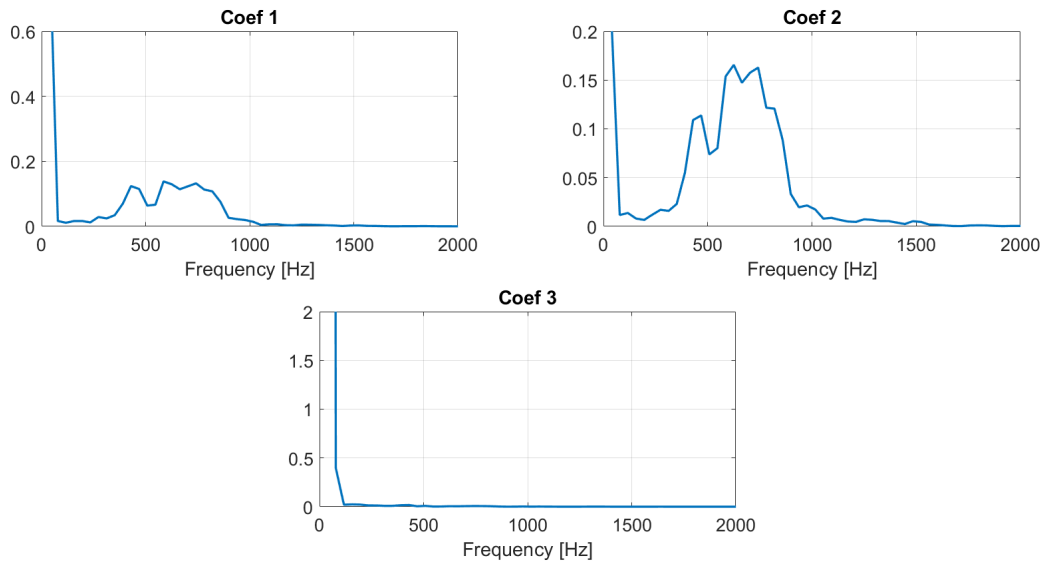


(b) PSD of the time coefficients

Figure 7.17: Contour plots and PSD of the first 3 spatial independent components (sICA) of test 233, computed with G_2

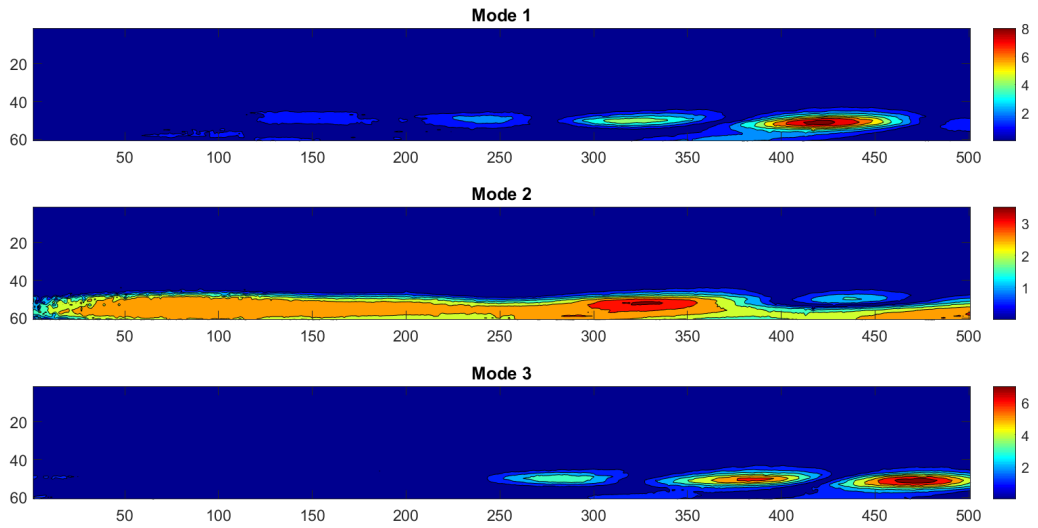


(a) Contour plots of the space coefficients (axes are in pixel; oxidizer flow from left to right)

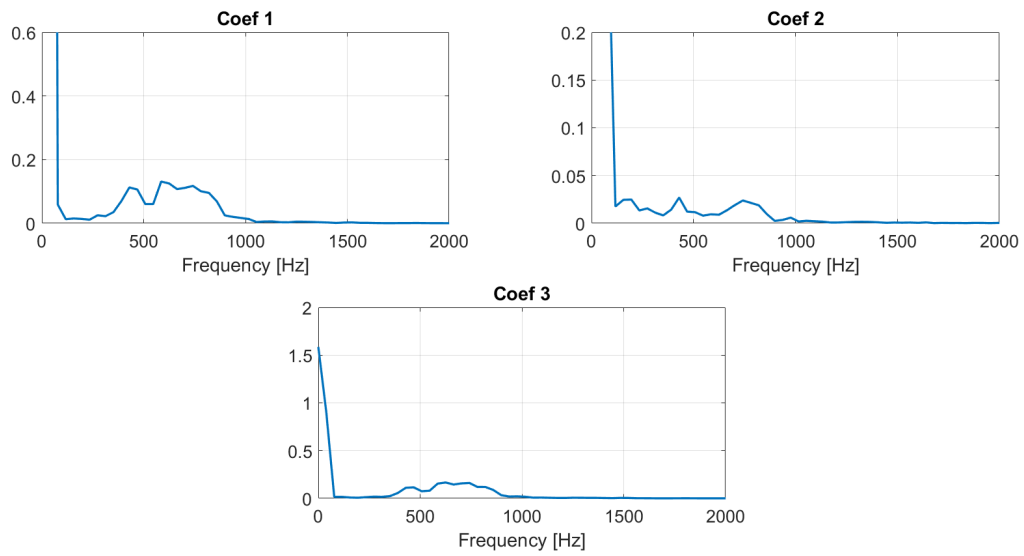


(b) PSD of the time coefficients

Figure 7.18: Contour plots and PSD of the first 3 spatial independent components (sICA) of test 233, computed with G_3

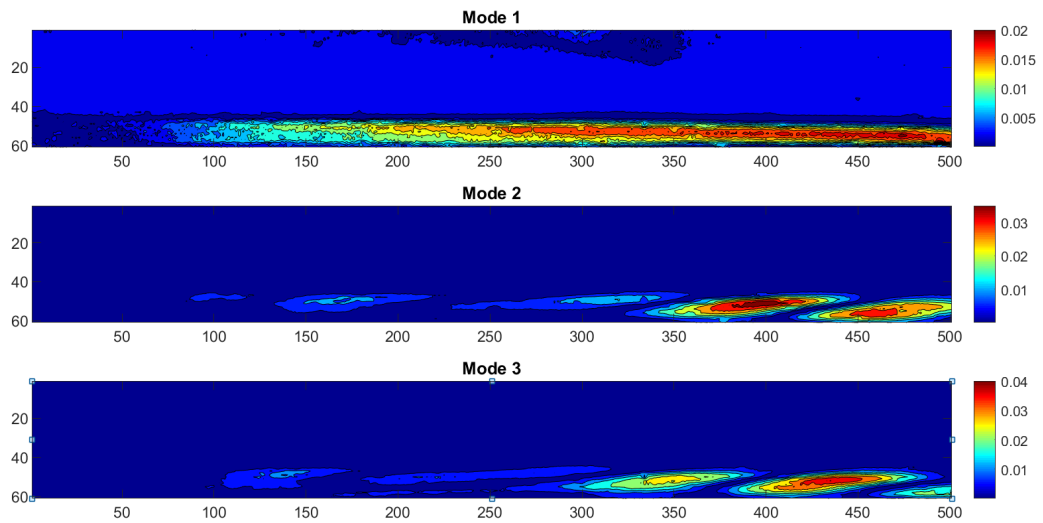


(a) Contour plots of the space coefficients (axes are in pixel; oxidizer flow from left to right)

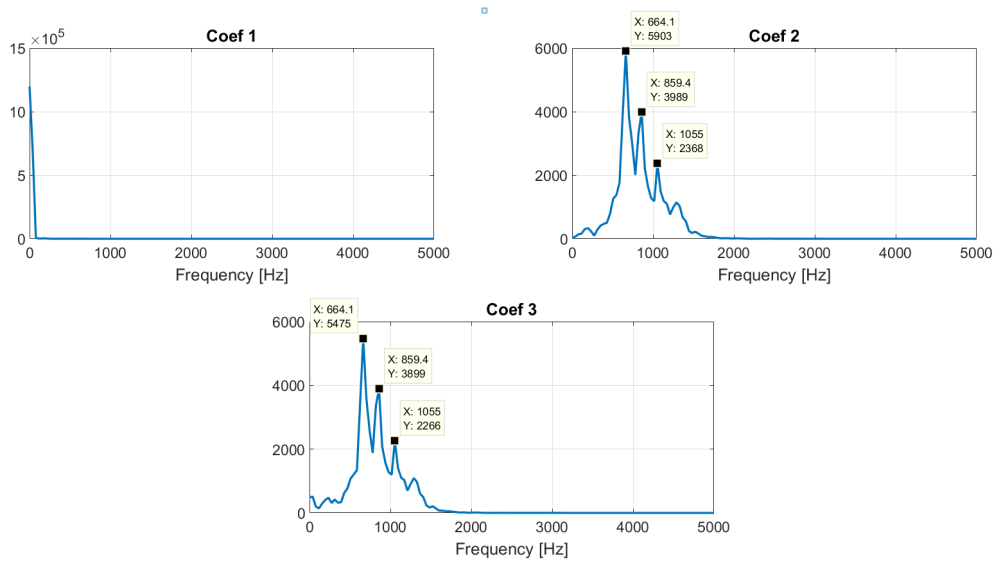


(b) PSD of the time coefficients

Figure 7.19: Contour plots and PSD of the first 3 spatial independent components (sICA) of test 233, computed with G_4

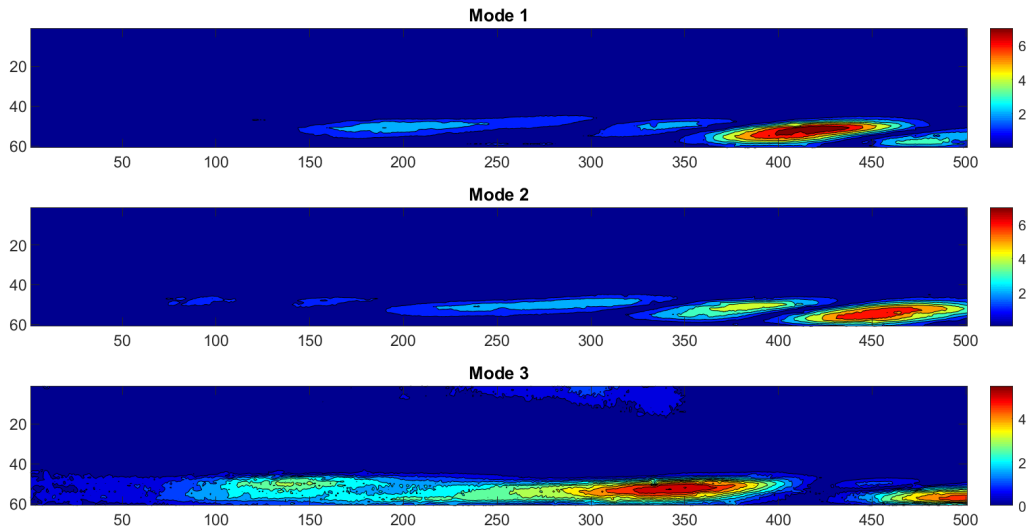


(a) Contour plots of the space coefficients (axes are in pixel; oxidizer flow from left to right)

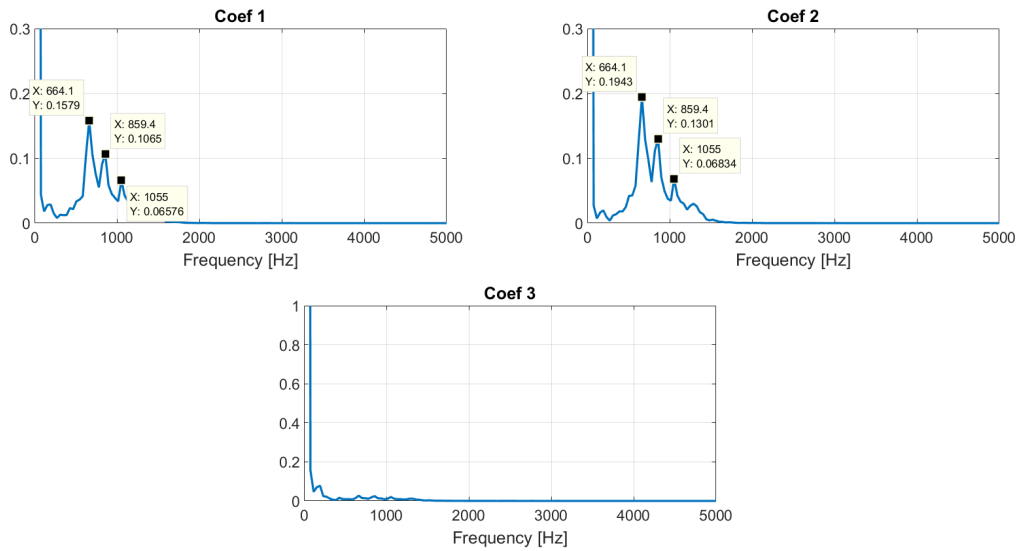


(b) PSD of the time coefficients

Figure 7.20: Contour plots and PSD of the first 3 principal components (POD) of test 279

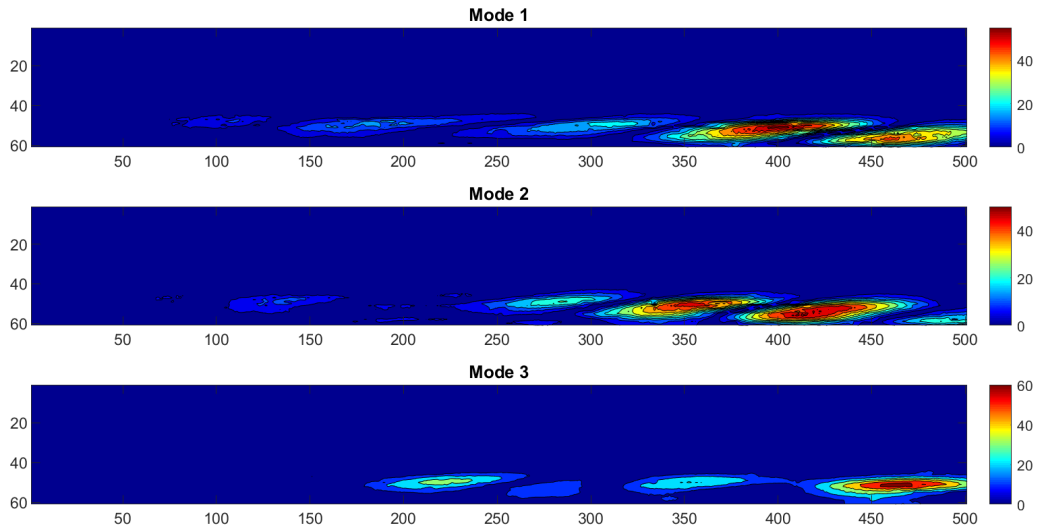


(a) Contour plots of the space coefficients (axes are in pixel; oxidizer flow from left to right)

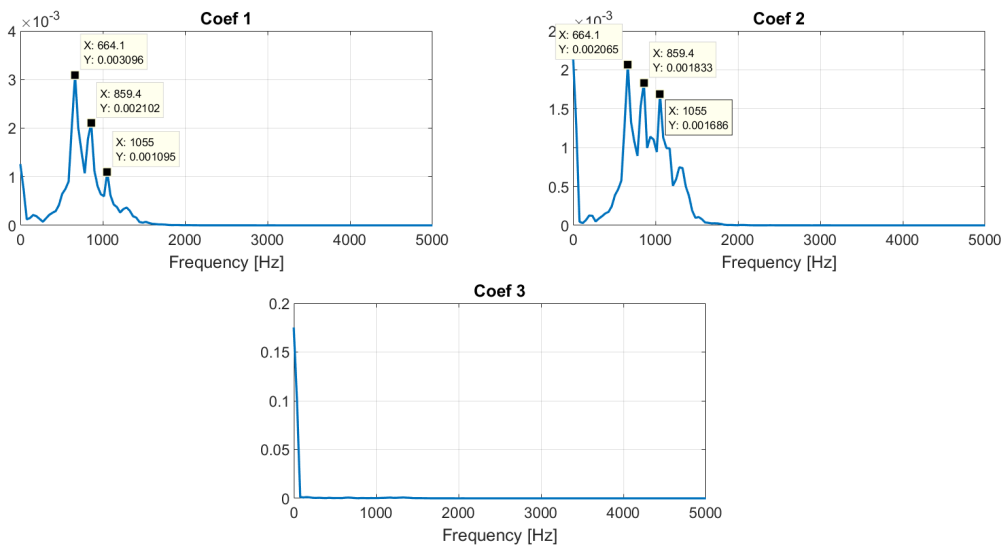


(b) PSD of the time coefficients

Figure 7.21: Contour plots and PSD of the first 3 spatial independent components (sICA) of test 279



(a) Contour plots of the space coefficients (axes are in pixel; oxidizer flow from left to right)



(b) PSD of the time coefficients

Figure 7.22: Contour plots and PSD of the first 3 temporal independent components (tICA) of test 279

7.3 Experimental Results of Atmospheric Combustion Tests

More than 200 combustion tests were successfully run with the atmospheric combustion set-up. Qualitative and quantitative analysis of high-speed and CH* chemiluminescence videos were performed. Once more, it is important to highlight that all the tests were analyzed with the same procedure, by using the same time (10000 frames during steady-state) and space (500x60 pixels) windows, thus obtaining comparable results. The results coming from the decomposition methods were all obtained by computing 12 POD modes and 12 independent components. Indeed, in this way, according to the energy criterion explained in Sec. 7.2, more than 90% of the whole energy content of the flow field has been retained. Obviously, it is not possible to discuss all the tests run in the framework of this research. However, some of these tests and their results will be discussed in this section. Nevertheless, all the other tests that will not be named or singularly commented in this work have been analyzed in this study and they contribute to the final results. The test parameters and the camera settings used for the tests discussed in this section can be found, respectively, in Tab. 7.3 and 7.4.

Table 7.3: Combustion test parameters

Test no.	Fuel	\dot{m}_{Ox} [g/s]	G_{Ox} [kg/(m ² s)]	r_f [mm/s]
203	6805+5%polymer	44.55	9.12	0.095
233	6805+5%polymer	86.22	17.3	0.105
234	6805+5%polymer	85.5	16.77	0.102
241	6805+5%polymer	11.35	2.33	0.085
250	6805	84.08	17.00	0.601
253	6805	45.22	9.1	0.496
254	6805	46.08	9.1	0.488
263	6805	11.36	2.19	0.378
279	6805	113.68	21.85	0.755
284	6805	46.45	7.48	0.284
290	6805+5%polymer	46.47	8.94	0.09
291	6805+5%polymer	89	16.77	0.115
295	6805	88.98	15.20	0.531
297	6805+5%polymer	12.48	2.43	0.087
304	6805	12.37	2.20	0.391

Typical results obtained from the PSD of time and space coefficients coming from POD and ICA have been shown in Sec. 6.1, respectively in Fig. 6.2

Table 7.4: Camera settings

Test no.	Image size [pixel x pixel]	Frame rate [1/s]	Shutter time [s]	CH* filter
203	1024x336	10000	1/1000000	
233	1024x336	10000	1/1000000	
234	1024x336	10000	1/1000000	
241	1024x336	10000	1/1000000	
250	1024x336	10000	1/1000000	
253	1024x336	10000	1/1000000	
254	1024x336	10000	1/1000000	
263	1024x336	10000	1/1000000	
279	1024x336	10000	1/1000000	
284	1024x336	10000	1/10000	✓
290	1024x336	10000	1/20000	✓
291	1024x336	10000	1/25000	✓
295	1024x336	10000	1/17000	✓
297	1024x336	10000	1/17000	✓
304	1024x336	10000	1/10000	✓

and 6.3. The peaks represent the most excited frequencies and wavelengths appearing during the analyzed time frame. Here, it is possible to notice that more frequency peaks are detected by the POD, while more longitudinal wavelengths peaks (represented from the column-wise spectral content of the space coefficients) are found by the sICA. The reason for this must be searched in the different principles the two decomposition techniques are based on. POD is able to find the most energetic structures in the flow, which means that they do not need to be periodic or independent (in time or space) from each other. On the other hand, sICA is able to find independent spatial components and the corresponding unconstrained temporal structures, which means that they need to be spatially independent from each other. Thus, energetic but not periodic structures can be found by POD, while the contrary is true for sICA. Of course, there are structures that can be detected with both methods: these are related to the main events characterizing the combustion process.

7.3.1 Study on the Liquid Film Destabilization

The main aim of this research is to quantify the influence of the hybrid engine operating conditions on the liquid film destabilization process (Kelvin-Helmholtz instability) and finally identify the connection between the liquid layer unstable waves, leading to the droplets entrainment, and the increase

in the regression rate. From literature studies, it is well known that some operating parameters have a bigger influence than others on this process. This is the reason why, this work is mainly focused on the investigation of four parameters: fuel slab geometry, fuel viscosity, oxidizer mass flow and combustion chamber pressure.

High speed videos of the combustion tests were recorded and analysed, as explained in Sec. 6.1. By examining the PSD results of POD and ICA, it is possible to obtain the most excited frequencies and wavelengths for each of them. POD enables the recognition of the main energetic structures of the flow field, ICA identifies the leading independent structures underlying the data. The analysis was carried out on 1 second (10000 frames) during the steady-state. Frequency and wavelength peaks were taken for each fuel formulation and oxidizer mass flow and then compared.

The results show that the combustion is dominated by wave-like structures and that the most excited frequencies and wavelengths characterizing the liquid melt layer depend on the fuel geometry and viscosity and on the oxidizer mass flux. Nevertheless, some limitations have to be taken into account when the results are analysed, as already explained in Sec. 6.3. First of all, the analysis is performed on 2D images. This means that what has been analysed can be the superposition of all the combustion phenomena appearing on the fuel surface along the whole width. Furthermore, the waves on the fuel surface do not probably move straight in the horizontal direction. Moreover, the brightness of the flame and the condensed products which polluted the window increase the complexity of the optical measurement. Finally, it must be stressed that at the base of the whole analysis there is the assumption that the flame front follows the liquid layer. This is the reason why it is assumed that the waves appearing on the flame correspond to the waves of the liquid layer.

Fuel Configuration

The first parameter to be analyzed, the fuel slab geometry, is not directly influencing the entrainment phenomenon, but it has an effect on the boundary layer development over the fuel surface, thus influencing the frequency and wavelengths peaks identified by the decomposition methods. In fact, in each combustion tests, a whole range of different frequencies and wavelengths is amplified: some of them are related to the KHI process (so to the entrainment process), some are connected to the vortex shedding caused by the fuel slab step and others just to random appearing vortices. In order to understand which frequencies and wavelengths are actually related to the entrainment process, it was necessary to perform a study on the influence of the fuel step on the combustion mechanism. In this way, it was possible to recognize all the frequencies related to the presence of the step. For what concerns random appearing vortices, a comparison between the POD and ICA results was performed: if a frequency peak appears only in the POD, it is most likely

related to a random energetic vortex. On the other hand, if a frequency peak appears only in the ICA, it is most likely a periodic but not energetic signal, thus not so important. Those peaks appearing in both POD and ICA are periodic and energetic signals, thus related to the main events characterizing the combustion process. Therefore, a combination of the two decomposition techniques is necessary in order to better understand the dynamic of the process.

In this test campaign all the combustion tests were performed with the fuel blend composition 6805 with 5% polymer and oxidizer mass flow of 50 g/s. Fuel slabs with 5°, 20° and 90° forward-facing ramp (FFR) were investigated.

The combustion of the fuel slab with 5° FFR is characterized by a poor flame holding. A wave-like structure can be seen but points of local extinction of the flame can be detected along the fuel surface as the flame is developing. The flame appears to be not even and made up of elongated filaments, see Fig. 7.23. Two ranges of frequencies are excited with this configuration: 170-190 Hz and 300-340 Hz. The lower frequency range is related to the vortex shedding at the beginning of the ramp (VS1).



Figure 7.23: Fuel slab and combustion flame with 5° FFR

A proper flame holding is reached with the fuel configuration with the 20° FFR. The recirculation zone created by the presence of the steeper ramp gives birth to large waves and a well attached flame front at the head of the fuel slab. The flame is burning continuously along the fuel surface with no points of local extinction, see Fig. 7.24. This coherent and regular wave-like structure is related to the vortex shedding at the end of the ramp. Three amplified frequency ranges can be detected with this configuration: 200-230 Hz, 300-340 Hz and 400-500 Hz. The first and the last range are related respectively to the vortex shedding produced at the beginning (VS1) and at the end of the ramp (VS2).



Figure 7.24: Fuel slab and combustion flame with 20° FFR

In the configuration with the 90° forward-facing step (FFS) a big flow separation and recirculation zone is visible just after the step, see Fig. 7.25. The separation region experiences a weak regular vortex shedding which leads to accumulation of vorticity within the recirculation zone. This makes the region grow in size until a large scale vortex is ejected from the recirculation zone, with a consequent reduction in recirculation region size and reattachment length. The vorticity accumulation process induces a low frequency flapping of the shear layer and, consequently, a fluctuation of the reattachment point within a “reattachment zone” [75] (see Fig. 7.26). In this configuration, three excited frequency ranges were found: 90-120 Hz, 320-330 Hz and 400-450 Hz. The first range is related to the low frequency flapping motion of the shear layer. The last range is linked to the vortex shedding produced at the end of the step (VS2).



Figure 7.25: Fuel slab and combustion flame with 90° FFS

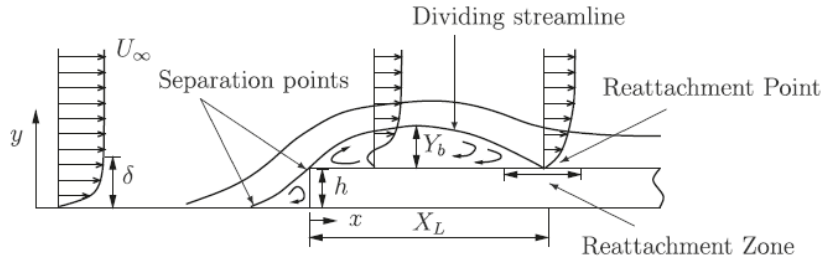


Figure 7.26: Flow field over a FFS [75]

The experimental vortex shedding frequencies were also compared to the theoretical ones, according to the formula taken from Carmicino et al. [11] for the vortex shedding at the inlet of the fuel grain:

$$f_{VS} = Sr \frac{4}{\pi} \frac{\dot{m}_{Ox}}{D^3} \frac{R_{ox} T_{ox}}{p_c} \quad (7.3)$$

Here, Sr is the Strouhal number, \dot{m}_{ox} is the oxidizer mass flow, D is the characteristic length, i. e. the port diameter in the case of a fuel grain, R_{ox} is the oxidizer gas constant, T_{ox} is the oxidizer temperature and p_c is the combustion chamber pressure.

This formula can be adapted to the single fuel slab configuration:

$$f_{VS} = Sr \frac{4}{\pi} \frac{\dot{m}_{Ox}}{D^3} \frac{R_{ox} T_{ox}}{p_c} = Sr \frac{G_{Ox}}{D} \frac{R_{ox} T_{ox}}{p_c} \quad (7.4)$$

where G_{Ox} is the oxidizer mass flux. For what concerns the Strouhal number, it mostly depends on the fluid dynamic characteristics of the velocity profile at the step. However, a Strouhal number varying in the range $0.25 < Sr < 0.5$ can be found in literature for the velocity fluctuations at the end of the jet core [11]. The theoretical vortex shedding frequencies were all in the range 150-220 Hz for VS1 (vortices at the beginning of the ramp) and in the range 400-550 Hz for VS2 (vortices at the end of the ramp). These results match really good with the frequencies experimentally obtained from the combustion tests.

At the end of this study, it was possible to state that the frequencies related to the KHI are those in the range 300-340 Hz for the investigated fuel formulation and oxidizer mass flow. In the same way it was also possible to identify the longitudinal wavelengths connected to the instability mechanism. A summary of the dependency of frequencies and wavelengths on the fuel configuration can be seen in Tab. 7.5. It has to be underlined that all these frequency and wavelength values were found both in POD and ICA results, so they are all connected to energetic and periodic structures. The only values that appeared only in the POD results are those connected to the VS2 in the configuration with 90° FFS. This means that those vortices bring a lot of energy in the flow field but they do not appear periodically. This is due to the fact that the recirculation zone on the step disturbs the periodicity of the vortex shedding.

Table 7.5: Amplified frequencies and wavelengths from POD and ICA for 6805+5%polymer at $\dot{m}_{Ox} = 50$ g/s

	Flap	VS1	KHI	VS2
5° FFR	-	170-190 Hz	300-340 Hz	-
	-	3.3-5 mm	2.5-3.5 mm	-
20° FFR	-	200-230 Hz	300-340 Hz	400-500 Hz
	-	3.7-5 mm	2.5-3.3 mm	1.4-2 mm
90° FFS	90-120 Hz	-	320-330 Hz	400-450 Hz (POD)
	5-7 mm	-	2.7-2.9 mm	2-2.5 mm (POD)

Fuel Viscosity and Oxidizer Mass Flow

After having identified the frequencies connected with the KHI for a particular fuel slab, it was possible to study the influence of the fuel viscosity and

oxidizer mass flux on the liquid layer break-up process, independently from the fuel configuration. Therefore, two main test campaigns were performed: the combustion behaviour of the pure paraffin 6805 and the paraffin blend with 5% polymer was investigated with an oxidizer mass flow varying in a range from 10 to 120 g/s. Fuel slabs with 20° forward facing ramp were used, due to the better flame quality (i.e. better flame holding and continuous flame front). The results show a strong dependence of the excited frequencies and wavelengths characterizing the melt layer from the fuel viscosity and oxidizer mass flow, see Fig. 7.27, 7.28, 7.29, 7.30.

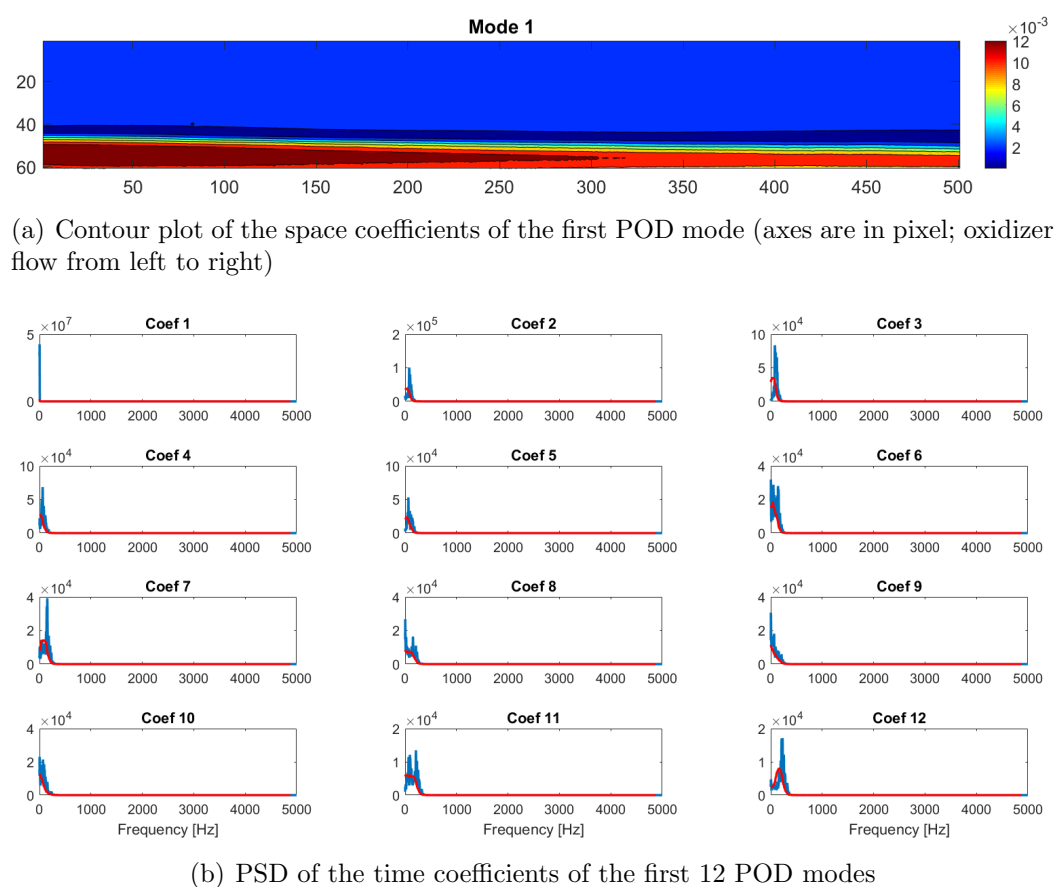
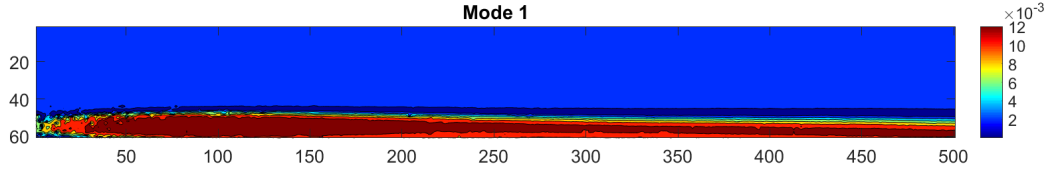
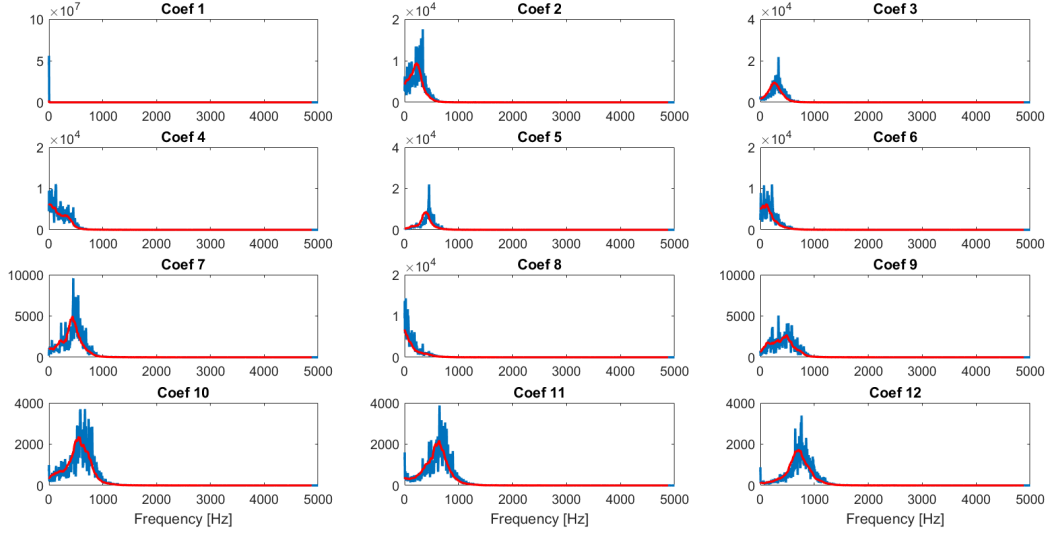


Figure 7.27: Contour plot and PSD of the POD modes of test 241 (Fuel 6805+5%polymer; $\dot{m}_{Ox} = 10$ g/s)

The final results coming from all the combustion tests run at different operating conditions are shown in Fig. 7.31, 7.32, 7.33 and 7.34. A linear dependency of the excited frequencies on the oxidizer mass flow/flux can be clearly seen. Since, in a hybrid rocket engine, the regression rate (which is the investigated parameter in this study) is expressed in terms of the mass flux (being the port diameter and, thus, the combustion chamber diameter varying in time), the excited frequencies characterizing the liquid layer are also expressed as a function of the oxidizer mass flux. For each fuel



(a) Contour plot of the space coefficients of the first POD mode (axes are in pixel; oxidizer flow from left to right)



(b) PSD of the time coefficients of the first 12 POD modes

Figure 7.28: Contour plot and PSD of the POD modes of test 203 (Fuel 6805+5%polymer; $\dot{m}_{O_x} = 50$ g/s)

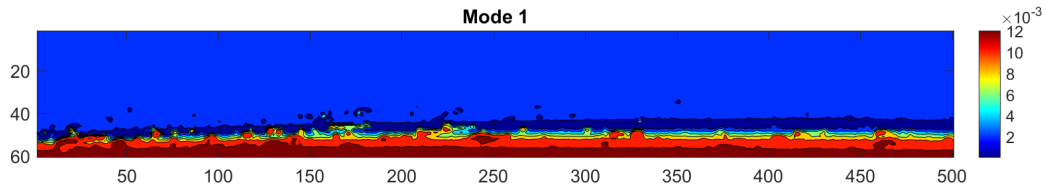
formulation, this dependency can be written as:

$$f = a_f + b_f G_{O_x} \quad (7.5)$$

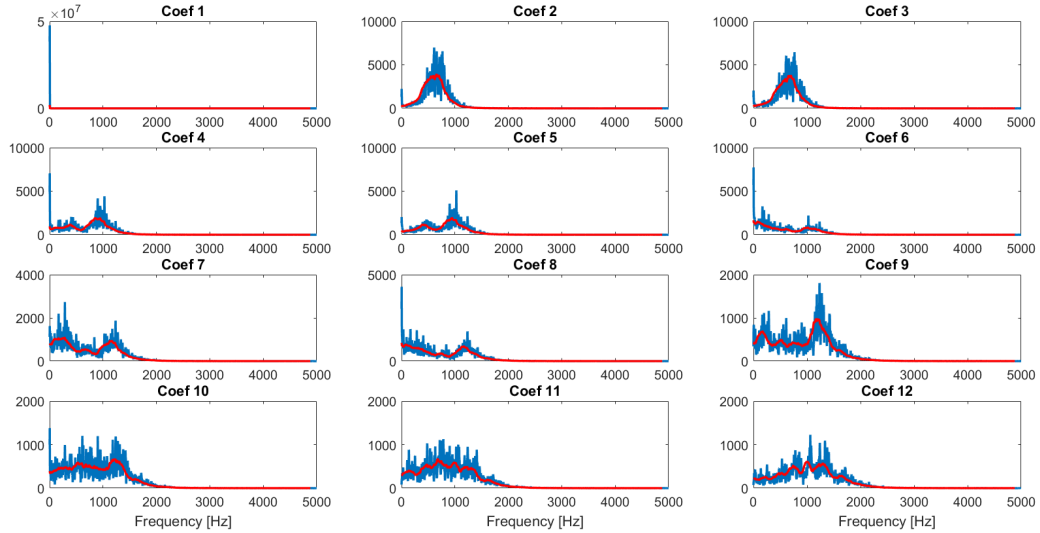
A power dependency of the excited wavelengths on the oxidizer mass flow/flux can be clearly seen. Also in this case, it is more useful to express the excited longitudinal wavelengths characterizing the liquid layer in terms of the oxidizer mass flux. For each fuel formulation, this dependency can be written as:

$$\lambda = a_\lambda G_{O_x}^{n_\lambda} \quad (7.6)$$

For what concerns the fuel viscosity, it is possible to notice that the most excited frequency values at the same oxidizer mass flow become lower as the viscosity increases. On the other hand, the longitudinal wavelengths become longer in the formulation with the polymer addition. So, the amplified frequency and wavelength values connected to the liquid layer instability process (Kelvin-Helmholtz Instability) are influenced by the liquid viscosity, as expected from the entrainment [43, 44] and Kelvin-Helmholtz [23] theories. In



(a) Contour plot of the space coefficients of the first POD mode (axes are in pixel; oxidizer flow from left to right)

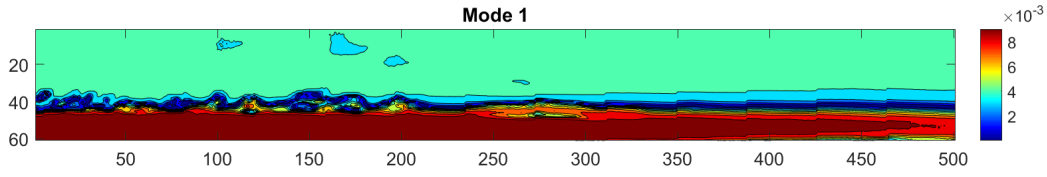


(b) PSD of the time coefficients of the first 12 POD modes

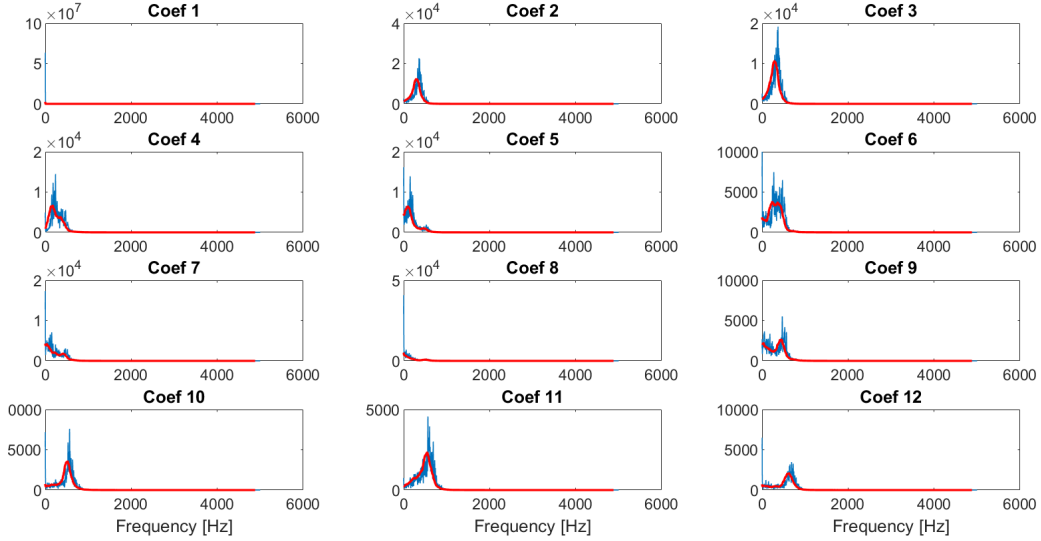
Figure 7.29: Contour plot and PSD of the POD modes of test 233 (Fuel 6805+5%polymer; $\dot{m}_{Ox} = 100$ g/s)

particular, by increasing the viscosity the frequency values decrease and the longitudinal wavelengths increase. This means that the higher the viscosity, the more stable the liquid layer. This leads to a lower number of released and, consequently, entrained droplets and, thus, to a lower regression rate.

For what concerns the oxidizer mass flow, the values of the excited frequencies become higher as the oxidizer mass flow increases, while the excited longitudinal wavelengths become smaller. Both fuel viscosities show the same trend. Furthermore, as the oxidizer mass flow increases, a broader frequency range is excited and almost no singular frequency peak can be detected. Even the visible peaks are much less defined and have a lower amplitude with respect to those at lower oxidizer mass flows (see Fig. 7.27, 7.28, 7.29). This is due to the faster flow dynamics and higher turbulence level in the combustion chamber, which brings to more variable burning conditions and large scale fluctuations (higher luminosity variations are also visible in the contour plots). Moreover, for very low mass flows, no distinct wavelength peaks are detected with both decomposition methods for the fuel with higher viscosity. This is in agreement with the Kelvin-Helmholtz instability model. The very



(a) Contour plot of the space coefficients of the first POD mode (axes are in pixel; oxidizer flow from left to right)



(b) PSD of the time coefficients of the first 12 POD modes

Figure 7.30: Contour plot and PSD of the POD modes of test 254 (Fuel 6805; $\dot{m}_{Ox} = 50 \text{ g/s}$)

low oxidizer mass flows have a speed below the critical one that is needed to achieve instability [23]. This is well visible in Fig. 7.35 and 7.36. In Fig. 7.35, it is possible to see the experimental gas flow speeds at different oxidizer mass flows, computed both at optimum conditions and at 65% efficiency for the two fuel formulations. The two curves represent the critical gas speed according to KHI theory, computed considering optimum conditions and 65% efficiency. Here, it is possible to notice that, for the pure paraffin, the gas speeds are all in the unstable region, considering both conditions. On the other hand, for the formulation with the polymer addition, the gas speeds connected to the lower mass flows are in the stable region, thus below the critical speeds needed to achieve the instability. The same consideration can be also done by looking at Fig. 7.36. Here, the critical oxidizer mass flows computed at optimum conditions and 65% efficiency are plotted versus the mixture ratios. The experimental oxidizer mass flows with the corresponding OF are also shown. In these plots, it can be seen that, for the pure paraffin, all the experimental values are in the unstable area. On the contrary, for the fuel blend, the tests with the lowest mass flows are in the stable zone.

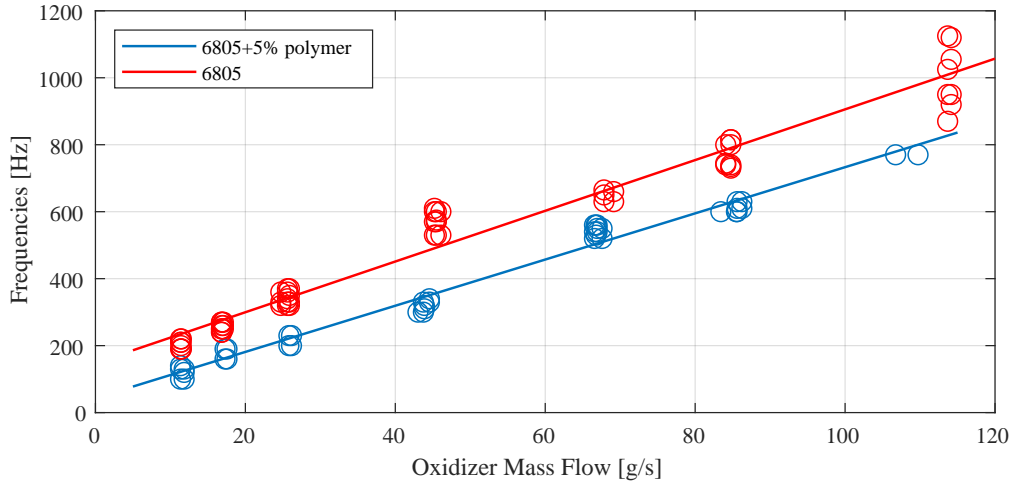


Figure 7.31: Dependency of the KHI frequencies on the fuel viscosity and oxidizer mass flow

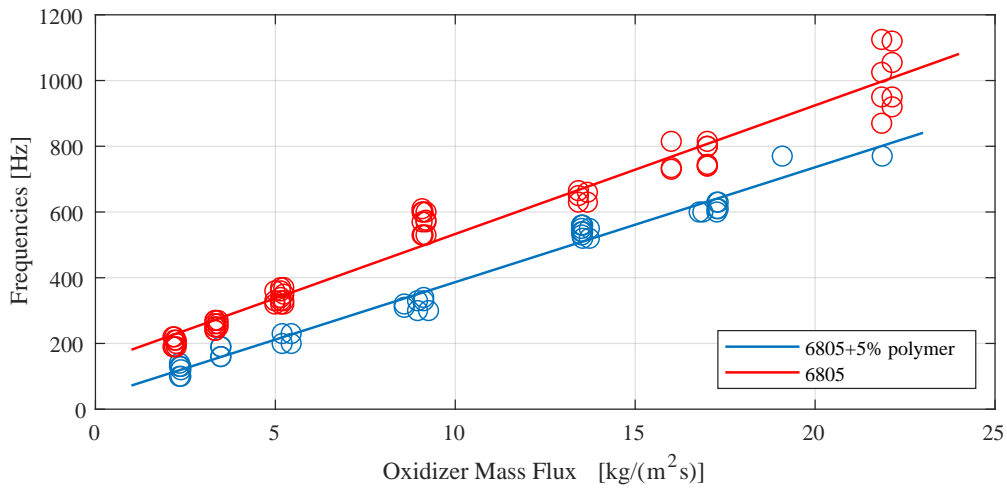


Figure 7.32: Dependency of the KHI frequencies on the fuel viscosity and oxidizer mass flux

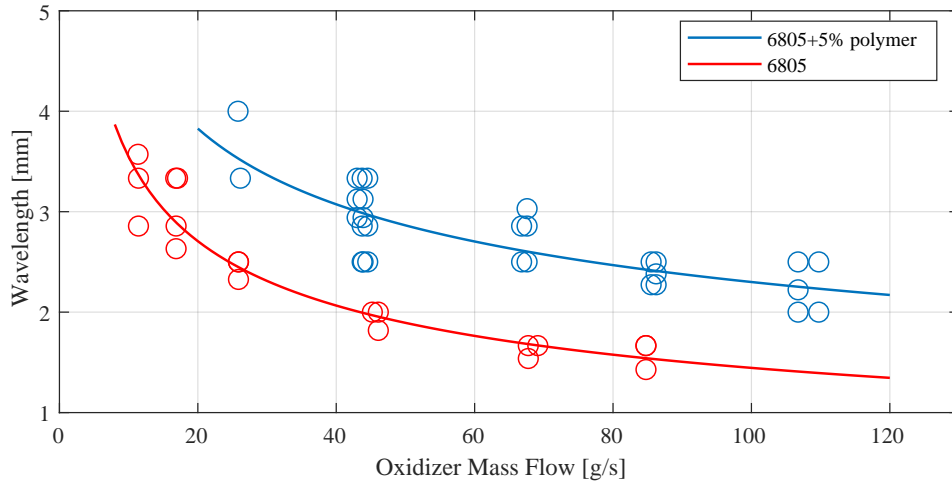


Figure 7.33: Dependency of the KHI longitudinal wavelengths on the fuel viscosity and oxidizer mass flow

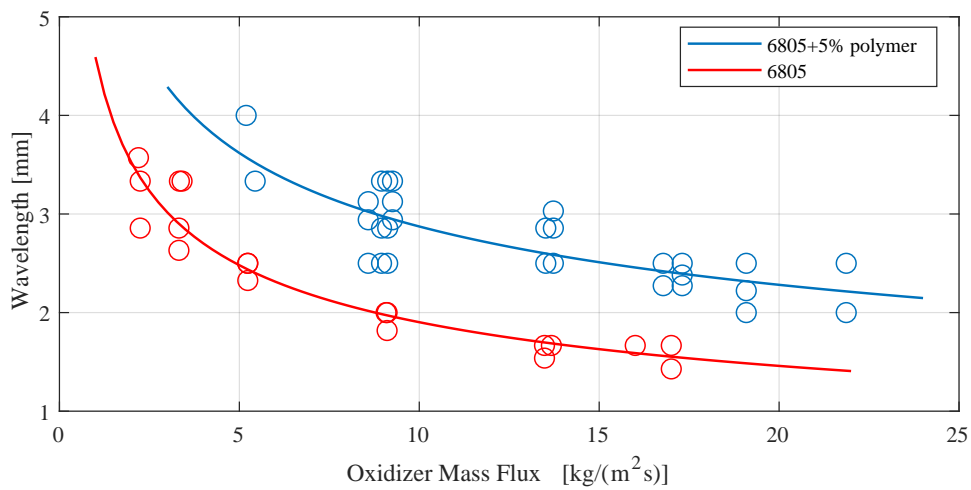


Figure 7.34: Dependency of the KHI longitudinal wavelengths on the fuel viscosity and oxidizer mass flux

Moreover, from both figures, it can be noticed that the critical gas speeds and mass flows for the pure paraffin are lower than those for the paraffin with polymer addition. This means that the stability limit is lower and, consequently, easier to achieve for fuels with lower viscosity (as already shown in Fig. 7.5). Finally, it can be also seen that, by decreasing the combustion efficiency, the critical mass flows are increasing, thus increasing the stability limit.

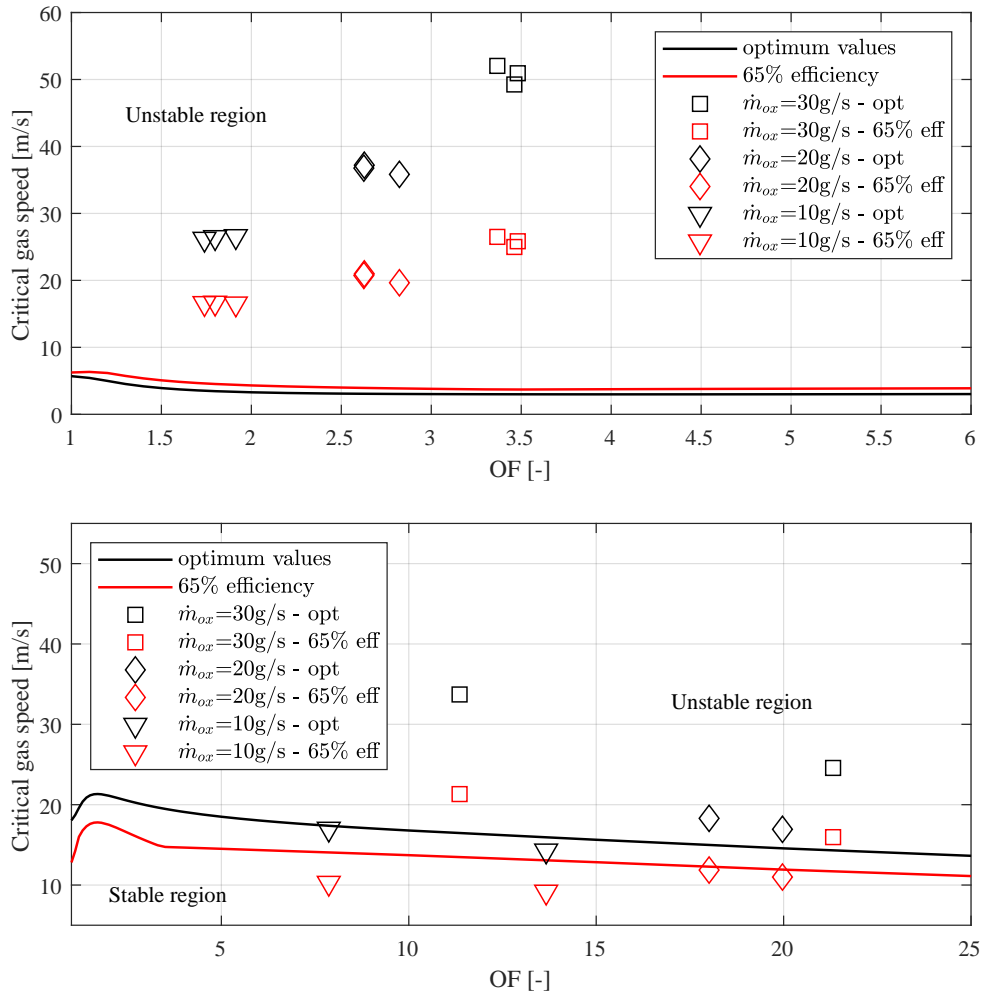


Figure 7.35: Critical gas speed curves with experimental values for 6805 (top) and 6805+5%polymer (bottom)

As already seen in Chap. 3, the critical speed depends on the liquid layer viscosity: the higher the viscosity, the higher its damping effect on the waves and, consequently, the higher the critical speed. This is the reason why, for the pure paraffin samples, it is still possible to detect waves at $\dot{m}_{Ox} \approx 10$ g/s, while with 6805+5% polymer (which has a higher viscosity) the last detectable waves are at $\dot{m}_{Ox} \approx 25$ g/s. This means that the critical speed for the pure paraffin is lower than that of the same paraffin with 5% polymer (see also Fig.

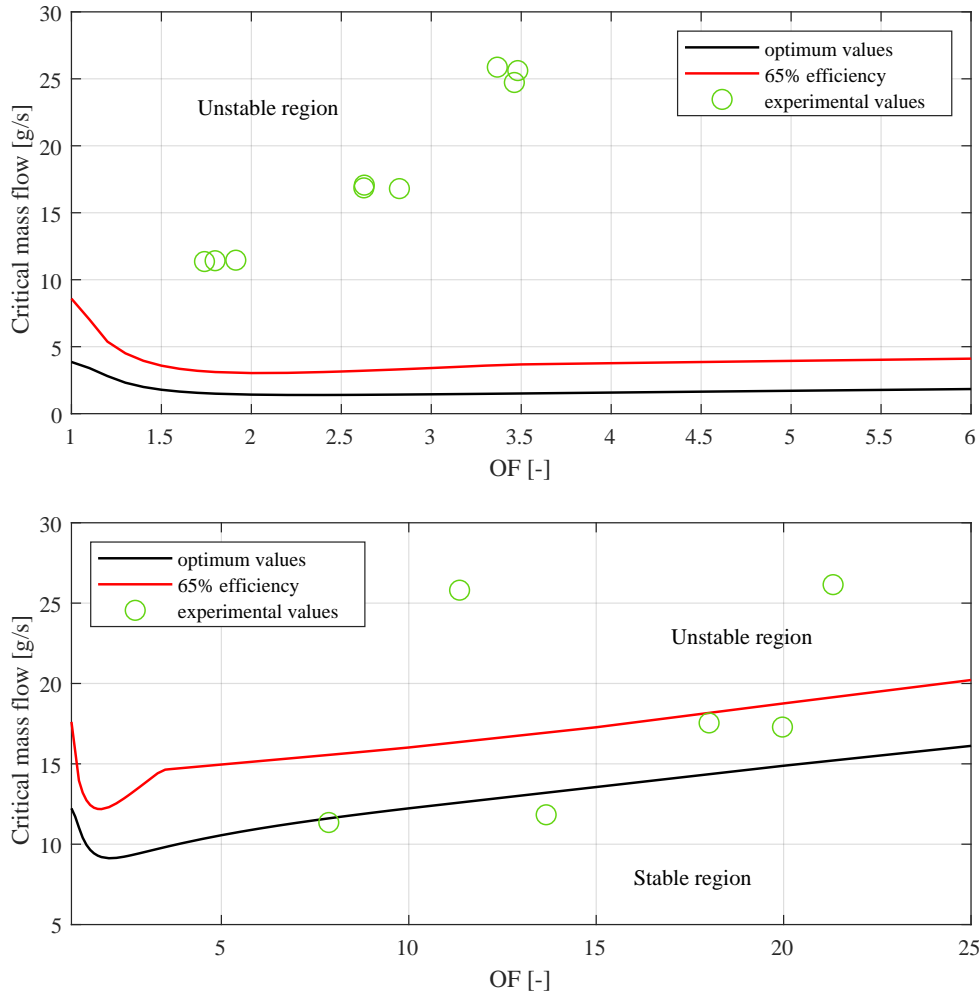


Figure 7.36: Critical mass flow curves with experimental values for 6805 (top) and 6805+5%polymer (bottom)

7.5) and, consequently, the range of unstable waves is also wider for 6805 with respect to the blend. Therefore, at flow speeds below the critical one, the disturbances of the liquid layer are damped by the liquid viscosity. On the other hand, at flow speed above the critical one, the same disturbances are able to produce waves that grow and may bring to instabilities. In this way, a range of wavelengths is excited and those wavelengths having the highest growth rate ultimately dominates. Moreover, at oxidizer mass flows just above the critical speed, longer waves (around 1-2 cm) are mostly appearing. These waves tend to be stable since their phase speed is higher and, therefore, the relative flow speed for a given mass flow is lower. On the other hand, viscous damping in the liquid dominates the very shortest waves, making them stable. Therefore, only waves with an intermediate range of wavelengths may be unstable (see also Fig. 7.6).

Regression Rate

From the results obtained in the previous section, it can be easily shown that there is a strong dependence between the excited frequencies and wavelengths and the oxidizer mass flux G_{Ox} . From the hybrid rocket combustion theory (see Marxman et al. [64, 63]), it is well known that the regression rate in a hybrid rocket engine is connected to the oxidizer mass flux through the regression rate law $r_f = aG_{Ox}^n$. The parameters a and n depend on the propellants formulation and have to be determined experimentally. In the framework of this research, the regression rate curves for each fuel formulation were obtained and, consequently, also the experimental parameters a and n (see Fig. 7.37).

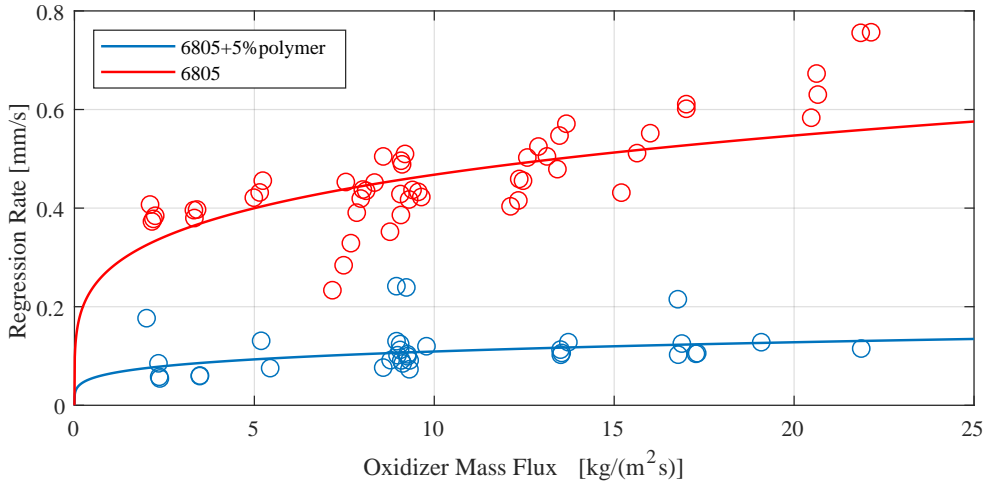


Figure 7.37: Experimental regression rate curves

At this point, the connection between the regression rate of the fuel slab and the excited frequencies and wavelengths of the fuel melt layer was straightforward, since they both depend on the oxidizer mass flux. Looking at Fig. 7.38 and 7.39, it is clearly visible that the regression rate has a linear dependence on the liquid layer frequencies, while a power law expresses its correlation with the longitudinal wavelengths. For each fuel formulation, the following general expressions are obtained:

$$r_f = a_r + b_r f \quad (7.7)$$

$$r_f = c_r \lambda^{n_r} \quad (7.8)$$

From the results, it is possible to notice that the higher the frequencies and the shorter the waves, the higher the regression rate. This is in agreement with what is predicted by the entrainment theory. For higher mass fluxes the liquid layer is characterized by higher frequencies and smaller longitudinal

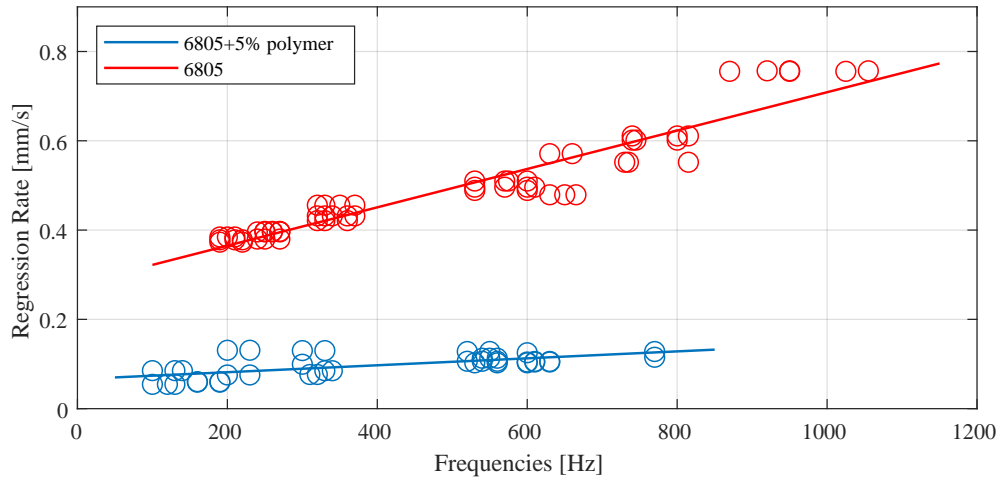


Figure 7.38: Dependency of the KHI frequencies on the regression rate

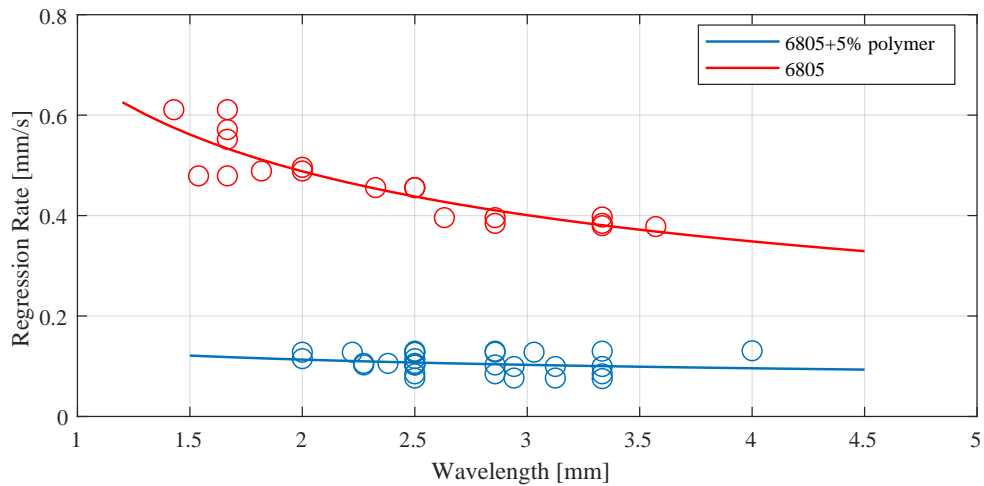


Figure 7.39: Dependency of the KHI longitudinal wavelengths on the regression rate

wavelengths. This means that it is more unstable (due to the higher shear stresses produced by the high speed flow) and more droplets are released from the unstable waves and entrained into the gas flow. Consequently, much more fuel can be transported into the flame zone before being totally vaporized and the blocking effect of the convective heat transfer is reduced, thus increasing the regression rate. Moreover, these results also show that the regression rate decreases as the viscosity increases, which once more confirms the previous results and the entrainment theory. The power relation between the fuel liquid viscosity and the regression rate has been experimentally found in this study and can be directly seen in Fig. 7.40, for the analyzed fuel compositions.

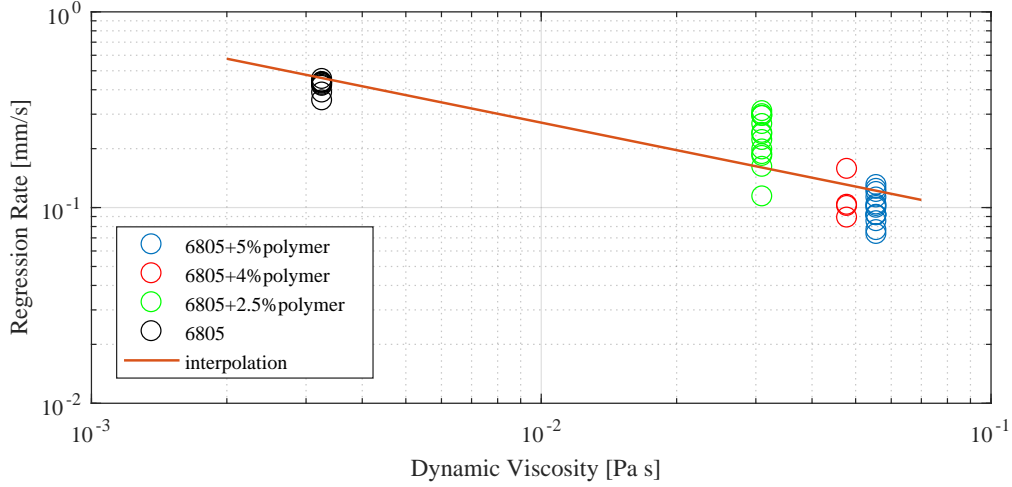


Figure 7.40: Dependency of the regression rate on the fuel liquid viscosity (values of r_f are taken at $G_{O_x} = 10 \text{ kg}/(\text{m}^2\text{s})$, values of μ are taken at $120 \text{ }^\circ\text{C}$)

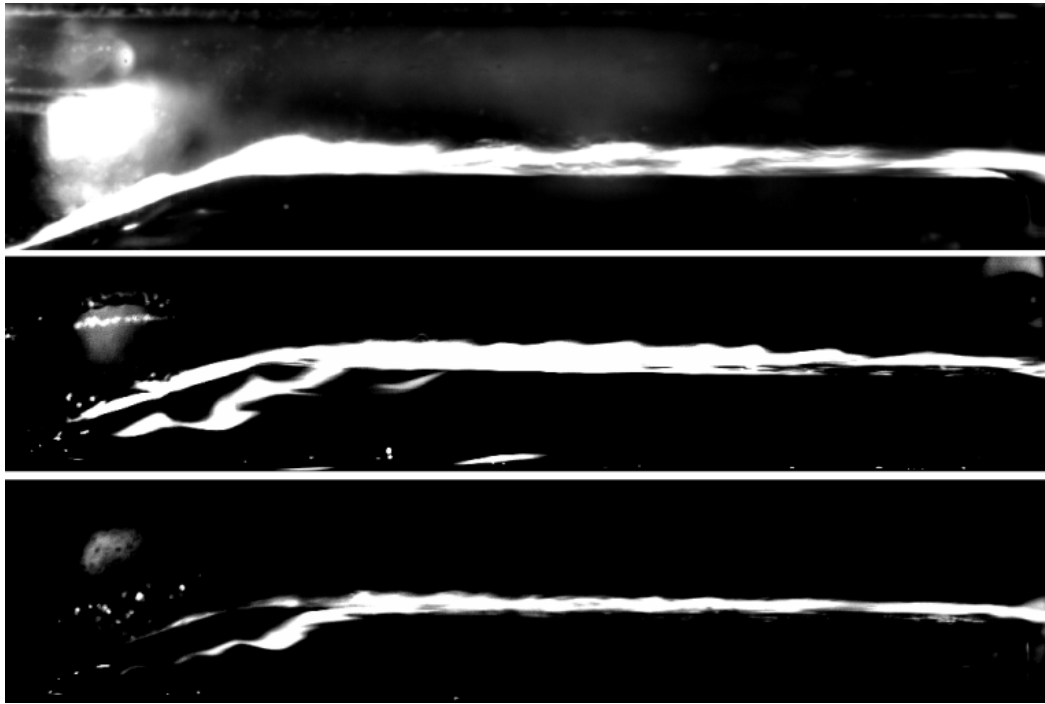
This dependency can be generally expressed by the following formula:

$$r_f = d_r \mu^{m_r} \quad (7.9)$$

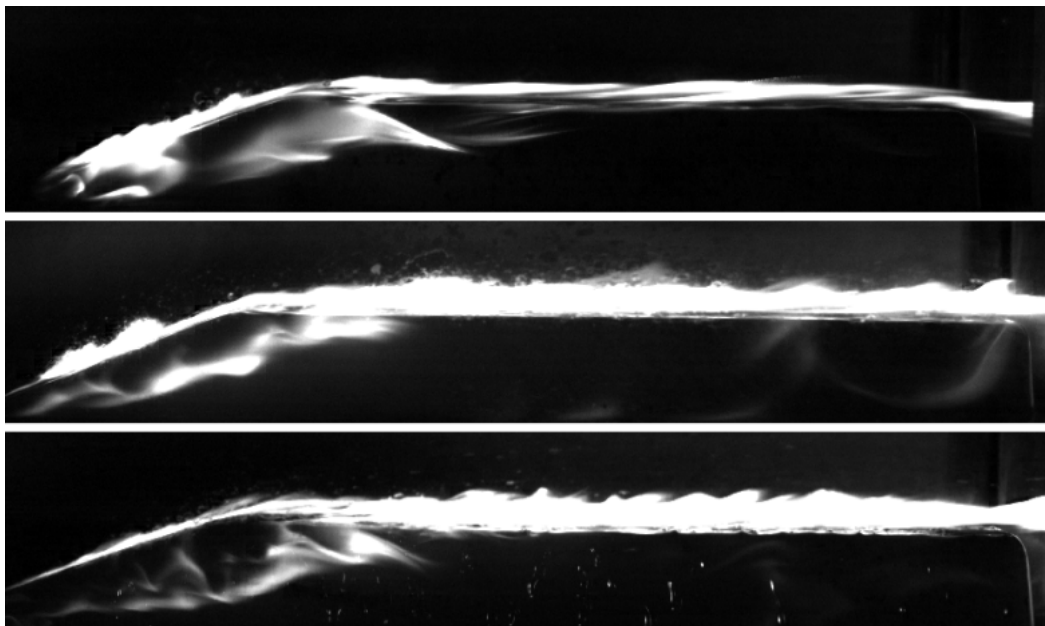
In this way, a direct dependency of the regression rate on the liquid layer stability is found, thus extending the results obtained by Karabeyoglu et al. [43], [44], who postulated an empirical expression for the entrainment rate of liquid droplets in terms of the relevant properties of the hybrid motor (i.e. mass flux, liquid layer thickness, surface tension and liquid viscosity). This means that it is possible to tailor the regression rate just by controlling the Kelvin-Helmholtz frequencies and wavelengths of the fuel liquid layer, without knowing the motor characteristics.

7.3.2 Flame Characteristics

Frame images taken from the recorded combustion videos are shown in Fig. 7.41. They show the combustion flame of the pure paraffin and of the paraffin blend at very low, intermediate and very high oxidizer mass flows. Looking at them, some qualitative considerations can be drawn. The frames are taken at the same point in time, around 2 seconds after ignition. Thus, they all show a steady-state combustion flame. From these images it can be noticed the difference in the flame stability for the different fuel compositions and mass flows. In the test run at $\dot{m}_{O_x} = 10 \text{ g/s}$, the flame of 6805 appears to be already quite wavy and unstable. In fact, as shown in Fig. 7.36, the liquid layer of the lower viscosity fuel is in the unstable regime already at this low oxidizer mass flow. On the other hand, the flame of the paraffin blend appears to be more flat, with some points of local extinction especially in the rear of the fuel slab,



(a) Fuel 6805; $\dot{m}_{O_x} = 10, 50, 100$ g/s (from top to bottom)



(b) Fuel 6805+5%polymer; $\dot{m}_{O_x} = 10, 50, 100$ g/s (from top to bottom)

Figure 7.41: Combustion flame of 6805 (top) and 6805+5% polymer (bottom) taken from high-speed videos (oxidizer flow from left to right)

where the flame appears to be made up of elongated filaments. In this case, the liquid layer has a too high viscosity and it cannot be destabilized by this low oxidizer mass flow. In the case with $\dot{m}_{O_x} = 100$ g/s, many short waves appear on the flame surface of the paraffin blend fuel and the typical shape of Kelvin-Helmholtz waves can be recognized in some of them. The flame is burning continuously along the fuel surface with no points of local extinction. The flame of the pure paraffin seems to be more flat, even if some small waves can be recognized. Finally, in the combustion tests at $\dot{m}_{O_x} = 50$ g/s, waves can be seen on the flame front of both fuels and typical Kelvin-Helmholtz waves can be detected. The flame front is continuous, without point of local extinction and well attached to the fuel surface.

A quantitative analysis of the flame characteristics was carried out for all the tests considering the same time (10000 frames, corresponding to 1 second, during steady-state) and space (500x60 pixels) windows, like in the previous analysis. In particular, the flame speed, longitudinal length and height were computed and compared for every fuel and oxidizer mass flow.

Flame Speed

To compute the average flame speed, the waves appearing on the flame surface are tracked as they move along the flame during the burning time. In order to do so, certain points in the flame must be easily and reliably identified between frames, and so it is decided that peaks fit this criteria the best. However, the peaks also suffer from short lifetime and are seen to collapse suddenly. Therefore, some limiters are placed on the peak criteria. The gradient between one point and the adjacent one must equal zero, thus identifying an inflection point and being sure that the peak is more robust and less likely to be an entrained droplet that will disappear. The gradient is then calculated using the central difference scheme. Moreover, only the highest peak in the frame is tracked, which reduces misidentification and hence errors. Also here, some criteria are applied in order to identify whether the peak is suitable to track. For example, the peak identified as suitable in the first frame will move forward in the x direction by the next frame; the difference in height of the same peak in subsequent frames is limited in the y direction (2 pixels): this eliminates collapsing peaks being misrecognized. Also, the forward distance moved by a wave is limited to a value computed as the frame interval multiplied by a constant which is pre-determined for the mass flow rate and fuel: this reduces misrecognizing a peak if it collapses or if a new peak develops downstream. If the criteria are satisfied, then the distances between the peaks in the x direction are calculated. The median distance, due to the large noise in the data, is taken in each test and then divided by the time step. The results of this analysis conducted on different tests are shown in Fig. 7.42.

The flame speed is strongly dependent on the oxidizer mass flow and almost independent from the fuel viscosity. It increases as the oxidizer speed increases, since the dynamics in the combustion chamber gets faster.

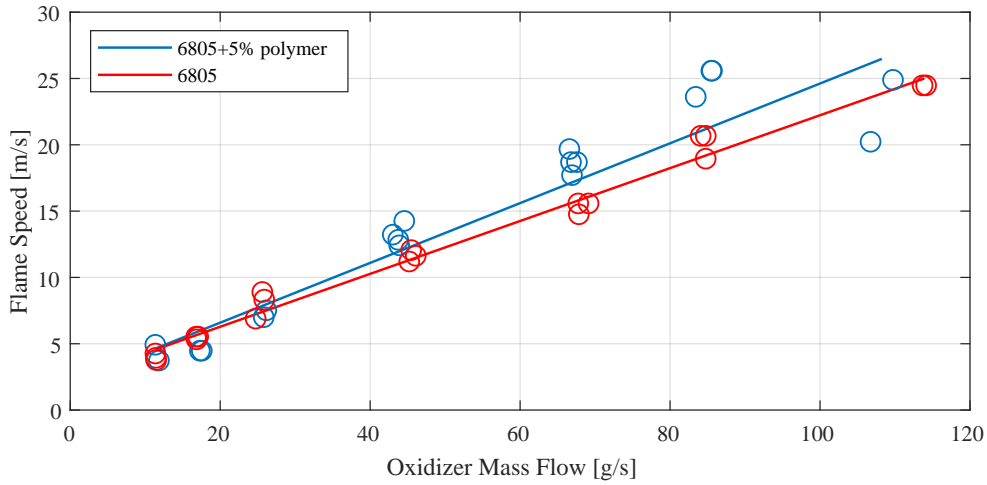


Figure 7.42: Flame speed dependence on fuel composition and oxidizer mass flow

Flame Surface Length

A similar analysis is conducted to compute the average flame surface length. Several points are taken along the flame edge in each frame and the length is calculated by taking the linear distance between points on the top surface, using Pythagoras, where the flame exists. The same procedure is performed on 10000 frames and then the median length is computed. The results of this analysis conducted on different tests are shown in Fig. 7.43.

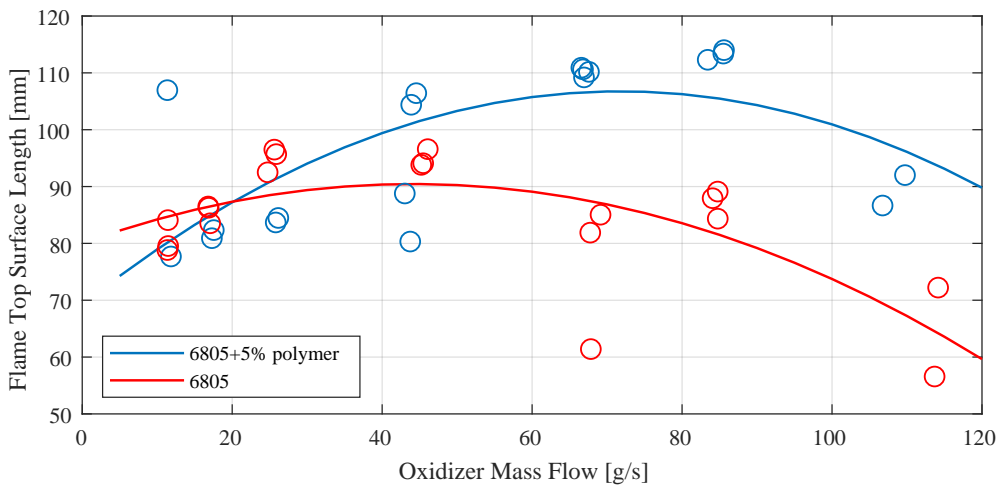


Figure 7.43: Flame surface length dependence on fuel composition and oxidizer mass flow

A similar trend can be seen in the behaviour of the two fuels. The flame surface length first increases as the oxidizer mass flow increases, then it starts

decreasing for increasing oxidizer mass flows. The reason for this behaviour could be found in the balance between the shear forces exerted by the oxidizer flow, which cause the flame to be more unstable, and the dynamic pressure coming from the same flow, which tends to flatten the flame over the fuel surface. For moderate oxidizer mass flows ($\dot{m}_{O_x} \leq 50$ g/s), the flame surface length increases as the mass flow increases, due to the increased flame instability (shorter waves). In this region, the shear forces exerted by the flow are higher than the dynamic pressure and small waves appear on the flame surface. The fact that the flame length of the pure paraffin results lower than that of the paraffin blend could be due to the resolution. It is most likely that too short waves are not detected as singular waves but merged together during the analysis. It must be also noticed that, for very low mass flows ($\dot{m}_{O_x} \approx 10$ g/s), the flame length of the paraffin blend is lower than that of the pure paraffin. In this case, no instability arises for the higher viscosity fuel (see Sec. 7.3.1). For higher oxidizer mass flows ($\dot{m}_{O_x} \geq 50$ g/s), an opposite trend can be noticed for both fuels: the flame length decreases as the mass flow increases. This could seem strange since the flame should become even more unstable as the flow speed (and thus the shear forces) increases. As already explained before, a reason for that is that too short waves are not detected and, again, merged together. Moreover, this behaviour is also due to the fact that, for higher gas speeds, the dynamic pressure exerted on the flame increases. This pressure tends to flatten the flame over the fuel surface, thus decreasing the flame length. This is more visible in the tests with pure paraffin, where the flame gets visibly closer to the fuel surface as the oxidizer mass flow increases (see Sec. 7.3.2 and Fig. 7.44).

Flame Height

As already explained in Sec. 6.1, from the PSD of the row-wise spectral content of the spatial coefficients given by the decomposition methods, the main flame height can be obtained. This allows to automatically compute, for every fuel viscosity and oxidizer mass flow, the average flame position. The results show that the two fuel compositions present a different dependency on the oxidizer mass flow, as it can be also observed from the combustion video frames (Fig. 7.41). For the lower viscosity fuel, the flame height decreases with increasing oxidizer mass flow. On the other hand, the flame height of the fuel with the higher viscosity increases with increasing oxidizer mass flow, see also Fig. 7.44.

This trend is also confirmed from the results given by automatically detecting the flame edge from the frames and averaging it over the amount of frames to analyze (in this study the analysis is always performed on 10000 frames taken during the steady-state). The results for the two paraffin mixtures at three different oxidizer mass flows are shown in Fig. 7.45. The explanation for this trend could be found in the balance between the vaporization and the entrainment regression rate, which contribute to the final total regression

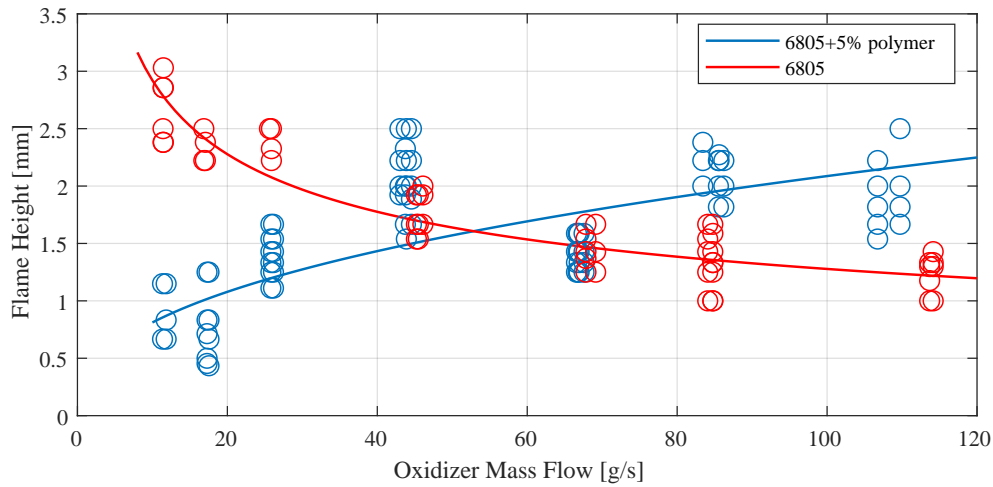


Figure 7.44: Flame height dependence on fuel composition and oxidizer mass flow

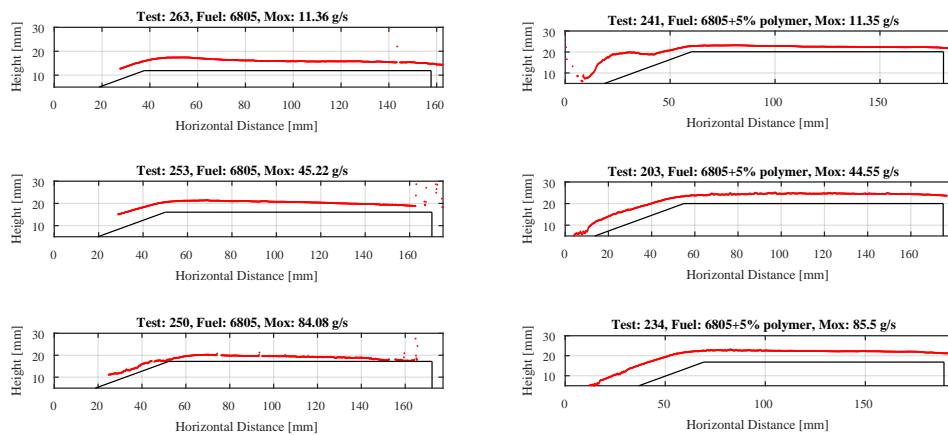


Figure 7.45: Average flame position (red) and fuel grain position (black) for 6805 (left) and 6805+5%polymer (right) at three oxidizer mass flows

rate in liquefying hybrid rocket fuels. The combination of fuel viscosity and oxidizer mass flow decides which of the two regression rates plays a more important role. For the lower viscosity fuel, the droplets entrainment at high oxidizer mass flows dominates direct gasification. This brings to an important increase in the regression rate and a decrease in the liquid layer thickness (see Fig. 7.46). Consequently, also the flame height tends to decrease. On the other hand, for the higher viscosity fuel, even at high oxidizer mass flows, the vaporization regression rate plays still an important role with respect to the entrainment mass transfer. Moreover, at higher oxidizer mass flows, the

turbulence level in the combustion chamber increases. This increases the convection processes, which, in turn, causes an increase in the heat exchanges rate between the fuel and the gas flow. As a result, the melting and evaporation rates of the liquid layer increase, thus causing an increase in the blowing of fuel vapours from the fuel surface to the flame. This “pushes” the flame sheet further away from the liquid layer and, consequently, increases the flame height.

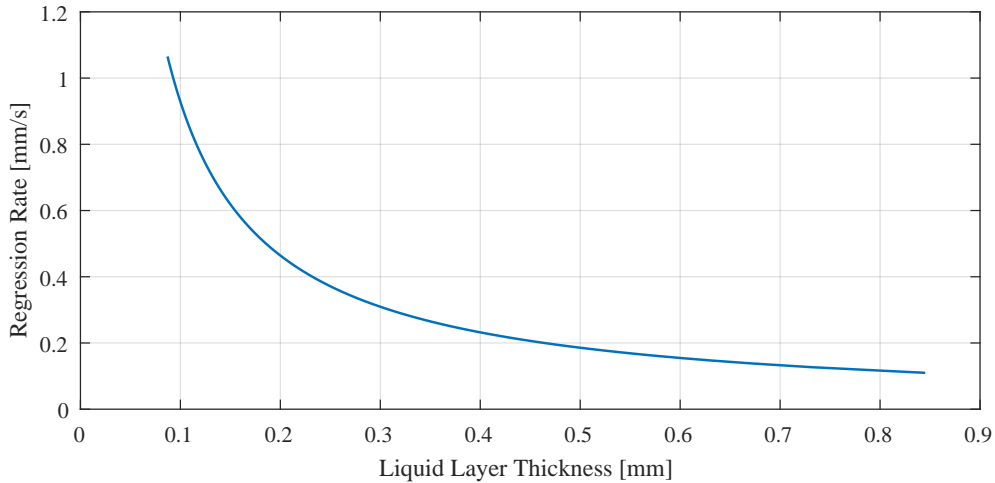


Figure 7.46: Regression rate dependence on liquid layer thickness for 6805 (computed with Eq. 2.47, taken from Karabeyoglu et al. [43])

Following Marxman’s theory [63] (see Sec. 7.1.2), the theoretical boundary layer thickness δ for the tested fuel mixtures and operating conditions is computed according to Eq. 7.1. The average flame position is also evaluated, considering its height as 20% of the boundary layer thickness [63]. In order to have a direct comparison with the burning tests analyzed in this section, the data taken from the same tests are considered in the computation of δ . Moreover, since both considered fuels are paraffin-based mixtures (liquefying fuels), a blowing parameter $B = 2$ is considered. The free stream properties are taken from the values given by the software NASA CEA (Chemical Equilibrium with Applications) at optimum conditions. Obviously, if a lower combustion efficiency (in this case 65%) is considered, the boundary layer and flame heights result lower than those at optimum conditions. The results at optimum conditions are shown in Fig. 7.47.

In order to facilitate a direct comparison of the theoretical results with the experimental ones, the space and time averaged flame heights obtained from the PSD given by the decomposition methods and shown in Fig. 7.44 are compared to the space averaged theoretical boundary layer thickness (the average is computed between $60 < x < 160$ mm, like in the experimental results) for each of the considered test. The results are summarized in Tab. 7.6 (note that δ is computed considering both optimal and 65% efficiency conditions of the free stream).

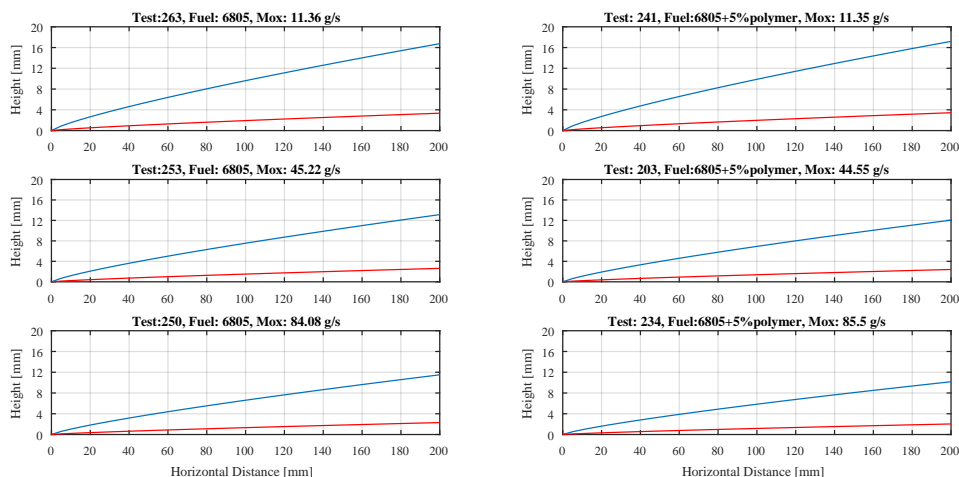


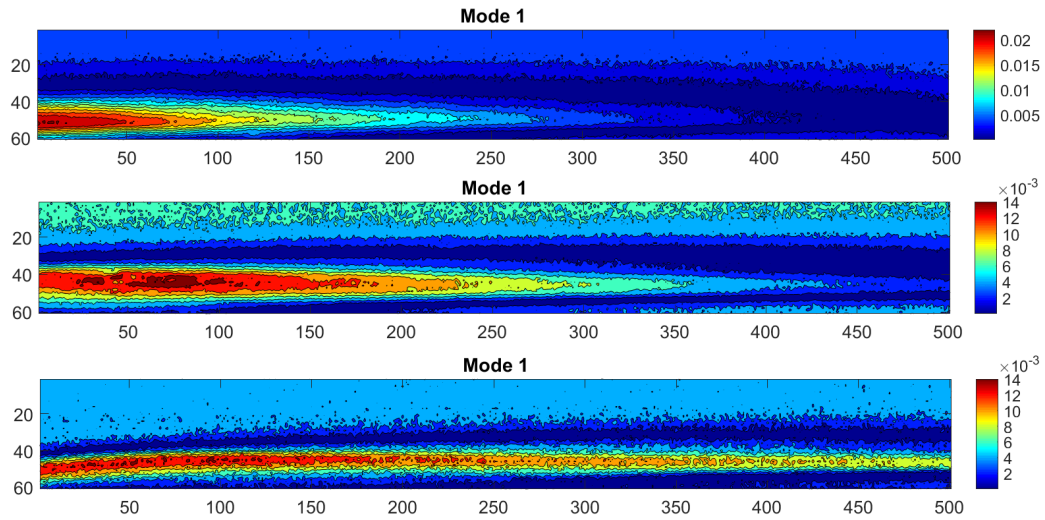
Figure 7.47: Boundary layer thickness δ (blue) and flame position (red) versus distance x for 6805 (left) and 6805+5%polymer (right) at three oxidizer mass flows ($B = 2$)

Table 7.6: Experimental flame height compared to the theoretical boundary layer thickness

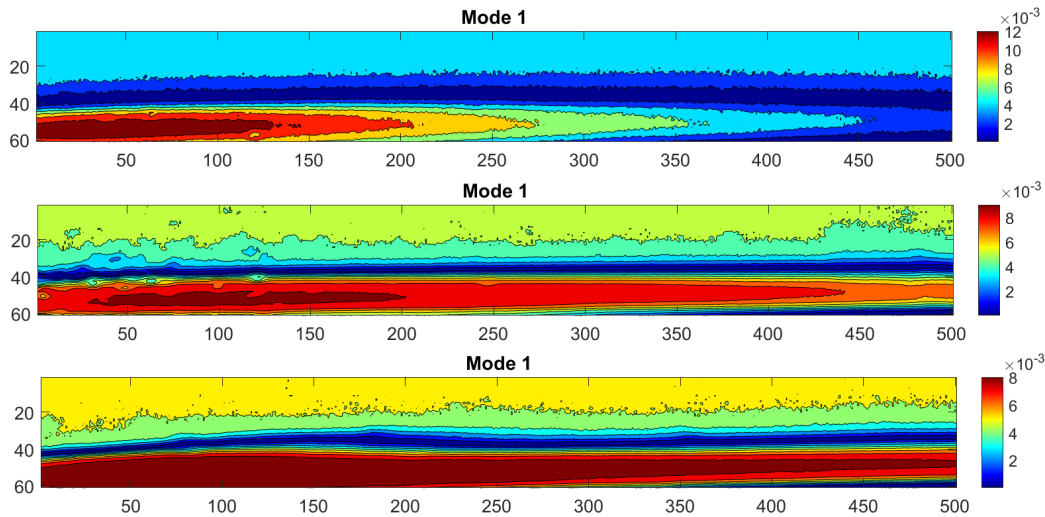
Test no.	Fuel	\dot{m}_{Ox} [g/s]	y_{flame} [mm]	y_{fl}/δ_{opt} [%]	$y_{fl}/\delta_{0.65}$ [%]
203	6805+5%polymer	44.55	2	26.9	28.5
234	6805+5%polymer	85.5	2.10	33.5	35.5
241	6805+5%polymer	11.35	1.15	10.8	11.5
250	6805	84.08	1.66	23.4	24.8
253	6805	45.22	1.92	23.7	25.1
263	6805	11.36	2.50	24.2	25.7

As shown in Tab. 7.6, the flame position oscillates between 10% and 35% of the theoretical boundary layer thickness, depending on the operating conditions. These results are in good agreement with those predicted from the Marxman’s theory (between 10% and 20%, see Sec. 7.1.2). It should be also taken into account that the turbulent boundary layer theory of Marxman is based on the assumptions that the flame has an infinitesimal thickness (“flame sheet” hypothesis) and that the combustion takes place at a stoichiometric local mixture ratio.

More information about the flame location and topology can be obtained from the CH^* images. In Fig. 7.48, the contour plots of the first POD mode of the two fuel compositions at three oxidizer mass flows are shown. It is important to remind that the first POD mode represents the average flame



(a) Fuel 6805; $\dot{m}_{O_x} = 10, 50, 100$ g/s (from top to bottom)



(b) Fuel 6805+5%polymer; $\dot{m}_{O_x} = 10, 50, 100$ g/s (from top to bottom)

Figure 7.48: Contour plots of the first POD mode taken from CH* images (axes are in pixels; oxidizer flow from left to right)

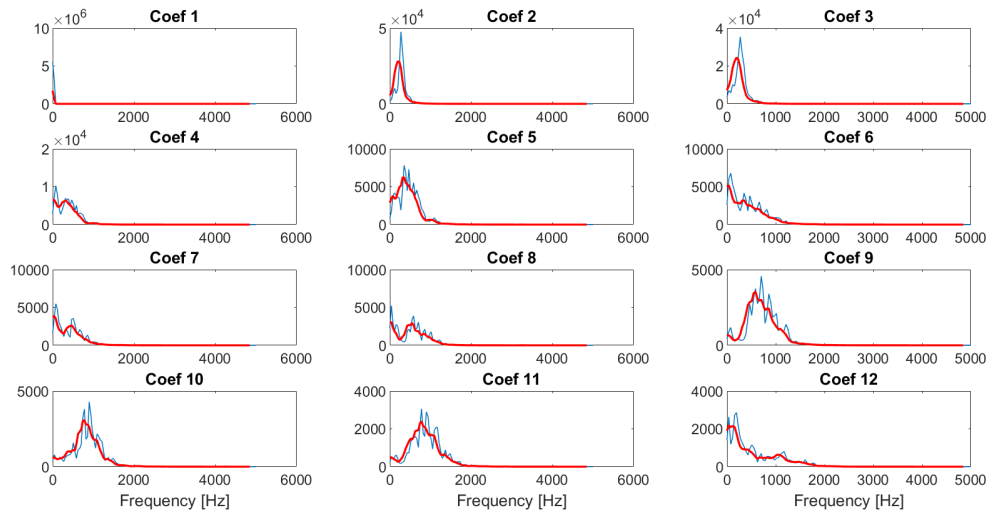
profile, while higher modes give information about fluctuations. From the contour plots, it can be clearly seen that, for both fuel compositions, the flame surface becomes more unstable and rough as the oxidizer mass flow increases. More “droplets” detaching from the main flame can be noticed. Moreover, by comparing the two fuel compositions at the same oxidizer mass flow, it is distinctly visible that the pure paraffin presents a more unstable flame surface, with more droplets. The CH* flame intensity is also higher for 6805, due to the higher flame temperatures (note that, at the same oxidizer mass flow, more fuel burns with the pure paraffin with respect to the paraffin blend, due to the higher regression rate. This means that the mixture ratio

OF is smaller for 6805 than for 6805+5%polymer. This brings to higher temperature in the combustion chamber). Finally, it can also be noticed that the flame height has the same trend like in the high-speed videos.

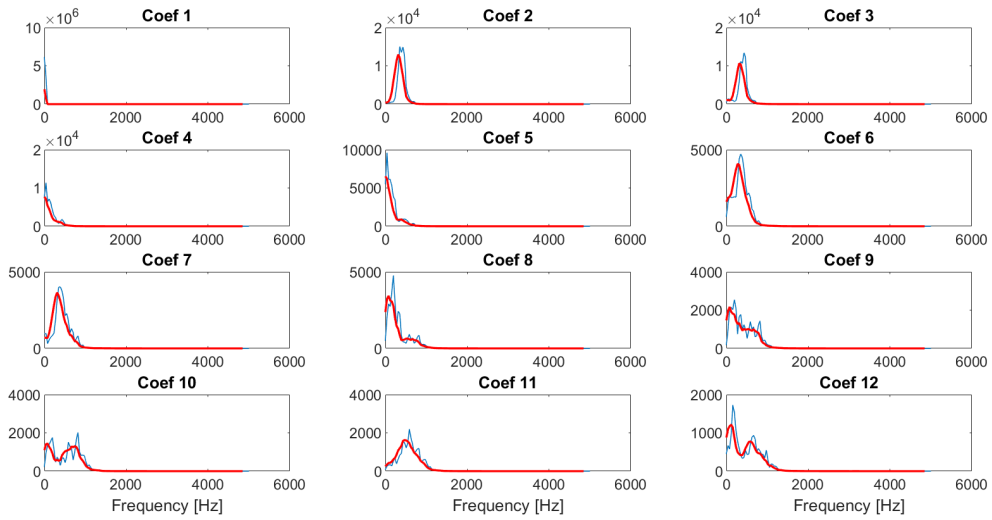
7.3.3 Analysis of the Burning Phases

All the results previously presented are referred to the steady-state combustion phase. This is the longest and the more stable part during the burning tests and, consequently, the decomposition algorithms have better performance and give more accurate results if applied on this time window. However, in order to check the difference between this stable phase and the transients, the analysis was also applied to a smaller time window taken from the ignition and extinction phases. In particular, a further analysis was carried out considering 1000 frames, corresponding to 0.1 seconds, taken from each of the three main combustion phases and the results compared.

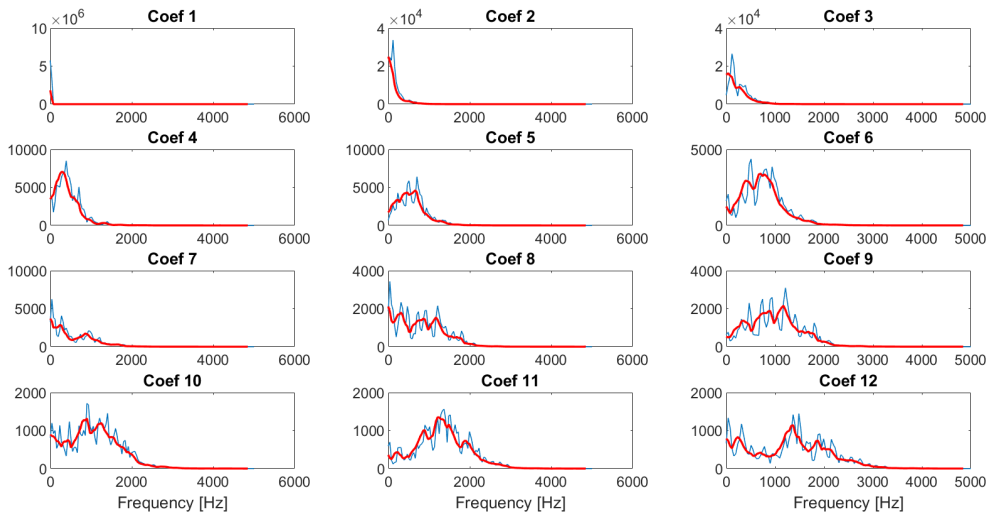
During the transients, the flow conditions change more rapidly than during the steady-state. Therefore, a broader range of frequencies is excited and almost no distinct peaks could be noticed both during ignition and extinction (see Fig. 7.49). This means that no real periodic structures can be detected on a bigger scale during the transients (some periodic patterns could be probably detected in small regions). Despite this, since the dynamics in the combustion chamber is much faster during the transients than during the steady-state, higher frequencies are excited during ignition and extinction. This means that shorter waves, associated to higher frequencies and wave speeds, are detected during these phases, as it can be seen from the frames shown in Fig. 7.50. In Fig. 7.51, the contour plots of the first POD mode computed during the three phases are shown. It can be noticed that the boundary layer is thicker during the transients than during the steady-state, where the flow conditions are well established in the combustion chamber and a flatter boundary layer profile is visible. During ignition, the oxidizer mass flow and, consequently, the temperature in the combustion chamber are rising. The melt layer becomes thicker and the flame moves away from the surface due to the increasing blowing of fuel gases. Moreover, higher intensity variations inside and outside the main flame region characterize the ignition and extinction phases. This is due to more variable conditions in the flow field and fluctuations in the combustion chamber parameters, especially during the blow-out of the flame in the extinction phase. Due to the high variability of flow conditions during the transients, the flame front changes rapidly and oscillates more, thus enhancing luminosity variations that are displayed over the whole fuel surface. On the other hand, during the steady-state, the luminosity variations are concentrated in a thin region near the fuel surface, since the flow conditions are constant and, therefore, the flame front does not change much. In the rear part of the fuel slab, the luminosity tends to change in a thicker region, due to the high turbulence that causes the flame front to oscillate more. Short longitudinal waves and droplets entrainment can be



(a) Ignition phase



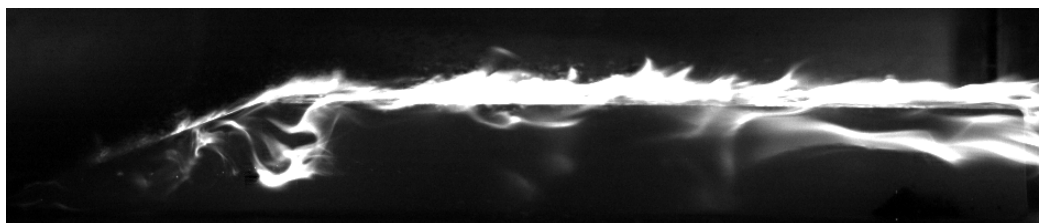
(b) Steady-state phase



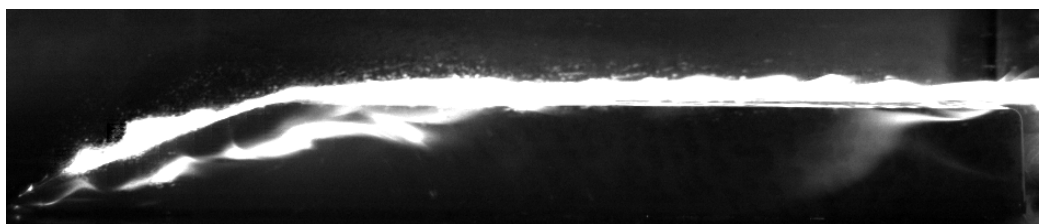
(c) Extinction phase

Figure 7.49: PSD of the time coefficients of the first 12 POD mode of test 203

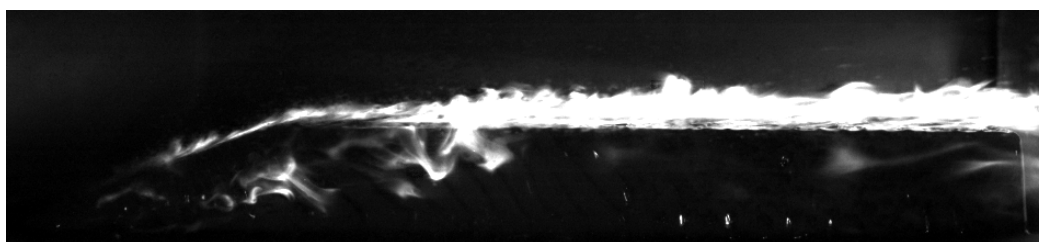
seen in the contour plots of all burning phases (see Fig. 7.51), despite, in the videos, droplets were visible only during the transients due to lower light emission.



(a) Ignition phase



(b) Steady-state phase



(c) Extinction phase

Figure 7.50: Combustion flame of the three burning phases taken from test 203

7.4 Experimental Results of Pressurized Combustion Tests

Three tests will be discussed to compare the effects of the chamber pressure on the combustion of paraffin-based hybrid fuels. The chosen tests are characterized by combustion pressures spanning from the sub-critical regime to the super-critical one, which, for paraffin wax with carbon number about 30, is predicted to be above approximately 6.5 bar [55]. In all the tests, the same fuel slab configuration (with a 20° forward-facing ramp) and composition (6805+5% polymer) are used. The oxidizer mass flow is kept constant at around 50 g/s and the oxidizer mass fluxes are, as well, comparable. The test parameters and the camera settings used for these tests can be found, respectively, in Tab. 7.7 and 7.8. The space-time averaged regression rates are

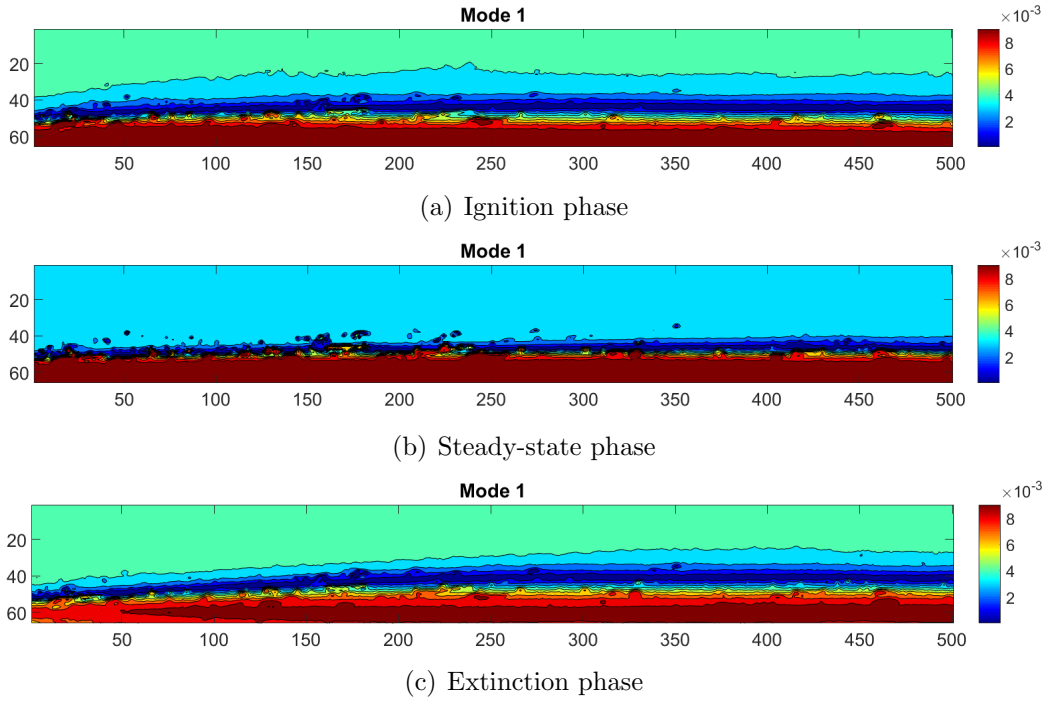


Figure 7.51: Contour plots of the first POD mode of test 203 (axes are in pixels; oxidizer flow from left to right)

computed by using the burned fuel mass, measured by removing the mass of the remaining fuel after the test from the original fuel mass. Some uncertainties are associated with this method, since there can be unburned fuel ejected from the nozzle during the hot fire (mainly unburned fuel pieces detaching from the slab) or during the nitrogen purge after the test (mainly melted fuel pushed out from the nitrogen flow).

Table 7.7: Combustion test parameters

	Test 203	Test 04	Test 01
Fuel	6805+5%polymer	6805+5%polymer	6805+5%polymer
p_c [bar]	1	13	40
d_t [mm]	-	9	5
\dot{m}_{Ox} [g/s]	44.55	42.75	46.60
G_{Ox} [kg/(m ² s)]	9.12	10.93	9.52
OF	30	2	1
t_b [s]	2.8	2.5	2.8
Ign. delay [s]	0.55-0.6	0.28-0.29	0.27-0.28
Δm_f [g]	4.1	56.2	120
r_f [mm/s]	0.085	4.8	10.1

Table 7.8: Camera settings

	Test 203	Test 04	Test 01
Image size [pixel x pixel]	1024x336	1024x336	1024x336
Frame rate [1/s]	10000	10000	10000
Shutter time [s]	1/1000000	1/1000000	1/1000000
f/stop [-]	5.6	8	8
Bit shift [-]	2	0	0

At sub-critical pressure conditions, the paraffin-based fuel is expected to form a liquid layer over its burning surface, from where droplets are entrained. In this test, droplets can be seen during the ignition phase, due to the fact that the flame is not yet completely developed and, consequently, not too bright. Moreover, the temperature in the combustion chamber is not yet too high. Therefore, the droplets are entrained in the oxidizer flow before being heated over the critical temperature (which is predicted to be around 840 K [55]). During the steady-state phase, only few droplets are visible above the flame. Most of them are burned already below the flame sheet, due to the fact that higher temperatures are reached in the combustion chamber. At some point during the burning process, the paraffin temperature is above the critical one, thus creating partial trans-critical combustion conditions (pressure is below the critical one, temperature is above the critical one). Moreover, the illumination from the flame is expected to obscure some of the droplets. The resolution can also limit the size of the visible droplets. At atmospheric conditions, the flame takes between 0.55 and 0.6 seconds to be fully developed and propagate to the end of the fuel slab. Once the steady-state is reached, the flame front appears to be continuous, without points of local extinction and well attached to the fuel surface. Many wave-like structures characterize the flame front until the end of the combustion process. Typical Kelvin-Helmholtz waves can be also recognized, like in the frame shown in Fig. 7.41. They develop and grow, before breaking up into droplets and being entrained into the flow. These waves appear to be periodic during the whole combustion process. Therefore, it was possible to compute their frequencies and wavelengths by using two automatic decomposition techniques. It has been found out that, for this particular fuel viscosity and oxidizer mass flow, the wave frequencies are around 300-340 Hz, while the longitudinal wavelengths are between 2.5 and 3.3 mm (see Sec. 7.3.1). These values are in the range of the most amplified frequencies and wavelengths predicted by the Kelvin-Helmholtz theory. The flame height has been also computed with two methods. First, the decomposition techniques have been used: the peaks of the power spectral density (PSD) of the row-wise content of the spatial coefficients matrix coming from the decomposition algorithms represent the flame height (see Sec. 7.3.2). The average flame height computed over 1 sec-

ond (10000 frames) during steady-state obtained with this method is between 1.5 and 2.5 mm. A more precise way to compute the mean flame height is to automatically detect it from the full frames. In this case, the frames are analysed in their original size (in the pre-processing phase of the decomposition methods the frames are cropped just up to the solid fuel surface). The average fuel grain location is determined by scanning the columns of each frame from the bottom to the top and detecting the edge with the Canny method. The same is done, from the top to the bottom, in order to detect the flame edge. The values of the heights are then computed for each column and then averaged in each frame. Afterwards, the time average, over 10000 frames, is computed. It is important to stress that the same time span as in the previous analysis was used. With this method, an average flame height between 4 and 5 mm is obtained (see Fig. 7.45).

For the elevated pressure tests, the updated test set-up, as described in Chap. 5, was used. In order to obtain different operating pressures, two nozzles with variable throat diameters were installed (see Tab. 7.7). The expected pressure in the combustion chamber was determined by conducting a series of cold flow tests and accounting for the pressure increase due to combustion. The pressure and oxidizer mass flow plots versus time are shown in Fig. 7.52 and 7.53 for, respectively, test 04 and 01. A photo of the exhaust plume during a firing test at elevated pressure is shown in Fig. 7.54.

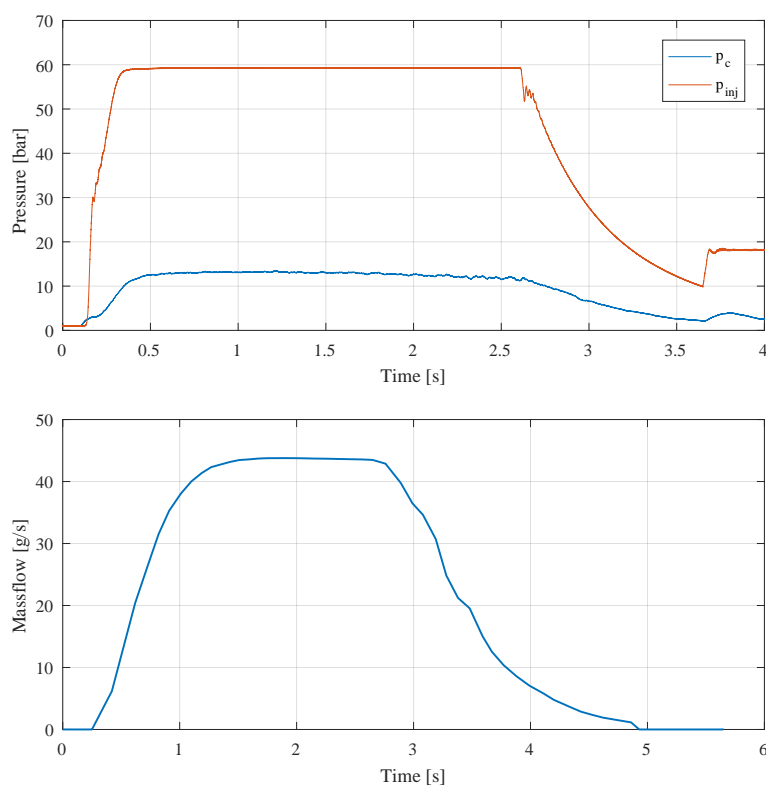


Figure 7.52: Pressure and oxidizer mass flow time traces of Test 04

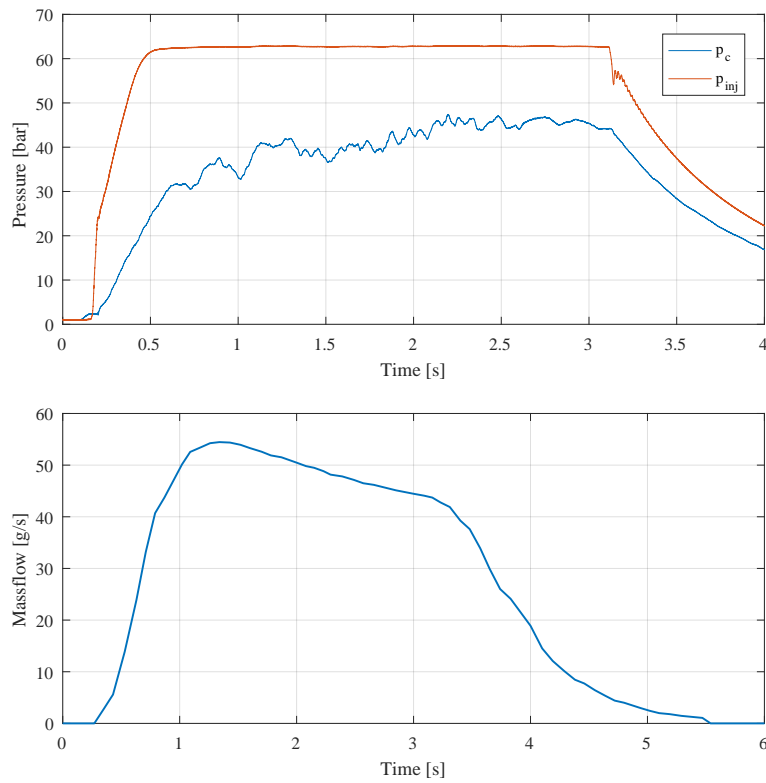


Figure 7.53: Pressure and oxidizer mass flow time traces of Test 01

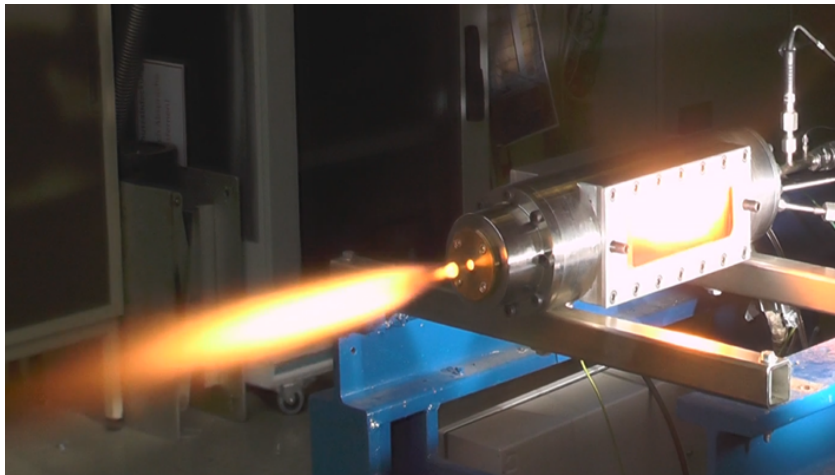


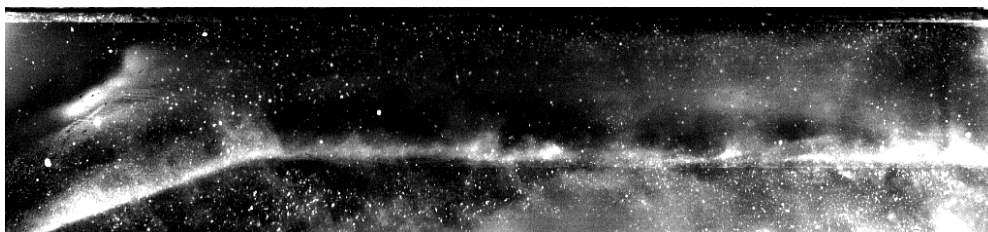
Figure 7.54: Exhaust plume during a high-pressure firing test

As it can be noticed from Fig. 7.52, the pressure and oxidizer mass flow curves of test 04 are steady for about 2 seconds. This allows to perform a steady-state analysis over 1 second, like in the atmospheric test. The start-up transient is quite fast: the pressure reaches the desired value (≈ 12 bar) after about 0.5 second. From the video, it can be seen that the flame takes about

0.28-0.29 seconds to fully develop and ignite the whole fuel slab surface. For what concern the plots of test 01, it can be seen that the pressure requires more time to reach a quasi-steady condition and more low frequency oscillations are present. These oscillations can be due to the presence of unburned fuel being carried downstream and impinging on the nozzle surface. The fuel surface appears to be fully ignited after about 0.27-0.28 seconds and the pressure reaches 30 bar after about 0.6 seconds. During the last second before shut-down, a quasi steady-state combustion seems to take place.

At critical pressure and temperature conditions ($p \approx 6.5$ bar, $T \approx 840$ K), no clear distinction between the liquid and the gas phase of the fuel is expected. The surface tension and the heat of vaporization of the melt layer are getting close to zero [55]. At super-critical conditions in T and p ($p \gtrsim 6.5$ bar, $T \gtrsim 840$ K), it is assumed that no droplets are entrained. On the contrary, the paraffin is expected to diffuse from a small liquid layer above the solid fuel. Moreover, there is the possibility that a pyrolysis layer above the melt layer is created [45].

In the tests at elevated pressures, some droplets can be seen during the ignition phase, when the conditions in the combustion chamber are still sub-critical. However, the number of visible fuel droplets during this initial phase is much lower at elevated pressures than at atmospheric conditions (see Fig. 7.55). This is due to the fact that the size of the droplets is expected to decrease with increasing chamber pressure and that their surface should become indistinct at super-critical pressure conditions [45]. Moreover, due to higher combustion temperatures, the flame is brighter at elevated pressures and, therefore, it becomes more difficult to distinguish the entrained droplets.



(a) Test 203



(b) Test 01

Figure 7.55: Comparison of ignition combustion flames

Numerous intense blowing events ejecting some droplets can be observed during the steady-state burning phase at super-critical pressures. Figures 7.56 and 7.57 show frames taken from the combustion video of test 01, where a blowing event with droplets ejection and a flame burst event can be seen. From the combustion videos, it is also possible to notice that the flame structure along the top of the fuel grain has much more vertical movement at elevated pressures than at atmospheric conditions. On the other side, the flame near the fuel grain and along the sides looks more filament-like.

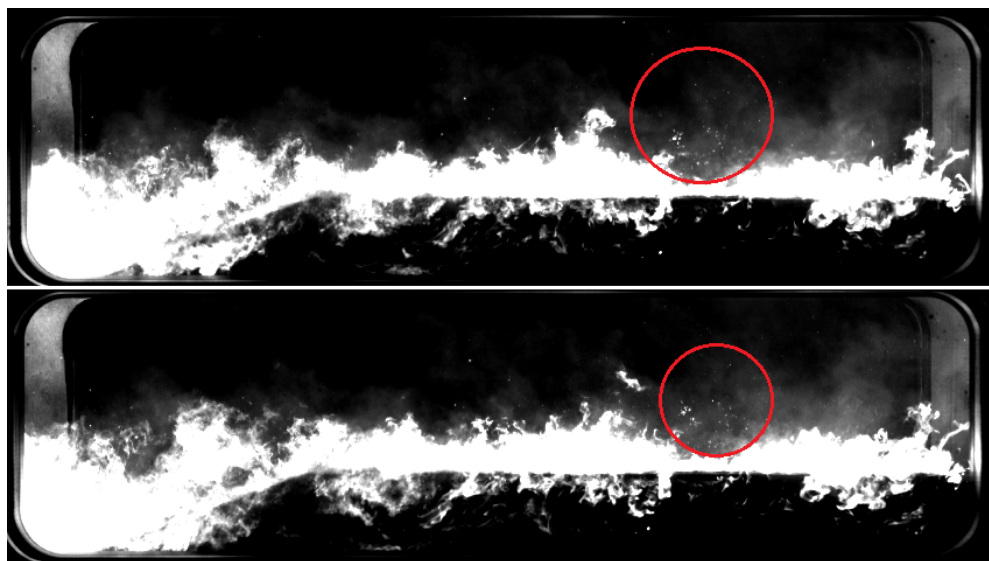


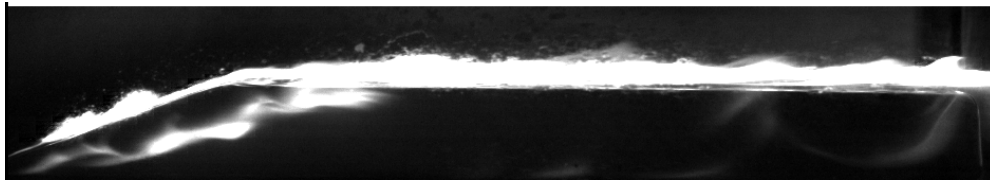
Figure 7.56: Blowing event with droplets ejection from Test 01

As the pressure increases, the flame appears to be much wavier and more turbulent and it extends both above and below the fuel slab. However, in contrast to the atmospheric case, no periodic wave-like structures in the flame can be recognized. As the chamber pressure increases, the Damköhler number (ratio between the characteristic fluid time, or convective mixing time, to the chemical time, or reaction time, of a flame) increases as well, since the chemical reactions become much faster than the fluid dynamics processes. This results in a more diffusion-limited combustion, where more localized reactions and higher temperatures are expected, as well as a thinner flame sheet with smaller turbulent structures (see Fig. 7.58). Moreover, both pressurized tests show unsteady blowing events, which become more intense and frequent as the chamber pressure increases. A higher turbulence level is achieved in the combustion chamber in comparison to the atmospheric pressure test. Oscillations of the instantaneous flame location are also visible. This could be due to localized reactions occurring in regions with a combustible oxidizer to fuel ratio or to pockets of air or gas embedded in the fuel grain that are released in the flow and reacting, thus disturbing the flame sheet. These oscillations seem to be connected to the flame blowing and bursting events,

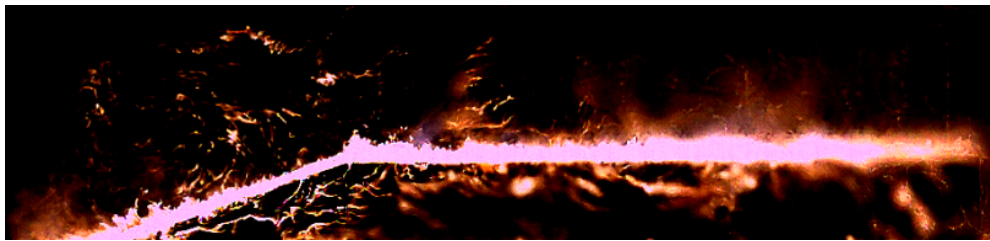


Figure 7.57: Flame bursting event from Test 01

with consequent droplets ejection. Some of the combustion chamber pressure oscillations could also derive from these unsteady phenomena.



(a) Test 203



(b) Test 04

Figure 7.58: Comparison of steady-state combustion flames

Looking at Tab. 7.7, it is possible to see that, for the same oxidizer mass flux, the amount of burned fuel and, consequently, the regression rate considerably increase with increasing chamber pressure. This pressure dependence of the regression rate may be a consequence of operating the motor in a low flux regime, where radiation effects are important. Moreover, as the chamber pressure increases, the flame becomes brighter, especially just before an intense blowing event. The increase in flame luminosity as the chamber pressure rises is consistent with the increase in soot production.

8 Conclusions and Future Developments

8.1 Overview

Hybrid rocket engines have clear advantages compared to solid and liquid systems. In particular, since the propellants are stored in two different states of matter, hybrids are safer than solid motors. This also contributes to reduce the total costs of the engine. Moreover, they are characterized by controllable thrust, including shut off and restart capability. With respect to liquid engines, they are mechanically simpler and, consequently, cheaper. Finally, they have increased performance compared to solids and generally a specific impulse nearly comparable to liquid systems. Unfortunately, because of some drawbacks deriving from their combustion behaviour, hybrid propulsion is still not a mature technology to be used in propulsive systems. However, in recent years, there has been a renewed interest in hybrid rocket engines due to the discovery of the so-called liquefying fuels, which show a regression rate 3-4 times higher than the polymeric fuels conventionally used in this kind of system. This allows to overcome one of the biggest problems of hybrid engines, without losing their simplicity and low cost advantages.

The mechanism responsible for the increased regression rate is the entrainment phenomenon. It consists in the formation of an unstable liquid layer over the fuel surface during the combustion. Due to the Kelvin-Helmholtz instability, the waves appearing on the liquid layer break-up into droplets, which, in turns, gets entrained into the gas flow. The entrainment is an additional burning mechanism that works like a spray injection along the length of the motor. This process increases the effective fuel burning area and reduces the blocking effect given from the pyrolysis of the fuel. Unfortunately, despite many recent researches, the combustion behaviour of this kind of fuels is not yet completely well understood. Until now, no general theoretical model exists for such a problem and the dependence of the entrainment mass transfer on the main influencing parameters needs to be experimentally assessed in every study on a case-by-case basis. In fact, modeling the combustion kinetics of this kind of engines is not an easy task, since it requires the knowledge of complex reactions mechanisms, the simulation of the fuel melt layer formation and its instability mechanism, roll-wave formation, droplets entrainment and combustion. On the other hand, experimental investigation on the hybrid combustion process under real operating conditions is also challenging,

because of high temperature and pressure conditions, which make it impossible to use in-situ diagnostics. For these reasons, combustion visualizations are a viable solution for studying the burning process within the turbulent boundary layer of a hybrid rocket engine under typical operating conditions. Therefore, the present research focuses on the optical study of the combustion behaviour of paraffin-based fuels under varying operating conditions. The final aim is to contribute to the understanding of the entrainment phenomenon and its influence on the regression rate, thus helping with the design of hybrid rocket engines.

8.2 Main Findings of the Study

In order to better understand and characterize the entrainment process, first of all, the Kelvin-Helmholtz instability theory and the liquid layer break-up process, extensively studied in the past, needs to be adapted to typical operating conditions encountered in hybrid engines. In this study, the theoretical models for the stability of stratified gas-liquid flow, already existing in literature, are considered and studied in a 2D domain. The dispersion relation giving the stability criterion for the liquid layer is derived and three different cases are identified, depending on the conditions considered. In this way, the inception criteria and stability limit for the arising of liquid film instabilities and droplets entrainment are found and analyzed. Moreover, the main parameters affecting Kelvin-Helmholtz instability are identified and discussed.

Once the experimental parameters influencing the entrainment mass transfer are determined, the combustion behaviour of different paraffin-based fuels burning with GOX is experimentally investigated with an optical combustion chamber. The burning process is recorded with a high speed camera and the videos are analyzed with two different decomposition algorithms (POD and ICA), which allows to get insights into the main combustion processes. The Proper Orthogonal Decomposition (POD) is able to find the most coherent and energetic structures of the dynamic field. The Independent Component Analysis (ICA) is able to recognize the essential and independent structures characterizing the flow field. In this way, principal and independent components describing the burning process are respectively identified and the most excited frequencies and wavelengths characterizing the fuel melt layer are found. Four main test campaigns are performed with the aim of studying the influence of the previously identified parameters on the liquid layer instability process under real combustion operating conditions.

First, the influence of the fuel configuration is analyzed, since the formation of the liquid waves over the fuel surface and their behaviour are influenced from the presence of a forward-facing step. Fuel slabs with 5° , 20° and 90° forward-facing ramp (FFR) are investigated. From the results it is possible to notice that different frequency and wavelength ranges are excited from different slab angles. Some of them are related to the vortex shedding pro-

duced at the beginning (VS1) and/or at the end (VS2) of the ramp, some to the flapping motion of the shear layer caused by the ejection of a large scale vortex from the recirculation region. Others are connected to the KHI, so to the liquid layer instability mechanism.

Once having identified which waves are connected to the Kelvin-Helmholtz instability process for a particular fuel formulation, the influence of the fuel viscosity and oxidizer mass flow is investigated in two different test campaigns. The results show that the combustion of paraffin-based hybrid rocket fuels is actually dominated by wave-like structures and that their behaviour is strongly influenced by these two parameters. In particular, the higher the viscosity, the lower the values of the excited frequencies and the longer the longitudinal waves. This means that the higher the viscosity, the more stable the liquid layer. Moreover, the values of the excited frequencies become higher as the oxidizer mass flow increases, while the excited longitudinal wavelengths become smaller. Both fuel viscosities show the same trend. For very low mass flows, no distinct wavelength peaks are detected for the paraffin blend fuels. This is due to the fact that at very low oxidizer mass flows the flow speed is below the critical one that is needed to achieve instability. The two fuel formulations have different critical speed, due to their different viscosity values: the critical speed for the pure paraffin is lower than that of the same paraffin with 5% polymer and, consequently, the range of unstable waves is also wider for 6805 with respect to the blend. A comparison of the experimental results with the neutral curves coming from the KHI model is also performed. Here it is clearly shown that all the experimental values for pure paraffin are in the unstable region. On the other hand, for the paraffin with 5% polymer the experimental values connected to the lower mass flows ($\dot{m}_{Ox} \approx 10\text{-}20$ g/s) are below the neutral curve and, consequently, in the stable zone.

The finding of a dependence of the Kelvin-Helmholtz wave characteristics on the oxidizer mass flow and fuel viscosity brought to the demonstration that the droplets entrainment rate, which partly controls the fuel regression rate, is directly connected to the liquid layer instability process. In particular, the higher the frequencies and the shorter the waves, the higher the regression rate. This is in agreement with what is predicted by the entrainment theory. For higher mass fluxes the liquid layer is characterized by higher frequencies and smaller longitudinal wavelengths. This means that it is more unstable (due to the higher shear stresses produced by the high speed flow) and more droplets are released from the unstable waves and entrained into the gas flow. Consequently, much more fuel can be transported into the flame zone before being totally vaporized and the blocking effect of the convective heat transfer is reduced, thus increasing the regression rate. Moreover, these results also show that the regression rate decreases as the viscosity increases, which once more confirms the previous results and the entrainment theory.

Until now, all the tests are performed at atmospheric pressures, therefore the influence of the chamber pressure on the combustion is not yet inves-

tigated. Thus, the aim of the last test campaign is to study the influence of higher combustion pressures on the liquid layer instability process. The experimental set-up is upgraded with an optical combustion chamber able to stand pressures up to 50 bar. A range of operating pressures, spanning from sub-critical to super-critical (above approximately 6.5 bar), is investigated and the results are qualitatively compared. It is observed that, at these low mass flux regimes, the combustion behaviour is strongly affected by the operating pressure. The pressurized combustion test visualizations all show unsteady phenomena, which cause unsteadiness also in the flame. At elevated pressures, the whole combustion process is characterized by flame bursting and blowing events, with consequent droplets ejection. These phenomena seem to represent the main mass transfer mechanism at super-critical pressures. As the pressure increases from sub-critical to super-critical conditions, the ignition transient becomes faster, but not much difference is found in the ignition delay between the tests conducted at super-critical pressures. The amount of burned fuel and, consequently, the regression rate are also greatly affected by the operating pressure: the higher the pressure, the faster the fuel burns. This pressure dependence of the regression rate may be a consequence of operating the motor in a low flux regime, where radiation effects are important.

To the author's knowledge, this is the first case in literature that proved the connection between the Kelvin-Helmholtz instability mechanism and the entrainment in paraffin-based hybrid rocket engines, by means of optical investigations on combustion tests. Although the stability of liquid layers has been extensively studied in the past [18], [14], [67], even under strong blowing conditions [25], [68], [38], the behaviour of films under real combustion conditions has not been explored yet. The presented work confirms and extends the results of the linear stability theory for a liquid film postulated by Karabeyoglu et al. [43], [44], which led to a general empirical expression for the entrainment rate of liquid droplets in terms of the relevant properties of the hybrid motor (i.e. mass flux, liquid layer thickness, surface tension and liquid viscosity). In fact, in the framework of this research, a direct dependency of the droplets entrainment rate, which partially influences the regression rate, on the liquid layer instability mechanism and on the combustive flow properties has been found, for every analysed liquid fuel viscosity and oxidizer mass flow. This means that it is possible to directly control the fuel regression rate by triggering precise frequencies and wavelengths of the liquid layer. The stability limit for the onset of the Kelvin-Helmholtz instability process and the inception criteria for the entrainment mechanism have also been found for the analyzed fuel compositions and oxidizer mass flows. Moreover, a complete flame characterization for different fuel formulations at varying operating conditions has been performed. Finally, the influence of the chamber pressure on the liquid layer stability and, consequently, on the entrainment process has been investigated. It was observed that, at super-

critical chamber pressures (above approximately 6.5 bar), the primary mass transfer mechanism is not dominated by entrainment of fuel droplets or filament structures, but by intermittent intense blowing events with consequent droplets ejection into the boundary layer.

8.3 Outlook

For the future, it would be interesting to use other optical techniques, like Schlieren or Shadowgraph imaging, in order to try to visualize the actual liquid layer over the fuel surface and its waves. In this way, the connection between the waves appearing on the flame surface and the liquid layer instability process could be better understood. Moreover, other data analysis techniques could be used to obtain further information from the huge amount of data accumulated during this research. For example, unsupervised as well as supervised learning techniques could be developed in order to get deeper insights into the hybrid combustion process. Typical Kelvin-Helmholtz waves, as well as liquid fuel droplets with their size and number, can be automatically detected with such methods. Also, the point in time and space where these phenomena appears during the combustion can be identified. Such a feature would be really useful in order to understand if these phenomena are particularly connected to other events or conditions in the combustion chamber. Finally, further tests at super-critical pressure conditions would be necessary to better characterize the dependence of the entrainment mechanism from the chamber pressure.

Bibliography

- [1] M. Adachi and T. Shimada. Liquid films instability analysis of liquefying hybrid rocket fuels under supercritical conditions. *AIAA Journal*, Vol. 53(No. 6):pp. 1578–1589, 2015.
- [2] M. Arienti, M. Corn, G. S. Hagen, R. K. Madabhushi, and M. C. Soteriou. Proper orthogonal decomposition applied to liquid jet dynamics. In *21st Annual Conference on Liquid Atomization and Spray Systems*, 2008.
- [3] B. J. Bayly, S. A. Orszag, and T. Herbert. Instability mechanisms in shear-flow transition. *Annual Review of Fluid Mechanics*, 20(1):359–391, January 1988.
- [4] M. Bestehorn. *Hydrodynamik und Strukturbildung*. Springer Berlin Heidelberg, 2006.
- [5] E. Bingham and A. Hyvarinen. A fast fixed-point algorithm for independent component analysis of complex valued signals. *International Journal of Neural Systems*, 10(01):1–8, February 2000.
- [6] K. Bizon, G. Continillo, S. Lombardi, E. Mancaruso, and B.M. Vaglieco. Spatial and temporal independent component analysis of flame dynamics in diesel engine. In *XXXVI Meeting of the Italian Section of the Combustion Institute*, June 2013.
- [7] K. Bizon, G. Continillo, E. Mancaruso, S.S. Merola, and B.M. Vaglieco. Pod-based analysis of combustion images in optically accessible engines. *Combustion and Flame*, 157(4):632–640, April 2010.
- [8] K. Bizon, S. Lombardi, G. Continillo, E. Mancaruso, and B. M. Vaglieco. Analysis of diesel engine combustion using imaging and independent component analysis. *Proceedings of the Combustion Institute*, 34(2):2921–2931, January 2013.
- [9] A. Cammilleri, F. Gueniat, J. Carlier, L. Pastur, E. Memin, F. Lusseyran, and G. Artana. POD-spectral decomposition for fluid flow analysis and model reduction. *Theoretical and Computational Fluid Dynamics*, 27(6):787–815, February 2013.
- [10] B. J. Cantwell. Aa283 aircraft and rocket propulsion. Chapter 11, Department of Aeronautics and Astronautics, Stanford University, 2007.

- [11] C. Carmicino. Acoustics, vortex shedding, and low-frequency dynamics interaction in an unstable hybrid rocket. *Journal of Propulsion and Power*, 25(6):1322–1335, November 2009.
- [12] A. A. Chandler, E. T. Jens, B. J. Cantwell, and G. S. Hubbard. Visualization of the liquid layer combustion of paraffin fuel at elevated pressures. In *63rd International Astronautical Congress*, 2012.
- [13] A. A. Chandler, E. T. Jens, B. J. Cantwell, and G. S. Hubbard. Visualization of the liquid layer combustion of paraffin fuel for hybrid rocket applications. In *48th AIAA/ASME/SAE/ASEE Joint Propulsion Conference and Exhibit*. American Institute of Aeronautics and Astronautics, July 2012.
- [14] I.-D. Chang and P. E. Russel. Stability of a liquid layer adjacent to a high-speed gas stream. *Physics of Fluids*, Vol. 8, No. 6:pp. 1018–1026, 1965.
- [15] A. Chatterjee. *An introduction to the proper orthogonal decomposition*, 2000.
- [16] M. J. Chiaverini and K. K. Kuo. *Fundamentals of Hybrid Rocket Combustion and Propulsion*, volume Vol. 218 of *Progress in Astronautics and Aeronautics*. American Institute of Aeronautics and Astronautics, Inc., 2007.
- [17] H. K. Ciezki, J. Sender, W. Clau-oslash, A. Feinauer, and A. Thumann. Combustion of solid-fuel slabs containing boron particles in step combustor. *Journal of Propulsion and Power*, 19(6):1180–1191, November 2003.
- [18] A. D. D. Craik. Wind generated waves in thin liquid films. *Journal of Fluid Mechanics*, Vol. 26, Pt.2:pp. 369–392, 1966.
- [19] R. Humble D. Altman. *Hybrid Rocket Propulsion Systems*. McGraw-Hill, 1995.
- [20] L. T. DeLuca, L. Galfetti, F. Maggi, G. Colombo, C. Paravan, A. Reina, P. Tadini, A. Sossi, and E. Duranti. An optical time-resolved technique of solid fuels burning for hybrid rocket propulsion. In *47th AIAA/ASME/SAE/ASEE Joint Propulsion Conference and Exhibit*. American Institute of Aeronautics and Astronautics, July 2011.
- [21] K. Devriendt, H. Van Hook, B. Ceursters, and J. Petters. *Chem. Phys. Lett.*, 261:450–456, 1996.
- [22] S. Dodel, J. M. Herrmann, and T. Geisel. Comparison of temporal and spatial ica in fmri data analysis. *Proceedings of ICA 2000*, 2000.

- [23] T. Funada and D. D. Joseph. Viscous potential flow analysis of kelvin-helmholtz instability in a channel. *Journal of Fluid Mechanics*, 445, October 2001.
- [24] L. Galfetti, L. Merotto, M. Boiocchi, F. Maggi, and L. T. DeLuca. Experimental investigation of paraffin-based fuels for hybrid rocket propulsion. *Progress in Propulsion Physics*, Vol. 4:pp. 59–74, 2013.
- [25] R. A. Gater and M. R. L’Ecuyer. A fundamental investigation of the phenomena that characterize liquid film cooling. *International Journal of Heat and Mass Transfer*, Vol. 13, No. 3:pp. 1925–1939, 1970.
- [26] P. Geladi and B. R. Kowalski. Partial least-squares regression: a tutorial. *Analytica Chimica Acta*, 185:1–17, 1986.
- [27] S. Gordon and B. J. McBride. Computer program for calculation of complex chemical equilibrium compositions and applications. techreport NASA Reference Publication 1311, NASA, October 1994.
- [28] S. Gordon and B. J. McBride. Computer program for calculation of complex chemical equilibrium compositions and applications. techreport NASA Reference Publication 1311, NASA, June 1996.
- [29] T. J. Hanratty and A. Hershman. Initiation of roll waves. *AIChE Journal*, Vol. 7(No. 3):pp. 488–497, 1961.
- [30] E. Hinch. A note on the mechanism of the instability at the interface between two shearing fluids. *Journal of Fluid Mechanics*, Vol. 144:pp. 463–465, 1984.
- [31] A. P. Hooper. Longwave instability at the interface between two viscous fluids: Thin layer effects. *Physics of Fluids*, Vol. 28, 1985.
- [32] A. P. Hooper and W. G. Boyd. Shear flow instability due to a wall and a viscosity discontinuity at the interface. *Journal of Fluid Mechanics*, Vol. 179:pp. 201–225, 1987.
- [33] P. Hoyer and A. Hyvärinen. Independent component analysis applied to feature extraction from colour and stereo images. *Network: Computation in Neural Systems*, 11(3):191–210, January 2000.
- [34] A. Hyvarinen. One-unit contrast functions for independent component analysis: a statistical analysis. *Neural Networks for Signal Processing VII. Proceedings of the 1997 IEEE Workshop*, 1997.
- [35] A. Hyvarinen. Fast and robust fixed-point algorithms for independent component analysis. *IEEE Trans. on Neural Networks*, 10(3):626–634, May 1999.

- [36] A. Hyvarinen. The fixed-point algorithm and maximum likelihood estimation for independent component analysis. *Neural Processing Letters*, 10:1–5, 1999.
- [37] A. Hyvarinen and E. Oja. Independent component analysis: algorithms and applications. *Neural Networks*, 13(4-5):411–430, June 2000.
- [38] M. Ishii and M. A. Grolmes. Inception criteria for droplet entrainment in two-phase concurrent film flow. *AIChE Journal*, 21(2):308–318, March 1975.
- [39] E. T. Jens, A. A. Chandler, B. Cantwell, G. S. Hubbard, and F. Mechen-
tel. Combustion visualization of paraffin-based hybrid rocket fuel at el-
evated pressures. In *50th AIAA/ASME/SAE/ASEE Joint Propulsion
Conference*. American Institute of Aeronautics and Astronautics, July
2014.
- [40] Elizabeth T. Jens, Victor A. Miller, and Brian J. Cantwell. Schlieren and
oh* chemiluminescence imaging of combustion in a turbulent boundary
layer over a solid fuel. *Experiments in Fluids*, 57(3), February 2016.
- [41] Elizabeth T. Jens, Victor A. Miller, Flora S. Mechentel, Brian J.
Cantwell, and Scott Hubbard. A visual study of the combustion
of high-regression rate and classical hybrid rocket fuels. In *51st
AIAA/SAE/ASEE Joint Propulsion Conference*. American Institute of
Aeronautics and Astronautics, July 2015.
- [42] Elizabeth T. Jens, Pavan Narsai, Brian Cantwell, and G. Scott Hubbard.
Schlieren imaging of the combustion of classical and high regression rate
hybrid rocket fuels. In *50th AIAA/ASME/SAE/ASEE Joint Propulsion
Conference*. American Institute of Aeronautics and Astronautics, July
2014.
- [43] A. Karabeyoglu, D. Altman, and B. J. Cantwell. Combustion of lique-
fying hybrid propellants: Part 1, general theory. *Journal of Propulsion
and Power*, Vol.18(No. 3):610–620, May 2002.
- [44] A. Karabeyoglu and B. J. Cantwell. Combustion of liquefying hybrid
propellants: Part 2, stability of liquid films. *Journal of Propulsion and
Power*, Vol. 18(No. 3):621–630, May 2002.
- [45] A. Karabeyoglu, Brian J. Cantwell, and Jose Stevens. Evaluation of
homologous series of normal-alkanes as hybrid rocket fuels. In *41st
AIAA/ASME/ASEE Joint Propulsion Conference*, July 2005.
- [46] A. Karabeyoglu, J. Stevens, D. Geyzel, B. Cantwell, and
D. Micheletti. High performance hybrid upper stage motor. In
*47th AIAA/ASME/SAE/ASEE Joint Propulsion Conference and
Exhibit*. American Institute of Aeronautics and Astronautics, July 2011.

- [47] G. Kerschen, J.-C. Golinval, A. F. Vakakis, and L. A. Bergman. The method of proper orthogonal decomposition for dynamical characterization and order reduction of mechanical systems: An overview. *Nonlinear Dynamics*, 41(1-3):147–169, August 2005.
- [48] M. Kobald. *Combustion Phenomena of Advanced Hybrid Rocket Fuels*. PhD thesis, Institute of Space System - University of Stuttgart German Aerospace Center (DLR), 2016.
- [49] M. Kobald, H. K. Ciezki, and S. Schleichtriem. Optical investigation of the combustion process in paraffin-based hybrid rocket fuels. In *49th AIAA/ASME/SAE/ASEE Joint Propulsion Conference*. American Institute of Aeronautics and Astronautics, July 2013.
- [50] M. Kobald, A. Petrarolo, and S. Schleichtriem. Combustion visualization and characterization of liquefying hybrid rocket fuels. In *51st AIAA/SAE/ASEE Joint Propulsion Conference*. American Institute of Aeronautics and Astronautics, July 2015.
- [51] M. Kobald and S. Schleichtriem. Investigation of different hybrid rocket fuels in a 2d slab burner with optical techniques. In *Tenth International Conference on Flow Dynamics*, 2013.
- [52] M. Kobald, C. Schmierer, H. K. Ciezki, S. Schleichtriem, E. Toson, and L. T. DeLuca. Viscosity and regression rate of liquefying hybrid rocket fuels. *Journal of Propulsion and Power*, Vol. 33(No. 5):1–7, March 2017.
- [53] M. Kobald, E. Toson, H. Ciezki, S. Schleichtriem, S. di Betta, M. Coppola, and L. T. DeLuca. Rheological, optical, and ballistic investigations of paraffin-based fuels for hybrid rocket propulsion using a two-dimensional slab-burner. *EUCASS Proceedings Series - Advances in AeroSpace Sciences*, Vol. 8:pp. 263–282, 2016.
- [54] M. Kobald, I. Verri, and S. Schleichtriem. Theoretical and experimental analysis of liquid layer instability in hybrid rocket engines. *CEAS Space Journal*, 7(1):11–22, January 2015.
- [55] G. M. Kontogeorgis and D. P. Tassios. Critical constants and acentric factors for long-chain alkanes suitable for corresponding states applications. a critical review. *Chemical Engineering Journal*, Vol. 66:pp. 35–49, 1997.
- [56] J. Kostas, J. Soria, and M. S. Chong. A comparison between snapshot pod analysis of piv velocity and vorticity data. *Experiments in Fluids*, 38(2):146–160, January 2005.
- [57] K. Kuo and R. Houim. Theoretical modeling and numerical simulation challenges of combustion processes of hybrid rockets. In *47th*

- AIAA/ASME/SAE/ASEE Joint Propulsion Conference and Exhibit*. American Institute of Aeronautics and Astronautics, July 2011.
- [58] S. S. Kutaleladze. Elements of the hydrodynamics of gas-liquid system. *Fluid Mechanic-Soviet Research*, Vol. 1 (4)(29), 1972.
- [59] D. Luenberger. *Optimization by Vector Space Methods*. Wiley, 1969.
- [60] J. J. Marano and G. D. Holder. A general equation for correlating the thermophysical properties of n-paraffins, n-olefins, and other homologous series. 3. asymptotic behavior correlations for thermal and transport properties. *Industrial and Engineering Chemistry Research*, 36(6):2399–2408, June 1997.
- [61] J. J. Marano and G. D. Holder. General equation for correlating the thermophysical properties of n-paraffins, n-olefins, and other homologous series. 1. formalism for developing asymptotic behavior correlations. *Industrial and Engineering Chemistry Research*, 36(5):1887–1894, May 1997.
- [62] J. J. Marano and G. D. Holder. General equation for correlating the thermophysical properties of n-paraffins, n-olefins, and other homologous series. 2. asymptotic behavior correlations for pvt properties. *Industrial and Engineering Chemistry Research*, 36(5):1895–1907, May 1997.
- [63] G. Marxman and M. Gilbert. Turbulent boundary layer combustion in the hybrid rocket. In *9th Symposium (International) on Combustion*, pages 371–383. Elsevier, 1963.
- [64] G. Marxman, R. Muzzy, and C. Wooldridge. Fundamentals of hybrid boundary layer combustion. In *Heterogeneous Combustion Conference*. American Institute of Aeronautics and Astronautics, December 1963.
- [65] L. Merotto, M. Boiocchi, A. Mazzetti, F. Maggi, L. Galfetti, and L.T. DeLuca. Characterization of a family of paraffin-based solid fuels. In *4th European Conference for Aerospace Sciences (EUCASS)*, 2011.
- [66] I. Nakagawa and S. Hikone. Study on the regression rate of paraffin-based hybrid rocket fuels. *Journal of Propulsion and Power*, Vol.27(No.6):1276–1279, November 2011.
- [67] A. H. Nayfeh and W. S. Saric. Non-linear kelvin-helmholtz instability. *Journal of Fluid Mechanics*, Vol. 46, Pt. 2:pp. 209–231, 1971.
- [68] R. I. Nigmatulin, B. I. Nigmatulin, Y. D. Khodzhaev, and V. E. Kroshilin. Entrainment and deposition rates in a dispersed-film flow. *International Journal of Multiphase Flow*, Vol. 22, No. 1:pp. 19–30, 1996.

- [69] N. Pelletier. *Etude des Phenomenes de Combustion dans un Propulseur Hybride. Modelisation et Analyse Experimentale de la Regression des Combustibles Liquefiables*. PhD thesis, Institut Supérieur de L'Aeronatique et de L'Espace, Toulouse, 2009.
- [70] A. Petrarolo and M. Kobald. Evaluation techniques for optical analysis of hybrid rocket propulsion. *Journal of Fluid Science and Technology*, 11(4):JFST0028–JFST0028, 2016.
- [71] A. Petrarolo, M. Kobald, and S. Schlechtriem. Optical analysis of hybrid rocket combustion with decomposition methods. In *Space Propulsion Conference*, May 2016.
- [72] H. Risvik. *Principal Component Analysis (PCA) & NIPALS algorithm*, 2007.
- [73] R. W. Schefer. Flame sheet imaging using CH chemiluminescence. *Combustion Science and Technology*, 126(1-6):255–279, July 1997.
- [74] R. W. Schefer. Flame sheet imaging using ch chemiluminescence. *Combustion Science and Technology*, 126: 1-6:255–279, 2010.
- [75] M. Sherry, D. Lo Jacono, and J. Sheridan. An experimental investigation of the recirculation zone formed downstream of a forward facing step. *Journal of Wind Engineering and Industrial Aerodynamics*, 98(12):888–894, December 2010.
- [76] J. V. Stone. Independent component analysis. *Encyclopedia of Statistics in Behavioral Science*, 2:907–912, October 2005.
- [77] A. Thumann and H. K. Ciezki. *Combustion of Energetic Materials, chap. Comparison of PIV and Colour-Schlieren Measurements of the Combustion Process of Boron Particle Containing Solid Fuel Slabs in a Rearward Facing Step Combustor*, volume Vol. 5, pp. 742-752. Begell House Inc., 2002.
- [78] J. J. van Rossum. Experimental investigations of horizontal liquid films. *Chemical Engineering Science*, Vol. 11(No. 35), 1959.
- [79] Y. Wada, Y. Kawabata, T. Itagaki, K. Seki, R. Kato, N. Kato, and K. Hori. Observation of combustion behavior of low melting temperature fuel for hybrid rocket using double slab motor. In *10th International Symposium on Special Topics in Chemical Propulsion*, June 2014.
- [80] D. E. Woodmansee and T. J. Hanratty. Mechanism for the removal of droplets from a liquid surface by parallel air flow. *Chem. Eng. Sci.*, Vol. 24:pp. 299–307, 1969.

- [81] Chia-Shun Yih. Instability due to viscosity stratification. *Journal of Fluid Mechanics*, Vol. 27:pp. 337–352, 1967.
- [82] L. Ya. Zhivaikin. Liquid film thickness in film-type units. *International Journal of Chemical Engineering*, Vol. 2 (3)(337), 1962.

A Appendix

A Sensors and Measurement Devices List

Photron Fastcam high-speed cameras:

Two different cameras have been used to record the high-speed combustion videos. Their specifications are listed in Tab. A.1.

Table A.1: Photron Fastcams specifications

	SA 1.1	SA-X2
Sensor	12 bit CMOS-sensor monochrome	12-bit ADC Bayer system color
Pixel size	20 μm	20 μm
Sensitivity	ISO 12232	ISO 12232 Ssat
Frame rate	60-5400 fps (complete) up to 675000 fps (partial)	up to 1080000 fps
Max. resolution	1024x1024 pixel	1024x1024 pixel
Shutter	global shutter up to 1 μs	global electronic shutter up to 1 μs
Memory	32 GB	128 GB
Recording time	21.84 s at 1000 images/s	87.375 s at 1000 images/s
Trigger	TTL or normally open contact, positive or negative edge	selectable positive or negative TTL 5Vp-p or switch closure
Interface	Gigabit Ethernet	High-speed Gigabit Ethernet
Software	Photron Fastcam Viewer	Photron Fastcam Viewer

Pressure sensors:

Tables A.2 and A.3 summarize the pressure sensors used in the test campaigns for the atmospheric and pressurized combustion chambers. The calibration of each sensor was done at the DLR Lampoldshausen according to the DLR norms and specifications.

Table A.2: Pressure sensors used in the atmospheric optical combustion chamber set-up

Channel	Type	Manufacturer	Position	Range
1	P913-G003	Schaevitz	Igniter GH ₂	0 - 100 bar
2	P913-G003	Schaevitz	Igniter GOX	0 - 100 bar
3	4043 A100	Kistler	Control valve GOX	0 - 100 bar
4	4045 A5	Kistler	Combustion chamber	0 - 5 bar
5	4043 A100	Kistler	Igniter	0 - 100 bar

Table A.3: Pressure sensors used in the pressurized optical combustion chamber set-up

Channel	Type	Manufacturer	Position	Range
1	P913-G003	Schaevitz	Igniter GH ₂	0 - 100 bar
2	P913-G003	Schaevitz	Igniter GOX	0 - 100 bar
3	4910953	Kistler	Control valve GOX	0 - 100 bar
4	1059528	STS	Igniter	0 - 50 bar
7	4910957	Kistler	Injector	0 - 100 bar
8	1059529	STS	Combustion chamber	0 - 50 bar

Thermocouples:

Standardize thermocouples Type K have been used for the temperature measurements in the tests. Their accuracy is given by the manufacturer. No special calibration was used for them since they were used mostly to monitor the operating conditions of the test bench.

Oxygen mass flow meter:

An Emerson Coriolis sensor CMF 050 is installed in the test bench M11.3 and measures the GOX oxidizer mass flow. The following details are given by the manufacturer (see Tab. A.4):

Table A.4: Coriolis mass flow meter specifications

Accuracy (for gaseous media)	$\pm 0.35\%$ of the measure
Reproducibility (for gaseous media)	$\pm 0.35\%$ of the measure
Zero point stability	0.163 kg/h

Rheometer:

A Haake RS6000 rotational rheometer has been used to measure the viscosity of the paraffin-based samples. A cone-plate (with different cone angles and radii) or plate-plate geometry are available for the user. All sensor cones are individually calibrated by the Thermo Fisher Scientific. The cone geometry used in this work is the C35/2 Ti L, whose parameters are reported in Fig. A.1. The measuring range of the used sensor is reported in Fig. A.2.

Tensiometer:

A K20 Krüss EasyDyne tensiometer was used to measure the surface tension and the liquid density of the paraffin mixtures. The surface tension measurements have been done using the Wilhelmy plate method, where the force acting on an immersed plate is measured (see Fig. A.3). When a vertically suspended plate touches a liquid surface, a force F , which correlates with the surface tension σ and with the contact angle θ according to the following equation, acts on this plate:

$$\sigma = \frac{F}{L \cdot \cos\theta} \quad (\text{A.1})$$

where the wetted length L of the plate is equal to its perimeter. The force F is measured through a force sensor attached to the plate. Platinum is chosen as the plate material as it is chemically inert and easy to clean. Moreover, it can be optimally wetted on account of its very high surface free energy and therefore generally forms a contact angle θ of 0° ($\cos\theta = 1$) with liquids. The variable σ can be directly calculated from the measured force F .

The liquid density measurements have been done using the buoyancy of a probe immersed in the sample. The specifications of the instrument can be found in Tab. A.5.

Thermal analyzer:

The simultaneous thermal analyzer NETZSCH STA 449 F3 Jupiter allows to simultaneously perform Thermogravimetry (TGA) and Differential Scanning

Cone-Plate measuring geometries with 2° Angle

Measuring geometries	C20/2 Ti L	C35/2 Ti L	C60/2 Ti L
Cone Order No.	222-1876	222-1871	222-1867
Inertia I (kg m ²)E-6	-	1.5	15
Material:	Titan		
Radius R _i (mm) *	10.0	17.5	30.0
± delta R _i (mm)	0.01		
Cone angle (Deg) *	2		
Distance a (mm)	0.104		
Measuring plate steel	Standard Ø 60 mm		
Measuring plate location	222-1893	222-1892	222-1891
Material: Steel, Din No.	1.4841		
Radius R _a (mm)	10.5	18.0	30.5
± delta R _a (mm)	0.025		
Sample volume (cm ³)	0.08	0.40	2.00
perm.temperature max. (°C)	350		
Calculation factors			
A (Pa/Nm) *	477500	89090	17680
± delta A (%)	0.6	0.2	0.1
M (s ⁻¹ /rad s ⁻¹) *	28.65		
± delta M (%)	3		

* The exact values are specified on the individual certificate.

Figure A.1: Cone-plate geometry parameters given by the manufacturer

Calorimetry (DSC) to the same sample in the same machine and to measure the thermal properties of the fuel samples. The use of various furnaces allows to cover the required temperature range. Through the vacuum tight design, measurements at defined atmospheres (e.g. inert) are possible. The system is controlled by a newly developed integrated digital electronic device. A sketch of the instrument can be seen in Fig. A.4.

The technical specification of the instruments can be found in Tab. A.6.

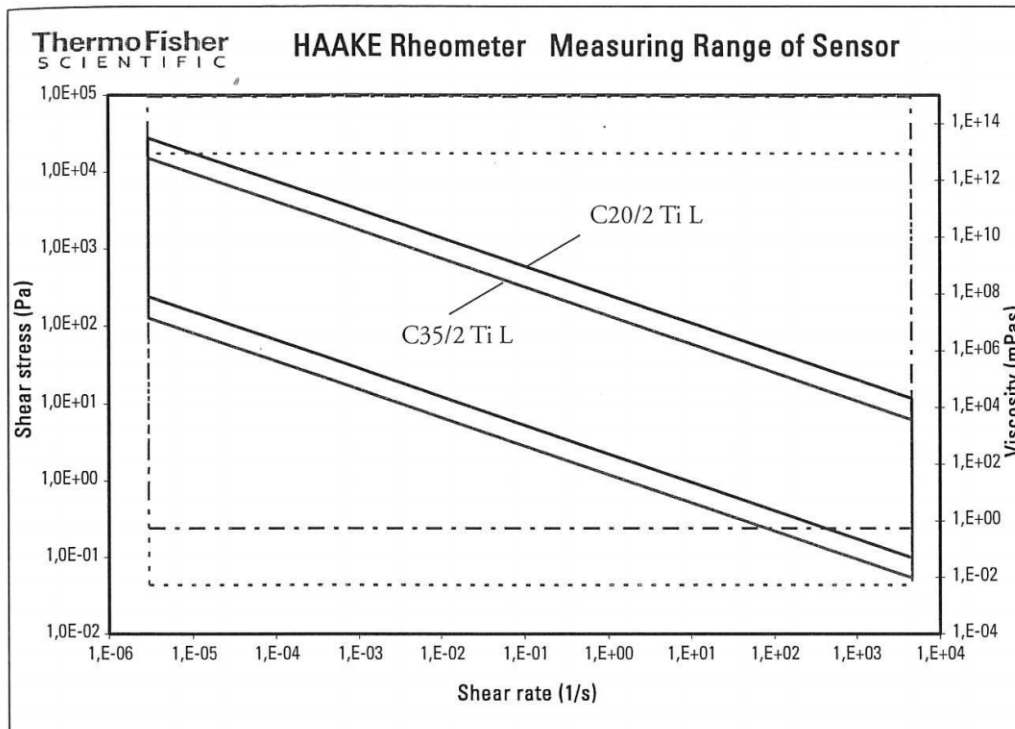


Figure A.2: Measuring range of sensor given by the manufacturer

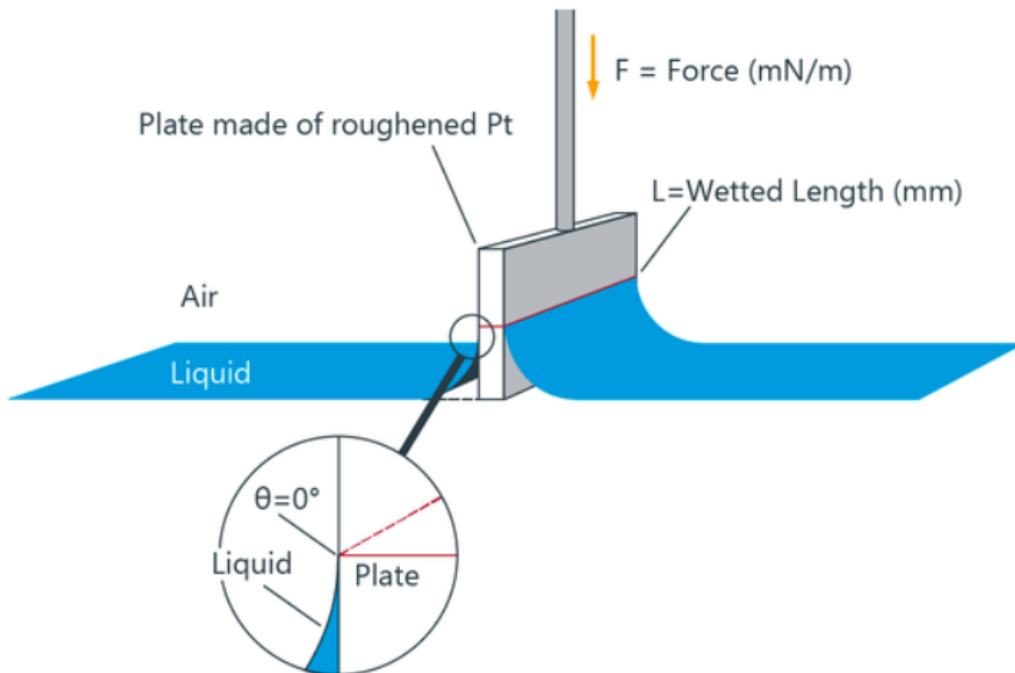


Figure A.3: Schematic diagram of the Wilhelmy plate method

Table A.5: Tensiometer specifications

Force Measurements	Maximum load	50 g
	Resolution	100 μg
	Precision	100 μg
	Measurement rate	5 Hz
Sample stage	Travel distance	90 mm
	Travel speed	2.4 to 14 mm/min
	Type of motor	DC motor
	Thermostated jacket	70 mm
Surface tension	Range	1 to 999 mN/m
	Resolution	0.1 mN/m
Liquid density	Range	1 to 2200 kg/m^3
	Resolution	1 kg/m^3
	Precision	$\pm 3 \text{ kg}/\text{m}^3$

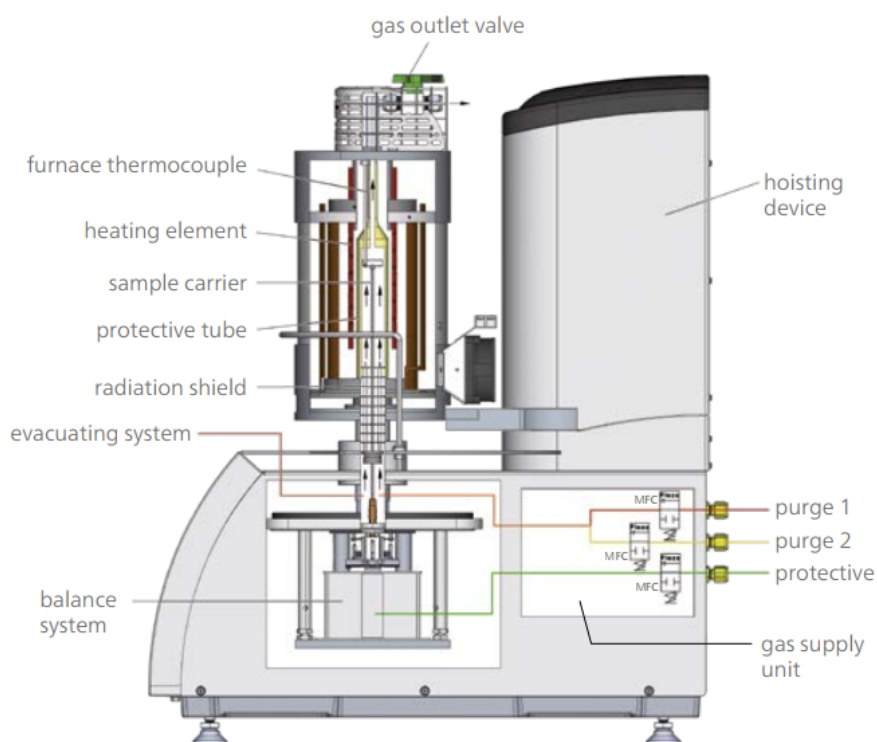


Figure A.4: Sketch of the thermal analyzer used in the framework of this work

Table A.6: Thermal analyzer specifications

Design	Top-loading
Temperature range	-150 °C to 2400 °C
Furnace	Silver, Copper, Steel, Platinum, Silicon Carbide, Rhodium, Graphite, Water vapour, High-speed, Tungsten
Heating rate	0.001 to 50 K/min (furnace-dependent) High-speed furnace: up to 1000 K/min
Sensors	TGA, TGA-DTA, TGA-DSC
Vacuum-tight	10^{-4} mbar
Atmospheres	Inert, oxidizing, static, dynamic, vacuum
Temperature resolution	0.001 K
Balance resolution	0.1 μg (over the entire weighing range)
Balance drift	< 5 $\mu\text{g}/\text{hour}$
Maximum sample load	35000 mg (incl. crucible)
Sample volume (max.)	TGA: up to 5 ml DSC: 0.19 ml DTA: 0.9 ml
DSC enthalpy accuracy	$\pm 2\%$

Acknowledgements

This research has been carried out at the German Aerospace Center (DLR), Institute of Space Propulsion in Lampoldshausen, in the Propellants Department. First, I would like to thank the head of the Institute, Prof. Dr.-Ing. Stefan Schleichriem, for the supervision of this work and for his useful suggestions in these years. I would also like to express my gratitude to the head of the department, Dr.-Ing. Helmut Ciezki, who gave me the opportunity to conduct this research and offered his support to the experimental work. A special thank goes to my supervisor, Dr.-Ing. Mario Kobald, for his motivation and support during all the time of this research. I would also like to thank all the persons who supported the presented work in several manners, especially the students who contributed to this work and all the colleagues who helped me in these years. Thank you for the stimulating discussions and the fun we had working together. The support of all the M11 team and the chemical laboratory is also greatly acknowledged. I will not forget to thank all the people inside and outside DLR who contributed to make this experience so unforgettable. Thank you for making me feel like home, even so far away from my place! I would also like to thank all the people who trusted and supported me and my work in all these years.

This work was partially funded by the DLR project ATEK (Antriebstechnologien und Komponenten fuer Traegersysteme: Propulsion Technologies and Components for Launcher Systems). Further funding was gratefully provided by internal resources for fundamental research of the DLR Lampoldshausen.

Curriculum Vitae

PERSONAL INFORMATION	Anna Petrarolo  anna.petrarolo@dlr.de Date of birth 2 May 1989 Nationality Italian
WORK EXPERIENCE	<hr/> Oct 2014–Present Research engineer German Aerospace Center (DLR), Institute of Space Propulsion, Hardthausen (Germany) Optical investigations on combustion processes, fuel production and characterization, research on novel fuel formulations, hybrid rocket engines testing
EDUCATION AND TRAINING	<hr/> Oct 2014–Present Doctor in Engineering Sciences (Dr.-Ing.) German Aerospace Center (DLR), Institute of Space Propulsion, Hardthausen (Germany) Optical investigations on the liquid layer instabilities of paraffin-based hybrid rocket engines Sep 2011–Apr 2014 Master of Science in Aeronautical Engineering (Specialization: Propulsion). Score: 110/110 Politecnico di Milano Thesis: "Ballistics, Performance and Stability Analysis of a Flight Hybrid Rocket Engine", conducted at German Aerospace Center (DLR), Institute of Space Propulsion, Hardthausen, Germany Sep 2008–Sep 2011 Bachelor in Aerospace Engineering. Score: 105/110 Politecnico di Milano Sep 2003–Jul 2008 High School Degree. Score: 100/100 Liceo Scientifico Dante Alighieri, Matera
ADDITIONAL INFORMATION	<hr/> Honours and awards Best Student Presentation Award, received at the 11th International Symposium on Special Topics in Chemical Propulsion and Energetic Material (ISICP) 2018, Stuttgart, Germany Memberships Since 2017: AIAA Member

Journal Articles

- “Evaluation Techniques for Optical Analysis of Hybrid Rocket Propulsion”, A. Petrarolo and M. Kobald, *Journal of Fluid Science and Technology (JFST)*, 2016
DOI: <https://doi.org/10.1299/jfst.2016jfst0028>
- “Hybrid Experimental Rocket Stuttgart: A Low-Cost Technology Demonstrator”, M. Kobald, U. Fischer, K. Tomilin, A. Petrarolo and C. Schmierer, *Journal of Spacecraft and Rockets*, Vol. 55, No. 2, 2018
DOI: <https://doi.org/10.2514/1.A34035>
- “Understanding Kelvin-Helmholtz Instability in Paraffin-Based Hybrid Rocket Fuels”, A. Petrarolo, M. Kobald and S. Schleichtriem, *Experiments in Fluids*, 59:62, 2018
DOI: <https://doi.org/10.1007/s00348-018-2516-1>
- “A Record Flight of the Hybrid Sounding Rocket HEROS 3”, M. Kobald, C. Schmierer, U. Fischer, K. Tomilin and A. Petrarolo, *Trans. JSASS Aerospace Tech. Japan*, Vol. 16, 2018
DOI: <https://doi.org/10.2322/tastj.16.312>
- “The HyEnD STERN Hybrid Sounding Rocket Project”, M. Kobald, C. Schmierer, U. Fischer, K. Tomilin and A. Petrarolo, *Progress in Propulsion Physics*, Vol. 11, pp. 25-64, 2019
DOI: <https://doi.org/10.1051/eucass/201911025>
- “Optical Analysis of the Liquid Layer Combustion of Paraffin-Based Hybrid Rocket Fuels”, A. Petrarolo, M. Kobald and S. Schleichtriem, *Acta Astronautica*, Vol. 158, pp. 313-322, 2019
DOI: <https://doi.org/10.1016/j.actaastro.2018.05.059>
- “Principal and Independent Component Analysis of Hybrid Combustion Flame”, A. Petrarolo, M. Kobald, H. K. Ciezki and S. Schleichtriem, *International Journal of Energetic Materials and Chemical Propulsion*, 18 (1), pp. 9-29, 2019
DOI: [10.1615/IntJEnergeticMaterialsChemProp.2019028035](https://doi.org/10.1615/IntJEnergeticMaterialsChemProp.2019028035)
- “Clustering of Paraffin-Based Hybrid Rocket Fuels Combustion Data”, A. Rüttgers, A. Petrarolo and M. Kobald, *Experiments in Fluids*, 61:4, 2020
DOI: <https://doi.org/10.1007/s00348-019-2837-8>

Conference Papers

- “Characterization of Advanced Hybrid Rocker Engines”, A. Petrarolo, C. Schmierer and M. Kobald, EUCASS 2015, Krakow, Poland
- “Test Campaign of a 10000 N Hybrid Rocket Engine”, M. Kobald, C. Schmierer and A. Petrarolo, EUCASS 2015, Krakow, Poland
- “Combustion Visualization and Characterization of Liquefying Hybrid Rocket Fuels”, M. Kobald, A. Petrarolo and S. Schlechtriem, 51st AIAA/SAE/ASEE Joint Propulsion Conference 2015, Orlando, USA
- “Evaluation Techniques for Optical Analysis of Hybrid Rocket Propulsion”, M. Kobald and A. Petrarolo, 12th International Conference on Fluid Dynamic (ICFD) 2015, Sendai, Japan
- “Optical Analysis of Hybrid Rocket Combustion with Decomposition Methods”, A. Petrarolo, M. Kobald and S. Schlechtriem, Space Propulsion Conference 2016, Rome, Italy
- “Optical Analysis of the Liquid Layer Combustion of Paraffin-Based Hybrid Rocket Fuels”, A. Petrarolo, M. Kobald and S. Schlechtriem, EUCASS 2017, Milan, Italy
- “Hybrid Sounding Rocket HEROS TRL 9”, M. Kobald, C. Schmierer, U. Fischer, K. Tomilin and A. Petrarolo, EUCASS 2017, Milan, Italy
- “A Record Flight of the Hybrid Sounding Rocket HEROS 3”, M. Kobald, C. Schmierer, U. Fischer, K. Tomilin and A. Petrarolo, 31st International Symposium on Space Technology and Science (ISTS) 2017, Matsuyama, Japan
- “Liquid Layer Combustion Visualization of Paraffin-Based Hybrid Rocket Fuels”, A. Petrarolo, M. Kobald and S. Schlechtriem, 53rd AIAA/SAE/ASEE Joint Propulsion Conference 2017, Atlanta, USA
- “Sounding Rocket HEROS – A Low Cost Hybrid Rocket Technology Demonstrator”, M. Kobald, C. Schmierer, U. Fischer, K. Tomilin, A. Petrarolo, P. Kysela, A. Pahler, J. Gauger, J. Breitingner, F. Hertel and B. Hochheimer, 53rd AIAA/SAE/ASEE Joint Propulsion Conference 2017, Atlanta, USA
- “Optical Analysis of Liquid Film Instabilities in Paraffin-Based Hybrid Rocket Fuels”, A. Petrarolo, M. Kobald, H. K. Ciezki and S. Schlechtriem, 68th International Astronautical Congress (IAC) 2017, Adelaide, Australia

- “Dimensionality Reduction of Hybrid Rocket Fuel Combustion Data”, A. Rüttgers and A. Petrarolo, ESCO 2018 - 6th European Seminar on Computing, Pilsen, Czech Republic
- “Investigation of the Kelvin-Helmholtz Instability Process in Liquefying Hybrid Rocket Fuels”, A. Petrarolo, M. Kobald and S. Schleichtriem, Space Propulsion Conference 2018, Sevilla, Spain
- “Visualization of Combustion Phenomena in Paraffin-Based Hybrid Rocket Fuels at Super Critical Pressures”, A. Petrarolo, M. Kobald and S. Schleichtriem, 54th AIAA/SAE/ASEE Joint Propulsion Conference 2018, Cincinnati, USA
- “A Visual Study of the Combustion Process in Paraffin-Based Hybrid Rocket Fuels”, A. Petrarolo, M. Kobald, H.K. Ciezki and S. Schleichtriem, 11th International Symposium on Special Topics in Chemical Propulsion and Energetic Material (ISICP) 2018, Stuttgart, Germany
- “Burning Phases Separation by Application of Clustering Algorithm to Hybrid Rocket Combustion Data”, A. Petrarolo, A. Rüttgers and M. Kobald, 32nd ISTS Conference 2019, Fukui, Japan
- “Modes Reconstruction of Hybrid Combustion Flame”, A. Petrarolo and M. Kobald, EUCASS 2019, Madrid, Spain
- “Data Clustering of Hybrid Rocket Combustion Flame”, A. Petrarolo, A. Rüttgers and M. Kobald, 55th AIAA/SAE/ASEE Joint Propulsion Conference 2019, Indianapolis, USA